Mitteilungen aus dem Institut für Mechanik

Lidija Stankovic

Describing multiple surface localised failure by means of strong discontinuities at finite strains

Heft Nr. 149

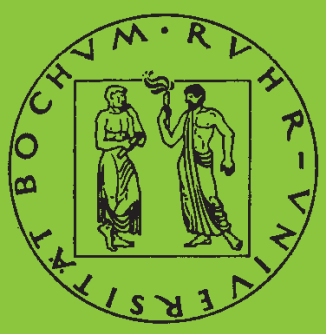

RUHR-UNIVERSITÄT BOCHUM

INSTITUT FÜR MECHANIK
RUHR-UNIVERSITÄT BOCHUM

Lidija Stanković

Describing multiple surface localised failure by means of strong discontinuities at finite strains

MITTEILUNGEN AUS DEM INSTITUT FÜR MECHANIK NR. 149

Februar 2009

Herausgeber:

Institut für Mechanik
Ruhr-Universität Bochum
D-44780 Bochum

ISBN 978-3-935892-27-8

Printed in Germany

Zusammenfassung

In dieser Arbeit wird der *Multiple Localisation Surface Approach* (MLSA) vorgestellt, der auf dem *Strong Discontinuity Approach* basiert und eine geometrisch nichtlineare Finite-Elemente-Anwendung darstellt. Er dient der Beschreibung lokalisierter Deformationen in Strukturen, die Materialversagen in der Form einer Entfestigung unterliegen. Die Haupteigenschaft des MLSA ist die simultane Ausbreitung von mehrfachen, sich überschneidenden Diskontinuitäten innerhalb eines jeden finiten Elementes. Die Flächentopologie und die Ausrichtung parallel zu einer der Elementseiten sind so gewählt, dass sie für die Beschreibung der Entfestigung in Materialien mit einer beliebigen Verteilung von bereits existierenden Mikrodefekten geeignet sind. Diese Wahl liefert einen aus numerischer Sicht zu bevorzugenden symmetrischen Tangentenoperator für die FE-Anwendung. Zwei alternative Formulierungen des MLSA werden im Detail beschrieben. Die implizite Formulierung ermöglicht die Einbindung plastizitätsbasierter kohäsiver Gesetze und kann auf ein breites Spektrum an Schädigungstheorien angewendet werden. Die explizite Formulierung eignet sich für numerische Simulationen eines lokalisierten Materialversagens, das plastischen Deformationen in Form von Gleitbändern unterliegt. Eine Validierung der vorgeschlagenen Ansätze findet abschließend anhand dreidimensionaler Beispiele statt.

Summary

The *Multiple Localisation Surface Approach* (MLSA), a geometrically nonlinear finite element application based on the *Strong Discontinuity Approach* which is used for the description of localised deformation in structures undergoing material failure in the form of strain softening, is presented in this thesis. The main property of the MLSA is the simultaneous propagation of multiple intersecting discontinuities within each element. The planar topology and the orientation parallel to one of the element sides for singular surfaces are chosen such to be suitable for the description of strain softening in materials with an arbitrary distribution of pre-existing micro-defects. This choice yields a numerically preferable, symmetric tangent operator in the finite element application. Two alternating formulations of the MLSA are described in detail. The implicit formulation allows the incorporation of any plasticity based cohesive law and can be applied to a broad range of damage theories as well. The explicit formulation can be employed for numerical simulations of localised failure in a wide range of materials experiencing plastic deformations in the form of slip bands. The basic properties of the proposed numerical solution are investigated in several three-dimensional numerical examples.

Vorwort

Die vorliegende Arbeit entstand während meiner Tätigkeit als wissenschaftliche Mitarbeiterin am Institut für Mechanik der Ruhr-Universität Bochum. Sie wurde im Rahmen des Projektes "Ein numerisches Homogenisierungsverfahren zur Bestimmung makroskopischer Materialkennwerte von Böden und Gesteinen basierend auf Oberflächeneigenschaften" von der Deutschen Forschungsgemeinschaft gefördert und von der Fakultät für Bau- und Umweltingenieurwesen der Ruhr-Universität Bochum als Dissertation angenommen.

Mein Dank gilt Herrn Prof. Dr.-Ing. Otto T. Bruhns und Herrn Prof. Dr.-Ing. Jörn Mosler für die Anregung zu dieser Arbeit und für die wissenschaftliche und persönliche Unterstützung bei ihrer Anfertigung.

Bei allen Mitarbeitern des Lehrstuhls für Technische Mechanik möchte ich mich für die angenehme und freundliche Arbeitsatmosphäre bedanken. Von der entgegengebrachten Hilfsbereitschaft und fast familierer Atmosphäre habe ich sehr profitiert.

Schließlich danke ich meiner Familie und insbesondere meinem Mann Zoran für ihre Unterstützung und ihren Zuspruch.

Bochum, im Februar 2009 Lidija Stanković

Referenten: Prof. Dr.-Ing. Otto T. Bruhns
Prof. Dr.-Ing. Jörn Mosler

Tag der Einreichung: 12.08.2008
Tag der mündlichen Prüfung: 02.12.2008

Contents

List of Figures

List of Tables

Conventions and Notations

Scalars (Latin characters - italic)

$\mathcal{D}$	energy dissipation
E	internal energy
H	entropy
$J(\mathbf{X}, t)$	Jacobian
m	mass
t	time
T	temperature

Scalars (Greek characters)

δ_{ij}	KRONECKER delta symbol
$\lambda_{1,2,3}$	principal stretches
λ, μ	LAMÉ constants
ρ_0	reference mass density
ρ	current mass density
ϕ	yield function
φ	ramp function
ψ_0	HELMHOLTZ free energy

Vectors (Latin characters - boldface roman)

$\mathbf{a}$	spatial acceleration
$\mathbf{A}$	material acceleration
$\mathbf{e}_{1,2,3}$	unit base vectors of a rectangular Cartesian coordinate system
$\mathbf{J}$	material displacement jump
$\mathbf{n}_{1,2,3}$	eigenvectors of a spatial tensor
$\mathbf{N}_{1,2,3}$	eigenvectors of a material tensor
$\mathbf{N}^{(\beta)}$	normal vector corresponding to the singular surface $\partial_s\Omega^{(\beta)}$
$\mathbf{R}$	residual
$\mathbf{u}$	displacement
$\mathbf{v}$	spatial velocity
$\mathbf{V}$	material velocity
$\mathbf{x}$	position vector in the current configuration
$\mathbf{X}$	position vector in the reference configuration

Vectors (Greek characters)

$\boldsymbol{\alpha}$	strain-like internal state variables

Second order tensors (Latin characters - boldface roman)

$\mathbf{b}$	left CAUCHY-GREEN deformation tensor

$\mathbf{C}$	right CAUCHY-GREEN deformation tensor
$\mathbf{e}$	ALMANSI strain tensor
$\mathbf{d}$	rate-of-deformation tensor
$\mathbf{E}$	GREEN-LAGRANGE strain tensor
$\mathbf{F}$	deformation gradient
$\mathbf{H}$	enhanced displacement gradient
$\mathbf{K}$	stiffness matrix
$\mathbf{l}$	velocity gradient
$\mathbf{t}$	spatial traction
$\mathbf{T}$	material traction
$\mathbf{P}$	first PIOLA-KIRCHOFF stress tensor
$\mathbf{S}$	second PIOLA-KIRCHOFF stress tensor
$[\![\mathbf{u}]\!]$	displacement jump
$\hat{\mathbf{u}}$	regular part of the displacement field
$\mathbf{U}$	right stretch tensor
$\mathbf{V}$	left stretch tensor
$\mathbf{w}$	spin tensor
$\mathbf{q}$	stress-like internal state variables

Second order tensors (Greek characters)

$\boldsymbol{\epsilon}^{\mathrm{p}}$	jump deformation tensor
$\boldsymbol{\sigma}$	CAUCHY stress tensor
$\boldsymbol{\Sigma}$	MANDEL stress tensor
$\boldsymbol{\tau}$	KIRCHOFF stress tensor

Fourth order tensors (Latin characters - boldface roman)

$\mathbf{c}$	spatial elastic tangent operator
$\mathbb{C}$	material elastic tangent operator
$\mathbb{C}^{\mathrm{e}}$	algorithmic tangent operator
$\mathbb{I}$	fourth order identity tensor
$\mathbb{I}^{\mathrm{sym}}$	symmetric fourth order identity tensor

Other symbols

Γ	boundary of the current configuration
Γ_0	boundary of the reference configuration
$\mathbb{E}_\sigma$	admissible stress space
$\mathbb{J}_{\mathrm{act}}$	set of active singular surfaces
Ω	current configuration
Ω_0	reference configuration
$\Omega^{\pm}$	current configuration of the bulk material
$\partial_{\mathrm{s}}\Omega$	singular surface

$\mathcal{H}_s$	HEAVISIDE function with respect to the discontinuity surface $\partial_s\Omega$

Superscripts

$(\cdot)^+$	right-hand limit at $\partial_s\Omega$
$(\cdot)^-$	left-hand limit at $\partial_s\Omega$
$(\cdot)^{(\beta)}$	quantity associated with the singular surface $\partial_s\Omega^{(\beta)}$
$(\cdot)^{tr}$	quantity associated with the trial state

Overlines

$\bar{(\cdot)}$	regular part of a tensorial quantity
$\tilde{(\cdot)}$	singular part of a tensorial quantity

1 Introduction

1.1 Motivation

One of the major challenges in the field of computational solid mechanics is the numerical simulation of material and structural failure. Such computations are necessary for the evaluation of the ultimate capacity of new materials and structures. Numerical methods for the calculation of limit situations close to intensive damage or collapse are designed to lead to a safe but practical estimation of the ultimate amount of loading. The Finite Element (FE) method, as an essential part of computer-aided design in engineering, is widely applied in calculations of this type. Therefore, a great amount of scientific effort is investigated in the enhancement of the FE tools for the treatment of such complex mechanical problems. Due to the very specific nature of the phenomenon of failure, the application of the FE method is not always a straightforward task. Namely, the failure of many engineering materials is often characterised by intense deformation modes restricted to narrow zones. Typical examples of such behaviour are the adiabatic shear-banding in metals, shear bands in soils, and localisation bands of cracking in brittle materials such as rocks and concrete. The technical importance of these highly localised zones lies in the fact that their occurrence which signifies the onset of failure, is a precursor to rapture. Localised deformation is regularly followed by a reduction in overall strength of the material as loading proceeds. This phenomenon is known as strain softening. In order to predict not only the ultimate load but also the post-peak softening response of the material, attention is drawn to creating numerical solutions that are robust and consistent. Although the general conditions for the occurrence of localised deformation are well understood and extensively analysed, the nature of the problem poses severe challenges to the numerical implementations. Due to the fact that the dimension of the narrow regions of localised strains is often distinctively smaller than the dimension of the structure, the phenomenon can be regarded as a multi-scale problem. In addition, the presence of strain softening which triggers the strain localisation leads by application of classical continuum models to the dependence of the numerical solution on the finite element discretization. The use of conventional FE method for the simulation of structural problems which involve localisation results in both a size and directional dependence on mesh topology. Additionally, the mesh refinement can lead to physically inappropriate solutions because energy dissipation in localisation zones decreases.
Various approaches have been developed in order to circumvent the mesh dependence of finite element based modelling of strain localisation: plastic evolution equations with an incorporated length scale ([Pietruszczak & Mroź 1981]), non-local approach ([Pijaudier-Cabot & Bažant 1987; Bažant & Pijaudier-Cabot 1988], weak-discontinuity approach ([Ortiz, Leroy & Needleman 1987]) and strong-discontinuity based approach ([Needleman

1990; DVORKIN, CUITIÑO & GIOIA 1990; SIMO, OLIVER & ARMERO 1993; ORTIZ & PANDOLFI 1999; MOËS, DOLBOW & BELYTSCHKO 1999]). Since the numerical model presented in this dissertation belongs to the class of strong-discontinuity based approaches, this group of numerical solutions is briefly presented in this introduction. Strong discontinuity approaches are based on the hypothesis of a discontinuous displacement field and implementation of cohesive laws ([DUGDALE 1960; BARENBLATT 1962]) connecting the traction vector to the discontinuity of the displacement field. Numerical implementations of strong discontinuities can be further separated in two general groups. The first group are the *interface elements* allowing the discontinuity of the displacement field only at the element boundaries ([NEEDLEMAN 1990; ORTIZ & PANDOLFI 1999]) and the *elements with an inner displacement jump* allowing the discontinuity of the displacement field inside the element. The latter can be branched into Strong Discontinuity Approach (SDA) [DVORKIN, CUITIÑO & GIOIA 1990; KLISINSKI, RUNESSON & STURE 1991; SIMO, OLIVER & ARMERO 1993; ARMERO & GARIKIPATI 1996] and EXtended Finite Element Method (X-FEM) ([MOËS, DOLBOW & BELYTSCHKO 1999; DOLBOW, MOËS & BELYTSCHKO 2002; SUKUMAR, MOËS, MORAN & BELYTSCHKO 2000]). SDA models use the enrichment of the displacement field on the element level and X-FEM utilises the Partition of Unity concept and nodal enrichments of the displacement field. Due to the fact that strong discontinuities in SDA are modelled element-wise, i.e. in an incompatible fashion, the numerical treatment of additional degrees of freedom resulting from their introduction is possible on the element or material point level. Further classification of the Strong Discontinuity Approach can be made according to the choice of the procedure for the elimination of the degrees of freedom associated with the discontinuity from the calculation. [ARMERO & GARIKIPATI 1996; LARSSON, STEINMANN & RUNESSON 1998; STEINMANN & BETSCH 2000; ARMERO 1999; OLIVER, HUESPE, PULIDO & SAMANIEGO 2003; GASSER & HOLZAPFEL 2003; CALLARI & ARMERO 2004] eliminate those degrees of freedom on the element level using the static condensation procedure. [BORJA 2000; MOSLER & MESCHKE 2000; MOSLER & MESCHKE 2001; MOSLER 2005A] suggest the elimination already at the material point level. This idea is extended to geometrically exact kinematics in [BORJA 2002; MOSLER 2006]. This short overview confirms that the decades of intense research in the field of constitutive modelling in the presence of localised deformation provided this field with a wealth of different numerical concepts. However, a need for fully three-dimensional, geometrically exact numerical solutions for the prediction of strain-softening still exists.

The method of choice for the numerical analysis of the localised failure in this work belongs to the class of SDAs. This choice is based on the following properties of the SDA. The possibility of an element-level condensation of additional degrees of freedom yields relatively inexpensive implementation, cf. [OLIVER, J., HUESPE, A.E. & SANCHEZ, P.J. 2006]. Additionally, [OLIVER,

J., HUESPE, A.E. & SANCHEZ, P.J. 2006] show that the computational costs of numerical implementation of SDA in the case of multiple localisation surfaces remain almost constant with an increase in the number of cracks. This thesis takes the SDA proposed by [MOSLER 2006] as a basis for the development of a new numerical model suitable for the description of the localised material failure in the presence of pre-existing micro-cracks. The factors responsible for localised deformation include, among others, initial imperfections and defects in the continuum. For instance, the ultimate load of jointed rocks is influenced by the roughness and orientation of pre-existing slip surfaces. Additionally, the evolution of those internal surfaces is very important. In order to study the influence of pre-existing microdefects on macroscopic properties of the material, an efficient numerical model based on finite element technology is developed. The essential properties of the implementation are:

- strong discontinuity kinematics
- fully three-dimensional model
- pre-existing defects in form of displacement discontinuities with known orientation
- symmetric formulation of the numerical procedure
- independence of the result from the spatial discretization
- simultaneous propagation of multiple localisation surfaces
- geometrically exact formulation

These characteristics ensure the applicability of the proposed model in the simulations of localised material failure in the presence of pre-existing defects, objectivity of the numerical results in the case of three-dimensional problems undergoing finite deformations, as well as the efficiency of the numerical procedure.

1.2 Outline

This dissertation is structured into six chapters. Subsequent to this introduction, a brief summary of selected topics in continuum mechanics and constitutive modelling, necessary for the development and understanding of the rest of this work, is given in Chapter 2. The introduction of basic notions in the finite kinematics of deformable bodies is followed by a brief overview of fundamental axioms of thermodynamics. Two different constitutive models, hyperelasticity and finite strain plasticity, are briefly explained with a special retrospect to the main principles of material modelling. For the reference, literature covering a wide range of topics in continuum mechanics is cited.

Chapter 3 is devoted to the extensive description of a numerical procedure for the modelling of material failure at finite strains by the Finite Element Method. In the opening sections, the kinematics of the Strong Discontinuity Approach (SDA), which is the core of the numerical implementation treated in this thesis, is proposed. The main trait of the SDA kinematics is the existence of a discontinuity in the displacement field which describes the motion of the body experiencing strain softening under loading. In order to accommodate this property, a corresponding deformation mapping with a continuous and a discontinuous part is created. The distinction between the singularity surface and the rest of the material is realised in the constitutive model by assuming a purely elastic bulk material and a strictly inelastic localised deformation. The application of the Enhanced Assumed Strain (EAS) concept in the kinematic frame renders constitutive equations similar to those of standard (finite) plasticity. A numerical finite element procedure for the solution of the constitutive model with a single discontinuity surface based on these facts is then presented. The numerical implementation does not require any assumption regarding neither the type of the finite elements, nor the constitutive behaviour. Any traction-separation law, connecting the displacement jump to the traction vector, can be applied. The topology and the orientation of the singularity are chosen such as to render a symmetric numerical formulation, i.e. singular surfaces are parallel to the sides of the tetrahedral finite elements. In this manner, the space of admissible internal surfaces spanned by the proposed numerical model is relatively rich and the continuity of the singular surface $\partial_s\Omega$ can be guaranteed.

As a next step, a simultaneous propagation of the multiple discontinuities inside finite elements is modelled. This advanced version of the SDA is presented in Chapter 4. Multiple Localisation Surface Approach (MLSA) leads to an alteration in the definition of the gradient of the localised deformation mapping which captures the influence of the multisurface singularities. The kinematics and the constitutive model of MLSA are defined with the assumption that the basic notions and postulates of the Strong Discontinuity Approach remain unchanged. The chapter offers a complete presentation of the necessary changes in the algorithm for the numerical implementation of SDA in the case of multisurface discontinuities. Two versions of the method, an implicit and an explicit MLSA are defined. They differ in the proposed form of the deformation gradient. The explicit formulation of MLSA is applicable for the type of inelastic behaviour involving sliding modes, which is characteristic for ductile metals and geomaterials.

The results of the application of MLSA in numerical simulations are presented in Chapter 5. The applicability and the performance of the presented three-dimensional finite element formulation is tested on three different numerical examples. First example is the evaluation of the ultimate load in a triaxial compression test of a soft rock sample. After that, a comparative analysis of

the explicit and the implicit formulation of MLSA is performed on a simulation of an uniaxial tension test of a bar. The chapter is concluded with an analysis of the crack propagation in a L-shaped slab.
The last part of the dissertation includes a summary and an outlook. Some remarks concerning possible further modifications of the proposed numerical model are given.

1.3 Mathematical notations

In addition to the conventions and notations defined on pages v to vii, some mathematical notations of importance for the understanding of the subsequent derivations are summarised here.
Tensor components are defined with respect to an orthogonal Cartesian coordinate system. The symmetric unit tensor of second order is given as

$$\mathbf{I} = \delta_{ij}\, \mathbf{e}_i \otimes \mathbf{e}_i \,. \tag{1.1}$$

Two different unit tensors of fourth order are defined. The non-symmetric tensor is

$$\mathbb{I} = (\delta_{im}\, \delta_{jn})\, \mathbf{e}_i \otimes \mathbf{e}_j \otimes \mathbf{e}_m \otimes \mathbf{e}_n \,, \tag{1.2}$$

while the symmetric unit tensor of fourth order has the form

$$\mathbb{I}^{\mathrm{sym}} = \frac{1}{2}\, (\delta_{im}\, \delta_{jn} + \delta_{in}\, \delta_{mj})\, \mathbf{e}_i \otimes \mathbf{e}_j \otimes \mathbf{e}_m \otimes \mathbf{e}_n \,. \tag{1.3}$$

Tensor operations are defined by

$$\begin{aligned}
\mathbf{a} \otimes \mathbf{b} &= a_i\, b_j\, \mathbf{e}_i \otimes \mathbf{e}_j \\
\mathbf{a} \cdot \mathbf{b} &= a_i\, b_i \\
\mathbf{A} \cdot \mathbf{B} &= A_{ij}\, B_{jk}\, \mathbf{e}_i \otimes \mathbf{e}_k \\
\mathbf{A} : \mathbf{B} &= A_{ij}\, B_{ij} \\
\mathbb{A} : \mathbf{B} &= \mathbb{A}_{ijmn}\, B_{mn}\, \mathbf{e}_i \otimes \mathbf{e}_j \\
\mathbb{A} : \mathbb{B} &= \mathbb{A}_{ijmn}\, \mathbb{B}_{mnkl}\, \mathbf{e}_i \otimes \mathbf{e}_j \otimes \mathbf{e}_k \otimes \mathbf{e}_l
\end{aligned} \tag{1.4}$$

for $i, j, k = 1, 2, 3$. Tensor operations defining trace, transpose and inverse have following definitions

$$\begin{aligned}
\mathrm{tr}\,(\mathbf{A}) &= A_{ii} \\
(\mathbf{A}^{\mathrm{T}})_{ij} &= A_{ji} \\
\mathbf{A} \cdot \mathbf{A}^{-1} &= \mathbf{I} \\
A_{ik}\, {A_{kj}}^{-1} = \delta_{ij} &= \begin{cases} 1 & : \quad i = j \\ 0 & : \quad i \neq j \end{cases} .
\end{aligned} \tag{1.5}$$

2 Continuum Mechanics

This chapter carries a brief summary of selected topics in continuum mechanics, necessary for the development and understanding of the main part of this work. In Section 2.1 a standard mathematical frame for the finite motion of deformable bodies is set. Section 2.2 offers a short overview of the mathematical description of the physical causes of the motion of the body and its deformation through axioms of thermodynamics. Section 2.3 postulates the main objective of constitutive modelling and draws attention to its main principles. The fundamentals of hyperelasticity and finite strain plasticity, as two constitutive models used in this work, are roughly sketched in Sections 2.4 and 2.5. This chapter is not intended as an introduction to continuum mechanics or constitutive modelling. It merely provides the minimum of constituents of both, necessary for the chapters to come. References for further investigation of the subject of continuum mechanics may include [TRUESDELL & TOUPIN 1960; TRUESDELL & NOLL 1965; WANG & TRUESDELL 1973; MARSDEN & HUGHES 1994; OGDEN 1997; ORTIZ 2003], and for the thorough analysis of modelling of dissipative materials [HILL 1950; LUBLINER 1997; SIMO & HUGHES 1998; SIMO 1998; ORTIZ 2002; XIAO, BRUHNS & MEYERS 2006].

2.1 Kinematics

2.1.1 Bodies and configurations

The object of interest is a *body*, mathematically defined as an oriented differentiable manifold $\mathcal{B}$ in $\mathbb{R}^3$ which can be covered by a global system of coordinates. Elements of this manifold are called *body-points* or *particles*. Any open submanifold of $\mathcal{B}$ is also a body and it is referred to as *subbody* of $\mathcal{B}$. A domain $\Omega_0 \subset \mathbb{R}^3$, defined as an open and connected set of particles bounded by the boundary Γ, is said to be the *initial configuration* of a certain body of interest $\mathcal{B}$ at time $t = 0$.

This configuration, shown in Figure 2.1, can also be used as a *reference configuration* and as an *undeformed configuration* in the analysis of the motion and the deformation of the body $\mathcal{B}$. The undeformed configuration is the configuration with respect to which the deformation of the body is measured. If not stated otherwise, it is to be assumed that the initial configuration, the reference configuration and the undeformed configuration coincide. A domain $\Omega \subset \mathbb{R}^3$, occupied by the body $\mathcal{B}$ at time t is the *current configuration*. It is also to be recognised as its *deformed configuration*.

A body $\mathcal{B}$, and consequently all its configurations, is associated with a scalar measure m, named the *mass distribution* or simply *mass*. The mass m can be assumed absolutely continuous for any configuration of the body, and therefore with a *mass density* ρ, which can depend on the configuration currently occupied by the body $\mathcal{B}$ (cf. [TRUESDELL & NOLL 1965]). Additionally, the

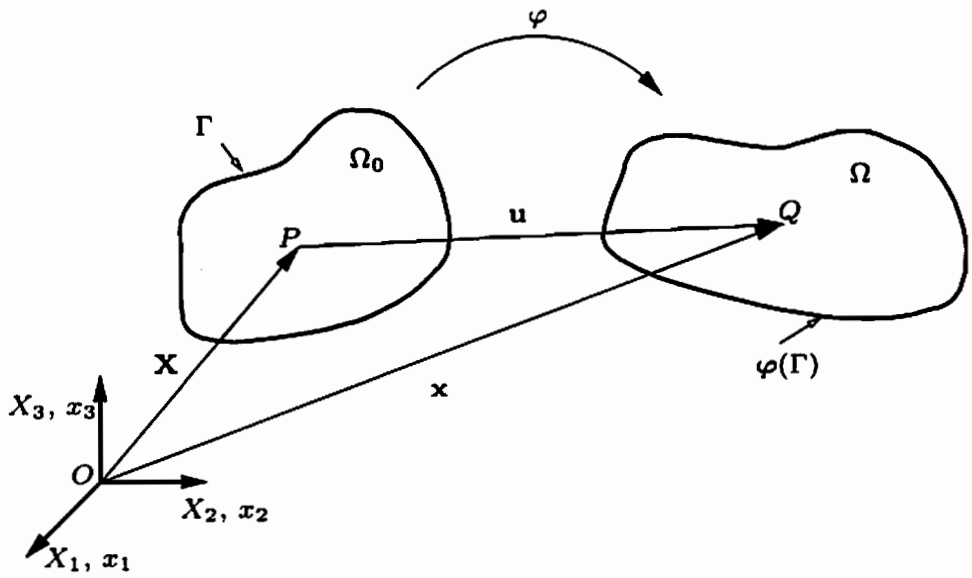

Figure 2.1: Reference and current configurations of a body $\mathcal{B}$.

considered body $\mathcal{B}$ belongs to the class of BOLTZMANN continua (see [BOLTZMANN 1874] for more details), without any supplementary rotational degrees of freedom.

2.1.2 Lagrangean and Eulerian coordinates

The physical reality of a body $\mathcal{B}$ is related to a three dimensional EUCLIDEAN point space (as defined e.g. in [OGDEN 1997]), and a real time axis by a *frame of reference*. It is then possible to mathematically describe it by a pair $\{\mathbf{x}, t\}$, including a point $\mathbf{x}$ and time t and known as an *event*. The totality of all events represents *space-time*. The position of an event can be defined only if a frame of reference, or equivalently an observer exists and this definition then depends on the choice of the observer. It is important to state here the distinction between a frame of reference and a coordinate system. The rectangular Cartesian coordinate system and its unit base vectors $\mathbf{e}_i$ are defined in an EUCLIDEAN point space and can in general case differ for the reference and the current configuration. Here, a unique coordinate system is used for both configurations.
The position vector $\mathbf{X}$ of each particle or *material point* P in the reference configuration Ω_0 is an one-to-one mapping between the particle and a set of real numbers (X_1, X_2, X_3), given by

$$\mathbf{X} = \sum_{i=1}^{3} X_i \mathbf{e}_i = X_i \mathbf{e}_i \,. \tag{2.1}$$

Here, X_i are the coordinates of P and $\mathbf{e}_i$ the unit vectors of an orthonormal base in a conveniently chosen rectangular Cartesian coordinate system, such as the one given in Figure 2.1. The second term in (2.1) shows the indicial notation of the summation, where indices repeated twice in a term are summed according to the Einstein notation. This reference frame is referred to as a *material* or *Lagrangean* reference frame and coordinates X_i are the *material* coordinates of the material point P.
The position vector $\mathbf{x}$ of a material point Q in the current configuration Ω is defined in the same manner, using the triple of Cartesian coordinates (x_1, x_2, x_3)

$$\mathbf{x} = \sum_{i=1}^{3} x_i \mathbf{e}_i = x_i \mathbf{e}_i \,. \tag{2.2}$$

This reference frame is a *spatial* or *Eulerian* reference frame and coordinates x_i are the *spatial* coordinates of the material point Q.

2.1.3 Deformation and motion

A *deformation* of the body $\mathcal{B}$ is a sufficiently smooth, one-to-one mapping $\varphi : \Omega \to \mathbb{R}^3$ of any of its configurations to the three-dimensional Euclidean space. The deformation mapping φ is an one-to-one correspondence between material points $P \in \Omega_0$ and $Q \in \Omega$. In vector form and in coordinates, φ takes the form

$$\mathbf{x} = \varphi(\mathbf{X}) \,, \quad x_i = \varphi_i(\mathbf{X}) \,, \quad \mathbf{X} \in \Omega_0 \,. \tag{2.3}$$

The transition from an undeformed configuration Ω_0 at time $t = 0$ to the deformed configuration Ω at time t is the total deformation of the body $\mathcal{B}$

$$\mathbf{x}(\mathbf{X}, t) = \varphi(\mathbf{X}, t) \,. \tag{2.4}$$

A *motion* of the body $\mathcal{B}$ is a mapping $\varphi : \Omega \times [t_1, t_2] \to \mathbb{R}^3$ which secures the injectivity of the mappings $\varphi(\cdot, t) \,, t \in [t_1, t_2]$, during the time interval $[t_1, t_2]$. The deformation φ is set to be an identity mapping at the time $t = 0$, i.e.

$$\mathbf{X} = \mathbf{x}(\mathbf{X}, 0) \equiv \varphi(\mathbf{X}, 0) \,. \tag{2.5}$$

If the description of the motion is done using $\mathbf{X}$ and t as independent variables it is a *material description.* If $\mathbf{x}$ and t are the independent variables it is a *spatial description.*

2.1.4 Displacement, velocity and acceleration

The *displacement* of the material point is introduced as a vector $\mathbf{u}(\mathbf{X}, t)$ connecting its place in the reference configuration P and its place in the current configuration Q (see Figure 2.1), so

$$\mathbf{u}(\mathbf{X}, t) = \mathbf{x}(\mathbf{X}, t) - \mathbf{X} = \varphi(\mathbf{X}, t) - \mathbf{X}\,. \tag{2.6}$$

The *material* or *Lagrangean velocity field* is the rate of change of the position vector $\mathbf{x}(\mathbf{X}, t)$ with respect to time, i.e. the first time derivative of the motion $\varphi(\mathbf{X}, t)$ and it is denoted by the superposed dot:

$$\mathbf{V}(\mathbf{X}, t) = \frac{\partial \varphi(\mathbf{X}, t)}{\partial t} = \frac{\partial \mathbf{x}(\mathbf{X}, t)}{\partial t} = \dot{\mathbf{x}} = \frac{\partial \mathbf{u}(\mathbf{X}, t)}{\partial t} = \dot{\mathbf{u}}\,. \tag{2.7}$$

With this definition in mind, the *material* or *Lagrangean acceleration field* is

$$\mathbf{A}(\mathbf{X}, t) = \frac{\partial \mathbf{V}(\mathbf{X}, t)}{\partial t} = \dot{\mathbf{V}} = \ddot{\mathbf{x}}\,. \tag{2.8}$$

The *spatial* or *Eulerian velocity field* is

$$\mathbf{v}(\mathbf{x}, t) = \frac{\partial \varphi(\mathbf{x}, t)}{\partial t} = \left(\frac{\partial \varphi}{\partial t} \circ \varphi^{-1}\right)(\mathbf{x}, t)\,. \tag{2.9}$$

Eulerian and Lagrangean velocity fields stand in following correlation:

$$\mathbf{v}(\mathbf{x}, t) = \mathbf{v}(\varphi(\mathbf{X}, t), t) = \frac{\partial \varphi(\mathbf{X}, t)}{\partial \mathbf{X}} \frac{\partial \mathbf{X}}{\partial t} + \frac{\partial \varphi(\mathbf{X}, t)}{\partial t} = \mathbf{V}(\mathbf{X}, t)\,. \tag{2.10}$$

The *spatial* or *Eulerian acceleration field* is

$$\mathbf{a}(\mathbf{x}, t) = \frac{\partial \mathbf{V}(\mathbf{x}, t)}{\partial t} = \left(\frac{\partial \mathbf{V}}{\partial t} \circ \varphi^{-1}\right)(\mathbf{x}, t)\,. \tag{2.11}$$

In (2.9) and (2.11) $\circ$ denotes the composition of mappings.
In general, one defines the *material (Lagrangean) time derivative* of any scalar, vectorial or tensorial field in Ω as a time derivative with material coordinate $\mathbf{X}$ held constant. The *spatial (Eulerian) time derivative* is the time derivative with spatial coordinate $\mathbf{x}$ held constant. They are related through

$$\left.\frac{\partial}{\partial t}\right|_{\mathbf{X}} = \left.\frac{\partial}{\partial t}\right|_{\mathbf{x}} + \mathbf{v} \cdot \operatorname{grad}\,. \tag{2.12}$$

2.1.5 Local deformation

An infinitesimal material neighbourhood of point P with the position vector $\mathbf{X}$ has a volume $\mathrm{d}V \in \Omega_0$, and an infinitesimal spatial neighbourhood of the point Q with the position vector $\mathbf{x}$ has a volume $\mathrm{d}v \in \Omega$ at time t.
If $\mathbf{X} + \mathrm{d}\mathbf{X}$ is a neighbouring point to P in $\mathrm{d}V$ and $\mathbf{x} + \mathrm{d}\mathbf{x}$ is a neighbouring point to Q in $\mathrm{d}v$, then

$$\mathbf{x} + \mathrm{d}\mathbf{x} = \boldsymbol{\varphi}(\mathbf{X} + \mathrm{d}\mathbf{X}, t) = \boldsymbol{\varphi}(\mathbf{X}, t) + \frac{\partial \boldsymbol{\varphi}(\mathbf{X}, t)}{\partial \mathbf{X}} \mathrm{d}\mathbf{X} \tag{2.13}$$

or, in coordinates

$$x_i + \mathrm{d}x_i = x_i + \frac{\partial \varphi_i(\mathbf{X}, t)}{\partial X_J} \mathrm{d}X_J \,, \quad \mathrm{d}x_i = \frac{\partial \varphi_i(\mathbf{X}, t)}{\partial X_J} \mathrm{d}X_J \,. \tag{2.14}$$

We define the *deformation gradient* of the motion $\boldsymbol{\varphi}$ as a second-order tensor field $\mathbf{F}$:

$$\mathbf{F} = \frac{\partial \boldsymbol{\varphi}(\mathbf{X}, t)}{\partial \mathbf{X}} \,, \quad F_{iJ} = \frac{\partial \varphi_i(\mathbf{X}, t)}{\partial X_J} \,. \tag{2.15}$$

This second-order tensor determines completely the deformation mapping of the infinitesimal vector $\mathrm{d}\mathbf{X}$ at $\mathbf{X}$ to the infinitesimal vector $\mathrm{d}\mathbf{x}$ at $\mathbf{x}$ and belongs to a group of orientation-preserving transformations.
According to [Ortiz 2003], if $\boldsymbol{\varphi}' : \Omega_0 \to \mathbb{R}^3$ and $\boldsymbol{\varphi}'' : \boldsymbol{\varphi}(\Omega_0)' \to \mathbb{R}^3$ are two successive deformations of Ω_0 and $\mathbf{F}'(\mathbf{X}, t)$ and $\mathbf{F}''(\boldsymbol{\varphi}'(\mathbf{X}, t), t)$ are the corresponding deformation gradients at material point $\mathbf{X}$ and time t, the total local deformation gradient is a multiplication of the incremental deformation gradients:

$$\mathbf{F}(\mathbf{X}, t) = \mathbf{F}''(\boldsymbol{\varphi}'(\mathbf{X}, t), t) \cdot \mathbf{F}'(\mathbf{X}, t) \,. \tag{2.16}$$

Following this line of thought and based on this multiplicative property of the deformation gradient $\mathbf{F}$, an *intermediate configuration* Ω_i can be introduced in order to materialise this composition rule (see Figure 2.2).
Since both reference frames are orthonormal, the square of the length of the infinitesimal spatial vector $\mathrm{d}\mathbf{x}$ is

$$\mathrm{d}s^2 = \mathrm{d}x_i \mathrm{d}x_i \,. \tag{2.17}$$

Using (2.14) it changes to

$$\mathrm{d}s^2 = F_{iI} F_{iJ} \mathrm{d}X_I \mathrm{d}X_J = C_{IJ} \mathrm{d}X_I \mathrm{d}X_J \,. \tag{2.18}$$

The second order tensor $\mathbf{C}$ is the *right* Cauchy-Green *deformation tensor*, which defines the deformation of the length of infinitesimal material vectors

$$\mathbf{C} = \mathbf{F}^{\mathrm{T}} \cdot \mathbf{F} \,, \quad C_{IJ} = F_{iI} F_{iJ} = C_{JI} \,. \tag{2.19}$$

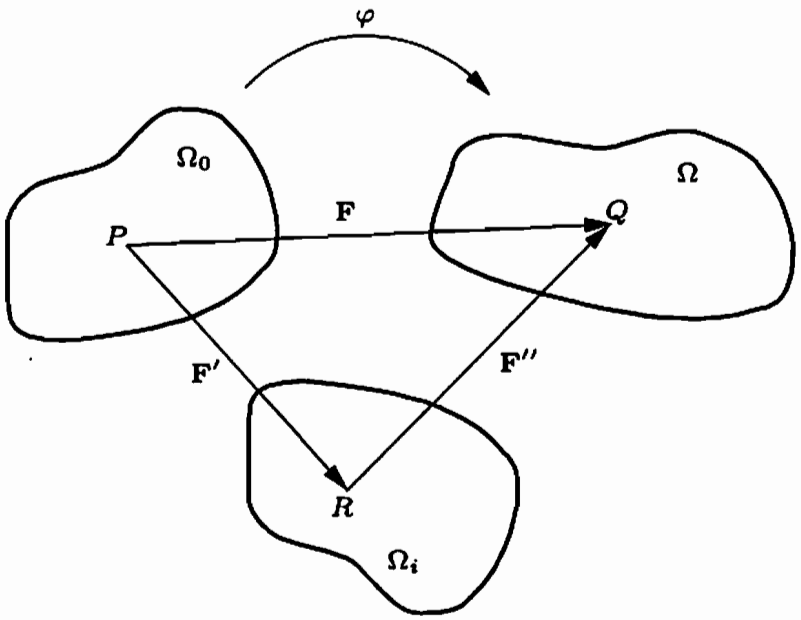

Figure 2.2: Multiplicative decomposition of the deformation gradient and the intermediate configuration of a body $\mathcal{B}$.

Volumes $\mathrm{d}V$ and $\mathrm{d}v$ are then related through

$$\frac{\mathrm{d}v}{\mathrm{d}V} = J(\mathbf{X}, t)\,, \tag{2.20}$$

where

$$J(\mathbf{X}, t) = \det \mathbf{F}(\mathbf{X}, t) \tag{2.21}$$

is the *Jacobian* of the deformation φ and a measure of the local *volumetric deformation.* Since the mapping φ is chosen to be an one-to-one mapping, the necessary condition to locally secure this choice is the local invertible nature of $\mathbf{F}$ and therefore

$$J(\mathbf{X}, t) \neq 0\,. \tag{2.22}$$

If $\mathrm{d}A$ is an infinitesimal material neighbouring area of P with the outward unit normal $\mathbf{N}$ and $\mathrm{d}a$ is an infinitesimal spatial neighbouring area of Q with the outward unit normal $\mathbf{n}$, then $\mathrm{d}A$ deforms into $\mathrm{d}a$ through PIOLA transformation

$$n_i \mathrm{d}a = J(\mathbf{X}, t) N_J F^{-1}_{Ji}(\mathbf{X}, t)\, \mathrm{d}A\,. \tag{2.23}$$

This transformation rule is also known as NANSON's formula.

2.1.6 Polar decomposition

Since the right CAUCHY-GREEN deformation tensor is symmetric and positive-definite, three positive real eigenvalues $\{\lambda_1^2, \lambda_2^2, \lambda_3^2\}$ and an orthonormal basis of eigenvectors $\{\mathbf{N}_1, \mathbf{N}_2, \mathbf{N}_3\}$ can be defined, such that the corresponding spectral decomposition of $\mathbf{C}$ has a form

$$\mathbf{C} = \sum_{i=1}^{3} \lambda_i^2 \, \mathbf{N}_i \otimes \mathbf{N}_i \,, \tag{2.24}$$

where the notation $\otimes$ represents a tensor or dyadic product of eigenvectors $\mathbf{N}_i$ as defined e.g. in [OGDEN 1997].
The eigenvectors $\{\mathbf{N}_1, \mathbf{N}_2, \mathbf{N}_3\}$ are usually referred to as the *material principal directions* and positive real numbers $\{\lambda_1, \lambda_2, \lambda_3\}$ are the *principal stretches.*
The three principal *invariants* of the right CAUCHY-GREEN deformation tensor $\mathbf{C}$ are to be calculated by

$$\begin{aligned} I_1(\mathbf{C}) &= \operatorname{tr}(\mathbf{C}) \,, \\ I_2(\mathbf{C}) &= \frac{1}{2}\left[\operatorname{tr}(\mathbf{C})^2 - \operatorname{tr}(\mathbf{C}^2)\right] \,, \\ I_3(\mathbf{C}) &= \det \mathbf{C} = J^2 \,. \end{aligned} \tag{2.25}$$

Based on the spectral decomposition of the right CAUCHY-GREEN deformation tensor (2.24), a positive definite, symmetric second-order tensor $\mathbf{U}$ is introduced as the *right stretch tensor*:

$$\mathbf{U} = \sum_{i=1}^{3} \lambda_i \, \mathbf{N}_i \otimes \mathbf{N}_i \,, \quad \mathbf{U}^2 = \mathbf{F}^{\mathrm{T}} \cdot \mathbf{F} = \mathbf{C} \,. \tag{2.26}$$

If the polar decomposition theorem (see [OGDEN 1997; MARSDEN & HUGHES 1994] for details) is exercised on the deformation gradient $\mathbf{F}$ using the right stretch tensor $\mathbf{U}$ and an orthogonal second-order tensor $\mathbf{R}$, it leads to its right polar decomposition

$$\mathbf{F} = \mathbf{R} \cdot \mathbf{U} \,. \tag{2.27}$$

Tensor $\mathbf{R}$ is the *rotation tensor* of the local deformation $\mathbf{F}$ with properties:

$$\mathbf{R}^{\mathrm{T}} \cdot \mathbf{R} = \mathbf{R} \cdot \mathbf{R}^{\mathrm{T}} = \mathbf{I} \quad \text{with} \quad \mathbf{I} = \delta_{ij} \, \mathbf{e}_i \otimes \mathbf{e}_i \quad \text{and} \quad \det \mathbf{R} = 1 \tag{2.28}$$

being the identity on Ω_0, $\mathbf{e}_i$ the unit vectors of an orthonormal base defined in (2.1) and δ_{ij} the KRONECKER *delta symbol*:

$$\delta_{ij} = \begin{cases} 1 & : \quad i = j \\ 0 & : \quad i \neq j \end{cases} \,. \tag{2.29}$$

Together with the right stretch tensor $\mathbf{U}$, the rotation tensor $\mathbf{R}$ decomposes the deformation φ with the gradient $\mathbf{F}$ into a pure stretch along the material principal directions followed by a finite rotation.
A motion φ with the gradient $\mathbf{F}$ can also be decomposed using a positive definite, symmetric second-order tensor named *left stretch tensor* $\mathbf{V}$ and the rotation tensor $\mathbf{R}$ and based on the polar decomposition theorem

$$\mathbf{F} = \mathbf{V} \cdot \mathbf{R}. \tag{2.30}$$

The spectral representation of $\mathbf{V}$ follows from its symmetry, positive definiteness, orthogonality of $\mathbf{R}$ and the spectral representation of $\mathbf{U}$:

$$\mathbf{V} = \mathbf{R} \cdot \left(\sum_{i=1}^{3} \lambda_i \mathbf{N}_i \otimes \mathbf{N}_i \right) \cdot \mathbf{R}^{\mathrm{T}} = \sum_{i=1}^{3} \lambda_i \left(\mathbf{R}\mathbf{N}_i \right) \otimes \left(\mathbf{R}\mathbf{N}_i \right) = \sum_{i=1}^{3} \lambda_i \, \mathbf{n}_i \otimes \mathbf{n}_i \,. \tag{2.31}$$

The directions $\mathbf{n}_i$ are the *spatial principal directions*, which are obtained by applying the rotation $\mathbf{R}$ to the material principal directions. The *left* CAUCHY-GREEN *deformation tensor* is introduced as

$$\mathbf{b} = \mathbf{V}^2 = \mathbf{F} \cdot \mathbf{F}^{\mathrm{T}}. \tag{2.32}$$

This polar decomposition of $\mathbf{F}$ is called the left polar decomposition and it interprets the deformation φ as a finite rotation followed by a pure stretch along the spatial principal directions.

2.1.7 Strain measures

If the change in the length of the infinitesimal material vector $\mathrm{d}\mathbf{X}$ after the deformation φ is to be evaluated, according to (2.18) and (2.19) it will read

$$\begin{aligned} \mathrm{d}s^2 - \mathrm{d}S^2 &= F_{iI} F_{iJ} \mathrm{d}X_I \mathrm{d}X_J - \mathrm{d}X_I \mathrm{d}X_I \\ &= \mathrm{d}X_I \left(F_{iI} F_{iJ} - \delta_{IJ} \right) \mathrm{d}X_J \\ &= \mathrm{d}\mathbf{X} \left(\mathbf{F}^{\mathrm{T}} \cdot \mathbf{F} - \mathbf{I} \right) \mathrm{d}\mathbf{X} \end{aligned} \tag{2.33}$$

in the reference configuration and

$$\begin{aligned} \mathrm{d}s^2 - \mathrm{d}S^2 &= \mathrm{d}x_i \mathrm{d}x_i - F_{Ii}^{-1} F_{Ij}^{-1} \mathrm{d}x_i \mathrm{d}x_j \\ &= \mathrm{d}x_i \left(\delta_{ij} - F_{Ii}^{-1} F_{Ij}^{-1} \right) \mathrm{d}x_j \\ &= \mathrm{d}\mathbf{x} \left(\mathbf{I} - \mathbf{F}^{-\mathrm{T}} \cdot \mathbf{F}^{-1} \right) \mathrm{d}\mathbf{x} \end{aligned} \tag{2.34}$$

in the current configuration. This change in length and relative direction is loosely called *strain*. The necessary and sufficient condition for the material

to be *unstrained* at $\mathbf{X}$ is that the right-hand side (RHS) of the (2.33) vanishes for arbitrary $\mathrm{d}\mathbf{X}$:

$$\mathbf{F}^{\mathrm{T}} \cdot \mathbf{F} = \mathbf{I}. \tag{2.35}$$

This condition allows for the deformation gradient in the form of rigid rotation $\mathbf{F} = \mathbf{R}$, which leads to the deformation φ in the form of rigid body motion with zero strain. A rigid body motion in general consists of a rigid translation $\mathbf{x}_{\mathrm{T}}(t)$ and a rigid rotation $\mathbf{R}(t)$:

$$\mathbf{x}(\mathbf{X}, t) = \mathbf{x}_{\mathrm{T}}(t) + \mathbf{R}(t) \cdot \mathbf{X}. \tag{2.36}$$

If condition (2.35) is satisfied for all $\mathbf{X}$ in Ω_0, then the deformation φ is globally described by (2.36) and the body $\mathcal{B}$ is unstrained.
If condition (2.35) is not satisfied at $\mathbf{X}$, then the material is *strained* and an acceptable tensor measure of finite strain is to be defined. According to [HILL 1968], certain families of finite strain measures can be described using the principal stretches $\{\lambda_1, \lambda_2, \lambda_3\}$ and material or spatial principal directions $\{\mathbf{N}_1, \mathbf{N}_2, \mathbf{N}_3\}$ and $\{\mathbf{n}_1, \mathbf{n}_2, \mathbf{n}_3\}$, depending on the choice of the description:

$$\mathbf{E}(\mathbf{U}) = \sum_{i=1}^{3} f(\lambda_i)\, \mathbf{N}_i \otimes \mathbf{N}_i \tag{2.37}$$

$$\mathbf{e}(\mathbf{V}) = \sum_{i=1}^{3} f(\lambda_i)\, \mathbf{n}_i \otimes \mathbf{n}_i \tag{2.38}$$

with $f(\lambda_i)$ being any sufficiently smooth and monotone function with properties

$$f(1) = 0, \quad f'(1) = 1. \tag{2.39}$$

With these conditions, it is ensured that all strain measures defined above are such that an increase in the length of the infinitesimal material vector $\mathrm{d}\mathbf{X}$ after the deformation φ leads to the increase in the corresponding strain, and that near the reference configuration they all agree to first order. One such family of functions is given by

$$f(\lambda_i) = \begin{cases} \left(\lambda_i^{2m} - 1\right)/2m & , \quad m \neq 0 \\ \ln(\lambda_i) & , \quad m = 0 \end{cases}. \tag{2.40}$$

For $m = 1$, (2.37) gives the strain measure known as GREEN-LAGRANGE *strain tensor*

$$\mathbf{E} = \frac{1}{2}\left(\mathbf{F}^{\mathrm{T}} \cdot \mathbf{F} - \mathbf{I}\right). \tag{2.41}$$

If $m = -1$, the strain measure resulting from (2.38) is the ALMANSI *strain tensor*

$$\mathbf{e} = \frac{1}{2}\left(\mathbf{I} - \mathbf{F}^{-\mathrm{T}} \cdot \mathbf{F}^{-1}\right). \tag{2.42}$$

If $m = 0$ the resulting strain measure is the HENCKY *strain tensor.*
A spatial gradient of the spatial velocity field $\mathbf{v}$ is another measure of local deformation rate which leads to a strain measure. This gradient is named *velocity gradient* and it is to be calculated as

$$\mathbf{l} = \frac{\partial \mathbf{v}(\mathbf{x}, t)}{\partial \mathbf{x}} = \operatorname{grad} \mathbf{v} \quad \text{or} \quad l_{ij} = \frac{\partial v_i}{\partial x_j} . \tag{2.43}$$

In order to find the correlation between the velocity gradient and the deformation gradient, first the material time derivative of the deformation gradient $\mathbf{F}$ is evaluated

$$\dot{\mathbf{F}} = \frac{\partial}{\partial t} \left(\frac{\partial \boldsymbol{\varphi}(\mathbf{X}, t)}{\partial \mathbf{X}} \right) = \frac{\partial \mathbf{V}(\mathbf{X}, t)}{\partial \mathbf{X}} = \operatorname{Grad} \mathbf{V} . \tag{2.44}$$

If this result is used together with the fact that for each vector field $\mathbf{V}(\mathbf{X}, t) = \mathbf{v}(\mathbf{x}, t) \in \Omega$

$$\operatorname{Grad} \mathbf{V} = \operatorname{grad} \mathbf{v} \cdot \mathbf{F} , \tag{2.45}$$

the velocity gradient and the deformation gradient are connected by the relation

$$\dot{F}_{iJ} = L_{ij} F_{jJ} \quad \text{or} \quad \dot{\mathbf{F}} = \mathbf{l} \cdot \mathbf{F} . \tag{2.46}$$

The velocity gradient tensor can be decomposed into symmetric and skew-symmetric parts by

$$\mathbf{l} = \frac{1}{2} \left(\mathbf{l} + \mathbf{l}^{\mathrm{T}} \right) + \frac{1}{2} \left(\mathbf{l} - \mathbf{l}^{\mathrm{T}} \right) . \tag{2.47}$$

The symmetric part of the velocity gradient is the *rate-of-deformation tensor* $\mathbf{d}$:

$$\mathbf{d} = \frac{1}{2} \left(\mathbf{l} + \mathbf{l}^{\mathrm{T}} \right) \quad \text{or} \quad d_{ij} = \frac{1}{2} \left(\frac{\partial v_i}{\partial x_j} + \frac{\partial v_j}{\partial x_i} \right) . \tag{2.48}$$

The skew-symmetric part of the velocity gradient is the *spin tensor* $\mathbf{w}$:

$$\mathbf{w} = \frac{1}{2} \left(\mathbf{l} - \mathbf{l}^{\mathrm{T}} \right) \quad \text{or} \quad w_{ij} = \frac{1}{2} \left(\frac{\partial v_i}{\partial x_j} - \frac{\partial v_j}{\partial x_i} \right) . \tag{2.49}$$

The spin tensor $\mathbf{w}$ measures the local rate of rigid rotation of the infinitesimal spatial neighbourhood at $\mathbf{x}$ and the rate-of deformation tensor $\mathbf{d}$ represents the local rate of change of its length. Therefore, the velocity gradient $\mathbf{l}$ can be summed up to a measure of the local rate of distortion (change of length and change of orientation) of the infinitesimal spatial neighbourhood at $\mathbf{x}$.

2.2 Conservation laws

After the kinematics of a body in motion is postulated and described by a set of variables, the action of the outside world on this body in motion and the interactions between different parts of the body can be addressed. In this section, a body $\mathcal{B}$ in motion through the deformation mapping $\varphi : \mathcal{B} \times [t_1, t_2] \rightarrow \mathbb{R}^3$ and occupying the space Ω at time $t \in [t_1, t_2]$ is under investigation.

2.2.1 Conservation of mass

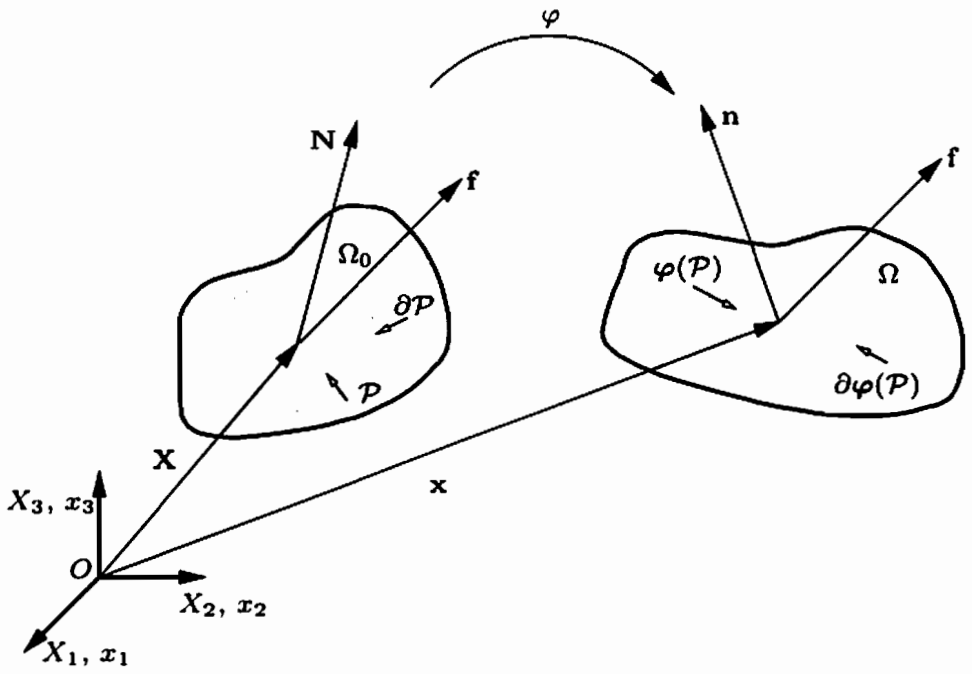

Figure 2.3: Forces acting on a body $\mathcal{B}$.

If subbody $\mathcal{P}$ is any part of the body $\mathcal{B}$ occupying the reference configuration Ω_0 at time $t = 0$ and current configuration Ω at time t (see Figure 2.3), $\rho_0 : \Omega_0 \rightarrow \mathbb{R}$ the referential mass density per unit undeformed volume and $\rho : \Omega \rightarrow \mathbb{R}$ the current mass density per unit deformed volume, then the *mass* contained in $\mathcal{P}$ is (for closed systems)

$$m(\mathcal{P}) = \int_{\mathcal{P}} \rho_0 \, \mathrm{d}V = \int_{\varphi(\mathcal{P})} \rho \, \mathrm{d}v \,. \tag{2.50}$$

The principle of mass conservation states that the mass contained in any subbody must remain constant in time, i.e.

$$\frac{\mathrm{d}m}{\mathrm{d}t}(\mathcal{P}) = \frac{\mathrm{d}}{\mathrm{d}t} \int_{\mathcal{P}} \rho_0 \, \mathrm{d}V = \frac{\mathrm{d}}{\mathrm{d}t} \int_{\varphi(\mathcal{P})} \rho \, \mathrm{d}v = 0 \,, \quad \forall \mathcal{P} \subset \Omega \,. \tag{2.51}$$

Here, both the material and the spatial form of the integral statement are given.
If the domain of integration in the material form of (2.51) is assumed not dependent on time for all $\mathcal{P}$, the local statement of the conservation of mass is obtained by simply removing the integrand:

$$\dot{\rho_0} = 0\,, \quad \text{in}\,\mathcal{P}\,. \tag{2.52}$$

Since the spatial domain of integration depends on time, the local spatial form of the conservation of mass cannot be determined in the same straightforward manner. However, if REYNOLD*'s transport theorem* which states that for any spatial field f and subbody $\mathcal{P}$

$$\frac{\mathrm{d}}{\mathrm{d}t}\int\limits_{\varphi(\mathcal{P})} f\,\mathrm{d}v = \int\limits_{\varphi(\mathcal{P})} \left(\dot{f} + f\mathrm{div}\mathbf{v}\right)\mathrm{d}v \tag{2.53}$$

is applied to the spatial form of (2.51), it leads to

$$\frac{\mathrm{d}m}{\mathrm{d}t}(\mathcal{P}) = \int\limits_{\varphi(\mathcal{P})} (\dot{\rho} + \rho\,\mathrm{div}\mathbf{v})\,\mathrm{d}v \tag{2.54}$$

with the material time derivative $\dot{(\,)}$, spatial divergence operator div and spatial velocity field $\mathbf{v}$. Since this identity must hold for all $\mathcal{P}$, the local spatial statement of the conservation of mass is

$$\dot{\rho} + \rho\,\mathrm{div}\mathbf{v} = 0\,, \quad \text{in}\,\varphi(\mathcal{P})\,. \tag{2.55}$$

2.2.2 Conservation of linear and angular momentum and stress measures

For all bodies $\mathcal{B}$, the *linear momentum* contained in subbody $\mathcal{P}$ is defined by

$$\mathcal{L}(\mathcal{P}) = \int\limits_{\mathcal{P}} \rho_0 \mathbf{V}\mathrm{d}V = \int\limits_{\varphi(\mathcal{P})} \rho\,\mathbf{v}\mathrm{d}v\,. \tag{2.56}$$

Here, $\mathbf{V}$ is the material velocity field and $\mathbf{v}$ is the spatial velocity field defined in (2.7) and (2.9).
If the body $\mathcal{B}$ occupying the space Ω at any time t and its motion φ are given (see Figure 2.3), a *system of forces* acting on any part $\mathcal{P}$ of the body $\mathcal{B}$ consists of the *external body force* acting across the domain $\mathcal{P}$ (e.g. gravity), and the *traction* or *contact force* acting across the boundary $\partial\mathcal{P}$ of $\mathcal{P}$. The starting assumption is that all acting forces are continuously distributed.

The differential body force $\mathrm{d}\mathbf{f}_\mathbf{b}$ acting on an infinitesimal material neighbourhood with volume $\mathrm{d}V$ at $\mathbf{X} \in \Omega_0$ or on an infinitesimal spatial neighbourhood with volume $\mathrm{d}v$ at $\mathbf{x} \in \Omega$ at time t is

$$\mathrm{d}\mathbf{f}_\mathbf{b} = \rho_0(\mathbf{X},t)\,\mathbf{B}(\mathbf{X},t)\,\mathrm{d}V = \rho(\varphi(\mathbf{X},t),t)\,\beta(\mathbf{X},t)\,\mathrm{d}v\,, \tag{2.57}$$

where $\mathbf{B}(\mathbf{X},t)$ and $\beta(\varphi(\mathbf{X},t),t)$ are vector fields of material and spatial body-force density per unit mass or simply material and spatial *body force*, and ρ_0 and ρ are the referential and current mass density per corresponding unit volume.
The differential contact force $\mathrm{d}\mathbf{f}_\mathbf{t}$ acting on an infinitesimal material neighbourhood with area $\mathrm{d}S$ at $\mathbf{X} \in \partial\mathcal{P}$ or on an infinitesimal spatial neighbourhood with area $\mathrm{d}s$ at $\mathbf{x} \in \partial\varphi(\mathcal{P})$ at time t is

$$\mathrm{d}\mathbf{f}_\mathbf{t} = \mathbf{T}(\mathbf{N},\mathbf{X},t)\,\mathrm{d}S = \mathbf{t}(\mathbf{n},\mathbf{x},t)\,\mathrm{d}s\,. \tag{2.58}$$

Vector fields $\mathbf{T}(\mathbf{N},\mathbf{X},t)$ and $\mathbf{t}(\mathbf{n},\mathbf{x},t)$ are the *material and spatial traction* per unit undeformed/deformed area defined according to the *stress principle* as given e.g. in [TRUESDELL & NOLL 1965], as functions of position, time and unit outward normal $\mathbf{N}$ at $\mathbf{X} \in \partial\mathcal{P}$ or $\mathbf{n}$ at $\mathbf{x} \in \partial\varphi(\mathcal{P})$.
If the additivity of forces is applied, the *total resultant* of all forces acting on $\mathcal{P}$ is to be calculated from the total body force and total contact force acting on $\mathcal{P}$ by

$$\begin{aligned}\mathbf{f}(\mathcal{P}) &= \int_{\mathcal{P}} \rho_0\,\mathbf{B}\,\mathrm{d}V + \int_{\partial\mathcal{P}} \mathbf{T}(\mathbf{N})\,\mathrm{d}S \\ &= \int_{\varphi(\mathcal{P})} \rho\beta\,\mathrm{d}v + \int_{\partial\varphi(\mathcal{P})} \mathbf{t}(\mathbf{n})\,\mathrm{d}s\,.\end{aligned} \tag{2.59}$$

The principle of conservation of linear momentum states that

$$\frac{\mathrm{d}\mathcal{L}}{\mathrm{d}t}(\mathcal{P}) = \mathbf{f}(\mathcal{P})\,, \quad \forall\mathcal{P} \subset \Omega\,. \tag{2.60}$$

If (2.56) and (2.59) are used in (2.60), this statement has the following form in material description

$$\frac{\mathrm{d}}{\mathrm{d}t}\int_{\mathcal{P}} \rho_0\mathbf{V}\mathrm{d}V = \int_{\mathcal{P}} \rho_0\,\mathbf{B}\,\mathrm{d}V + \int_{\partial\mathcal{P}} \mathbf{T}(\mathbf{N})\,\mathrm{d}S\,, \tag{2.61}$$

and its spatial form is

$$\frac{\mathrm{d}}{\mathrm{d}t}\int_{\varphi(\mathcal{P})} \rho\,\mathbf{v}\mathrm{d}v = \int_{\varphi(\mathcal{P})} \rho\beta\,\mathrm{d}v + \int_{\partial\varphi(\mathcal{P})} \mathbf{t}(\mathbf{n})\,\mathrm{d}s\,. \tag{2.62}$$

Two statements can be made about the *material traction* per unit undeformed area $\mathbf{T}(\mathbf{N}, \mathbf{X}, t)$ if the motion φ of the body $\mathcal{B}$ conserves linear momentum. The first follows the NEWTON*'s law of action and reaction* and states that

$$\mathbf{T}(-\mathbf{N}) = -\mathbf{T}(\mathbf{N}), \quad \mathbf{T}(\mathbf{N}) + \mathbf{T}(-\mathbf{N}) = \mathbf{0}. \tag{2.63}$$

The second is the CAUCHY*'s Tetrahedron Theorem*, which states that there exists a *stress-tensor field* $\mathbf{P}$ such that the traction field $\mathbf{T}(\mathbf{N})$ is linear in the unit normal:

$$\mathbf{T}(\mathbf{N}) = \mathbf{P} \cdot \mathbf{N}, \quad T_I(\mathbf{N}) = P_{IJ} N_J. \tag{2.64}$$

The stress-tensor $\mathbf{P}$ is the *first* PIOLA-KIRCHOFF *stress tensor* and it measures the actual contact force when it is taken per unit undeformed area.
The first RHS of (2.59) can be transformed under the assumption of conservation of mass by bringing the time derivative under the integral and using CAUCHY's theorem and the *divergence theorem* as given in [TRUESDELL & TOUPIN 1960]:

$$\int_{\mathcal{P}} (\rho_0 \mathbf{A} - \rho_0 \mathbf{B} - \mathrm{Div}\mathbf{P}) \, \mathrm{d}V = 0, \tag{2.65}$$

with the material divergence operator Div and the material acceleration $\mathbf{A}$ defined in (2.8). Taking into account that this identity must hold for all $\mathcal{P}$ leads to the localised material form of conservation of linear momentum:

$$\mathrm{Div}\mathbf{P} + \rho_0 \mathbf{B} = \rho_0 \mathbf{A}, \quad \text{in } \mathcal{P}. \tag{2.66}$$

When (2.64) is applied in (2.59), the following statement can be made

$$\int_{\partial\mathcal{P}} \mathbf{T}(\mathbf{N}) \, \mathrm{d}S = \int_{\partial\mathcal{P}} \mathbf{P}\mathbf{N} \mathrm{d}S = \int_{\partial\varphi(\mathcal{P})} \mathbf{t}(\mathbf{n}) \, \mathrm{d}s. \tag{2.67}$$

If surface integrals in (2.67) are transformed according to the NANSON's formula given in (2.23), it becomes

$$\int_{\partial\varphi(\mathcal{P})} \left[\mathbf{t}(\mathbf{n}) - \left(J^{-1}\mathbf{P} \cdot \mathbf{F}^{\mathrm{T}}\right)\mathbf{n}\right] \mathrm{d}s = \int_{\partial\varphi(\mathcal{P})} \left[\mathbf{t}(\mathbf{n}) - \boldsymbol{\sigma} \cdot \mathbf{n}\right] \mathrm{d}s = \mathbf{0}. \tag{2.68}$$

Since this relation must hold for all $\mathcal{P}$:

$$\mathbf{t}(\mathbf{n}) = \boldsymbol{\sigma} \cdot \mathbf{n}, \quad \boldsymbol{\sigma} = J^{-1}\mathbf{P} \cdot \mathbf{F}^{\mathrm{T}}. \tag{2.69}$$

The stress-tensor field $\boldsymbol{\sigma}$ is referred to as the CAUCHY *stress tensor* or *true stress tensor* and it measures the actual contact force when it is taken per unit deformed area.

The localised form of (2.68) is derived using the REYNOLD's transport theorem given in (2.53) and the divergence theorem as given in [TRUESDELL & TOUPIN 1960]:

$$\int_{\varphi(\mathcal{P})} (\rho\,\mathbf{a} - \rho\,\boldsymbol{\beta} - \operatorname{div}\boldsymbol{\sigma})\,\mathrm{d}v = 0 \quad \Rightarrow \quad \operatorname{div}\boldsymbol{\sigma} + \rho\,\boldsymbol{\beta} = \rho\,\mathbf{a}, \quad \text{in}\,\varphi(\mathcal{P})\,. \tag{2.70}$$

Here, the fact that the left-hand side (LHS) of the statement (2.70) must hold for all $\mathcal{P}$ is exploited. Equations (2.66) and (2.70) are the material and the spatial form of CAUCHY*'s first law of motion.*
If $\mathcal{G}(\mathcal{P}) \in \mathbb{R}^3$ is the total angular momentum contained in the subbody $\mathcal{P}$:

$$\mathcal{G}(\mathcal{P}) = \int_{\varphi(\mathcal{P})} \mathbf{x} \times \rho\,\mathbf{v}\mathrm{d}v\,, \tag{2.71}$$

and $\mathcal{M}(\mathcal{P}) \in \mathbb{R}^3$ is the resultant moment of all forces acting on $\mathcal{P}$:

$$\mathcal{M}(\mathcal{P}) = \int_{\varphi(\mathcal{P})} \mathbf{x} \times \rho\,\boldsymbol{\beta}\,\mathrm{d}v + \int_{\partial\varphi(\mathcal{P})} \mathbf{x} \times \mathbf{t}\,(\mathbf{n})\,\mathrm{d}s\,, \tag{2.72}$$

then the principle of angular momentum states that

$$\frac{\mathrm{d}\mathcal{G}}{\mathrm{d}t}(\mathcal{P}) = \mathcal{M}\,(\mathcal{P})\,, \quad \forall \mathcal{P} \subset \Omega\,. \tag{2.73}$$

Assuming the conservation of mass and applying (2.69) to the integral form of this identity in spatial form

$$\int_{\varphi(\mathcal{P})} \mathbf{x} \times \rho\,\mathbf{v}\mathrm{d}v = \int_{\varphi(\mathcal{P})} \mathbf{x} \times \rho\,\boldsymbol{\beta}\,\mathrm{d}v + \int_{\partial\varphi(\mathcal{P})} \mathbf{x} \times \mathbf{t}\,(\mathbf{n})\,\mathrm{d}s \tag{2.74}$$

leads to the CAUCHY*'s second law of motion* which states that for a mass, linear and angular momentum conserving motion of a body $\mathcal{B}$ the CAUCHY stress tensor $\boldsymbol{\sigma}$ is symmetric, i.e.

$$\sigma_{ij} = \sigma_{ji}\,. \tag{2.75}$$

The symbol $\times$ denotes the cross-product of two vectors.
The first PIOLA-KIRCHOFF stress tensor $\mathbf{P}$ is not, in general, a symmetric tensor. In order to provide a symmetric tensor representation of the stress in the reference configuration, the *second* PIOLA-KIRCHOFF *stress tensor* $\mathbf{S}$ is introduced:

$$\mathbf{S} = \mathbf{F}^{-1} \cdot \mathbf{P} = J\,\mathbf{F}^{-1} \cdot \boldsymbol{\sigma} \cdot \mathbf{F}^{-\mathrm{T}}\,. \tag{2.76}$$

The second PIOLA-KIRCHOFF stress tensor $\mathbf{S}$ is a symmetric tensor if and only if CAUCHY's second law of motion holds.
An additional stress measure to be introduced here is the KIRCHHOFF *stress tensor*

$$\tau = J\sigma = \mathbf{F} \cdot \mathbf{S} \cdot \mathbf{F}^{\mathrm{T}} . \tag{2.77}$$

This stress measure is also known as weighted CAUCHY stress tensor and can be useful in some constitutive models.

2.2.3 Principal of virtual work

For each body in motion $\mathcal{B}$, occupying the configuration Ω_0 with boundary Γ at time $t = 0$ and the configuration Ω with the boundary $\varphi(\Gamma)$ at time t, a set of boundary conditions can be prescribed:

$$\begin{aligned} &\varphi = \bar{\varphi} \quad \text{on} \quad \Gamma_u \\ &\mathbf{P} \cdot \mathbf{N} = \bar{\mathbf{T}} \quad \text{on} \quad \Gamma_\sigma \quad \text{or} \quad \sigma \cdot \mathbf{n} = \bar{\mathbf{t}} \quad \text{on} \quad \varphi(\Gamma_\sigma) . \end{aligned} \tag{2.78}$$

Here, $\bar{\varphi}$ is the prescribed deformation mapping across the *displacement* or DIRICHLET boundary Γ_u, $\bar{\mathbf{T}}$ are the prescribed material tractions across the *traction* or NEUMANN boundary Γ_σ and $\bar{\mathbf{t}}$ are the prescribed spatial tractions across the *traction* or NEUMANN boundary $\varphi(\Gamma_\sigma)$. The DIRICHLET and NEUMANN boundaries are the subsets of the boundary Γ, such that $\Gamma = \Gamma_u \cup \Gamma_\sigma$, $\Gamma_u \cap \Gamma_\sigma = \emptyset$.
Together with the material and the spatial form of CAUCHY's first law of motion given in (2.66) and (2.70), (2.78) define the local form of the *Boundary Value Problem* (BVP) of a body $\mathcal{B}$, which under the isothermal and static restrictions put upon the reference configuration reads:

$$\begin{aligned} &\mathrm{Div}\mathbf{P} + \rho_0 \mathbf{B} = \mathbf{0} , \quad \forall \mathbf{X} \in \mathcal{B} \\ &\varphi = \bar{\varphi} , \quad \forall \mathbf{X} \in \Gamma_u \\ &\mathbf{P} \cdot \mathbf{N} = \bar{\mathbf{T}} , \quad \forall \mathbf{X} \in \Gamma_\sigma . \end{aligned} \tag{2.79}$$

The local or *strong* form of the BVP is not well suited for the numerical solution using finite-element methods. In order to discretise (2.79), an alternative form of conservation of linear momentum is needed. The *principle of virtual work* or *weak* form is such an equivalent.
An admissible *test function* $\eta(\mathbf{X})$ is defined such that it vanishes identically on the prescribed DIRICHLET boundary Γ_u: $\eta(\mathbf{X}) = \mathbf{0} , \quad \forall \mathbf{X} \in \Gamma_u$. Assuming that (2.65) holds, one can state

$$\int_{\mathcal{B}} (-\rho_0 \mathbf{B} - \mathrm{Div}\mathbf{P}) \cdot \eta \, \mathrm{d}V = 0 . \tag{2.80}$$

Applying the divergence theorem and using the fact that the test function vanishes on Γ_u as well as the material NEUMANN boundary condition given in (2.78), this equation leads to

$$\int_{\mathcal{B}} (\mathbf{P} : \operatorname{Grad} \boldsymbol{\eta} - \rho_0 \mathbf{B} \cdot \boldsymbol{\eta}) \, \mathrm{d}V - \int_{\Gamma_\sigma} \bar{\mathbf{T}} \cdot \boldsymbol{\eta} \, \mathrm{d}S = 0 \,, \tag{2.81}$$

which is a material form of the principle of virtual work or a weak form of the linear momentum balance in the reference configuration. Same procedure can be applied to (2.70) and it leads to the spatial form of the principle of virtual work or a weak form of the linear momentum balance in the current configuration:

$$\int_{\varphi(\mathcal{B})} (\boldsymbol{\sigma} : \operatorname{grad} \boldsymbol{\eta} - \rho \mathbf{b} \cdot \boldsymbol{\eta}) \, \mathrm{d}v - \int_{\varphi(\Gamma_\sigma)} \bar{\mathbf{t}} \cdot \boldsymbol{\eta} \, \mathrm{d}s = 0 \,. \tag{2.82}$$

If now a *space of admissible displacements* V is defined by all displacement fields satisfying homogeneous displacement boundary conditions, one can summarise the numerical effort to reach the solution of the BVP as:
Find $\varphi \in V$ such that the weak form of the linear momentum balance (2.81) stands $\forall \boldsymbol{\eta} \in V$.

2.2.4 Conservation of energy

If the existence of the body $\mathcal{B}$ in $\mathbb{R}^3$ is to be put into a thermodynamic frame, some basic notions must be defined. According to [ORTIZ 2003], a *thermodynamic system* describes the body $\mathcal{B}$ as a fixed amount of matter with constant chemical composition and subjected to mechanical processes. Its mathematical definition is a *state*. A state of body $\mathcal{B}$ includes the configuration of the body Ω and additional parameters associated with heat and temperature. Its properties can be *intensive* or *extensive*. *Intensive properties* stay constant if two identical systems join into one. The density ρ, the absolute temperature T and the velocity $\mathbf{v}$ are such properties. *Extensive properties* double if two identical systems join into one. The mass m, the volume V and the entropy H are such properties. Additional variables $\mathbf{q}$ necessary to fully define the state of the system are *internal variables*. A thermodynamic system is said to be in the state of *uniform thermodynamic equilibrium* if all its properties are independent of time and its intensive properties are independent of the position.
In order to postulate the balance of energy of the body $\mathcal{B}$, the resulting kinetic energy of a subbody $\mathcal{P}$ of a body $\mathcal{B}$, in motion through the deformation mapping φ is defined

$$K(\mathcal{P}) = \int_{\mathcal{P}} \frac{1}{2} \rho_0 \, \|\mathbf{V}\|^2 \, \mathrm{d}V = \int_{\varphi(\mathcal{P})} \frac{1}{2} \rho \, \|\mathbf{v}\|^2 \, \mathrm{d}v \,. \tag{2.83}$$

Here, ρ_0 and ρ are the referential and spatial mass density, and $\|\mathbf{V}\|$ and $\|\mathbf{v}\|$ are the EUCLIDIAN norms of the material and spatial velocity fields.
Additional kinetic energy due to thermal fluctuations is the *heat*. The total rate of heat input into the subbody $\mathcal{P}$ is

$$\begin{aligned} Q^R(\mathcal{P}) &= \int_{\mathcal{P}} \rho_0 S \, \mathrm{d}V - \int_{\partial\mathcal{P}} \mathbf{H} \cdot \mathbf{N} \, \mathrm{d}S \\ &= \int_{\varphi(\mathcal{P})} \rho s \, \mathrm{d}v - \int_{\partial\varphi(\mathcal{P})} \mathbf{h} \cdot \mathbf{n} \, \mathrm{d}s , \end{aligned} \tag{2.84}$$

where $S : \mathcal{B} \times [t_1, t_2] \to \mathbb{R}$ is the material heat-source density per unit mass, $s : \mathcal{B} \times [t_1, t_2] \to \mathbb{R}$ is the spatial heat-source density per unit mass, $\mathbf{H} \cdot \mathbf{N}$ is the outward material heat flux defined for the infinitesimal material area $\mathrm{d}S$ of the boundary $\partial\mathcal{P}$ and corresponding outward normal $\mathbf{N}$ at $\mathbf{X}$ and $\mathbf{h} \cdot \mathbf{n}$ is the outward material heat flux defined for the infinitesimal material area $\mathrm{d}s$ of the boundary $\partial\varphi(\mathcal{P})$ and corresponding outward normal $\mathbf{n}$ at $\mathbf{x}$.
The *external power* is the power of the body forces and tractions applied to a subbody $\mathcal{P}$:

$$\begin{aligned} P^E(\mathcal{P}) &= \int_{\mathcal{P}} \rho_0 \mathbf{B} \cdot \mathbf{V} \, \mathrm{d}V + \int_{\partial\mathcal{P}} \mathbf{T}(\mathbf{N}) \cdot \mathbf{V} \, \mathrm{d}S \\ &= \int_{\varphi(\mathcal{P})} \rho \beta \cdot \mathbf{v} \, \mathrm{d}v + \int_{\partial\varphi(\mathcal{P})} \mathbf{t}(\mathbf{n}) \cdot \mathbf{v} \, \mathrm{d}s . \end{aligned} \tag{2.85}$$

The *stress power* represents the externally supplied power which does not provide the raise of the kinetic energy:

$$P^D(\mathcal{P}) = P^E(\mathcal{P}) - \dot{K}(\mathcal{P}) . \tag{2.86}$$

If the motion φ of a body $\mathcal{B}$ satisfies conservation of mass, linear momentum and angular momentum, the stress power can be evaluated by

$$P^D(\mathcal{P}) = \int_{\mathcal{P}} \mathbf{P} : \dot{\mathbf{F}} \, \mathrm{d}V = \int_{\mathcal{P}} \mathbf{S} : \frac{1}{2}\dot{\mathbf{C}} \, \mathrm{d}V = \int_{\varphi(\mathcal{P})} \boldsymbol{\sigma} : \mathbf{d} \, \mathrm{d}v , \tag{2.87}$$

using the first PIOLA-KIRCHOFF stress tensor $\mathbf{P}$ and the material time derivative of the deformation gradient $\mathbf{F}$, or the CAUCHY stress tensor $\boldsymbol{\sigma}$ and the rate-of-deformation tensor $\mathbf{d}$, or the second PIOLA-KIRCHOFF stress tensor $\mathbf{S}$ and the material time derivative of the right CAUCHY-GREEN deformation tensor $\mathbf{C}$. These pairs of stress and rate-of-deformation measures are introduced by [HILL 1968] as *work-conjugates* and this conjugacy is determined through the stress power. The symbol : in the above equation represents the double contraction of two tensors.

The first function of state to be introduced here is the *internal energy* $E(\mathcal{P})$, defined for each subbody $\mathcal{P}$ of $\mathcal{B}$. It can be empirically confirmed that if $\mathcal{P}$ is taken from state 1 to state 2 along a certain path Γ, the time integral

$$\triangle E(\mathcal{P}) = \oint_{\Gamma} \dot{E}(\mathcal{P})\, dt = \oint_{\Gamma} \left[P^D(\mathcal{P}, t) + Q^R(\mathcal{P}, t) \right] dt \tag{2.88}$$

is independent of the path Γ and vanishes for any closed circle. This statement opens a possibility to define the internal energy of the subbody $\mathcal{P}$ as

$$E(\mathcal{P}) = \int_{\mathcal{P}} \rho_0 U \, \mathrm{d}V = \int_{\varphi(\mathcal{P})} \rho u \, \mathrm{d}v \,, \tag{2.89}$$

where U is the material internal energy density per unit mass and u is the spatial internal energy density per unit mass.
The use of (2.87) for the integrands of (2.88) leads to the *principle of conservation of energy* or *first law of thermodynamics*:

$$\dot{E}(\mathcal{P}) + \dot{K}(\mathcal{P}) = P^E(\mathcal{P}) + Q^R(\mathcal{P}) \,, \tag{2.90}$$

which sets a demand of the exact conversion of the external power and heat input into either kinetic energy or internal energy for any subbody $\mathcal{P}$.
The integral material form of (2.90) is then

$$\frac{\mathrm{d}}{\mathrm{d}t} \int_{\mathcal{P}} \rho_0 U \, \mathrm{d}V = \int_{\mathcal{P}} \mathbf{P} : \dot{\mathbf{F}} \, \mathrm{d}V + \int_{\mathcal{P}} \rho_0 S \, \mathrm{d}V - \int_{\partial \mathcal{P}} \mathbf{H} \cdot \mathbf{N} \, \mathrm{d}S \,, \tag{2.91}$$

and its local material form, which follows from (2.91) by the similar mathematical transformation as in the case of balance of linear momentum, is

$$\rho_0 \dot{U} = \mathbf{P} : \dot{\mathbf{F}} + \rho_0 S - \mathrm{Div}\mathbf{H} \,, \quad \text{in } \mathcal{B} \,. \tag{2.92}$$

The Eulerian or spatial form of energy balance reads, as an integral statement

$$\frac{\mathrm{d}}{\mathrm{d}t} \int_{\varphi(\mathcal{P})} \rho u \, \mathrm{d}v = \int_{\varphi(\mathcal{P})} \boldsymbol{\sigma} : \mathbf{d} \, \mathrm{d}v + \int_{\varphi(\mathcal{P})} \rho s \, \mathrm{d}v - \int_{\varphi(\partial \mathcal{P})} \mathbf{h} \cdot \mathbf{n} \, \mathrm{d}s \,, \tag{2.93}$$

and as a local statement

$$\rho \dot{u} = \boldsymbol{\sigma} : \mathbf{d} + \rho s - \mathrm{div}\mathbf{h} \,, \quad \text{in } \varphi(\mathcal{B}) \,. \tag{2.94}$$

2.2.5 The second law of thermodynamics

The main interest of this section lies in the thermodynamics of continua. Based on the definition of state given in previous section, the thermodynamic system during a dynamic process is defined by its configuration $\Omega(t)$ at time t and some additional variables associated with this process and with the current configuration $\Omega(t)$. Those are the internal energy E defined in (2.88) and the heat Q defined in (2.84), a temperature field $T(t)$ or $\theta(t)$ of the infinitesimal material or spatial neighbourhood of a particle at time t, with a constraint

$$T > 0, \theta > 0, \tag{2.95}$$

and the entropy H of the subbody $\mathcal{P}$ of $\mathcal{B}$ defined by the integral

$$H = \int_{\mathcal{P}} \rho_0 N \, \mathrm{d}V = \int_{\varphi(\mathcal{P})} \rho n \, \mathrm{d}v . \tag{2.96}$$

Here, $N(t)$ and $n(t)$ are the material and the spatial *entropy density* per unit mass.

If for a given dynamical process $\{\Omega, \bullet\}$, corresponding entropy field $n(t)$ and temperature field $\theta(t)$, a heat flux $\mathbf{h}$ and a heat-source density field s satisfy the balance of energy given in (2.94), the process can be defined as a *thermodynamic process.* Here, $\bullet$ represents the free choice of the description and the dependence of all variables on the position $\mathbf{X}$ or $\mathbf{x}$ is omitted. All dependent state variables may be computed from $\{\Omega, \sigma, E, n, \mathbf{h}\}$ at each point in time t by means of appropriate state functions.

Rational thermodynamics according to [TRUESDELL & NOLL 1965] states that the rate of external entropy supply into subbody $\mathcal{P}$ or the rate *production of entropy* can be defined by

$$\begin{aligned} \dot{H}^{ext}(\mathcal{P}) &= \int_{\mathcal{P}} \frac{\rho_0 S}{T} \, \mathrm{d}V - \int_{\partial\mathcal{P}} \frac{\mathbf{H} \cdot \mathbf{N}}{T} \, \mathrm{d}S \\ &= \int_{\varphi(\mathcal{P})} \frac{\rho s}{\theta} \, \mathrm{d}v - \int_{\partial\varphi(\mathcal{P})} \frac{\mathbf{h} \cdot \mathbf{n}}{\theta} \, \mathrm{d}s . \end{aligned} \tag{2.97}$$

The second law of thermodynamics states that the internal entropy of an isolated system always tends to increase or stay constant:

$$\dot{H}^{int} = \dot{H} - \dot{H}^{ext} \geq 0 . \tag{2.98}$$

The equality holds if and only if the dynamic process is reversible.

The integral form of the second law or CLAUSIUS-DUHEM *inequality* in Lagrangean description reads

$$\frac{\mathrm{d}}{\mathrm{d}t} \int_{\mathcal{P}} \rho_0 N \, \mathrm{d}V - \int_{\mathcal{P}} \frac{\rho_0 S}{T} \, \mathrm{d}V + \int_{\partial\mathcal{P}} \frac{\mathbf{H} \cdot \mathbf{N}}{T} \, \mathrm{d}S \geq 0 . \tag{2.99}$$

The local form of the CLAUSIUS-DUHEM inequality in Lagrangean description follows from its integral form with an assumption of smoothness of solutions:

$$\rho_0 \dot{N} - \frac{\rho_0 S}{T} + \mathrm{Div}\frac{\mathbf{H}}{T} \geq 0\,, \quad \text{in}\,\mathcal{B}\,. \tag{2.100}$$

The integral form of the second law or CLAUSIUS-DUHEM *inequality* in Eulerian description reads

$$\frac{\mathrm{d}}{\mathrm{d}t}\int\limits_{\varphi(\mathcal{P})} \rho n \,\mathrm{d}v - \int\limits_{\varphi(\mathcal{P})} \frac{\rho s}{\theta}\,\mathrm{d}v + \int\limits_{\partial\varphi(\mathcal{P})} \frac{\mathbf{h}\cdot\mathbf{n}}{\theta}\,\mathrm{d}s \geq 0\,. \tag{2.101}$$

The local form of the CLAUSIUS-DUHEM inequality in Eulerian description follows for sufficiently smooth solutions from its integral form:

$$\rho \dot{n} - \frac{\rho s}{\theta} + \mathrm{div}\frac{\mathbf{h}}{\theta} \geq 0\,, \quad \text{in}\,\varphi(\mathcal{B})\,. \tag{2.102}$$

It is possible to introduce thermodynamic potentials alternative to the entropy H if the properties of the Legendre transformation are used. Assuming that the material internal energy density $U(\bullet, N)$ defined in (2.89) is given, one can define HELMHOLTZ *free energy* using the Legendre transformation of internal energy as

$$\psi_0(\bullet, N) = \inf_N \{U(\bullet, N) - TN\}\,. \tag{2.103}$$

An alternative form of the CLAUSIUS-DUHEM inequality can be derived if it is assumed that the conservation of mass, linear and angular momentum hold and (2.103) is used together with the local material form of the energy balance (2.92) in (2.100):

$$\mathbf{P} : \dot{\mathbf{F}} - \rho_0 \left(\dot{T}N + \dot{\psi}_0\right) - \frac{1}{T}\,\mathbf{H}\cdot\mathrm{Grad}\,T \geq 0\,, \quad \text{in}\,\mathcal{B}\,. \tag{2.104}$$

2.3 Constitutive modelling and material frame-indifference

The object of investigation in Section 2.1 and 2.2, a body $\mathcal{B}$, is described by its configuration Ω and its mass distribution m and its motion and deformation are assigned to the causes mathematically described by concepts of energy and forces under axioms of thermodynamics. However, two physical bodies with the same shape and mass distribution can have different motion and deformation under the influence of the same forces if they consist of different *materials*. This leads to the conclusion that the principles of thermodynamics are in general not sufficient to mathematically determine the motion of a deformable body even if force and energy sources are known. A theory can be successfully used for mathematical models of physical events for different materials only if it includes a concept of *material response*. The mathematical apparatus of this concept are the *constitutive relations*. In order to craft such an apparatus certain principles must be set as a guidance.

2.3.1 Change of frame and objectivity

The *change of frame* is an one-to-one mapping of space-time onto itself with the restriction that the distances, time intervals and the temporal order must stay preserved. According to [TRUESDELL & NOLL 1965] it is possible to express the change of frame for an arbitrary origin in space and for a point with a position vector $\mathbf{x}$ at time t through a rigid body motion as defined in (2.36) and a time-shift:

$$\mathbf{x}^* = \mathbf{c}(t) + \mathbf{Q}(t) \cdot \mathbf{x}\,, \tag{2.105}$$

$$t^* = t - a\,. \tag{2.106}$$

Here, a is a constant, $\mathbf{c}(t)$ is a point function and $\mathbf{Q}(t)$ is a second-order orthogonal tensor which depend on t.
The transformations of an arbitrary scalar field α, vector field $\boldsymbol{\alpha}$ and tensor field $\mathbf{A}$ under the change of frame are regulated by a set of rules which, according to [OGDEN 1997], differ for Lagrangean and Eulerian fields and are bound by the choice of the basis. They are based on the preservation restrictions imposed not only on the one-to-one mapping defined above, but also on various relations between scalars, vectors and tensors in both descriptions and read

	Lagrangean field	Eulerian field
scalar	$\alpha_0^*(\mathbf{X},t) = \alpha_0(\mathbf{X},t)$	$\alpha^*(\mathbf{x},t) = \alpha(\mathbf{x},t)$
vector	$\boldsymbol{\alpha}_0^*(\mathbf{X},t) = \boldsymbol{\alpha}_0(\mathbf{X},t)$	$\boldsymbol{\alpha}^*(\mathbf{x},t) = \mathbf{Q}(t) \cdot \boldsymbol{\alpha}(\mathbf{x},t)$
tensor	$\mathbf{A}_0^*(\mathbf{X},t) = \mathbf{A}_0(\mathbf{X},t)$	$\mathbf{A}^*(\mathbf{x},t) = \mathbf{Q}(t) \cdot \mathbf{A}(\mathbf{x},t) \cdot \mathbf{Q}(t)^{\mathrm{T}}$

(2.107)

The transformation rule for two-point (or mixed Eulerian-Lagrangean) tensor fields $\mathbf{F}$ is also regulated by the choice of the basis and it reads

$$\mathbf{F}^* = \mathbf{Q}(t) \cdot \mathbf{F}\,. \tag{2.108}$$

The form of (2.108) depends on the actual orientation of the two-point tensor in two configurations, i.e. if $\mathbf{F}$ is an invertible function $\mathbf{F}^{-1^*} = \mathbf{F}^{-1} \cdot \mathbf{Q}(t)$.
Scalar, vector and tensor valued functions and fields are said to be *frame-indifferent* or *objective* if the change of both the dependent and independent variables induced by change of frame follows the rules defined in (2.107) and (2.108).
The deformation gradient $\mathbf{F}$ is an example of an objective two-point tensor. Based on this fact, the objectivity of the scalar valued Jacobian J of the deformation can be proven:

$$J^* = \det \mathbf{F}^* = \det(\mathbf{Q} \cdot \mathbf{F}) = \det \mathbf{Q} \det \mathbf{F} = \det \mathbf{F} = J\,, \tag{2.109}$$

as well as the objectivity of the Eulerian left CAUCHY-GREEN deformation tensor:

$$\mathbf{b}^* = \mathbf{F}^* \cdot \mathbf{F}^{*\mathrm{T}} = \mathbf{Q} \cdot \mathbf{F} \cdot \mathbf{F}^{\mathrm{T}} \cdot \mathbf{Q}^{\mathrm{T}} = \mathbf{Q} \cdot \mathbf{b} \cdot \mathbf{Q}^{\mathrm{T}}. \tag{2.110}$$

The same logic leads to the conclusion that the velocity gradient $\mathbf{l}$ and its skew-symmetric part, the spin tensor $\mathbf{w}$, are non-objective Eulerian tensors, whereas its symmetric part, the rate-of-deformation tensor $\mathbf{d}$, is an objective Eulerian tensor.
If an arbitrary objective Eulerian tensor $\mathbf{A}(\mathbf{x}, t)$ is given, its material time derivative after the change of frame is, according to the transformation rule given in (2.107):

$$\begin{aligned} \frac{\mathrm{d}}{\mathrm{d}t}\mathbf{A}^* &= \frac{\mathrm{d}}{\mathrm{d}t}\left(\mathbf{Q} \cdot \mathbf{A} \cdot \mathbf{Q}^{\mathrm{T}}\right) \\ &= \dot{\mathbf{Q}} \cdot \mathbf{A} \cdot \mathbf{Q}^{\mathrm{T}} + \mathbf{Q} \cdot \dot{\mathbf{A}} \cdot \mathbf{Q}^{\mathrm{T}} + \mathbf{Q} \cdot \mathbf{A} \cdot \dot{\mathbf{Q}}^{\mathrm{T}} \\ &\neq \mathbf{Q} \cdot \dot{\mathbf{A}} \cdot \mathbf{Q}^{\mathrm{T}}. \end{aligned} \tag{2.111}$$

This shows that the material time derivative of an objective Eulerian tensor field may not be objective. In order to secure the objectivity of rates of Eulerian measures, a wide range of time derivatives has been developed. Prominent classical objective time derivatives include according to e.g. [XIAO, BRUHNS & MEYERS 2000A] the ZAREMBA-JAUMANN, GREEN-NAGHDI, OLDROYD and TRUESDELL rate. Introduction of a *logarithmic rate* by [XIAO, BRUHNS & MEYERS 2000B] showed that for Eulerian HENCKY strain $\mathbf{h}$ an objective time-derivative can be defined and it yields the stretching tensor $\mathbf{d}$:

$$\overset{\circ}{h}{}^{\log} = \mathbf{d}. \tag{2.112}$$

Another concept which deals with the problem of objective time derivatives is the LIE *concept*. In order to introduce this concept, the notion of *push-forward* and *pull-back* operations must be presented. These operations give the relations between components of a tensor in the Lagrangean and Eulerian configuration and are bound by the choice of the basis and the nature of the tensor field, i.e. they differ for work conjugated kinetic and kinematic tensor fields based on the invariance of the resulting power. Generally, the push-forward of a Lagrangean tensor $\phi_*(\mathbf{A_0})$ can be interpreted as its mathematical description in terms of the basis of the current configuration and the pull-back $\phi^*(\mathbf{A})$ of an Eulerian tensor can be interpreted as its mathematical description in terms of the basis of the referential configuration. Here are some examples for both transformations:

$$\begin{aligned} &\phi_*(\dot{\mathbf{E}}) = \mathbf{F}^{-\mathrm{T}} \cdot \dot{\mathbf{E}} \cdot \mathbf{F}^{-1} = \mathbf{d}, \qquad && \phi^*(\mathbf{d}) = \mathbf{F}^{\mathrm{T}} \cdot \mathbf{d} \cdot \mathbf{F} = \dot{\mathbf{E}}, \\ &\phi_*(\mathbf{S}) = \mathbf{F} \cdot \mathbf{S} \cdot \mathbf{F}^{\mathrm{T}} = \boldsymbol{\tau}, && \phi^*(\boldsymbol{\tau}) = \mathbf{F}^{-1} \cdot \boldsymbol{\tau} \cdot \mathbf{F}^{-\mathrm{T}} = \mathbf{S}. \end{aligned} \tag{2.113}$$

The algorithm of the LIE concept as well as any other objective rate is based on these transformation rules and may be put into words in the following manner:

1. An Eulerian tensor $\mathbf{A}$ is pulled back into a configuration which provides an objective use of the material time derivative of $\mathbf{A}$.

2. The material time derivative is applied.

3. A push-forward is applied to the resulting term.

The mathematical form of a LIE derivative reads

$$\mathcal{L}_v \mathbf{A} = \phi_* \left(\frac{\mathrm{d}}{\mathrm{d}t} \{\phi^*(\mathbf{A})\} \right). \tag{2.114}$$

This procedure yields a material time derivative of $\mathbf{A}$ which leads to objective measures.
As an example, the LIE derivative of the KIRCHHOFF stress tensor is derived based on the results of (2.113):

$$\mathcal{L}_v \boldsymbol{\tau} = \mathbf{F} \cdot \frac{\mathrm{d}\mathbf{S}}{\mathrm{d}t} \cdot \mathbf{F}^{\mathrm{T}} = \mathbf{F} \cdot \dot{\mathbf{S}} \cdot \mathbf{F}^{\mathrm{T}}. \tag{2.115}$$

2.3.2 Constitutive modelling

The central principle on which the material modelling is based is the *the principle of material frame-indifference* which states that *constitutive equations must be invariant under changes of frame of reference.* If an arbitrary motion $\boldsymbol{\varphi}$ and an arbitrary symmetric time-dependent tensor field $\boldsymbol{\sigma}$ are paired $\{\boldsymbol{\varphi}, \boldsymbol{\sigma}\}$ to form a dynamical process for a body $\mathcal{B}$, and a constitutive equation is satisfied for this process:

$$\mathbf{x} = \boldsymbol{\varphi}(\mathbf{X}, t), \quad \boldsymbol{\sigma} = \boldsymbol{\sigma}(\mathbf{X}, t), \tag{2.116}$$

then it must be satisfied for any equivalent process $\{\boldsymbol{\varphi}^*, \boldsymbol{\sigma}^*\}$ defined by

$$\begin{aligned} \mathbf{x}^* &= \boldsymbol{\varphi}^*(\mathbf{X}, t^*) = \mathbf{c}(t) + \mathbf{Q}(t) \cdot \boldsymbol{\varphi}(\mathbf{X}, t), \\ \boldsymbol{\sigma}^* &= \boldsymbol{\sigma}^*(\mathbf{X}, t^*) = \mathbf{Q}(t) \cdot \boldsymbol{\sigma}(\mathbf{X}, t) \cdot \mathbf{Q}(t)^{\mathrm{T}}, \\ t^* &= t - a, \end{aligned} \tag{2.117}$$

where a is an arbitrary constant, $\mathbf{c}(t)$ is an arbitrary point function and $\mathbf{Q}(t)$ is an arbitrary second-order orthogonal tensor which depend on t.
According to [WANG & TRUESDELL 1973] additional to the principle of material frame-indifference, guidelines in the modern approach to the constitutive modelling include the principles of determinism, local action, equipresence, universal dissipation and material symmetry.

2.4 Hyperelasticity

This sections draws attention to a special class of non-dissipative material models, namely *hyperelastic* models and gives a very rough review of their basic properties.
Following [TRUESDELL & NOLL 1965] and their definition of a *simple material*, any material can be recognised as an *elastic* material if it is simple and if the stress at time t is dependent only on the local configuration at time t and not on the history of the motion from $t \in \{0, t\}$. The general constitutive equation of an elastic material has a form

$$\mathbf{P} = \wp(\mathbf{F}), \tag{2.118}$$

where $\mathbf{P}$ is the first PIOLA-KIRCHOFF stress tensor at time t, $\wp$ is the *response function* of the elastic material and $\mathbf{F}$ is the deformation gradient at time t.
The *hyperelastic material* is defined as an elastic material whose response function $\wp$ has a special form:

$$\wp(\mathbf{F}) = \mathbf{P} = \frac{\partial \Psi(\mathbf{F})}{\partial \mathbf{F}} \quad \text{with} \quad \dot{\Psi} = \mathbf{P} : \dot{\mathbf{F}} = \mathbf{S} : \frac{1}{2}\dot{\mathbf{C}} = \boldsymbol{\tau} : \mathbf{d}. \tag{2.119}$$

Here, $\Psi(\mathbf{F})$ is a potential whose time derivative equals the stress power. According to the *first work theorem* for a homogeneous deformation process, the stress power is a non-negative work of deformation depending only on the initial and final configuration. Assuming a mechanical process which satisfies (2.104) for isothermal processes, this potential satisfies the identity

$$\Psi(\mathbf{F}) = \rho_0 \psi_0(\mathbf{F}), \tag{2.120}$$

which leads to a conclusion that a hyperelastic material can be defined uniquely using the HELMHOLTZ free energy. If the necessary material frame indifference is taken into account alongside the material covariance as defined by e.g. [MARSDEN & HUGHES 1994], then a possibility to describe ψ_0 as a function of the right CAUCHY-GREEN deformation tensor must exist and it leads to the following statement:

$$\mathbf{P} = 2\,\mathbf{F} \cdot \frac{\partial \Psi(\mathbf{C})}{\partial \mathbf{C}} = 2\,\rho_0\,\mathbf{F} \cdot \frac{\partial \psi_0(\mathbf{C})}{\partial \mathbf{C}}. \tag{2.121}$$

The principle of material symmetry demands that the material response is not influenced by the rigid rotation with respect to the reference configuration. A rotation $\mathbf{Q} \in SO(3)$ is a material symmetry of an elastic body if

$$\Psi(\mathbf{F} \cdot \mathbf{Q}) = \Psi(\mathbf{F}) \quad \text{and} \quad \Psi(\mathbf{Q}^{\mathrm{T}} \cdot \mathbf{C} \cdot \mathbf{Q}) = \Psi(\mathbf{C}). \tag{2.122}$$

The set $S \subset SO(3)$ collects all symmetries of an elastic body out of all proper orthogonal mappings over $\mathbb{R}^3$. If $S = SO(3)$, every rigid rotation of the reference configuration is a symmetry and the elastic body is *isotropic*. For all

hyperelastic and isotropic materials, the HELMHOLTZ free energy depends only on any complete set of invariants of the right CAUCHY-GREEN deformation tensor $\mathbf{C}$

$$\psi_0(\mathbf{C}) = \psi_0\left(I_1(\mathbf{C}), I_2(\mathbf{C}), I_3(\mathbf{C})\right). \tag{2.123}$$

One such set are the principal stretches $\{\lambda_1, \lambda_2, \lambda_3\}$:

$$\psi_0(\mathbf{C}) = \psi_0(\lambda_1, \lambda_2, \lambda_3). \tag{2.124}$$

Due to the symmetry of $\mathbf{C}$, the symmetry of the second PIOLA-KIRCHOFF stress tensor $\mathbf{S}$ results from the hyperelastic constitutive equation (2.121), since the partial derivative $\mathbf{S} = 2\,\partial_{\mathbf{C}}\Psi(\mathbf{C})$ can be represented by a symmetric tensor. That way, the conservation of angular momentum is a priori satisfied.
In the present work, a neo-HOOKE hyperelastic and isotropic material model with a polyconvex stored-energy functional Ψ of the following form

$$\Psi(\mathbf{C}) = \lambda \frac{J^2 - 1}{4} - \left(\frac{\lambda}{2} + \mu\right) \log J + \frac{1}{2}\mu\,(\operatorname{tr}\mathbf{C} - 3) \tag{2.125}$$

is used. Here, λ and μ are the LAMÉ constants. For more details about this specific choice of stored-energy function and the importance of its polyconvexity for the existence of solutions of constitutive equations refer to [CIARLET 1988].
Since the rate form of the hyperelastic constitutive relations plays a central role in the incremental formulation of plasticity, starting from (2.119) and (2.121), a rate form involving the second PIOLA-KIRCHOFF stress tensor $\mathbf{S}$ and the right CAUCHY-GREEN deformation tensor $\mathbf{C}$ can be stated:

$$\dot{\mathbf{S}} = \mathbb{C} : \frac{1}{2}\dot{\mathbf{C}} \quad \text{or} \quad S_{IJ} = \mathbb{C}_{IJKL}\frac{1}{2}\dot{C}_{KL} \tag{2.126}$$

with the introduction of the *material elastic tangent operator* $\mathbb{C}$:

$$\mathbb{C}_{IJKL} = 4\,\frac{\partial^2 \Psi(\mathbf{C})}{\partial C_{IJ}\partial C_{KL}}. \tag{2.127}$$

Using (2.113), (2.115) and (2.126) leads to:

$$(\mathcal{L}_v\,\tau)_{ij} = F_{iI}\dot{S}_{IJ}F_{Jj} = F_{iI}F_{Jj}F_{kK}F_{lL}\mathbb{C}_{IJKL}d_{kl} = c_{ijkl}\,d_{kl} \tag{2.128}$$

with the *spatial elastic tangent operator* $c_{ijkl} = F_{iI}F_{Jj}F_{kK}F_{lL}\mathbb{C}_{IJKL}$ and the rate-of-deformation tensor $\mathbf{d}$. It follows from the definitions (2.127) and (2.128) that the elastic tangents introduced above, i.e. $\mathbb{C}$ and $\mathbf{c}$ possess major and minor symmetries, e.g. $\mathbb{C}_{IJKL} = \mathbb{C}_{IJLK} = \mathbb{C}_{JILK} = \mathbb{C}_{LKJI}$.

2.5 Theory of plasticity

This section offers a short overview of another class of a material models, namely finite strain plasticity. According to [HILL 1950], *theory of plasticity* is a mathematical treatment of stress and strain in bodies permanently distorted in any way. It has its roots in results of experiments observing macroscopic behaviour of plastic materials. It aims to define a set of constitutive relations between stress and strain fields agreeable enough with experimental results and to provide a mathematical technique for calculating a non-uniform distribution of stress and strain in plastic solids. The plasticity of a material body describes its fixed rigidity up to a certain stress limit after which its motion produces a deformation similar to a fluid flow if the stress is kept above this limit value and permanent deformation if the unloading process takes place. Unlike elastic deformation, plastic deformation is irreversible, dissipative and path-dependent. The major properties of the mathematical model include

1. A set of internal variables $\mathbf{q}$ defined by evolution equations modelling the dissipative process in the material response.

2. A *yield function* $f(\boldsymbol{\sigma}, \mathbf{q}) \leq 0$ which is the mathematical definition of a stress limit mentioned above and which governs the onset and the continuance of plastic deformation. The surface $f(\boldsymbol{\sigma}, \mathbf{q}) = 0$ defined in a six-dimensional or nine-dimensional stress space is known as a *yield surface.*

3. Decomposition of the deformation into elastic and plastic part. There is a large number of theories falling into the finite strain plasticity frame and according to [XIAO, BRUHNS & MEYERS 2006] they can all be differentiated into three classes:

   - *Classical* EULERIAN *rate formulations*, e.g. [HILL 1958], which are based on the additive decomposition of the rate-of-deformation tensor $\mathbf{d}$ into an elastic part $\mathbf{d}^{\mathrm{e}}$ and a plastic part $\mathbf{d}^{\mathrm{p}}$:

   $$\mathbf{d} = \mathbf{d}^{\mathrm{e}} + \mathbf{d}^{\mathrm{p}} . \tag{2.129}$$

   - LAGRANGEAN *formulations with additive decomposition of the strain field*, e.g. [GREEN & NAGHDI 1965], which are based on the additive decomposition of the LAGRANGEAN strain field into an elastic part $\mathbf{A}^{\mathrm{e}}$ and a plastic part $\mathbf{A}^{\mathrm{p}}$:

   $$\mathbf{A} = \mathbf{A}^{\mathrm{e}} + \mathbf{A}^{\mathrm{p}} . \tag{2.130}$$

   - *Formulations with unstressed configuration*, e.g. [LEE 1969], which are based on the local multiplicative decomposition of the deformation gradient $\mathbf{F}$ into an elastic part $\mathbf{F}^{\mathrm{e}}$ and a plastic part $\mathbf{F}^{\mathrm{p}}$:

$$\mathbf{F} = \mathbf{F}^{\mathrm{e}} \cdot \mathbf{F}^{\mathrm{p}} \quad \text{with} \quad \det \mathbf{F}^{\mathrm{e}} > 0\,, \quad \det \mathbf{F}^{\mathrm{p}} > 0\,. \tag{2.131}$$

Small strain kinematics renders all three classes equivalent.
This work is based on models from the class exploiting the local multiplicative decomposition of the deformation gradient in order to provide the desired numerical efficiency.

2.5.1 Multiplicative finite strain plasticity: fundamentals

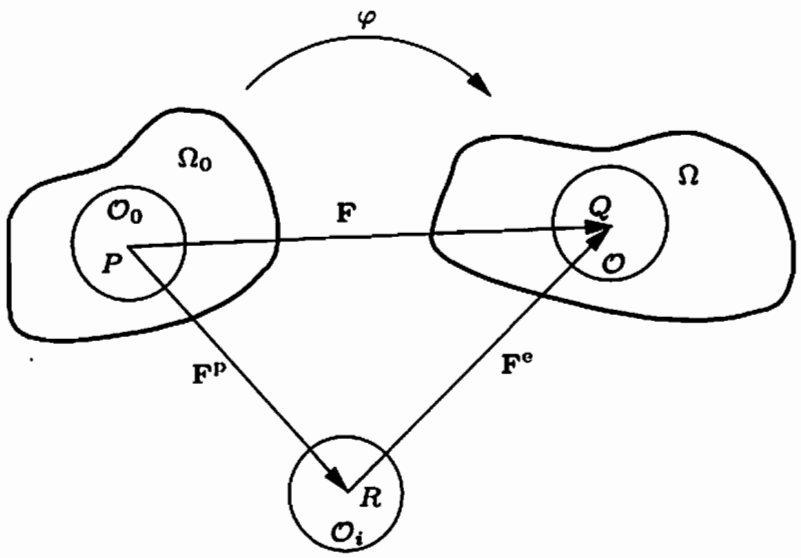

Figure 2.4: Local multiplicative decomposition of the deformation gradient into elastic and plastic part.

The notion of intermediate unstressed configuration is motivated by the micromechanics of single-crystal metal plasticity, with basic ideas following the line from the fundamental work of [Taylor 1938] to e.g. [Hill 1965], [Hill & Rice 1973] and the review article of [Asaro 1983].
From a micromechanical point of view, single crystal plasticity of a material is a motion seen as a flow of material through deformable crystal lattice. Having in mind the conclusion mathematically defined in (2.16) and visualised in Figure 2.2, this motion can be decomposed into a dislocation of the material through the lattice followed by the distortion of the crystal lattice. The total deformation from the reference configuration $\Omega_0 \subset \mathbb{R}^3$ to the current configuration $\Omega \subset \mathbb{R}^3$ via the deformation φ is characterised by its deformation gradient $\mathbf{F}$. If the deformation φ maps the material infinitesimal neighbourhood $\mathcal{O}_0(\mathbf{X})$ of the point P with the position vector $\mathbf{X}$ into the spatial infinitesimal neighbourhood $\mathcal{O}(\mathbf{x})$ of the point Q with the position vector $\mathbf{x}$ (see Figure 2.4),

then an *intermediate configuration* of the infinitesimal neighbourhood $\mathcal{O}_i$ of the point R can be introduced based on the micromechanical picture described above and a local decomposition of the form

$$\mathbf{F}(\mathbf{X},t) = \mathbf{F}^{\mathrm{e}}(\mathbf{X},t) \cdot \mathbf{F}^{\mathrm{p}}(\mathbf{X},t) \tag{2.132}$$

can be defined. The intermediate configuration is mathematically defined by a local deformation with a deformation gradient $\mathbf{F}^{\mathrm{e}-1}$ and phenomenologically interpreted as a local deformation which releases the stresses from any spatial infinitesimal neighbourhood $\mathcal{O}(\mathbf{x}) \subset \Omega$ in the current configuration. That leaves the local intermediate configuration $\mathcal{O}_i$ stress-free. It also leads to the elastic strain measures

$$\mathbf{C}^{\mathrm{e}} = \mathbf{F}^{\mathrm{e}\mathrm{T}} \cdot \mathbf{F}^{\mathrm{e}}, \quad \mathbf{b}^{\mathrm{e}} = \mathbf{F}^{\mathrm{e}} \cdot \mathbf{F}^{\mathrm{e}\mathrm{T}}, \tag{2.133}$$

and an additive split of the velocity gradient $\mathbf{l}$:

$$\begin{aligned} \mathbf{l} &= \dot{\mathbf{F}} \cdot \mathbf{F}^{-1} \\ &= \dot{\mathbf{F}}^{\mathrm{e}} \cdot \mathbf{F}^{\mathrm{e}-1} + \mathbf{F}^{\mathrm{e}} \cdot \dot{\mathbf{F}}^{\mathrm{p}} \cdot \mathbf{F}^{\mathrm{p}-1} \cdot \mathbf{F}^{\mathrm{e}-1} \\ &= \mathbf{l}^{\mathrm{e}} + \mathbf{F}^{\mathrm{e}} \cdot \mathbf{L}^{\mathrm{p}} \cdot \mathbf{F}^{\mathrm{e}-1} \\ &= \mathbf{l}^{\mathrm{e}} + \mathbf{l}^{\mathrm{p}}. \end{aligned} \tag{2.134}$$

Elastic and plastic parts of the velocity gradient are then split into symmetric and skew-symmetric parts:

$$\mathbf{l}^{\mathrm{e}} = \mathbf{d}^{\mathrm{e}} + \mathbf{w}^{\mathrm{e}}, \quad \mathbf{l}^{\mathrm{p}} = \mathbf{d}^{\mathrm{p}} + \mathbf{w}^{\mathrm{p}}, \tag{2.135}$$

with $\mathbf{d}^{\mathrm{e}}$ and $\mathbf{d}^{\mathrm{p}}$ defined as elastic and plastic rate-of-deformation tensors and $\mathbf{w}^{\mathrm{e}}$ and $\mathbf{w}^{\mathrm{p}}$ as elastic and plastic spin tensors.
If the material is assumed hyperelastic, its stored energy function can be regarded in general as a function of the elastic and plastic part of the deformation gradient and a set of strain-like internal state variables $\boldsymbol{\alpha} \in \mathbb{R}^n$ which describe the dissipative process in the material. Following the guidelines of the infinitesimal theory of plasticity, it is assumed that the stored energy functional locally depends on the deformation through the elastic part of the deformation gradient and in the micromechanical frame it represents the energy used for the elastic deformation of the crystal lattice. Additional assumptions are the material frame indifference and the decoupling of the elastic deformation from the internal dissipation materialised through internal variables:

$$\Psi(\mathbf{F}^{\mathrm{e}}, \mathbf{F}^{\mathrm{p}}, \boldsymbol{\alpha}) = \Psi^{\mathrm{e}}(\mathbf{F}^{\mathrm{e}}) + \Psi^{\mathrm{p}}(\boldsymbol{\alpha}) = \Psi^{\mathrm{e}}(\mathbf{C}^{\mathrm{e}}) + \Psi^{\mathrm{p}}(\boldsymbol{\alpha}). \tag{2.136}$$

For the purely mechanical process in a hyperelastic material, (2.104) becomes

$$\mathcal{D} = \mathbf{P} : \dot{\mathbf{F}} - \dot{\Psi} = \mathbf{S} : \frac{1}{2}\dot{\mathbf{C}} - \dot{\Psi} = \boldsymbol{\tau} : \mathbf{d} - \dot{\Psi} \geq 0, \tag{2.137}$$

where $\mathbf{P}$ is the first PIOLA-KIRCHOFF stress tensor, $\mathbf{S}$ the second PIOLA-KIRCHOFF stress tensor and $\boldsymbol{\tau}$ the KIRCHOFF stress tensor.
Using the kinematic relation based on the push-forward of the elastic right CAUCHY-GREEN deformation tensor $\mathbf{C}^{\mathrm{e}}$ into the current configuration according to (2.41) and (2.113):

$$\dot{\mathbf{C}}^{\mathrm{e}} = 2\,\mathbf{F}^{\mathrm{e}\mathrm{T}} \cdot \mathbf{d}^{\mathrm{e}} \cdot \mathbf{F}^{\mathrm{e}}\,, \tag{2.138}$$

the time derivative of the stored energy functional is evaluated as

$$\dot{\Psi} = \frac{\partial \Psi^{\mathrm{e}}}{\partial \mathbf{C}^{\mathrm{e}}} : \dot{\mathbf{C}}^{\mathrm{e}} + \mathbf{q} \cdot \dot{\boldsymbol{\alpha}} \tag{2.139}$$

and the local dissipation $\mathcal{D}$ as

$$\left(\boldsymbol{\tau} - 2\,\mathbf{F}^{\mathrm{e}\mathrm{T}} \cdot \frac{\partial \Psi^{\mathrm{e}}}{\partial \mathbf{C}^{\mathrm{e}}} \cdot \mathbf{F}^{\mathrm{e}}\right) : \mathbf{d}^{\mathrm{e}} + \boldsymbol{\tau} : \mathbf{d}^{\mathrm{p}} + \mathbf{q} \cdot \dot{\boldsymbol{\alpha}} \geq 0\,. \tag{2.140}$$

Here, $\mathbf{q} = -\partial_{\boldsymbol{\alpha}} \Psi^{\mathrm{p}}$ is a stress-like internal variable conjugated to $\boldsymbol{\alpha}$.
Recalling the fact that elastic and inelastic deformation are assumed uncoupled, in the case of the purely elastic response $\dot{\Psi} = \dot{\Psi}^{\mathrm{e}}$. Having in mind the standard argument in elastic constitutive theory that the inequality (2.104) must hold for all histories of motion and temperature in the body $\mathcal{B}$ and therefore becomes an identical equality (see [TRUESDELL & NOLL 1965]), it can be stated:

$$\boldsymbol{\tau} = 2\,\mathbf{F}^{\mathrm{e}\mathrm{T}} \cdot \frac{\partial \Psi}{\partial \mathbf{C}^{\mathrm{e}}} \cdot \mathbf{F}^{\mathrm{e}}\,. \tag{2.141}$$

This leads to the reduced form of the dissipation inequality in the current configuration:

$$\boldsymbol{\tau} : \mathbf{d}^{\mathrm{p}} + \mathbf{q} \cdot \dot{\boldsymbol{\alpha}} \geq 0\,. \tag{2.142}$$

Taking into account the fact that $\boldsymbol{\tau}$ is a symmetric tensor and that $\boldsymbol{\tau} = \mathbf{F}^{\mathrm{e}} \cdot \mathbf{S} \cdot \mathbf{F}^{\mathrm{e}\mathrm{T}}$ and using (2.134), the reduced dissipation inequality can be expressed in terms of objects defined on the intermediate configuration $\mathcal{O}_i$:

$$\begin{aligned}
\boldsymbol{\tau} : \mathbf{d}^{\mathrm{p}} + \mathbf{q} \cdot \dot{\boldsymbol{\alpha}} &= \left(\mathbf{F}^{\mathrm{e}} \cdot \mathbf{S} \cdot \mathbf{F}^{\mathrm{e}\mathrm{T}}\right) : \left(\mathbf{F}^{\mathrm{e}} \cdot \mathbf{L}^{\mathrm{p}} \cdot \mathbf{F}^{\mathrm{e}-1}\right) + \mathbf{q} \cdot \dot{\boldsymbol{\alpha}} \\
&= \left[\mathbf{C}^{\mathrm{e}} \cdot \mathbf{S}\right] : \mathbf{L}^{\mathrm{p}} + \mathbf{q} \cdot \dot{\boldsymbol{\alpha}} \\
&= \left[2\,\mathbf{C}^{\mathrm{e}} \cdot \frac{\partial \Psi}{\partial \mathbf{C}^{\mathrm{e}}}\right] : \mathbf{L}^{\mathrm{p}} + \mathbf{q} \cdot \dot{\boldsymbol{\alpha}} \\
&= \boldsymbol{\Sigma} : \mathbf{L}^{\mathrm{p}} + \mathbf{q} \cdot \dot{\boldsymbol{\alpha}} \geq 0\,.
\end{aligned} \tag{2.143}$$

This form of the dissipation inequality appeared for the first time in [MANDEL 1972] and it introduces a new stress measure $\boldsymbol{\Sigma} = 2\,\partial^{\mathrm{e}}_{\mathbf{C}} \Psi$. This stress measure is known as MANDEL stress tensor and it is generally a non-symmetric tensor

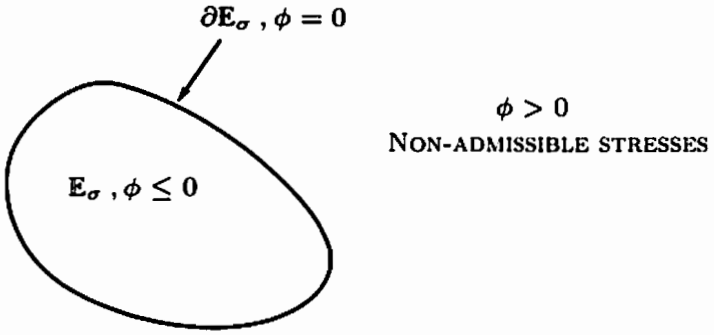

Figure 2.5: Illustration of the elastic domain in stress space.

defined on the intermediate configuration and conjugated to the *plastic distortion rate* $\mathbf{L}^{\mathrm{P}}$. The MANDEL stress tensor becomes symmetric for the isotropic hyperelastic material.
In order to complete the constitutive model, the evolution equations for the internal variables $(\mathbf{L}^{\mathrm{P}}, \boldsymbol{\alpha})$ are to be derived in line with the procedure known from infinitesimal theory of plasticity. The first step is the definition of the *elastic domain* and the *yield function*. This is the aspect of the theory where the choice of description is of great importance. Here, a description relative to the intermediate configuration is adopted.
The *yield function* is a convex and sufficiently smooth function $\phi : \mathbb{R}^{9+n} \to \mathbb{R}$, defined according to the empirical investigations. The dimension n represents the total number of internal variables in the material model. Admissible stresses $(\boldsymbol{\Sigma}, \mathbf{q})$ are constrained to lie in the *elastic domain* which becomes the *admissible stress space* in the case when the internal variables $\mathbf{q}$ are fixed:

$$\mathbb{E}_\sigma = \{(\boldsymbol{\Sigma}, \mathbf{q}) \in \mathbb{R}^{9+n} \mid \phi(\boldsymbol{\Sigma}, \mathbf{q}) \leq 0\}\,. \tag{2.144}$$

The boundary $\partial\mathbb{E}_\sigma$ of the admissible stress space $\mathbb{E}_\sigma$

$$\partial\mathbb{E}_\sigma = \{(\boldsymbol{\Sigma}, \mathbf{q}) \in \mathbb{R}^{9+n} \mid \phi(\boldsymbol{\Sigma}, \mathbf{q}) = 0\} \tag{2.145}$$

is the *yield surface*. Stress states $(\boldsymbol{\Sigma}, \mathbf{q}) \in \mathrm{int}\mathbb{E}_\sigma$ lead to an elastic material response and for those on the yield surface $(\boldsymbol{\Sigma}, \mathbf{q}) \in \partial\mathbb{E}_\sigma$ a plastic material response is possible. Stress states outside the space $\mathbb{E}_\sigma$ are non-admissible.
Evolution equations for $(\mathbf{L}^{\mathrm{P}}, \boldsymbol{\alpha})$ are derived based on the *principle of maximum dissipation* which states that out of all possible stress states $(\tilde{\boldsymbol{\Sigma}}, \tilde{\mathbf{q}})$, the actual stress state is the one maximising the dissipation $\mathcal{D}$:

$$\max_{(\tilde{\boldsymbol{\Sigma}}\,, \tilde{\mathbf{q}}) \in \mathbb{E}_\sigma} \left[\tilde{\boldsymbol{\Sigma}} : \mathbf{L}^{\mathrm{P}} + \tilde{\mathbf{q}} \cdot \dot{\boldsymbol{\alpha}}\right]. \tag{2.146}$$

This postulate yields the evolution equations:

$$\mathbf{L}^{\mathrm{P}} = \lambda\, \partial_{\boldsymbol{\Sigma}}\, \phi\,, \quad \dot{\boldsymbol{\alpha}} = \lambda\, \partial_{\mathbf{q}}\, \phi \tag{2.147}$$

and the loading/unloading conditions following from the optimisation theory and known as the KUHN-TUCKER conditions:

$$\phi \leq 0\,, \quad \lambda \geq 0\,, \quad \lambda\phi = 0\,. \tag{2.148}$$

Additionally, the plastic consistency condition stating that as long as the plastic flow continues, the yield condition $\phi(\boldsymbol{\Sigma}, \mathbf{q}) = 0$ must hold:

$$\dot{\phi}(\boldsymbol{\Sigma}, \mathbf{q}) = 0 \tag{2.149}$$

yields the LAGRANGE multiplier λ.
The choice of the admissible stress space defined in (2.144) and the form of the postulate of maximum dissipation (2.146) given by MANDEL lead in general to the nine-dimensional flow rule given in (2.147). This flow rule is marked as questionable by [LUBLINER 1997] for the inability to fulfil the symmetry constraint posed on the MANDEL stress measure. However, for the isotropic hyperelastic material models the symmetry can be accounted for and the flow rule (2.147) degenerates to six dimensions.
Flow rules (2.147) accompanying the maximum dissipation constraint (2.146) are said to be *associative* or *normality* rules because they restrict the direction of the flow in the stress space to be proportional to the gradient of the yield function ϕ. Absence of this restriction renders *non-associative* evolution equations. For many materials associative flow rule is an appropriate choice for the modelling of the material response, but for some a generalisation of the evolution equations is necessary. In those cases, a *plastic potential* g and a hardening potential h are introduced such that

$$\mathbf{L}^{\mathrm{p}} = \lambda\, \partial_{\boldsymbol{\Sigma}}\, g\,, \quad \dot{\boldsymbol{\alpha}} = \lambda\, \partial_{\mathbf{q}}\, h\,. \tag{2.150}$$

Associative evolution equations are obtained from (2.150), if $g = h = \phi$.
This work will exploit the possibility to define the yield function based on an admissible space domain $\mathbb{E}_\sigma$ defined in (2.144) in the following form:

$$\phi(\boldsymbol{\Sigma}, \mathbf{q}) = f(\boldsymbol{\Sigma}, \mathbf{q}) - f_{\mathrm{ini}} \leq 0\,. \tag{2.151}$$

Here, $f(\boldsymbol{\Sigma}, \mathbf{q})$ is an equivalent stress measure which is convex and homogeneous of degree one, i.e. $f(c(\boldsymbol{\Sigma}, \mathbf{q})) = c f(\boldsymbol{\Sigma}, \mathbf{q}), \forall c \in \mathbb{R}_+$ and $f_{\mathrm{ini}} > 0$ is a function depending on the size of the elastic domain in the undeformed material. This property of the equivalent stress measure together with the associative flow rule and the KUHN-TUCKER conditions delivers according to [SIMO 1998] the dissipation $\mathcal{D}$ in the form

$$\mathcal{D} = \lambda\, f_{\mathrm{ini}} \geq 0\,. \tag{2.152}$$

Considering the fact that $\lambda \geq 0$ and the restriction $f_{\mathrm{ini}} > 0$ are in force, the second law of thermodynamics is satisfied a priori.

1. *Kinematics*

$$\mathbf{l}^{\mathrm{p}} = \mathbf{l} - \mathbf{l}^{\mathrm{e}} = \mathbf{F}^{\mathrm{e}} \cdot \mathbf{L}^{\mathrm{p}} \cdot \mathbf{F}^{\mathrm{e}-1} \quad \text{with} \quad \mathbf{L}^{\mathrm{p}} = \dot{\mathbf{F}}^{\mathrm{p}} \mathbf{F}^{\mathrm{p}-1} .$$

2. *Constitutive equations*

$$\Psi = \Psi^{\mathrm{e}}(\mathbf{C}^{\mathrm{e}}) + \Psi^{\mathrm{p}}(\boldsymbol{\alpha}) , \quad \boldsymbol{\Sigma} = 2\,\partial_{\mathbf{C}^{\mathrm{e}}} \Psi , \quad \mathbf{q} = -\partial_{\boldsymbol{\alpha}} \Psi^{\mathrm{p}} .$$

3. *Admissible stress space and the yield criterion*

$$\mathbb{E}_{\sigma} = \{(\boldsymbol{\Sigma}, \mathbf{q}) \in \mathbb{R}^{9+n} \mid \phi(\boldsymbol{\Sigma}, \mathbf{q}) \leq 0\} .$$

4. *Evolution equations*

$$\mathbf{L}^{\mathrm{p}} = \lambda\, \partial_{\boldsymbol{\Sigma}} \phi , \quad \dot{\boldsymbol{\alpha}} = \lambda\, \partial_{\mathbf{q}} \phi .$$

5. *Loading/unloading and consistency conditions*

$$\phi \leq 0 , \quad \lambda \geq 0 , \quad \lambda \phi = 0 , \quad \dot{\phi}(\boldsymbol{\Sigma}, \mathbf{q}) = 0 .$$

Figure 2.6: Elastoplastic model of multiplicative plasticity

The mathematical model of material response according to the theory of plasticity based on the notion of intermediate stress-free configuration which is herewith completely defined, is summarised in Figure 2.6. Next, two choices of yield criterion which shape the elastic domain of the material model presented above are briefly addressed.

Example 2.5.1 VON MISES *plasticity*

One example for such definition of the yield function can be found in the fundamental theory of VON MISES. The classical yield condition of VON MISES reads

$$\phi(\boldsymbol{\Sigma}, q) = \|\mathrm{dev}\,(\boldsymbol{\Sigma})\| - R = \|\mathrm{dev}\,(\boldsymbol{\Sigma})\| - q(\epsilon_{\mathrm{p}}) - \Sigma_{\mathrm{ini}} , \tag{2.153}$$

where R is the radius of the yield surface, dev $(\boldsymbol{\Sigma})$ is the deviatoric part of the MANDEL stress tensor, ϵ_{p} is the VON MISES effective plastic strain and Σ_{ini} is the yield stress of the virgin material. This yield criterion is shown to be in excellent agreement with experiments for many ductile metals, such as copper, nickel, aluminium and iron.

Example 2.5.2 *Single crystal plasticity for a single slip system*

The constitutive equations of single crystal plasticity can serve as an example for the theory presented above. According to [ASARO 1983] the multiplicative

decomposition (2.132) is then a composition of a deformation due solely to crystallographic slip embodied in the plastic part of the deformation gradient $\mathbf{F}^{\mathrm{p}}$ and the deformation due to the stretching and the rotation of the crystal lattice with the deformation gradient $\mathbf{F}^{\mathrm{e}}$. For a crystal with a single slip, the plastic part of the deformation gradient $\mathbf{F}^{\mathrm{p}}$ is evaluated as

$$\mathbf{F}^{\mathrm{p}} = \mathbf{I} + \tilde{\lambda}\, \mathbf{m} \otimes \mathbf{n}\,. \tag{2.154}$$

Vectors $\mathbf{m}$ and $\mathbf{n}$ are orthogonal unit vectors on the intermediate configuration defining the slip system $(\mathbf{m}, \mathbf{n})$, with $\mathbf{m}$ being the slip direction and $\mathbf{n}$ being the normal to the slip plane and $\tilde{\lambda}$ is the plastic shearing on the crystallographic slip system.
If the component of the stress tensor producing the forces on dislocations causing them to slip is pinpointed according to SCHMID's law, it is recognised as a component of the shear stress and it is work conjugated to the slipping rate. The constitutive equations are then based on the statement that the plastic flow occurs on the slip system after this critical resolved shear stress or SCHMID stress reaches certain critical value $\Sigma_c(\alpha)$ and therefore the yield condition reads:

$$\phi(\boldsymbol{\Sigma}, \alpha) = \|\boldsymbol{\Sigma} : (\mathbf{m} \otimes \mathbf{n})\| - \Sigma_c(\alpha)\,. \tag{2.155}$$

Keeping (2.151) in mind, terms in (2.155) can be rearranged:

$$\phi(\boldsymbol{\Sigma}, \alpha) = \|\boldsymbol{\Sigma} : (\mathbf{m} \otimes \mathbf{n})\| - q(\alpha) - f_{\mathrm{ini}} = f(\boldsymbol{\Sigma}, q) - f_{\mathrm{ini}}\,, \tag{2.156}$$

where $q(\alpha)$ is the yield stress depending on the strain-like internal variable α associated with the isotropic hardening/softening process in the material. According to (2.147), differentiating the yield function with respect to $\boldsymbol{\Sigma}$ delivers the plastic distortion rate

$$\mathbf{L}^{\mathrm{p}} = \lambda\, \partial_{\boldsymbol{\Sigma}}\, \phi = \lambda\, \mathrm{sign}\left[\|\boldsymbol{\Sigma} : (\mathbf{m} \otimes \mathbf{n})\|\right]\, (\mathbf{m} \otimes \mathbf{n})\,. \tag{2.157}$$

This mathematical description of the material response in single crystals can be extended to systems with multiple slips. The detailed presentation of crystal plasticity can be found in [ASARO 1983].

2.5.2 Multiplicative finite strain plasticity: numerical implementation

After the basic mathematical relations defining a material model of finite plasticity are set, an adequate solution procedure should be defined. If the problem to be solved is summarised as in Figure 2.6, its numerical implementation could be divided into two major parts:

1. *Time discretization* of the interval of interest $[0, T] = \cup_{n=1}^{N} [t_n, t_{n+1}]$.

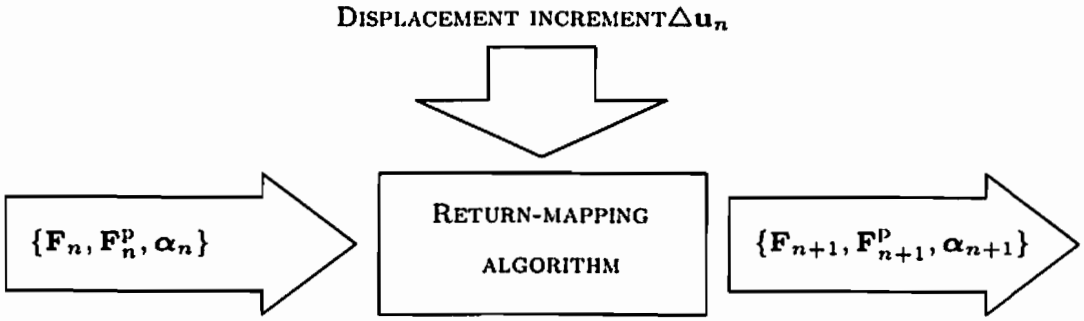

Figure 2.7: The return-mapping algorithm in constitutive updates [SIMO & HUGHES 1998].

2. *Space discretization* $\mathcal{B}^d$ of the domain of interest $\mathcal{B}$ leading to the discrete form of the principal of virtual work as given in Section 2.2.3.

In most computational algorithms, the space discretization is accomplished by the standard finite-element method (see e.g. [BATHE 1995], [BELYTSCHKO & MORAN 2000]) which remains independent of the particular choice of the constitutive model.
The discrete form of the weak form of the linear momentum balance paired with the time-dependent constitutive equations is the central problem of computational plasticity. Available solution strategies are based on the local formulation of the evolution equations at each quadrature point of the discrete space model according to the finite-element method. An overview of the algorithmic procedures for the numerical time integration of the evolution equations (2.147) and their properties can be found in the literature on computational mathematics, e.g. [HAIRER & WANNER 2000]. Numerical procedures specified to the finite plasticity can be found in e.g. [SIMO & HUGHES 1998; SIMO 1998].
The numerical procedure for the time integration of the evolution equations (2.147) used in this work is the *return-mapping algorithm* according to [SIMO & HUGHES 1998]. Its key feature, i.e. the possibility to compute the dissipation driven variables according to a given deformation history, is schematically represented in Figure 2.7.
The return-mapping algorithm is in essence an operator split procedure, where the solution is evaluated by introducing an elastic loading step (the *trial state*). If the resulting stress field does not belong to the space of admissible stresses $\mathbb{E}_\sigma$, a plastic corrector step must be performed. The time integration of the evolution equations in this correction procedure is based on the use of the implicit backward-EULER difference method for the discretization of the time domain. According to [SIMO 1998], the choice of this iterative method is advocated by its first-order accuracy and its unconditional stability, i.e. it possesses a set of linearized stability properties necessary to secure a bounded response

1. *Initialise the state and the deformation update*

$$(\mathbf{F}_n, \mathbf{F}^{\mathrm{p}}_n, \mathbf{q}_n)\,, \mathbf{F}_{n+1}\,.$$

2. ELASTIC PREDICTOR STEP: *Compute the trial state*

$$\mathbf{F}^{\mathrm{p}}_{n+1} = \mathbf{F}^{\mathrm{p}}_n \quad \boldsymbol{\alpha}_{n+1} = \boldsymbol{\alpha}_n \quad \Rightarrow \mathbf{C}^{\mathrm{e}}_{n+1} = {\mathbf{F}^{\mathrm{p}}_{n+1}}^{-\mathrm{T}} \cdot \mathbf{C}_{n+1} \cdot {\mathbf{F}^{\mathrm{p}}_{n+1}}^{-1}\,.$$

3. *Evaluate the yield function*

$$\phi^{trial}_{n+1}\,(\boldsymbol{\Sigma}^{trial}_{n+1}\,, \boldsymbol{\alpha}_n)\,.$$

IF $\phi^{trial}_{n+1}\,(\boldsymbol{\Sigma}^{trial}_{n+1}\,, \boldsymbol{\alpha}_n) \leq 0$ THEN:

Set $(\bullet)_{n+1} = (\bullet)_n$ & EXIT.

ENDIF.

4. PLASTIC CORRECTOR STEP: *Evolution equations*

$$\mathbf{F}^{\mathrm{p}}_{n+1} = \mathbf{F}^{\mathrm{p}}_n + \Delta\lambda\, \partial_{\boldsymbol{\Sigma}}\, g\,|_{\boldsymbol{\Sigma}_{n+1}, \mathbf{q}_{n+1}} \cdot \mathbf{F}^{\mathrm{p}}_{n+1}\,,$$

$$\boldsymbol{\alpha}_{n+1} = \Delta\lambda\, \partial_{\mathbf{q}}\, h\,|_{\boldsymbol{\Sigma}_{n+1}, \mathbf{q}_{n+1}}\,,$$

$$\Delta\lambda = \lambda(t_{n+1}) - \lambda(t_n)\,.$$

5. PLASTIC CORRECTOR STEP: *Residual*

$$\mathbf{R}_{n+1} = \left[\mathbf{R}^{\mathbf{F}^{\mathrm{p}}}_{n+1}\,, \mathbf{R}^{\boldsymbol{\alpha}}_{n+1}\right] = \mathbf{0} \quad \wedge \quad \phi_{n+1}\,(\boldsymbol{\Sigma}_{n+1}\,, \mathbf{q}_{n+1}) = 0\,,$$

$$\mathbf{R}^{\mathbf{F}^{\mathrm{p}}}_{n+1} = -\mathbf{F}^{\mathrm{p}}_{n+1} + \mathbf{F}^{\mathrm{p}}_n + \Delta\lambda\, \partial_{\boldsymbol{\Sigma}}\, g\,|_{\boldsymbol{\Sigma}_{n+1}, \mathbf{q}_{n+1}} \cdot \mathbf{F}^{\mathrm{p}}_{n+1}\,,$$

$$\mathbf{R}^{\boldsymbol{\alpha}}_{n+1} = -\boldsymbol{\alpha}_{n+1} + \Delta\lambda\, \partial_{\mathbf{q}}\, h\,|_{\boldsymbol{\Sigma}_{n+1}, \mathbf{q}_{n+1}}\,.$$

6. PLASTIC CORRECTOR STEP: *Linearization - algorithmic tangent*

$$\mathbb{C}^{el}_{n+1} = \frac{\mathrm{d}\mathbf{P}_{n+1}}{\mathrm{d}\mathbf{F}_{n+1}}\,.$$

Figure 2.8: Return-mapping algorithm for multiplicative plasticity

of the integration procedure.
An overview of the return-mapping procedure is given in Figure 2.8. The object of the procedure is a quadrature point $\mathbf{x} \in \mathcal{B}^d$ of the space discretization within a typical time interval $[t_n, t_{n+1}]$.

Step 1. The starting point of the numerical procedure is the assumption that the problem can be regarded as strain driven and the initial state $(\mathbf{F}_n, \mathbf{F}_n^{\mathrm{p}}, \mathbf{q}_n)$ and the updated deformation gradient $\mathbf{F}_{n+1}$ are given.

Step 2. A purely elastic trial step is calculated.

Step 3. The resulting stress field $\boldsymbol{\Sigma}_{n+1}^{trial}$ is used for the assessment of the trial value of the yield function ϕ_{n+1}^{trial}. If the trial stress state is inside the space of admissible stresses $\mathbb{E}_\sigma$ or on the yield surface $\partial\mathbb{E}_\sigma$, the loading step leads to an elastic material response and the predicted trial state is the actual state.

Step 4. If the yield function has a positive value, a plastic corrector step must be performed in order to render an admissible stress state by finding a closest point projection of the trial state onto the yield surface. Applying the backward-EULER scheme to the evolution equations of the constitutive model of the multiplicative plasticity with the restrictions of KUHN-TUCKER conditions (2.148) and consistency condition (2.149) transforms the set of algebraic differential conditions into a set of purely algebraic equations.

Step 5. A vanishing residual $\mathbf{R}_{n+1}$ and a vanishing yield function ϕ_{n+1} form a set of nonlinear algebraic equations to be solved in order to correct the trial state.

Step 6. Following the idea of [SIMO & HUGHES 1998], the system is solved by a systematic application of the NEWTON iterative procedure, which guarantees an asymptotic quadratic convergence for sufficiently smooth functions. It is based on the linearization of the residual about the current iterate. The linearized problem is completely specified only when the explicit expression for the consistent algorithmic tangent $\mathbb{C}_{n+1}^{el}$ is given.

The dimension of the problem presented above is $9+\dim\boldsymbol{\alpha}+1$ in a general case. However, in the case of a hyperelastic, fully isotropic material response, the tensors $\boldsymbol{\Sigma}$, $\mathbf{C}^{\mathrm{e}}$ and $\partial_{\boldsymbol{\Sigma}}\, g$ are coaxial. It reduces the dimension of the problem to $3 + \dim\boldsymbol{\alpha} + 1$.
A detailed presentation of the numerical procedure and its performance can be found in [SIMO & HUGHES 1998; SIMO 1998] and will be omitted here. A specification of the return-mapping algorithm to the modelling of localised material failure will be presented in detail in the following sections.

3 Single surface Strong Discontinuity Approach

A three-dimensional finite element formulation applicable for the simulation of a highly localised material failure in solids is presented in this chapter. The adopted finite element model captures the localised fully nonlinear kinematics associated with the failure by means of the Strong Discontinuity Approach (SDA). In contrast to classical continuum mechanics, the deformation gradient is additively decomposed into a conforming part corresponding to a smooth deformation mapping and an enhanced part reflecting the final failure kinematics of the micro-scale. The advocated implementation of the Enhanced Assumed Strain (EAS) concept leads to the elimination of the additional degrees of freedom (displacement jump) on the material point level. More precisely, the applied numerical implementation is similar to that of standard (finite) plasticity. The model is not restricted by the choice of finite-element type or the material model. Any cohesive law defining the connection between the displacement discontinuity and the traction vector can be applied.
The kinematics induced by localised failure is presented in Section 3.1. The fundamental postulates for the implementation of the strong discontinuities are followed by a detailed description of the kinematics and its numerical implementation. A proposition for an effective constitutive model is given in Section 3.2. A detailed discussion of the numerical implementation can be found in Section 3.3.

3.1 Kinematics

3.1.1 Kinematics of strong discontinuities

This section sets the basic notions and postulates of the kinematics associated with the Strong Discontinuity Approach (SDA), based on the propositions made in [Mosler 2004c; Mosler 2005a; Mosler 2006; Mosler 2007].
Following the idea of [Oliver & Simo 1994; Oliver 1995b; Oliver 1995a], a body $\mathcal{B}$ which occupies the domain $\Omega \subset \mathbb{R}^3$ in the reference configuration (see Figure 3.1) is assumed to be separated into two parts by a cut denoted as $\partial_s\Omega$. This cut defines the subsets Ω^- and Ω^+ and may represent a crack surface or a slip plane with respect to Ω. In order to guarantee a well-defined normal vector field $\mathbf{N}$ (piecewise), it is sufficient to postulate the submanifold $\partial_s\Omega$ to be piecewise a hyperplane of class C^1. The subsets Ω^- and Ω^+ are well defined, if $\partial_s\Omega$ is connected and the subsets Ω^- ,Ω^+ and the material surface $\partial_s\Omega$ form a partition of Ω:

$$\Omega = \Omega^- \cup \Omega^+ \cup \partial_s\Omega\,. \tag{3.1}$$

Under these assumptions, the motion of the body $\mathcal{B}$ can be described by a discontinuous deformation mapping φ, which connects each point P with a

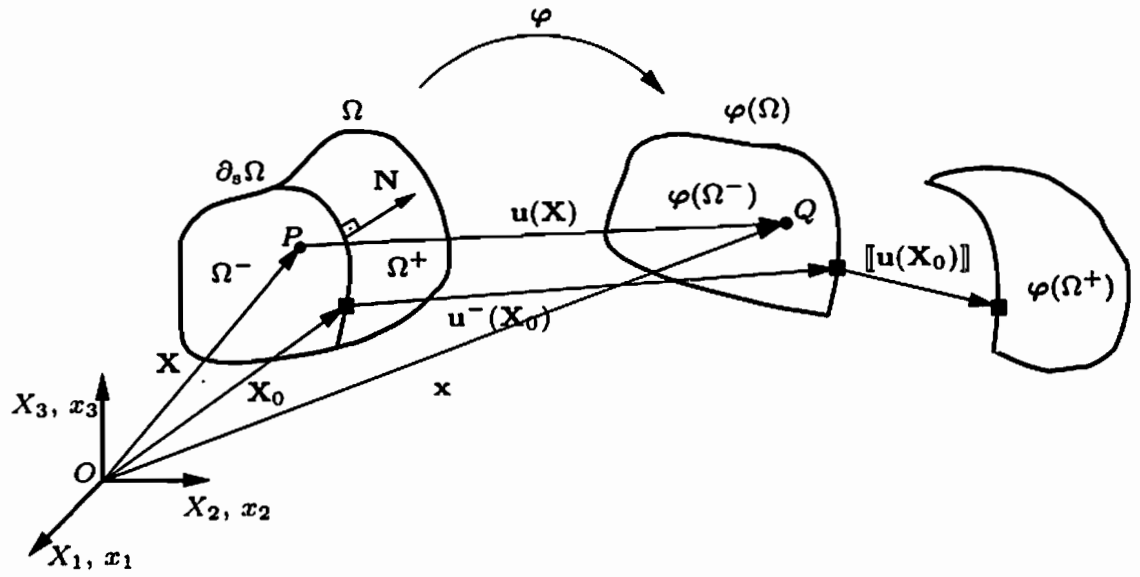

Figure 3.1: Reference and current configurations of a body $\mathcal{B}$ separated into two parts Ω^- and Ω^+ by a singular surface $\partial_s\Omega$.

position $\mathbf{X}$ in the reference configuration Ω to the corresponding point Q with a position $\mathbf{x}$ in the current configuration $\varphi(\Omega)$. Based on the assumed connectivity of Ω and $\varphi = \mathrm{id}_\Omega + \mathbf{u}$, an equivalence between a discontinuous deformation mapping $\varphi(\Omega)$ and a discontinuous displacement field $\mathbf{u}$ can be stated. This leads to the definition of the displacement field of the following type:

$$\mathbf{u}|_{\Omega^\pm} \in C^\infty(\Omega^\pm, \mathbb{R}^3), \quad \Omega^\pm := \Omega^+ \cup \Omega^- . \tag{3.2}$$

In order to describe the discontinuity of the displacement field $\mathbf{u} : \Omega \to \mathbb{R}^3$, condition (3.2) is used for the definition of the left-hand limit $\mathbf{u}^-(\mathbf{X}_0)$ and the right-hand limit $\mathbf{u}^+(\mathbf{X}_0)$ at $\mathbf{X}_0 \in \partial_s\Omega$:

$$\mathbf{u}^\pm(\mathbf{X}_0) := \lim_{n\to\infty} \mathbf{u}(\mathbf{X}_n^\pm), \quad (\mathbf{X}_n^\pm)_{n\in\mathbb{N}} \in (\Omega^\pm)^{\mathbb{N}}, \quad \mathbf{X}_n^\pm \to \mathbf{X}_0 \ (n \to \infty). \tag{3.3}$$

The discontinuity is restricted to the singular surface $\partial_s\Omega$ while $\mathbf{u}$ is smooth on $\Omega^\pm$. After the limiting values of the displacement field at the singular surface $\partial_s\Omega$ are defined, the discontinuity $[\![\mathbf{u}(\mathbf{X}_0)]\!]$ of $\mathbf{u}$ at $\mathbf{X}_0$ is to be evaluated as the difference

$$[\![\mathbf{u}(\mathbf{X}_0)]\!] := \mathbf{u}^+(\mathbf{X}_0) - \mathbf{u}^-(\mathbf{X}_0), \quad \forall \mathbf{X}_0 \in \partial_s\Omega . \tag{3.4}$$

A displacement mapping according to (3.2) can then be defined using a HEAVISIDE function shifted to the discontinuity surface $\partial_s\Omega$

$$\mathcal{H}_s = \begin{cases} 1 & : \ \forall \mathbf{X} \in \Omega^+ \cup \partial_s\Omega \\ 0 & : \ \forall \mathbf{X} \in \Omega^- , \end{cases} \tag{3.5}$$

in the form

$$\mathbf{u}(\mathbf{X}) = \mathbf{u}_-(\mathbf{X}) + \mathcal{H}_s\,(\mathbf{u}_+(\mathbf{X}) - \mathbf{u}_-(\mathbf{X}))\,,$$
$$\mathbf{u}_-, \mathbf{u}_+ \in \mathcal{C}^\infty(\Omega, \mathbb{R}^3)\,. \tag{3.6}$$

Two independent variables $\mathbf{u}|_{\Omega^-} = \mathbf{u}_-|_{\Omega^-}$ and $\mathbf{u}|_{\Omega^+} = \mathbf{u}_+|_{\Omega^+}$ reflect a non-vanishing jump of the deformation gradient at the discontinuity surface $\partial_s\Omega$:

$$[\![\mathbf{F}(\mathbf{X}_0)]\!] \neq \mathbf{0}\,, \quad \mathbf{X}_0 \in \partial_s\Omega\,. \tag{3.7}$$

According to [MOSLER 2007], the displacement field of this kind and its corresponding deformation mapping are piecewise continuous and it belongs to the space of special functions with bounded variations.
The preceding concept of deformation mapping which describes the localised discontinuities in materials is used in various finite element method (FEM) models involving SDA, e.g. [SIMO & OLIVER 1994; ARMERO & GARIKIPATI 1995; LARSSON, RUNESSON & ÅKESSON 1995; OLIVER 1996; WELLS & SLUYS 2001A; WELLS & SLUYS 2001B; BORJA & REGUEIRO 2001; MOSLER & MESCHKE 2003A; MOSLER & BRUHNS 2004; FEIST & HOFSTETTER 2007].

3.1.2 Kinematics: Strong Discontinuity Approach

If the proposed form of the displacement field (3.6) is evaluated from the point of its application in the numerical solution procedure for the BVP (2.79), it could be marked as non-suitable. This is based on the fact that the essential DIRICHLET boundary conditions cannot be exercised without implementing the displacement jump $[\![\mathbf{u}]\!]$. Therefore, a reformulation of the kinematics into a form suitable for the implementation of the DIRICHLET boundary conditions is necessary.
Based on the assumptions and postulates of Section 3.1.1 and according to [SIMO, OLIVER & ARMERO 1993; SIMO & OLIVER 1994; OLIVER 1996], the displacement field describing strong discontinuities at $\partial_s\Omega$ can be assumed in the form

$$\mathbf{u} = \hat{\mathbf{u}} + [\![\mathbf{u}]\!]\;(\mathcal{H}_s - \varphi) \quad \text{with} \quad \hat{\mathbf{u}} \in \mathcal{C}^\infty(\Omega, \mathbb{R}^3),\; \varphi \in \mathcal{C}^\infty(\Omega, \mathbb{R})\,. \tag{3.8}$$

Here, $\hat{\mathbf{u}}$ denotes the regular part of the displacement field in Ω and φ (not to be confused with the deformation mapping $\varphi(\Omega)$) is a smooth ramp function allowing the prescription of the DIRICHLET boundary conditions in terms of the regular part of the displacement field $\hat{\mathbf{u}}$. If DIRICHLET boundary conditions can be applied exclusively to the regular part of the displacement field $\hat{\mathbf{u}}$, the kinematic description (3.8) becomes more convenient for numerical applications.

Comparing the formulations (3.6) and (3.8), the correlation between the featured displacement fields could be formulated in the following manner:

$$\mathbf{u}_- = \hat{\mathbf{u}} - [\![\mathbf{u}]\!]\ \varphi\,, \quad \mathbf{u}_+ = \hat{\mathbf{u}} + [\![\mathbf{u}]\!]\ (1-\varphi)\,. \tag{3.9}$$

The deformation gradient $\mathbf{F}$ of such a deformation mapping cannot be evaluated in standard manner due to the fact that the HEAVISIDE function is not continuous at $\partial_s\Omega$ and its gradient can only be defined in generalised form, i.e. $D\mathcal{H}_s = \mathbf{N}\,\delta_s$. Here, δ_s represents the DIRAC delta-distribution at the singular surface $\partial_s\Omega$:

$$\int_\Omega \delta_s\ \varphi_0\,\mathrm{d}\Omega = \int_{\partial_s\Omega} \varphi_0\,\mathrm{d}S\,, \quad \forall\,\varphi_0 \in C_0^\infty(\Omega)\,. \tag{3.10}$$

Differentiating (3.8) with respect to $\mathbf{X}$ leads to

$$\mathbf{F} = \mathbf{1} + \frac{\partial\hat{\mathbf{u}}}{\partial\mathbf{X}} + \frac{\partial[\![\mathbf{u}]\!]}{\partial\mathbf{X}}\,(\mathcal{H}_s - \varphi) + [\![\mathbf{u}]\!]\otimes\mathbf{N}\,\delta_s - [\![\mathbf{u}]\!]\otimes\frac{\partial\varphi}{\partial\mathbf{X}}\,. \tag{3.11}$$

It is essential for the further development of the numerical procedure to identify particular parts of the deformation gradient as

$$\mathbf{F} = \begin{cases} \text{regular part} & \mathbf{1} + \dfrac{\partial\hat{\mathbf{u}}}{\partial\mathbf{X}} - \dfrac{\partial[\![\mathbf{u}]\!]}{\partial\mathbf{X}}\,\varphi - [\![\mathbf{u}]\!]\otimes\dfrac{\partial\varphi}{\partial\mathbf{X}} \\ +\,\text{jump part} & \dfrac{\partial[\![\mathbf{u}]\!]}{\partial\mathbf{X}}\,\mathcal{H}_s \\ +\,\text{singular part} & [\![\mathbf{u}]\!]\otimes\mathbf{N}\,\delta_s\,. \end{cases} \tag{3.12}$$

According to [STAKGOLD 1967; STAKGOLD 1998], this deformation gradient is to be understood only in a distributional sense.

3.1.3 Numerical implementation

After a suitable kinematic setup for the description of local material failure via strong discontinuities is presented, a numerical implementation based on the discretization by finite elements is to be described. The finite element approximation of the solution of the strong discontinuity problem presented in Sections 3.1.1 and 3.1.2 follows [SIMO, OLIVER & ARMERO 1993; SIMO & OLIVER 1994; OLIVER 1996]. It is based on the enrichment of the standard displacement field of FEM by an additional displacement field according to the *Enhanced Assumed Strain* concept presented in [SIMO, J.C. & RIFAI, M.S. 1990; SIMO, J. & ARMERO, F. 1992; SIMO, ARMERO & TAYLOR 1993].
The regular part of the deformation field $\hat{\mathbf{u}}$ featured in (3.8), is approximated in a standard finite element fashion, i.e. globally conforming

$$\hat{\mathbf{u}} = \sum_{i=1}^{n_{\text{node}}} N_i\ \hat{\mathbf{u}}_i^{\text{e}}\,. \tag{3.13}$$

Here, N_i are standard interpolation functions associated with node i, n_{node} is the number of nodes in the finite element mesh and $\hat{\mathbf{u}}_i^{\text{e}}$ is the nodal displacement at the node i.
In order to secure the necessary properties of the ramp function φ addressed in previous section, [MOSLER 2006] suggests the definition

$$\varphi = \sum_{i=1}^{n_{\overline{\Omega^+}}} N_i \,, \tag{3.14}$$

where $n_{\overline{\Omega^+}}$ is the number of nodes of the respective finite element which belong to the closure of Ω^+ depicted by $\overline{\Omega^+}$. This number is easily formulated if the singular surface $\partial_{\text{s}}\Omega$ is planar in each finite element. Due to the basic properties of standard interpolation functions, the displacement field at each node i of the finite element mesh with the position vector $\mathbf{X}_i^{\text{e}}$ reduces to its regular part

$$\mathbf{u}(\mathbf{X}_i^{\text{e}}) = \hat{\mathbf{u}}(\mathbf{X}_i^{\text{e}}) \,, \quad \forall \mathbf{X}_i^{\text{e}} \tag{3.15}$$

and the DIRICHLET boundary conditions can be formulated in terms of the regular part of the displacement field $\hat{\mathbf{u}}$.
The interpolation (3.13) of $\hat{\mathbf{u}}$ leads to the identification of the corresponding regular part of the deformation gradient $\mathbf{F}$ in (3.11):

$$\hat{\mathbf{F}} := \mathbf{1} + \frac{\partial \hat{\mathbf{u}}}{\partial \mathbf{X}} = \mathbf{1} + \operatorname{Grad} \hat{\mathbf{u}} \,. \tag{3.16}$$

Since this finite element formulation is based on the Enhanced Assumed Strain concept (EAS), the enhanced part of the deformation gradient is modelled in an incompatible fashion and the additive decomposition of the deformation gradient $\mathbf{F}$ yields an incompatible enhanced displacement gradient

$$\mathbf{H} = \frac{\partial [\![\mathbf{u}]\!]}{\partial \mathbf{X}} \, (\mathcal{H}_{\text{s}} - \varphi) + [\![\mathbf{u}]\!] \otimes \mathbf{N} \, \delta_{\text{s}} - [\![\mathbf{u}]\!] \otimes \frac{\partial \varphi}{\partial \mathbf{X}} \,. \tag{3.17}$$

According to [SIMO & OLIVER 1994; OLIVER 1996], the function of the displacement jump $[\![\mathbf{u}]\!]$ is assumed piece-wise constant (over elements), i.e.

$$\frac{\partial [\![\mathbf{u}]\!]}{\partial \mathbf{X}} = \mathbf{0} \,. \tag{3.18}$$

This assumption results in an alternative form of the deformation gradient

$$\mathbf{F} = \mathbf{1} + \frac{\partial \hat{\mathbf{u}}}{\partial \mathbf{X}} + [\![\mathbf{u}]\!] \otimes \mathbf{N} \, \delta_{\text{s}} - [\![\mathbf{u}]\!] \otimes \frac{\partial \varphi}{\partial \mathbf{X}} \,. \tag{3.19}$$

The displacement field and the corresponding deformation gradient based on the restriction (3.18) render the underlying formalism as a method of incompatible modes, or more precisely EAS. This assumption about the spatial

behaviour of the displacement jump is adopted in a large number of numerical simulations based on SDA, see e.g. [SIMO & OLIVER 1994; OLIVER 1996; ARMERO & GARIKIPATI 1996; LARRSON & RUNESSON 1996; BORJA 2000]. In order to benefit from the algorithms of computational plasticity, the foregoing kinematic concept based on the SDA is implemented in the context of multiplicative finite strain plasticity. On this account, the additive decomposition of the deformation gradient given above must be replaced with a suitable local multiplicative decomposition in accordance with the idea elaborated in Sections 2.5.1 and 2.5.2. Following [GARIKIPATI 1996; ARMERO & GARIKIPATI 1996], the material counterpart of the displacement jump function $\mathbf{J}$ is introduced (see Figure 3.2):

$$\mathbf{J} := \bar{\mathbf{F}}^{-1} \cdot [\![\mathbf{u}]\!] \,. \tag{3.20}$$

$\mathbf{J}$ can be understood as the pull-back of the displacement jump function $[\![\mathbf{u}]\!]$ from the current to the intermediate configuration by the mapping $\bar{\mathbf{F}}$.

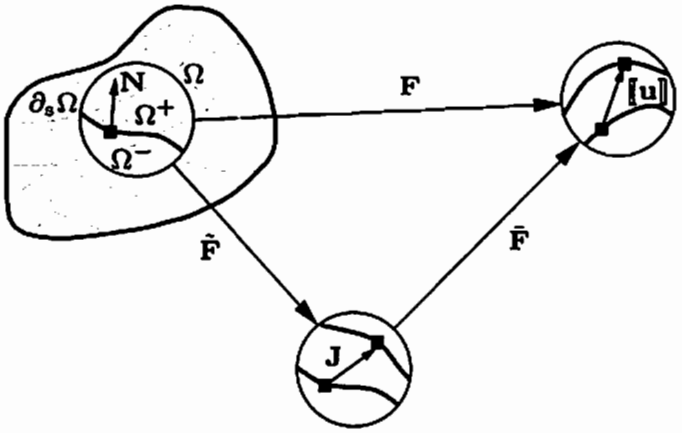

Figure 3.2: Multiplicative decomposition of the deformation gradient $\mathbf{F}$ in a regular and singular part [ARMERO & GARIKIPATI 1996].

A suitable local multiplicative decomposition of the deformation gradient reads

$$\mathbf{F} = \begin{cases} \bar{\mathbf{F}} \cdot \tilde{\mathbf{F}}, & \forall \mathbf{X}_0 \in \partial_s\Omega \\ \bar{\mathbf{F}}, & \forall \mathbf{X} \in \Omega^{\pm} \end{cases} \tag{3.21}$$

with

$$\begin{aligned} \bar{\mathbf{F}} &= 1 + \operatorname{Grad} \hat{\mathbf{u}} - [\![\mathbf{u}]\!] \otimes \operatorname{Grad} \varphi = 1 + \operatorname{Grad} \hat{\mathbf{u}} - \bar{\mathbf{F}} \cdot \mathbf{J} \otimes \operatorname{Grad} \varphi \\ \tilde{\mathbf{F}} &= 1 + \mathbf{J} \otimes \mathbf{N}\, \delta_s \,. \end{aligned} \tag{3.22}$$

$\bar{\mathbf{F}}$ is the regular part of the deformation gradient and $\tilde{\mathbf{F}}$ is associated with the singular distribution. The later is a result of the generalised derivative of the

displacement jump. The distinction between the bulk material $\Omega^{\pm}$ and the discontinuity surface $\partial_s\Omega$ in (3.21) means that the appearance of bifurcation of the mapping (3.8) at the discontinuity $\partial_s\Omega$ leads to the local multiplicative decomposition of the corresponding deformation gradient, while the rest of the material outside the discontinuity is subjected to the regular part of the deformation gradient $\bar{\mathbf{F}}$.
Based on the prerequisite that the regular part and the ramp function of the deformation mapping (3.8) are smooth, the deformation gradient $\mathbf{F}$ has a zero jump at the singular surface $\partial_s\Omega$, i.e.

$$[\![\mathbf{F}]\!] = [\![\bar{\mathbf{F}}]\!] = \mathbf{0}\,, \quad \forall \mathbf{X}_0 \in \partial_s\Omega\,. \tag{3.23}$$

This fact leads to the conclusion that the material responses in two parts of the bulk material Ω^+ and Ω^- are not independent of one another (for a detailed elaboration of this fact see e.g. [MOSLER & BRUHNS 2004]).
Argument in line with (2.134) leads to the additive decomposition of the spatial velocity gradient $\mathbf{l} := \dot{\mathbf{F}} \cdot \mathbf{F}^{-1}$ at the discontinuity $\partial_s\Omega$

$$\mathbf{l} = \bar{\mathbf{l}} + \tilde{\mathbf{l}} \quad \text{with} \quad \begin{aligned} \bar{\mathbf{l}} &= \dot{\bar{\mathbf{F}}} \cdot \bar{\mathbf{F}}^{-1} \\ \tilde{\mathbf{l}} &= \bar{\mathbf{F}} \cdot \dot{\tilde{\mathbf{F}}} \cdot \tilde{\mathbf{F}}^{-1} \cdot \bar{\mathbf{F}}^{-1} \end{aligned} \tag{3.24}$$

into $\bar{\mathbf{l}}$ and $\tilde{\mathbf{l}}$, associated with the continuous and discontinuous part of the displacement field, respectively. The regularly distributed part of the deformation gradient $\bar{\mathbf{F}}$ is locally invertible and $\bar{\mathbf{l}}$ can be computed in a standard manner. In order to calculate $\tilde{\mathbf{l}}$, an inversion of a singular distribution must be performed. Based on the idea of [GARIKIPATI 1996; ARMERO & GARIKIPATI 1996], $\tilde{\mathbf{F}}$ is to be understood as a linear mapping between two vector spaces with a distributional component. The resulting distributional velocity gradient has the form:

$$\begin{aligned} \tilde{\mathbf{l}} &= \bar{\mathbf{F}} \cdot \dot{\tilde{\mathbf{F}}} \cdot \tilde{\mathbf{F}}^{-1} \cdot \bar{\mathbf{F}}^{-1} \\ &= \bar{\mathbf{F}} \cdot \dot{\mathbf{J}} \otimes \mathbf{N} \cdot \bar{\mathbf{F}}^{-1} \delta_s \\ &= \bar{\mathbf{F}} \cdot \frac{\partial}{\partial t} \left(\bar{\mathbf{F}}^{-1} \cdot [\![\mathbf{u}]\!] \right) \otimes \cdot \mathbf{N} \cdot \bar{\mathbf{F}}^{-1} \delta_s \\ &= \mathcal{L}_v \, [\![\mathbf{u}]\!] \otimes \mathbf{N} \cdot \bar{\mathbf{F}}^{-1} \delta_s\,. \end{aligned} \tag{3.25}$$

$\mathcal{L}_v\,[\![\mathbf{u}]\!]$ represents the objective, LIE-type derivative of the displacement jump defined in (2.114).
If the constitutive model of the material behaviour under the assumption of localised failure includes evolution equations for the material description of the displacement jump function $\mathbf{J}$, the singular part of the deformation gradient $\tilde{\mathbf{F}}$ can be calculated and a unique local multiplicative decomposition of the total deformation gradient can be stated.

3.2 Constitutive relations

The kinematics describing the SDA to the localised failure in materials presented in the previous section posts a severe limitation to the use of standard constitutive modelling for the description of the material response. From a physical point of view, the phenomenon can be separated in two distinct phases: the phase before the local failure and the phase after the local failure. From the point of view of mathematical modelling, these two phases are recognised as a pre-localisation phase and a post-localisation phase. Here, the term *localisation* refers to the strain concentration in some critical zone in the material due to the bifurcation of the homogeneous deformation field.
In regard of the pre-localisation phase, it is commonly assumed within the SDA formulation that the classical continuum constitutive model chosen for this phase is capable to predict the onset of the strain localisation (see [SIMO, OLIVER & ARMERO 1993; SIMO & OLIVER 1994; MIEHE & SCHRÖDER 1994; OLIVER 1996; ARMERO & GARIKIPATI 1996; BORJA 2002; MOSLER 2004C]). It is usually agreed that this event is to be predicted by the bifurcation analysis. The bifurcation analysis renders, according to [SIMO, OLIVER & ARMERO 1993] among others, the local strain localisation condition as the singularity of the properly chosen localisation tensor, together with the direction of the localisation mode.
In regard of the response of the material to the evaluated localisation mode after bifurcation, the solutions differ significantly. The onset of the localisation results in a mathematical sense in the loss of strong ellipticity of the partial differential equations governing the continuum based constitutive model. As a result, they cease to deliver a well-posed apparatus for the analysis of the material behaviour. The result is a well known pathological mesh dependence of the numerical solution by finite element method ([DE BORST 1986; DE BORST 2001]). In order to overcome this difficulty, a number of approaches are developed. The driving traction $\mathbf{T} = \mathbf{P} \cdot \mathbf{N}$ and the displacement jump $[\![\mathbf{u}]\!]$ along the discontinuity $\partial_s\Omega$ can be conjugated using a localised softening law known also as the *traction-separation law* and *cohesive law* ([DUGDALE 1960; BARENBLATT 1962]). This cohesive behaviour can be described using a discrete framework where the projection of the standard stress-strain constitutive equations onto the singular surface defines the traction-separation law. The introduction of a distributional form is a key feature to make the standard continuum models consistent with the appearance of the strong discontinuities. This discrete approach is extended and elaborated by e.g. [SIMO & OLIVER 1994; OLIVER 1996; OLIVER 2000; OLIVER, HUESPE, PULIDO & SAMANIEGO 2003].
However, a number of authors dispute the consideration of the pre-localised constitutive model in the post-localised material response ([SNYMAN, BIRD & MARTIN 1991; MIEHE & SCHRÖDER 1994; ARMERO & GARIKIPATI 1996; BORJA 2002; MOSLER 2004C]). For example [BORJA 2002] justifies this re-

mark by comparing the material response of an intact rock to the material response of the particulated material after the strain localisation. As well as [BORJA 2002], [MIEHE & SCHRÖDER 1994; ARMERO & GARIKIPATI 1996; MOSLER 2004C] opt for a traction-separation law independent of the constitutive model used for the surrounding material. This completely decouples the material response in $\Omega^{\pm}$ from the material response at $\partial_s\Omega$. This decoupling leads to the additive decomposition of the HELMHOLTZ free energy in a manner similar to (2.136), which is a common ground for both discrete and domain-independent constitutive models.
Following [MOSLER 2006], this work is based on the softening laws independent of the response in the bulk material. The next two sections will be used to separately define a framework for the constitutive modelling in the virgin material $\Omega^{\pm}$ and at the singular surface $\partial_s\Omega$.

3.2.1 Constitutive relations for $\mathbf{X} \in \Omega^{\pm}$

The choice of the multiplicative decomposition (3.21) of the deformation gradient $\mathbf{F}$ gives this operator a regular character in the bulk material $\Omega^{\pm}$. It opens a possibility to model the material response in terms of the standard stress-strain constitutive equations of the type presented in Section 2.3.2. An additional assumption regarding the bulk material is a purely elastic material response (cf. [MOSLER 2006]). Following the methodology highlighted in Section 2.4, a polyconvex stored-energy functional $\Psi_{\text{reg}}(\bar{\mathbf{C}})$ according to (2.125) is postulated for the region $\Omega^{\pm}$. Here, $\bar{\mathbf{C}}$ represents the regular part of the right CAUCHY-GREEN deformation tensor

$$\bar{\mathbf{C}} := \bar{\mathbf{F}}^{\mathrm{T}} \cdot \bar{\mathbf{F}} \quad \text{with} \quad \bar{\mathbf{F}}|_{\Omega^{\pm}} = \mathbf{F}|_{\Omega^{\pm}} \wedge \bar{\mathbf{C}}|_{\Omega^{\pm}} = \mathbf{C}|_{\Omega^{\pm}} \,. \tag{3.26}$$

The pure elasticity of the bulk material renders a vanishing dissipation $\mathcal{D}$:

$$\mathcal{D} = \boldsymbol{\tau} : \bar{\mathbf{d}} - \partial_{\bar{\mathbf{C}}} \Psi_{\text{reg}} : \dot{\bar{\mathbf{C}}} = 0 \quad \text{with} \quad \bar{\mathbf{d}} := \bar{\mathbf{I}}_{\text{sym}} \tag{3.27}$$

and the resulting KIRCHOFF and second PIOLA-KIRCHOFF stress measures have the form

$$\boldsymbol{\tau} = 2\, \bar{\mathbf{F}} \cdot \partial_{\bar{\mathbf{C}}} \Psi_{\text{reg}} \cdot \bar{\mathbf{F}}^{\mathrm{T}} \quad \text{and} \quad \mathbf{S} = 2\, \partial_{\bar{\mathbf{C}}} \Psi_{\text{reg}} \,. \tag{3.28}$$

Due to the fact that those stress measures apply only to the material points with the position in regions $\Omega^{\pm}$ where the singular part of the deformation gradient vanishes, the bar over the second PIOLA-KIRCHHOFF stress tensor $\boldsymbol{S}$ is omitted.
The assumption of a purely elastic material response in the virgin material is not obligatory. According to [MOSLER 2006], other constitutive formulations such as plasticity are also applicable.

3.2.2 Constitutive relations for $\mathbf{X} \in \partial_s\Omega$

Relying on the key feature of the SDA, that is the kinematics (3.8) describing the deformation in locally defected material by two independent displacement fields $\hat{\mathbf{u}}$ and $[\![\mathbf{u}]\!]$, the multiplicative decomposition of the deformation gradient (3.21) yields two independent parts $\bar{\mathbf{F}}$ and $\tilde{\mathbf{F}}$. Based on this independence, [MOSLER 2004C; MOSLER 2006] proposes for all material points with a position in the discontinuity surface $\partial_s\Omega$ two separate constitutive models for the two parts of the deformation characterised by the regular part of the deformation gradient $\bar{\mathbf{F}}$ and the singular part of the deformation gradient $\tilde{\mathbf{F}}$, respectively. The constitutive model corresponding to the regular part of the deformation is described in Section 3.2.1. Based on (3.20) and the material invariance of the normal vector $\mathbf{N}$, the constitutive model corresponding to the singular part of the deformation gradient $\tilde{\mathbf{F}}$ should depend on some measure of the displacement jump, preferably on the material measure $\mathbf{J}$ although the true measure $[\![\mathbf{u}]\!]$ can also be used.
The idea presented in the introduction to Section 3.2 concerning the additive decomposition of the HELMHOLTZ free energy into a part characterising the hyperelastic material response in $\Omega^{\pm}$ and an additional term which captures the localised deformation resulting from the bifurcation of the homogeneous deformation in an adequate form, leads to the relation:

$$\Psi(\bar{\mathbf{C}}, \mathbf{J}, \boldsymbol{\alpha}) = \Psi_{\text{reg}}(\bar{\mathbf{C}}) + \Psi_{\text{sing}}(\mathbf{J}, \boldsymbol{\alpha})\, \delta_s \,. \tag{3.29}$$

The singular part of the localised deformation is introduced by the DIRAC-delta distribution multiplied with the functional Ψ_{sing} of the material displacement jump $\mathbf{J}$ and internal displacement-like variables $\boldsymbol{\alpha}$. $\mathbf{J}$ and $\boldsymbol{\alpha}$ describe the dissipative process in the material.
Amplifying the idea to restrict the attention only to the localised phenomena, [MOSLER 2006] further defines the localised deformation as strictly inelastic. This limitation yields a purely inelastic $\mathbf{J}$ and sets it in the family of displacement-like internal variables. The resulting singular term in the HELMHOLTZ free energy is then a function depending on a single argument $\Psi_{\text{sing}}(\boldsymbol{\alpha}(\mathbf{J}))$. A different approach with both elastic and inelastic parts of the displacement jump $\mathbf{J}$ can be found in e.g. [MIEHE & SCHRÖDER 1994; ARMERO 1999].
In order to connect the material response in the bulk material to the material response at the discontinuity, the principal of virtual work (Section 2.2.3) is applied to the body $\mathcal{B}$ with a surface of discontinuity $\partial_s\Omega$ characterised by a normal $\mathbf{N}$. If the body $\mathcal{B}$ is in static equilibrium under the action of body forces $\mathbf{B}$ and applied tractions $\mathbf{T}$, a proper choice of space of admissible variations η_0 and integration by parts lead to the condition of continuity of the traction vector $\mathbf{T} := \mathbf{P} \cdot \mathbf{N}$

$$\mathbf{T}^-(\mathbf{X}_0) = \mathbf{T}^+(\mathbf{X}_0) = \mathbf{T}(\mathbf{X}_0)\,, \quad \mathbf{X}_0 \in \partial_s\Omega\,. \tag{3.30}$$

Vectors $\mathbf{T}^-(\mathbf{X}_0)$ and $\mathbf{T}^+(\mathbf{X}_0)$ are the left-hand limit and the right-hand limit of the traction vector at the surface of singularity $\mathbf{X}_0 \in \partial_s\Omega$ in the sense of (3.3). The choice of the space of admissible test functions which leads to this jump condition must enable numerical solutions which accurately resolute the SDA kinematics presented in Section 3.1.3. According to [SIMO & OLIVER 1994], this can be achieved if a BUBNOV-GALERKIN-type of admissible variations is used. The condition of traction continuity (3.30) opens a possibility to use the hyperelastic material law associated with $\mathbf{X} \in \Omega^{\pm}$ in the calculation of the traction vector $\mathbf{T}(\mathbf{X}_0)$.
In a similar manner as in the case of multiplicative plasticity (Section 2.5.1), the additive decomposition of the stored energy functional (3.29), together with restriction (3.30) and the formulation of the spatial velocity gradient (3.24), leads to the spatial form of the dissipation in the purely inelastic material at the singular surface $\partial_s\Omega$

$$\mathcal{D} = \boldsymbol{\tau} : \mathbf{l} - \dot{\Psi} = \left[\left(\boldsymbol{\tau} \cdot \bar{\mathbf{F}}^{-\mathrm{T}} \cdot \mathbf{N}\right) \cdot \mathcal{L}_v \, [\![\mathbf{u}]\!] + \mathbf{q} \cdot \dot{\boldsymbol{\alpha}}\right] \delta_s \geq 0 \tag{3.31}$$

or in the intermediate configuration using the MANDEL stress tensor $\boldsymbol{\Sigma} = \bar{\mathbf{C}} \cdot \mathbf{S}$

$$\mathcal{D} = \left[\left(\bar{\mathbf{C}} \cdot \mathbf{S} \cdot \mathbf{N}\right) \cdot \dot{\mathbf{J}} + \mathbf{q} \cdot \dot{\boldsymbol{\alpha}}\right] \delta_s = \left(\bar{\mathbf{C}} \cdot \mathbf{S}\right) : \tilde{\mathbf{L}} + \mathbf{q} \cdot \dot{\boldsymbol{\alpha}} \, \delta_s \geq 0 \,. \tag{3.32}$$

As already noted in Section 2.5.1, $\mathbf{q} = -\partial_{\boldsymbol{\alpha}} \Psi_{\mathrm{sing}}$ is a stress-like internal variable conjugated to $\boldsymbol{\alpha}$. Similarly to the plastic distortion rate $\mathbf{L}^P$ in the case of multiplicative finite strain plasticity, the tensor $\tilde{\mathbf{L}}$ represents the pull-back of the distributional velocity gradient $\tilde{\mathbf{l}}$ to the intermediate configuration

$$\tilde{\mathbf{L}} = \dot{\mathbf{J}} \otimes \mathbf{N} \, \delta_s \,. \tag{3.33}$$

Since $\boldsymbol{\alpha} = \boldsymbol{\alpha}(\mathbf{J})$, this internal variable and its conjugate $\mathbf{q}$ are also defined on the intermediate configuration. Therefore, $\dot{\boldsymbol{\alpha}}$ is an objective time derivative.
In order to complete the constitutive model, the evolution equations for the internal variables $(\mathbf{J}, \boldsymbol{\alpha})$ are to be defined. If the formerly derived form of the reduced dissipation inequality in (3.32) is compared to the corresponding form derived in (2.143), it could be concluded that they are formally identical and the computation of the evolution equations for the internal variables can be in line with the procedure known from the theory of finite strain multiplicative plasticity.
According to [MOSLER 2004B; MOSLER 2004A], the traction continuity constraint (3.30) can be rewritten using the positive definiteness of a norm $\| \bullet \|$

$$\phi := \|\mathbf{T}^+(\mathbf{X}_0) - \mathbf{T}(\mathbf{X}_0)\| = 0 \,. \tag{3.34}$$

In the intermediate configuration, this yield condition reads

$$\phi := \|\bar{\mathbf{T}}^+(\mathbf{X}_0) - \bar{\mathbf{T}}(\mathbf{X}_0)\| = 0 \quad \text{with} \quad \bar{\mathbf{T}} := \bar{\mathbf{C}} \cdot \mathbf{S} \cdot \mathbf{N} \,. \tag{3.35}$$

Here, the vector $\bar{\mathbf{T}}$ is the pull-back of the traction vector $\mathbf{T}$ to the intermediate configuration. The form (3.35) of the traction continuity condition is formally equivalent to the yield condition of standard plasticity. Based on this equivalence, admissible stresses are constrained to lie in the space

$$\mathbb{E}_{\bar{\mathbf{T}}} := \left\{ (\bar{\mathbf{T}}^+, \mathbf{q}) \in \mathbb{R}^3 \times \mathbb{R}^n \mid \phi(\bar{\mathbf{T}}^+, \mathbf{q}) \leq 0 \right\}. \tag{3.36}$$

If the jump condition (3.30) is exercised on the reduced dissipation inequality (3.32), the problem to be solved in order to obtain $\dot{\mathbf{J}}$ and $\dot{\boldsymbol{\alpha}}$ can be defined as

$$\text{find:} \quad \max_{(\bar{\mathbf{T}}^+, \mathbf{q}) \in \mathbb{E}_{\bar{\mathbf{T}}}} \mathcal{D}(\bar{\mathbf{T}}^+, \mathbf{q}). \tag{3.37}$$

This postulate yields the evolution equations:

$$\dot{\mathbf{J}} = \lambda \, \partial_{\bar{\mathbf{T}}^+} \phi, \quad \dot{\boldsymbol{\alpha}} = \lambda \, \partial_{\mathbf{q}} \phi. \tag{3.38}$$

Relying on the standard plasticity procedure, the consistency condition yields the LAGRANGE multiplier λ.
For materials for which the associative flow rule is not an appropriate choice for the modelling of the material response, a generalisation of the evolution equations is possible. In those cases, a *plastic potential* $g(\bar{\mathbf{T}}^+, \mathbf{q})$ and a *hardening potential* $h(\bar{\mathbf{T}}^+, \mathbf{q})$ are introduced such that

$$\dot{\mathbf{J}} = \lambda \, \partial_{\bar{\mathbf{T}}^+} g, \quad \dot{\boldsymbol{\alpha}} = \lambda \, \partial_{\mathbf{q}} h. \tag{3.39}$$

Associative evolution equations are obtained from (3.39) if $g = h = \phi$.
If the space of admissible stresses (3.36) is articulated in MANDEL stresses, the evolution equation $(3.39)_1$ can be replaced by the evolution equation governing the inelastic velocity gradient $\tilde{\mathbf{L}}$ if the time invariance of the singular surface $\partial_s\Omega$ is taken into account

$$\dot{\mathbf{J}} \otimes \mathbf{N} = \lambda \, \partial_{\bar{\mathbf{C}} \cdot \mathbf{S}} \phi^*(\bar{\mathbf{C}} \cdot \mathbf{S}) \quad \text{with} \quad \phi^*(\bar{\mathbf{C}} \cdot \mathbf{S}, \mathbf{q}) := \phi(\bar{\mathbf{C}} \cdot \mathbf{S} \cdot \mathbf{N}, \mathbf{q}). \tag{3.40}$$

The equivalence between $(3.40)_1$ and $(2.147)_1$ complements the formal equivalence between the equations describing the constitutive model in the presence of localised inelastic deformation and those known from standard finite strain multiplicative plasticity. The localised inelastic behaviour materialised through $\mathbf{J}$ can also be treated using damage based material models. A damage type analysis of localised failure in materials can be found in e.g. [MOSLER & BRUHNS 2004; MOSLER 2005c].

Remark 3.2.1 *The choice of an adequate yield function*

The choice of a suitable yield function corresponding to the nature of the inelastic process occurring in the material is based on the fact that the elastic

and inelastic part of the deformation are completely separated by the assumptions made in this and the previous section. This is the reason why the traction continuity condition (3.30) is enforced only during the computation of the inelastic part of the deformation $\dot{\mathbf{J}}$ and $\dot{\boldsymbol{\alpha}}$, and then only to those components of the traction vector $\bar{\mathbf{T}}$ which are conjugated to non-vanishing components of the material displacement jump $\mathbf{J}$.
Based on this remark, the yield function appropriate for ductile materials such as metals or geomaterials could be chosen having in mind that inelastic deformations occurring in slip bands in those materials depend exclusively on the resultant of the shear components of $\bar{\mathbf{T}}$:

$$\phi(\bar{\mathbf{T}}, \mathbf{q}) = ||\bar{\mathbf{T}}_m||_2 - q(\alpha) \quad \text{with} \quad \bar{\mathbf{T}}_m := \bar{\mathbf{T}} - (\bar{\mathbf{T}} \cdot \mathbf{N})\,\mathbf{N}\,. \tag{3.41}$$

This type of yield function which belongs to the class of VON MISES plasticity models, is proposed in [MOSLER 2004B] for the geometrically linear kinematics. It will be exploited in the numerical examples presented in Chapter 5.
In order to prevent confusion, it should be pointed out that $\bar{\mathbf{T}}^+ := \bar{\mathbf{T}}$ at $\partial_s\Omega$ is used and the + sign is omitted in (3.41).

3.3 Numerical implementation

This section offers a detailed overview of the numerical implementation of the geometrically exact kinematics induced by strong discontinuities presented in Section 3.1 and the constitutive model presented in Section 3.2, which are assumed applicable for the description of the material behaviour in the presence of localised failure.
Based on the existing range of scientific efforts in this particular field of material modelling, two general directions of implementation can be observed. Those are the *interface elements* and the *elements with an inner displacement jump*. Interface elements allow the discontinuity of the displacement field only at the element boundaries. Such models are proposed by e.g. [NEEDLEMAN 1990; ORTIZ & PANDOLFI 1999]. Elements with an inner displacement jump allow the discontinuity of the displacement field inside the element. This class of numerical models can be further branched according to the technique of enrichment of the displacement field into *element-wise enrichment* and *nodal enrichment*.
Strong Discontinuity Approach - SDA advocating the enrichment of the displacement field on the element level belongs to the class of element-wise enrichments. Such models can be found in e.g. [DVORKIN, CUITIÑO & GIOIA 1990; KLISINSKI, RUNESSON & STURE 1991; SIMO, OLIVER & ARMERO 1993; ARMERO & GARIKIPATI 1996].
EXtended Finite Element Method X-FEM and *Partition of Unity Finite Element Method PU-FEM* advocating the enrichment of the displacement field based on the special choice of an additional nodal function belong to the class

of nodal enrichments. This class of models can be found in e.g. [MOËS, DOLBOW & BELYTSCHKO 1999; DOLBOW, MOËS & BELYTSCHKO 2002; SUKUMAR, MOËS, MORAN & BELYTSCHKO 2000].
It should be noted that there exists a significant body of contrasting comparative studies of the above named models, e.g. [JIRÁSEK 2000; JIRÁSEK & BELYTSCHKO 2002; MOSLER & MESCHKE 2003B; DUMSTORFF, MOSLER & MESCHKE 2003; OLIVER, J., HUESPE, A.E. & SANCHEZ, P.J. 2006].
As far as the SDA based on the EAS concept of [SIMO, OLIVER & ARMERO 1993; SIMO & OLIVER 1994] is concerned, one can distinguish between two kinds of preliminary ideas regarding the numerical implementation. The majority of authors, e.g. [ARMERO & GARIKIPATI 1996; LARSSON, STEINMANN & RUNESSON 1998; STEINMANN & BETSCH 2000; ARMERO 1999; OLIVER, HUESPE, PULIDO & SAMANIEGO 2003; GASSER & HOLZAPFEL 2003; CALLARI & ARMERO 2004] base their numerical models on the standard static condensation procedure and eliminate the degrees of freedom associated with the discontinuity from the calculation at the element level.
Another possibility, presented in [BORJA 2000; MOSLER & MESCHKE 2000; MOSLER & MESCHKE 2001; MOSLER 2005A] for linearized kinematics, is to eliminate those degrees of freedom already at the material point level. This idea is extended to nonlinear kinematics in [BORJA 2002; MOSLER 2006]. It should be noted that the model proposed by [BORJA 2002] is restricted to a specific class of constant strain triangle finite elements and the sliding mode of the discontinuity, whereas [MOSLER 2006] offers a model not limited by either the type of finite element or the material interface model. The model of numerical implementation according to [MOSLER 2006] uses standard procedures known from the finite strain multiplicative plasticity for the solution of constitutive equations based on their formal equivalence to the corresponding equations of the plasticity based model.
The numerical model in accordance with [MOSLER 2006] will be presented in the following sections. It includes alterations of the underlying model with respect to the direction of the singular surface and the choice of the principal unknowns driving the localisation process. The finite element formulation therein is specifically based on the proposition presented in [GARIKIPATI 1996; ARMERO & GARIKIPATI 1996].

3.3.1 Fundamentals

The additive decomposition of the deformation gradient given in (3.19)

$$\mathbf{F} = \mathbf{1} + \frac{\partial \hat{\mathbf{u}}}{\partial \mathbf{X}} + \underbrace{[\![\mathbf{u}]\!] \otimes \mathbf{N}\, \delta_s - [\![\mathbf{u}]\!] \otimes \frac{\partial \varphi}{\partial \mathbf{X}}}_{=: \tilde{\mathbf{H}}} \tag{3.42}$$

has an enhanced part $\tilde{\mathbf{H}}$ which includes both regular and singular terms and belongs to the space

$$\tilde{\mathbb{H}} := \left\{ [\![\mathbf{u}]\!] \otimes \mathbf{N}\, \delta_s - [\![\mathbf{u}]\!] \otimes \frac{\partial \varphi}{\partial \mathbf{X}} |\ [\![\mathbf{u}]\!] \in \mathbb{R}^3 \right\}, \tag{3.43}$$

and is therefore formally in line with the formulations according to the EAS concept considered in [SIMO & RIFAI 1990; SIMO, ARMERO & TAYLOR 1993]. Based on this fact, the numerical approach presented in [MOSLER 2006] follows the methodology set therein.
The starting point of the numerical implementation are the stationarity conditions of the respective two field functional for the enhanced deformation mapping

$$\begin{aligned} \int_{\Omega^e} \operatorname{Grad} \eta_0 : \mathbf{P}\, \mathrm{d}V &= \int_{\Omega^e} \rho_0 \mathbf{B} \cdot \eta_0\, \mathrm{d}V + \int_{\partial_\sigma \Omega} \mathbf{T}^* \cdot \eta_0\, \mathrm{d}A\,, \\ \int_{\Omega^e} \hat{\mathbf{H}} : \mathbf{P}\, \mathrm{d}V &= 0\,. \end{aligned} \tag{3.44}$$

Here, $\mathbf{P}$ is the first PIOLA-KIRCHOFF stress tensor, η_0 is a continuous test function, $\mathbf{B}$ are the body forces, $\mathbf{T}^*$ denotes the prescribed tractions across the NEUMANN boundary $\partial_\sigma \Omega$ and $\hat{\mathbf{H}}$ is a variation of the enhanced part of the deformation mapping.
The SDA kinematics is approximated in accordance with (3.13) and (3.14) and the continuous test functions η_0 by

$$\eta_0 = \sum_{i=1}^{n_{\text{node}}} N_i\, \eta_{0\,i}^{\text{e}}\,, \tag{3.45}$$

where $\eta_{0\,i}^{\text{e}}$ are the related nodal values.
The second equation in (3.44), the so-called L_2-orthogonality condition, is in general not fulfilled for the enhanced strains $\tilde{\mathbf{H}} \in \tilde{\mathbb{H}}$ (the virtual work of the stress on these strains is in general case not zero). Instead of using the standard Galerkin method, [GARIKIPATI 1996; ARMERO & GARIKIPATI 1996] apply the Petrov-Galerkin type of variation for the enhanced part of the deformation mapping $\hat{\mathbf{H}} \in \hat{\mathbb{H}}, \hat{\mathbb{H}} \neq \tilde{\mathbb{H}}$:

$$\hat{\mathbf{H}} := -\frac{1}{V^{\text{e}}}\, \boldsymbol{\beta} \otimes \mathbf{N} + \frac{1}{A_s} \boldsymbol{\beta} \otimes \mathbf{N}\, \delta_s\,. \tag{3.46}$$

Here, V^{e} is the volume of the finite element e, A_s is the volume of the localisation surface $\partial_s \Omega$, i.e. $A_s := \int_{\partial_s \Omega} \Omega\, \mathrm{d}A$, $\mathbf{N}$ is the normal vector corresponding to $\partial_s \Omega$ and $\boldsymbol{\beta}$ is the variation of the displacement jump $[\![\mathbf{u}]\!]$. The tensor $\hat{\mathbf{H}}$ is constructed in such manner that it satisfies the patch test [TAYLOR, SIMO,

ZIENKIEWICZ & CHAN 1986] and the resulting L_2-orthogonality condition is equivalent to the weak form of traction continuity across the singular surface

$$\frac{1}{V^e}\int_{\Omega^e} \mathbf{P}\cdot\mathbf{N}\,\mathrm{d}V = \frac{1}{A_s}\int_{\partial_s\Omega} \mathbf{T}_s\,\mathrm{d}A\,. \tag{3.47}$$

The implementations of most finite element models treating the existence of strong discontinuities such as [SIMO, OLIVER & ARMERO 1993; SIMO & OLIVER 1994; ARMERO & GARIKIPATI 1996; LARSSON, STEINMANN & RUNESSON 1998; ARMERO 1999; OLIVER, HUESPE, PULIDO & SAMANIEGO 2003] follow the numerical procedure suggested in the original EAS concept. However, [MOSLER 2005A; MOSLER 2006] proposed a different solution strategy. The idea is to turn the L_2-orthogonality condition $(3.44)_2$ into a traction continuity condition, which in its strong form bears the formal equivalence to the yield conditions of standard plasticity. The first step in this direction is the introduction of the average value of $\mathbf{T} = \mathbf{P}\cdot\mathbf{N}$

$$\mathrm{ave}(\mathbf{T}) := \frac{1}{V^e}\int_{\Omega^e} \mathbf{P}\cdot\mathbf{N}\,\mathrm{d}V\,. \tag{3.48}$$

Recalling (3.18) and having in mind that $\mathbf{T}_s = \mathbf{T}_s(\llbracket\mathbf{u}\rrbracket)$ leads to the simplified form of the right-hand side of (3.47)

$$\frac{1}{A_s}\int_{\partial_s\Omega} \mathbf{T}_s\,\mathrm{d}A = \mathbf{T}_s\,. \tag{3.49}$$

With (3.48) and (3.49), (3.47) is recast into

$$\phi = ||\mathrm{ave}(\mathbf{T}) - \mathbf{T}_s|| = 0 \tag{3.50}$$

or, based on the same considerations which lead to (3.35), into

$$\phi = ||\mathrm{ave}(\bar{\mathbf{T}}) - \bar{\mathbf{T}}_s|| = 0\,. \tag{3.51}$$

Based on the choice of the space of admissible stresses (3.36), this equation is a special form of the statement

$$\phi\,(\mathrm{ave}(\bar{\mathbf{T}}), \mathbf{q}) \leq 0\,. \tag{3.52}$$

The discussed numerical implementation will be applied in the standard finite element procedure for the 4-node tetrahedral constant strain elements. The main feature of this class of finite elements is that the regular part of the displacement field is spatially constant on the element level, i.e. $\mathrm{Grad}\,\hat{\mathbf{u}} = \mathrm{const}$. The consequences of this choice are

$$\begin{aligned}&\mathrm{Grad}\,\hat{\mathbf{u}} = \mathrm{const} \Rightarrow \mathrm{Grad}\,\varphi = \mathrm{const} \Rightarrow \bar{\mathbf{F}} = \mathrm{const}\\ &\Rightarrow \bar{\mathbf{C}} = \mathrm{const} \Rightarrow \mathbf{S} = \mathrm{const} \Rightarrow \bar{\mathbf{T}} = \mathrm{const} \Rightarrow \mathrm{ave}(\bar{\mathbf{T}}) = \bar{\mathbf{T}}\,.\end{aligned} \tag{3.53}$$

Based on this conclusion, the weak form of the traction continuity (3.52) can be assumed equivalent to its strong form

$$\phi\left(\bar{\mathbf{T}}, \mathbf{q}\right) \leq 0\,, \tag{3.54}$$

and the stationarity conditions in the loading regime ($\lambda > 0$) have the form

$$\begin{aligned} &\int_{\Omega^e} \operatorname{Grad}\boldsymbol{\eta}_0 : \mathbf{P}\, \mathrm{d}V \quad = \int_{\Omega^e} \rho_0\, \mathbf{B}\cdot\boldsymbol{\eta}_0\, \mathrm{d}V + \int_{\partial_\sigma\Omega} \mathbf{T}^*\cdot\boldsymbol{\eta}_0\, \mathrm{d}A\,, \\ &\phi\left(\bar{\mathbf{T}}, \mathbf{q}\right) = 0\,. \end{aligned} \tag{3.55}$$

This set of equations confirms the formal equivalence of the proposed material model with the model of standard finite strain plasticity and opens a possibility to choose a method of numerical implementation from the variety of known and reasonably well developed computing methods. [Mosler 2005a; Mosler 2006] adopts the return-mapping algorithm according to [Simo 1998; Simo & Hughes 1998]. The method, as presented in 2.5.2, solves the set of equations according to the algorithm shown in Figure 2.8. If the elastic predictor step signals an inelastic loading step, the traction continuity condition $(3.55)_2$ is solved for constant $\hat{\mathbf{u}}$. With the results of that computation, the condition $(3.55)_1$ is solved. This procedure will be presented in detail in the next sections. First, the choice of the possible orientation and the topology of the singular surface $\partial_s\Omega$ is advocated and then the specific algorithm is presented. The trial step is defined, followed by the differentiation of an elastic unloading step from the inelastic loading step and introduction of the linearization procedure.

3.3.2 The normal vector N and the topology of the surface $\partial_s\Omega$

The kinematics and the constitutive model presented in previous sections of this chapter are labelled suitable for the description of strain localisation materialised in a singular surface $\partial_s\Omega$. Up to this point, a complete material model is developed starting with an assumption that the local topology of the singular surface, i.e. the normal vector $\mathbf{N}$ is known. However, the scientific effort to predict and compute the formation, the orientation and both local and global topology of such discontinuity in the material is decisively large. The criteria for the prediction and description of the singular surface of order zero could be classified in at least five general groups, namely energy-based criteria, stress-based criteria, strain-based criteria, transition from weak to strong discontinuities and the bifurcation analysis. An overview of the significant contributions to the solution of this problem as well as a detailed presentation of a possible choice for the prediction of formation of discontinuities in rate independent media can be found in [Mosler 2005b; Mosler 2007].

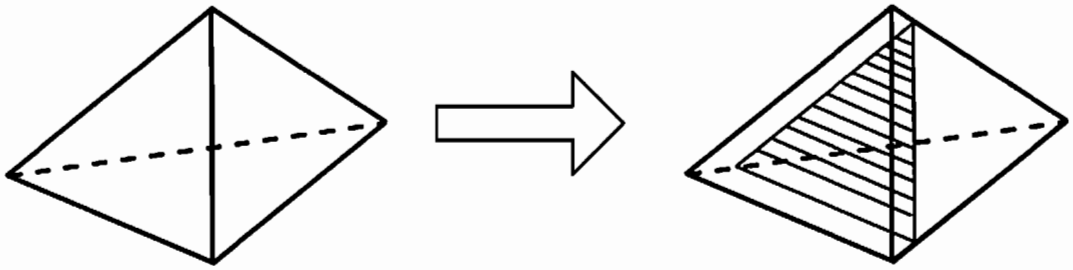

Figure 3.3: A possible choice for the singular surface $\partial_s\Omega$

In this work, the choice of the topology and the orientation of the singular surface $\partial_s\Omega$ is based on the fact that the mechanical behaviour of many materials depends on the distribution of pre-existing micro-defects. For instance, the ultimate load of jointed rocks is influenced by the roughness and orientation of pre-existing slip surfaces. Additionally, the evolution of those internal surfaces is very important. The choice of a material model presented in this chapter is based on these considerations. As for the local topology of the singular surface $\partial_s\Omega$, the discontinuities are assumed already formed.
In an effort to simulate pre-existing discontinuities which are the result of some previous evolution processes, the pre-existing internal surface could be for example defined element-wise by a stochastically distributed normal vector $\mathbf{N}$ as well as the initial material strength, i.e. $\mathbf{q}(t = 0)$. However, the numerical model for the micro-scale with a single stochastically generated time invariant localisation surface in each element can lead to both non-physical results and to locking effects.
In order to enlighten this behaviour, a brief definition of the numerical length scale, known as the *characteristic length* l_c presented in [MOSLER & MESCHKE 2003B] is given. If the softening response in the material is governed by the stress-strain relation

$$\dot{q} = -H\,\dot{\alpha}\,, \tag{3.56}$$

where $\dot{\alpha}$ is a strain-like internal variable and H is the softening modulus, this softening modulus depends on the fracture energy per unit of crack surface $\mathcal{G}_f$ and the geometry of the finite element (see [PIETRUSZCZAK & MROŹ 1981]). The fracture energy per unit of crack surface $\mathcal{G}_\mathrm{f}$ can be defined by

$$\mathcal{G}_\mathrm{f} := \frac{E}{A_s} = \underbrace{\frac{E}{V}}_{g_\mathrm{f}}\, l_c = \int_{\alpha=0}^{\alpha_u} q\,(\alpha)\,\mathrm{d}\alpha\, l_c\,. \tag{3.57}$$

E represents the total dissipated energy in an element with the volume V necessary for the formation and the propagation of a macro discontinuity with

area A_s up to the final failure, g_f is the fracture energy per unit of volume, α_u is the parameter characterising the complete softening in the material and l_c is the characteristic length. The total dissipated energy E is evaluated based on the following assumptions:

- The strong discontinuities kinematics is assumed (see Section 3.1.2).
- The ramp function φ has the form (3.14).
- Constant strain finite elements are used for the spatial discretization.
- The direction of the crack is defined by the normal $\mathbf{N}$.

According to [MOSLER & MESCHKE 2002], the total dissipated energy E reads:

$$E = \int_{\Omega^e} \mathcal{G}_f \operatorname{Grad}\varphi \cdot \mathbf{N} \, \mathrm{d}V \,. \tag{3.58}$$

Application of (3.57) in (3.58) leads to

$$l_c = (\operatorname{Grad}\varphi \cdot \mathbf{N})^{-1} \,. \tag{3.59}$$

If this numerical length scale is taken into account, the stochastically generated time invariant normal vector $\mathbf{N}$ can lead to a non-physical, negative or zero characteristic length l_c, based on the angle between two vectors $\mathbf{N}$ and $\operatorname{Grad}\varphi$. The possibility of locking is not surprising in this case, since the stochastically generated internal surfaces $\partial_s\Omega$ are, in general, non-conforming (see Figure 3.4a). More precisely, only for selected problems, the local surfaces span a globally continuous failure surface. The continuity of $\partial_s\Omega$ is essential for finite element formulations based on the SDA, as reported for instance in [JIRÁSEK & ZIMMERMANN 2001]. Different approaches to the solution of such mechanical problems can be found in the literature. Most of the proposed methods belong to a group of solutions known as *tracking algorithms* [OLIVER 1995A; OLIVER 2000]. Several authors propose algorithms for computing a globally continuous topology of $\partial_s\Omega$, cf. [OLIVER, HUESPE, SAMANIEGO & CHAVES 2002]. In this global tracking algorithm, single or multiple crack surfaces are stored in an additional scalar valued field of unknowns. This requires the solution of a "thermal-like" problem before each mechanical loading step. In principle, those techniques could be adopted. However, the number of different surfaces $\partial_s\Omega$ in the whole model is considerably large resulting in a prohibitive numerical effort. Furthermore, the internal surfaces may interact or cross each other.

In this work, a different method is advocated. It is based on the so-called *Multiple Localisation Surface Approach.* The main property of the numerical model presented here is that the number of possible orientations of the localisation surface per element is set to four. Each of the four possible orientations

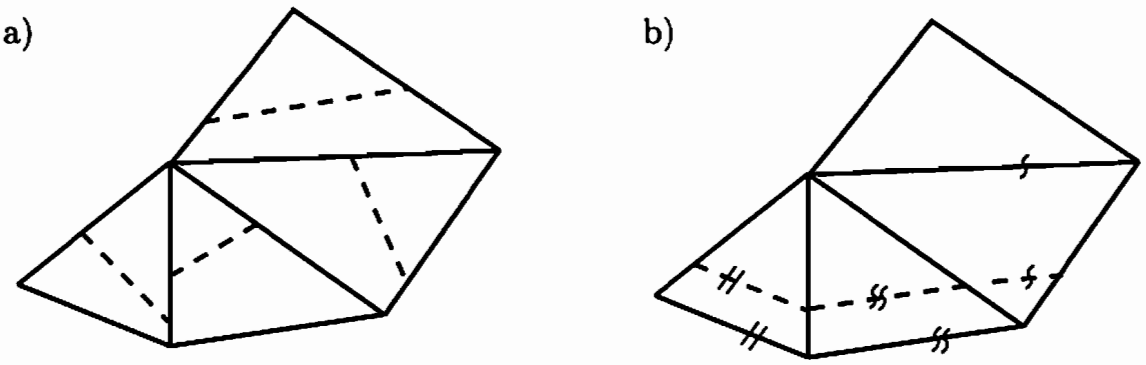

Figure 3.4: Continuity of the singular surface $\partial_s\Omega$ across elements: a) stochastically generated discontinuities; b) discontinuities parallel to the element faces

of $\partial_s\Omega$ is chosen such that it is a plane parallel to one of the faces of the tetrahedral finite element. Figure 3.3 shows one possible choice of the singular surface $\partial_s\Omega$. Analogously, the other three possible orientations are generated. As a consequence $\mathbf{N}$ is parallel to $\operatorname{Grad}\varphi$. More precisely, $\mathbf{N} = \operatorname{Grad}\varphi/||\operatorname{Grad}\varphi||$ and hence, $\mathbf{N}\cdot\operatorname{Grad}\varphi = ||\operatorname{Grad}\varphi||$. On the one hand, this procedure improves the numerical implementation of the proposed model significantly. For instance, since $\mathbf{N}$ is parallel to $\operatorname{Grad}\varphi$, the resulting stiffness matrix is symmetric. Furthermore, if the characteristic diameter of the finite elements goes to zero, $\mathbf{N}\cdot\operatorname{Grad}\varphi \to \infty$. As a result, snap-backs as reported in [JIRÁSEK 1999] can be avoided, cf. [MOSLER & BRUHNS 2004]. Additionally, the space of admissible internal surfaces spanned by the proposed numerical model is relatively rich. More specifically, the continuity of $\partial_s\Omega$ can be guaranteed (see Figure 3.4b). It should be noted that the finite element discretization can be generated such that the normal vectors of the facets defining the tetrahedra are stochastically distributed.

3.3.3 Return-mapping algorithm - elastic predictor step

According to the scheme given in Figure 2.8, the elastic predictor step is actually the computation of a trial step characterised by purely elastic deformation. This constraint influences the variables associated with the strain localisation in the material. The description of the deformation mapping assumed for the trial step has the form

$$\begin{aligned} \lambda = 0 \quad &\Longleftrightarrow \quad \dot{\mathbf{J}} = \mathbf{0}, \quad \dot{\alpha} = 0, \quad \dot{\mathbf{q}} = \mathbf{0} \\ &\Longrightarrow \quad \bar{\mathbf{F}}^{\mathrm{tr}}_{n+1} = \mathbf{1} + \operatorname{Grad}\hat{\mathbf{u}}_{n+1} - \bar{\mathbf{F}}^{\mathrm{tr}}_{n+1}\cdot\mathbf{J}_n \otimes \operatorname{Grad}\varphi\,. \end{aligned} \tag{3.60}$$

The trial value of the deformation gradient $\bar{\boldsymbol{F}}^{\mathrm{tr}}_{n+1}$ is computed from (3.60). At this point, a new variable characterising the localisation process is introduced.

Based on facts that $\mathbf{N}$ is parallel to $\operatorname{Grad}\varphi$ and $\dot{\mathbf{N}} = \mathbf{0}$, a variable named *jump deformation tensor* is defined

$$\epsilon^{\mathrm{p}} = \mathbf{J} \otimes \operatorname{Grad}\varphi\,, \quad \dot{\epsilon}^{\mathrm{p}} = \lambda\, \partial_{\bar{\mathbf{T}}}\phi \otimes \operatorname{Grad}\varphi\,. \tag{3.61}$$

Along with ϵ^{p}, the existing form of the regular part of the deformation gradient $\bar{\mathbf{F}}$ can be rewritten as

$$\begin{aligned} &\bar{\mathbf{F}}^{\mathrm{tr}}_{n+1} = \mathbf{1} + \operatorname{Grad}\hat{\mathbf{u}}_{n+1} - \bar{\mathbf{F}}^{\mathrm{tr}}_{n+1} \cdot \epsilon^{\mathrm{p}}{}_n = \mathbb{A}^{-1} : [\mathbf{1} + \operatorname{Grad}\hat{\mathbf{u}}_{n+1}]\,, \\ &\mathbb{A}_{ikpq} := \mathbb{I}_{ikpq} + \left[\mathbb{I}_{ijpq}\, \epsilon^{\mathrm{p}}_{jk}\right]\big|_{t_n}\,. \end{aligned} \tag{3.62}$$

Here, $\mathbb{I}$ is the fourth order identity tensor. Based on $\bar{\boldsymbol{F}}^{\mathrm{tr}}_{n+1}$, the right CAUCHY-GREEN trial tensor $\bar{\boldsymbol{C}}^{\mathrm{tr}}_{n+1}$ and the second PIOLA-KIRCHHOFF trial stresses $\boldsymbol{S}^{\mathrm{tr}}_{n+1}$ can be computed and used for the calculation of the trial traction vector

$$\bar{\mathbf{T}}^{\mathrm{tr}}_{n+1} = \bar{\mathbf{C}}^{\mathrm{tr}}_{n+1} \cdot \mathbf{S}^{\mathrm{tr}}_{n+1} \cdot \mathbf{N}\,. \tag{3.63}$$

The trial value of the discrete loading condition (3.52) is then given as

$$\phi^{\mathrm{tr}} := \phi(\bar{\mathbf{T}}^{\mathrm{tr}}_{n+1}, \mathbf{q}^{\mathrm{tr}}_{n+1}) > 0 \quad \text{with} \quad \mathbf{q}^{\mathrm{tr}}_{n+1} = \mathbf{q}_n\,. \tag{3.64}$$

According to the scheme in Figure 2.8, a non-positive trial value of the yield function $\phi^{\mathrm{tr}} \leq 0$ signals a purely elastic loading step. For all variables whose trial values are calculated, $(\bullet)_{n+1} = (\bullet)^{\mathrm{tr}}_{n+1}$ is set and the material response is computed according to Section 3.3.5. A positive trial value of the yield function $\phi^{\mathrm{tr}} > 0$ signals an inelastic loading step and an inelastic corrector step must be performed.

3.3.4 Inelastic corrector step

Since the conditions defined in (3.60) are not valid in the case of inelastic loading, a backward-EULER integration is applied to the evolution equations $(3.38)_2$ and (3.61). The backward-EULER scheme transforms the set of algebraic differential conditions into a nonlinear set of purely algebraic equations. The jump deformation tensor ϵ^{p} and the internal displacement-like variable α at time t_{n+1} are computed from:

$$\epsilon^{\mathrm{p}}{}_{n+1} = \epsilon^{\mathrm{p}}{}_n + \Delta\lambda_{n+1}\, \partial_{\bar{\mathbf{T}}}\phi|_{n+1} \otimes \operatorname{Grad}\varphi\,, \tag{3.65}$$

$$\alpha_{n+1} = \alpha_n + \Delta\lambda_{n+1}\, \partial_{\mathbf{q}}\phi|_{n+1}\,. \tag{3.66}$$

Here, $\Delta\lambda_{n+1} := \lambda_{n+1}\,(t_{n+1} - t_n)$.
The definition of the residual $\mathbf{R}$ in the return-mapping algorithm is

$$\mathbf{R} := \left\{ \begin{array}{c} \mathbf{R}^{\epsilon^{\mathrm{p}}} \\ \mathbf{R}^{\alpha} \end{array} \right\} := \left\{ \begin{array}{l} -\epsilon^{\mathrm{p}}{}_{n+1} + \epsilon^{\mathrm{p}}{}_n + \Delta\lambda_{n+1}\, \partial_{\bar{\mathbf{T}}}\phi|_{n+1} \otimes \operatorname{Grad}\varphi \\ -\alpha_{n+1} + \alpha_n + \Delta\lambda_{n+1}\, \partial_{\mathbf{q}}\phi|_{n+1} \end{array} \right\}. \tag{3.67}$$

A vanishing residual $\mathbf{R}_{n+1}$ and a vanishing yield function ϕ_{n+1} form a set of nonlinear algebraic equations to be solved in order to correct the trial state

$$\mathbf{R} = 0 \quad \wedge \quad \phi_{n+1} = 0\,. \tag{3.68}$$

Following [SIMO 1998; SIMO & HUGHES 1998], the system is solved by a systematic application of the NEWTON iterative procedure. It is based on the linearization of the residual about the current iterate.
If it is assumed that the current iteration is the iteration (k), the valid starting values of the traction vector $\bar{\mathbf{T}}^{(1)}_{n+1}$, the internal variable $\mathbf{q}^{(1)}_{n+1}$ and the yield function $\phi^{(1)}_{n+1}$ are

$$\bar{\mathbf{T}}^{(1)}_{n+1} = \bar{\mathbf{T}}^{\mathrm{tr}}_{n+1}\,, \quad \mathbf{q}^{(1)}_{n+1} = \mathbf{q}^{\mathrm{tr}}_{n+1}\,, \quad \phi^{(1)}_{n+1} = \phi^{\mathrm{tr}}_{n+1}\,. \tag{3.69}$$

For the choice of the yield function according to (3.41), following second derivatives vanish

$$\partial_{\bar{\mathbf{T}}\otimes\mathbf{q}}\,\phi|_{n+1} = \mathbf{0}\,, \quad \partial_{\mathbf{q}\otimes\bar{\mathbf{T}}}\,\phi|_{n+1} = \mathbf{0}\,, \quad \partial_{\mathbf{q}\otimes\mathbf{q}}\,\phi|_{n+1} = \mathbf{0}\,. \tag{3.70}$$

For an arbitrary choice of the yield function, these derivatives should be included in the linearization procedure.
For the sake of clarity, the indices describing the current time iteration step $n+1$ and the current NEWTON iteration step (k) will be omitted in the derivation of the linearized residuals.
The residual tensor $\mathbf{R}$ is linearized with the chain rule with respect to $\bar{\mathbf{T}}$, $\mathbf{q}$ and $\Delta\lambda$, for a fixed $\hat{\mathbf{u}}$ from (3.67) and (3.70):

$$\begin{aligned}
\mathrm{d}R^{\epsilon^{\mathrm{p}}}_{ij} &= -\mathrm{d}\epsilon^{\mathrm{p}}_{ij} + \mathrm{d}\Delta\lambda\,\partial_{\bar{\mathbf{T}}}\,\phi_i\,\mathrm{Grad}\,\varphi_j + \Delta\lambda\,\partial_{\bar{\mathbf{T}}\otimes\bar{\mathbf{T}}}\,\phi_{ik}\,\mathrm{d}T_k\,\mathrm{Grad}\,\varphi_j \\
&= \mathbb{T}^{C}_{ijlp}\,\mathrm{d}\epsilon^{\mathrm{p}}_{lp} + \mathrm{d}\Delta\lambda\,G^{t}_{ij}\,, \\
\mathrm{d}R^{\alpha}_{i} &= -\partial_{\mathbf{q}}\,\alpha_{ij}\,\mathrm{d}q_j + \mathrm{d}\Delta\lambda\,\partial_{\mathbf{q}}\,\phi_i \\
&= D_{ij}{}^{-1}\,\mathrm{d}q_j + \mathrm{d}\Delta\lambda\,\partial_{\mathbf{q}}\,\phi_i\,,
\end{aligned} \tag{3.71}$$

where

$$\begin{aligned}
G^{t}_{ij} &= \partial_{\bar{\mathbf{T}}}\,\phi_i\,\mathrm{Grad}\,\varphi_j\,, \\
\mathbb{T}^{C}_{ijlp} &= -\mathbb{I}_{ijlp} + \mathbb{G}^{C}_{ijko}\,\mathbb{G}^{M}_{kolp}\,.
\end{aligned} \tag{3.72}$$

If the traction vector is transformed according to the identity $\bar{\mathbf{T}} = \bar{\mathbf{C}}\cdot\mathbf{S}\cdot\mathbf{N} = \boldsymbol{\Sigma}\cdot\mathbf{N}$ then

$$\mathbb{G}^{C}_{ijko} = \Delta\lambda\,\partial_{\bar{\mathbf{T}}\otimes\bar{\mathbf{T}}}\,\phi_{ik}\,N_o\,\mathrm{Grad}\,\varphi_j\,. \tag{3.73}$$

The fourth order tensor $\mathbb{G}^{M}$ in (3.72) linearizes the MANDEL stress tensor $\boldsymbol{\Sigma}$ with respect to the jump deformation tensor $\boldsymbol{\epsilon}^{\mathrm{p}}$. This linearization is derived at the end of this chapter, in Section 3.3.7.

The choice of independent variables for the linearization procedure is not strictly restrained to the set $(\bar{\mathbf{T}}, \mathbf{q}, \Delta\lambda)$. According to [MOSLER 2006], choosing the MANDEL stress tensor $\boldsymbol{\Sigma}$ instead of the traction vector $\bar{\mathbf{T}}$ is also possible and delivers the formal equivalence to the standard multiplicative plasticity. However, the dimension of the residuals increases with this change. For the isotropic softening ($\dim q = 1$) the dimension of the problem to be solved increases by a factor greater then 2. As a consequence, this alternative choice of independent variables has not been utilised in this work.
In order to switch from the tensor description to the matrix description of the problem, following transformations are necessary:

$$\begin{aligned}
\boldsymbol{\epsilon}^{\mathrm{p}} &\Longrightarrow \mathbf{E}^{\mathrm{p}} \quad \text{with} \quad \epsilon^{\mathrm{p}}_{ij} = E^{\mathrm{p}}_{(i-1)*3+j}\,, \\
\mathbb{T}^{C} &\Longrightarrow \mathbf{T}^{C} \quad \text{with} \quad \mathbb{T}^{C}_{ijkl} = T^{C}_{(i-1)*3+j,(k-1)*3+l}\,, \\
\mathbf{G}^{t} &\Longrightarrow \mathbf{g}^{t} \quad \text{with} \quad G^{t}_{ij} = g^{t}_{(i-1)*3+j}\,.
\end{aligned} \tag{3.74}$$

The resulting residual *vector* $\mathbf{R}$ can be derived as

$$\begin{aligned}
\mathrm{d}R_i^{\epsilon^{\mathrm{p}}} &= T^{C}_{ij}\ \mathrm{d}E^{\mathrm{p}}_{j} + \mathrm{d}\Delta\lambda\ g^{t}_{i}\,, \\
\mathrm{d}R_i^{\alpha} &= {D_{ij}}^{-1}\ \mathrm{d}q_j + \mathrm{d}\Delta\lambda\ \partial_{\mathbf{q}}\,\phi_i\,.
\end{aligned} \tag{3.75}$$

The linearization of the yield function $\phi\,(\bar{\mathbf{T}}, \mathbf{q})$ follows the same procedure and leads to

$$\begin{aligned}
\mathrm{d}\phi &= \partial_{\bar{\mathbf{T}}}\,\phi_i\ \mathrm{d}T_i + \partial_{\mathbf{q}}\,\phi_i\ \mathrm{d}q_i \\
&= F^{t}_{lp}\ \mathrm{d}\epsilon^{\mathrm{p}}_{lp} + \partial_{\mathbf{q}}\,\phi_i\ \mathrm{d}q_i && (3.76) \\
&= f^{t}_{i}\ \mathrm{d}E^{\mathrm{p}}_{i} + \partial_{\mathbf{q}}\,\phi_i\ \mathrm{d}q_i\,, && (3.77)
\end{aligned}$$

where

$$F^{t}_{lp} = \partial_{\bar{\mathbf{T}}}\,\phi_i\ N_j\ \mathbb{G}^{M}_{ijlp}\,, \quad F^{t}_{ij} = f^{t}_{(i-1)*3+j}\,. \tag{3.78}$$

In the matrix notation, these results have the form

$$\mathrm{d}\mathbf{R} = \mathbf{A}^{-1}\cdot\boldsymbol{\Delta} + \mathrm{d}\Delta\lambda^{(k)}_{n+1}\ \nabla\mathbf{M}\,, \quad \mathrm{d}\phi = \boldsymbol{\nabla}\boldsymbol{\phi}^{\mathrm{T}}\cdot\boldsymbol{\Delta}\,, \tag{3.79}$$

where the notations

$$\mathbf{A}^{-1} := \left[\begin{array}{cc} \mathbf{T}^{C} & 0 \\ 0 & \mathbf{D}^{-1} \end{array}\right]\Bigg|^{(k)}_{n+1}\,, \quad \boldsymbol{\Delta} := \left[\begin{array}{c} \mathrm{d}\mathbf{E}^{\mathrm{p}} \\ \mathrm{d}\mathbf{q} \end{array}\right]\Bigg|^{(k)}_{n+1} \tag{3.80}$$

and

$$\nabla\mathbf{M} := \left[\begin{array}{c} \mathbf{g}^{t} \\ \partial_{\mathbf{q}}\,\phi \end{array}\right]\Bigg|^{(k)}_{n+1}\,, \quad \boldsymbol{\nabla}\boldsymbol{\phi}^{\mathrm{T}} := \left[\mathbf{f}^{\mathbf{t}}\,;\partial_{\mathbf{q}}\,\phi\right]\Big|^{(k)}_{n+1} \tag{3.81}$$

are used. The linearized form of the set of equations (3.68)

$$\mathbf{R} + \mathbf{A}^{-1} \cdot \boldsymbol{\Delta} + \mathrm{d}\Delta\lambda_{n+1}^{(k)} \, \nabla \mathbf{M} = \mathbf{0}, \quad \phi + \nabla\boldsymbol{\phi}^{\mathrm{T}} \cdot \boldsymbol{\Delta} = 0 \tag{3.82}$$

is solved and the update of the LAGRANGE multiplier $\mathrm{d}\Delta\lambda_{n+1}^{(k)}$ is computed from

$$\mathrm{d}\Delta\lambda_{n+1}^{(k)} = \left. \frac{\phi - \nabla\boldsymbol{\phi}^{\mathrm{T}} \cdot \mathbf{A} \cdot \mathbf{R}}{\nabla\boldsymbol{\phi}^{\mathrm{T}} \cdot \mathbf{A} \cdot \nabla \mathbf{M}} \right|_{n+1}^{(k)} \quad \Rightarrow \quad \Delta\lambda_{n+1}^{(k+1)} = \Delta\lambda_{n+1}^{(k)} + \mathrm{d}\Delta\lambda_{n+1}^{(k)} . \tag{3.83}$$

The update of of the state variables is calculated from $(3.82)_1$

$$\boldsymbol{\Delta}_a = -\mathbf{D}^J \cdot \mathbf{A} \cdot (\mathbf{R} + \mathrm{d}\Delta\lambda \, \nabla \mathbf{M}) \Big|_{n+1}^{(k)} , \tag{3.84}$$

where

$$\mathbf{D}^J := \left[\begin{array}{cc} \mathbf{I} & 0 \\ 0 & -\mathbf{D} \end{array} \right] \Big|_{n+1}^{(k)} , \quad \boldsymbol{\Delta}_a := \left[\begin{array}{c} \mathrm{d}\mathbf{E}^{\mathrm{p}} \\ \mathrm{d}\boldsymbol{\alpha} \end{array} \right] \Big|_{n+1}^{(k)} , \tag{3.85}$$

and consequently

$$\left[\begin{array}{c} \mathbf{E}^{\mathrm{p}} \\ \boldsymbol{\alpha} \end{array} \right] \Big|_{n+1}^{(k+1)} = \left[\begin{array}{c} \mathbf{E}^{\mathrm{p}} \\ \boldsymbol{\alpha} \end{array} \right] \Big|_{n+1}^{(k)} + \left[\begin{array}{c} \mathrm{d}\mathbf{E}^{\mathrm{p}} \\ \mathrm{d}\boldsymbol{\alpha} \end{array} \right] \Big|_{n+1}^{(k)} . \tag{3.86}$$

The whole procedure is summarised in Figure 3.5.

3.3.5 Elastic unloading

The negative trial value of the yield function (3.64) leads to the conclusion that the material response is elastic and the predicted trial state is the actual state. The solution of an elastic loading step $\hat{\mathbf{u}}_{n+1}$ is the solution of the set of equations

$$\begin{aligned} &\int_{\Omega^{\mathrm{e}}} \mathrm{Grad}\, \boldsymbol{\eta}_0 : \mathbf{P} \, \mathrm{d}V \quad = \int_{\Omega^{\mathrm{e}}} \rho_0 \, \mathbf{B} \cdot \boldsymbol{\eta}_0 \, \mathrm{d}V + \int_{\partial_\sigma \Omega} \mathbf{T}^* \cdot \boldsymbol{\eta}_0 \, \mathrm{d}A , \\ &\epsilon_{n+1}^{\mathrm{p}} = \epsilon_n^{\mathrm{p}} . \end{aligned} \tag{3.87}$$

Since the material description of the principle of virtual work is not the best choice from the computational point of view, relation $(3.87)_1$ is pushed-forward to the current configuration such that the spatial form of the given set of equations reads

$$\begin{aligned} &\int_{\Omega^{\mathrm{e}}} \overline{\mathrm{grad}}\, \boldsymbol{\eta} : \boldsymbol{\tau} \, \mathrm{d}V \quad = \int_{\Omega^{\mathrm{e}}} \rho_0 \, \mathbf{B} \cdot \boldsymbol{\eta}_0 \, \mathrm{d}V + \int_{\partial_\sigma \Omega} \mathbf{T}^* \cdot \boldsymbol{\eta}_0 \, \mathrm{d}A , \\ &\epsilon_{n+1}^{\mathrm{p}} = \epsilon_n^{\mathrm{p}} . \end{aligned} \tag{3.88}$$

1. *Evaluate the residuals (3.67) and the yield function*

$$\mathbf{R} := \left\{ \begin{array}{c} \mathbf{R}^{\epsilon^p} \\ \mathbf{R}^{\alpha} \end{array} \right\}\Big|_{n+1}^{(k)}, \quad \phi_{n+1}^{(k)} = \phi_{n+1}^{\mathrm{tr}} .$$

2. *Check convergence*

IF $\phi_{n+1}^{(k)} \leq TOL_1$ and $\|\mathbf{R}\|_{n+1}^{(k)} \leq TOL_2$ THEN: *EXIT*

3. *Calculate elastic moduli (2.127) and consistent tangent moduli (3.80)*
4. *Obtain the increment to the consistency parameter* $\mathrm{d}\Delta\lambda$ *(3.83)*
5. *Obtain the incremental state variables* $\boldsymbol{\Delta}_a$ *(3.85)*
6. *Update the state variables (3.86) and the consistency parameter (3.83)*

Set $k \leftarrow k+1$ and Goto 1.

Figure 3.5: Return-mapping algorithm - plastic corrector iteration

Here, the push-forward of $\mathrm{Grad}\,\boldsymbol{\eta}_0$, denoted by $\overline{\mathrm{grad}\,\boldsymbol{\eta}}$ is based on the interpolation (3.45). It takes the form

$$\overline{\mathrm{grad}\,\boldsymbol{\eta}} = \sum_{i=1}^{n_{\mathrm{node}}} \boldsymbol{\eta}_{0\,i}^{\mathrm{e}} \otimes \mathrm{Grad}\,N_i \cdot \bar{\mathbf{F}}^{-1} . \tag{3.89}$$

Following the standard procedure of the displacement based finite element method, the displacement field $\hat{\mathbf{u}}_{n+1}$ satisfying the conditions of the (3.88) is computed through the iterative NEWTON algorithm. In the process, the global residual at the global node $I \in \{1, \ldots, n_{\mathrm{gl}}\}$

$$\begin{aligned} \mathbf{R}_I = \mathop{\mathbf{A}}_{e=1}^{n_{\mathrm{ele}}} & \int_{\Omega^e} \left[\mathrm{Grad}\,N_i \cdot \bar{\mathbf{F}}^{-1}\right] \cdot \boldsymbol{\tau}\, \mathrm{d}V \\ & - \int_{\Omega^e} N_i\, \rho_0\, \mathbf{B}\, \mathrm{d}V - \int_{\partial_\sigma \Omega^e} N_i\, \mathbf{T}^*\, \mathrm{d}A \end{aligned} \tag{3.90}$$

has to be driven to zero $\mathbf{R}_I = \mathbf{0}$ for all global nodes. Here, $\mathbf{A}$ denotes the assembly of all element contributions at the local element node i ($i =$

$1, \ldots, n_{\text{node}}$) to the global residual at the global node I. The linearization of the residual $\mathbf{R}_I$ is calculated with the update of the regular part of the displacement field $\Delta\hat{\mathbf{u}}$ as the independent variable:

$$\mathbf{R}_I\,|_n + \mathbf{K}^{IJ}\Big|_n\ \Delta\hat{\mathbf{u}}_J|_{n+1} = \mathbf{0}\,, \quad \forall I, J = 1, \ldots, n_{\text{gl}}\,. \tag{3.91}$$

Here, $\mathbf{K}^{IJ}$ denotes the IJ component of the global stiffness matrix, i.e.

$$\mathbf{K}^{IJ} = \frac{\partial \mathbf{R}_I}{\partial \hat{\mathbf{u}}_J}\,. \tag{3.92}$$

The update of the regular part of the displacement field at global node J is calculated from

$$\hat{\mathbf{u}}_{n+1} = \hat{\mathbf{u}}_n + \Delta\hat{\mathbf{u}}_{n+1} \tag{3.93}$$

within each iteration cycle.
The components of the stiffness matrix $\mathbf{K}^{IJ}$ are obtained starting with the transformation of the rate form of the equation $(3.87)_1$

$$\int_{\Omega^e} \operatorname{Grad}\boldsymbol{\eta}_0 : \dot{\mathbf{P}}\,\mathrm{d}V = \int_{\Omega^e} \rho_0\,\dot{\mathbf{B}}\cdot\boldsymbol{\eta}_0\,\mathrm{d}V + \int_{\partial_\sigma\Omega} \dot{\mathbf{T}}^*\cdot\boldsymbol{\eta}_0\,\mathrm{d}A = 0 \tag{3.94}$$

into

$$\int_{\Omega^e} \overline{\operatorname{grad}}\,\boldsymbol{\eta} : \left[\bar{\mathbf{l}}\cdot\boldsymbol{\tau} + \mathcal{L}_v\ \boldsymbol{\tau}\right]\,\mathrm{d}V = \int_{\Omega^e} \rho_0\,\dot{\mathbf{B}}\cdot\boldsymbol{\eta}_0\,\mathrm{d}V + \int_{\partial_\sigma\Omega} \dot{\mathbf{T}}^*\cdot\boldsymbol{\eta}_0\,\mathrm{d}A = 0\,, \tag{3.95}$$

where the relations (3.88), (2.115) and (3.24) are utilised.
Based on the symmetry of the spatial elastic tangent operator $\mathbf{c}$: $c_{ijkl} = \bar{F}_{iI}\bar{F}_{Jj}\bar{F}_{kK}\bar{F}_{lL}\mathbb{C}_{IJKL}$, the LIE-type derivative of the KIRCHOFF stress tensor can be rewritten following (2.128) and (3.95):

$$\int_{\Omega^e} \overline{\operatorname{grad}}\,\boldsymbol{\eta} : \left[\bar{\mathbf{l}}\cdot\boldsymbol{\tau} + \mathbf{c} : \bar{\mathbf{l}}\right]\,\mathrm{d}V = \int_{\Omega^e} \rho_0\,\dot{\mathbf{B}}\cdot\boldsymbol{\eta}_0\,\mathrm{d}V + \int_{\partial_\sigma\Omega} \dot{\mathbf{T}}^*\cdot\boldsymbol{\eta}_0\,\mathrm{d}A = 0\,. \tag{3.96}$$

The regularly distributed part of the spatial velocity gradient $\bar{\mathbf{l}}$ is the only element of this equation to be linearized with respect to $\Delta\hat{\mathbf{u}}$. The iterative nature of the procedure leads to the following relation

$$\bar{\mathbf{l}} = \mathrm{d}\bar{\mathbf{F}}\cdot\bar{\mathbf{F}}^{-1}\,. \tag{3.97}$$

The linearization yields

$$\mathrm{d}\bar{\mathbf{F}} = \frac{\partial\bar{\mathbf{F}}}{\partial\hat{\mathbf{u}}}\cdot\Delta\hat{\mathbf{u}}\,. \tag{3.98}$$

The implicit equation (3.62) defining the deformation gradient $\bar{\mathbf{F}}$ is linearized for fixed ϵ^{p} with the result

$$\mathrm{d}\bar{\mathbf{F}}_{n+1} = \mathbb{A}^{-1} : \mathrm{Grad}\,\Delta\hat{\mathbf{u}}_{n+1}\,, \tag{3.99}$$

and (3.97) is rewritten as

$$\bar{\mathbf{l}} = \left(\mathbb{A}^{-1} : \mathrm{Grad}\,\Delta\hat{\mathbf{u}}_{n+1}\right) \cdot \bar{\mathbf{F}}^{-1} \tag{3.100}$$

or, equivalently,

$$\bar{\mathbf{l}} = \mathbb{L}^{\mathrm{e}} : \mathrm{Grad}\,\Delta\hat{\mathbf{u}}_{n+1} \quad \text{with} \quad \mathbb{L}^{\mathrm{e}}_{ijkl} = \mathbb{A}^{-1}_{ipkl}\,\bar{F}^{-1}_{pj}\,. \tag{3.101}$$

The stiffness matrix $\mathbf{K}^{IJ}$ can be evaluated from (3.96) based on (3.101). If the standard distinction between the geometric and material part of the stiffness matrix is made, $\mathbf{K}^{IJ}$ is the sum

$$\mathbf{K}^{IJ} = \mathbf{K}^{IJ}_{\mathrm{geo}} + \mathbf{K}^{IJ}_{\mathrm{mat}}\,. \tag{3.102}$$

In the case of linearized kinematics, $\mathbf{K}^{IJ}_{\mathrm{geo}} = \mathbf{0}$. In index form, the geometric tangent operator $\mathbf{K}^{IJ}_{\mathrm{geo}}$ is defined as

$$\left(K^{IJ}_{\mathrm{geo}}\right)_{ab} = \mathop{\mathsf{A}}_{e=1}^{n_{\mathrm{ele}}} \int_{\Omega^{\mathrm{e}}} (\mathrm{Grad}\,N_i)_c\;\bar{F}^{-1}_{cd}\;\tau_{de}\;\mathbb{L}^{\mathrm{e}}_{aebf}\;(\mathrm{Grad}\,N_j)_f\,\mathrm{d}V \tag{3.103}$$

and the material tangent operator $\mathbf{K}^{IJ}_{\mathrm{mat}}$ as

$$\left(K^{IJ}_{\mathrm{mat}}\right)_{ab} = \mathop{\mathsf{A}}_{e=1}^{n_{\mathrm{ele}}} \int_{\Omega^{\mathrm{e}}} (\mathrm{Grad}\,N_i)_c\;\bar{F}^{-1}_{cd}\;c_{adef}\;\mathbb{L}^{\mathrm{e}}_{efbg}\;(\mathrm{Grad}\,N_j)_g\,\mathrm{d}V\,. \tag{3.104}$$

3.3.6 Linearization

According to [Simo 1998; Simo & Hughes 1998], the linearization of the algorithm presented in Section 3.3.4 is essential for the preservation of the quadratic rate of asymptotic convergence characterising the Newton method. This numerical procedure is presented in Section 3.3.5 for the case of an elastic loading step. In the case of an inelastic loading step, the procedure is similar. In order to evaluate the regularly distributed part of the spatial velocity gradient $\bar{\mathbf{l}}$ in the rate form of the principal of virtual work (3.96), the regular part of the deformation gradient $\bar{\mathbf{F}}$ has to be linearized using the return-mapping algorithm as presented in Section 3.3.4 with respect to a set of independent variables $(\bar{\mathbf{T}}, \mathbf{q}, \Delta\hat{\mathbf{u}})$. All calculations are performed on the basis of the converged state of the inelastic corrector step.

Assuming the residual in the form (3.67), the linearization yields

$$\begin{aligned} \mathrm{d}R_{ij}^{\epsilon^{\mathrm{p}}} &= -\mathrm{d}\epsilon_{ij}^{\mathrm{p}} + \mathrm{d}\Delta\lambda\, \partial_{\bar{\mathbf{T}}}\phi_i\, \mathrm{Grad}\,\varphi_j + \Delta\lambda\, \partial_{\bar{\mathbf{T}}\otimes\bar{\mathbf{T}}}\phi_{ik}\, \mathrm{d}T_k\, \mathrm{Grad}\,\varphi_j \\ &= \mathbb{T}_{ijlp}^{C}\, \mathrm{d}\epsilon_{lp}^{\mathrm{p}} + \mathrm{d}\Delta\lambda\, G_{ij}^{t} + \mathbb{U}_{ijsp}^{C}\mathrm{Grad}\,\Delta\hat{u}_{sp}\,, \\ \mathrm{d}R_i^{\alpha} &= -\partial_{\mathbf{q}}\alpha_{ij}\, \mathrm{d}q_j + \mathrm{d}\Delta\lambda\, \partial_{\mathbf{q}}\phi_i \\ &= D_{ij}{}^{-1}\, \mathrm{d}q_j + \mathrm{d}\Delta\lambda\, \partial_{\mathbf{q}}\phi_i\,. \end{aligned} \tag{3.105}$$

$\mathbf{G}^{\mathbf{t}}$ and $\mathbb{T}^{C}$ are the tensor operators defined in (3.72) and

$$\mathbb{U}_{ijsp}^{C} = \mathbb{G}_{ijko}^{C}\mathbb{Q}_{kosp}\,. \tag{3.106}$$

Tensor $\mathbb{Q}$ is derived at the end of this chapter, in Section 3.3.8. The vector form of $\mathrm{d}\mathbf{R}^{\epsilon^{\mathrm{p}}}$ can be derived as

$$\begin{aligned} &\mathrm{d}R_i^{\epsilon^{\mathrm{p}}} = T_{ij}^{C}\, \mathrm{d}E_j^{\mathrm{p}} + U_{ij}^{C}\, D_j^{\mathrm{u}} + \mathrm{d}\Delta\lambda\, g_i^{t}\,, \\ &\mathrm{d}R_i^{\alpha} = D_{ij}{}^{-1}\, \mathrm{d}q_j + \mathrm{d}\Delta\lambda\, \partial_{\mathbf{q}}\phi_i\,, \end{aligned} \tag{3.107}$$

where the transformation rules for $\mathbf{T}^{C}$, $\mathbf{g}^{t}$ and $\mathbf{E}^{\mathrm{p}}$ can be found in (3.74) and

$$\begin{aligned} &\mathrm{Grad}\,\Delta\hat{\mathbf{u}} \Longrightarrow \mathbf{D}^{\mathrm{u}} \quad \text{with} \quad \mathrm{Grad}\,\Delta\hat{u}_{ij} = D_{(i-1)*3+j}^{\mathrm{u}}\,, \\ &\mathbb{U}^{C} \Longrightarrow \mathbf{U}^{C} \qquad\quad \text{with} \quad \mathbb{U}_{ijkl}^{C} = U_{(i-1)*3+j,(k-1)*3+l}^{C}\,. \end{aligned} \tag{3.108}$$

The linearization of the yield function $\phi\,(\bar{\mathbf{T}}, \mathbf{q}, \Delta\hat{\mathbf{u}})$ leads to

$$\begin{aligned} \mathrm{d}\phi &= \partial_{\bar{\mathbf{T}}}\phi_i\, \mathrm{d}T_i + \partial_{\mathbf{q}}\phi_i\, \mathrm{d}q_i \\ &= F_{lp}^{t}\, \mathrm{d}\epsilon_{lp}^{\mathrm{p}} + F_{lp}^{u}\, \mathrm{Grad}\,\Delta\hat{u}_{lp} + \partial_{\mathbf{q}}\phi_i\, \mathrm{d}q_i \qquad (3.109) \\ &= f_i^{t}\, \mathrm{d}E_i^{\mathrm{p}} + f_i^{u}\, D_i^{\mathrm{u}} + \partial_{\mathbf{q}}\phi_i\, \mathrm{d}q_i\,. \qquad (3.110) \end{aligned}$$

$\mathbf{F}^{t}$ and $\mathbf{f}^{t}$ are defined in (3.78) and

$$F_{lp}^{u} = \partial_{\bar{\mathbf{T}}}\phi_i\, N_j\, \mathbb{Q}_{ijlp}\,, \quad F_{ij}^{u} = f_{(i-1)*3+j}^{u}\,. \tag{3.111}$$

In matrix notation, these results take the form

$$\begin{aligned} &\mathrm{d}\mathbf{R} = \mathbf{A}^{-1}\cdot\boldsymbol{\Delta} + \mathrm{d}\Delta\lambda_{n+1}\, \nabla\mathbf{M} + \nabla\mathbf{U}\,, \\ &\mathrm{d}\phi = \boldsymbol{\nabla}\boldsymbol{\phi}^{\mathrm{T}}\cdot\boldsymbol{\Delta} + \boldsymbol{\nabla}\boldsymbol{\phi}_u{}^{\mathrm{T}}\cdot\mathbf{D}^{\mathrm{u}}\,. \end{aligned} \tag{3.112}$$

The definitions of $\mathbf{A}^{-1}$, $\nabla\mathbf{M}$, $\boldsymbol{\Delta}$ and $\boldsymbol{\nabla}\boldsymbol{\phi}^{\mathrm{T}}$ can be found in (3.80) and (3.81), and

$$\nabla\mathbf{U} := \begin{bmatrix} \mathbf{U}^{C}\cdot\mathbf{D}^{\mathrm{u}} \\ \mathbf{0} \end{bmatrix}, \quad \boldsymbol{\nabla}\boldsymbol{\phi}_u{}^{\mathrm{T}} := [\mathbf{f}^{\mathrm{u}}]\,. \tag{3.113}$$

Next, the set of equations

$$\begin{aligned} &\mathbf{R} + \mathbf{A}^{-1}\cdot\boldsymbol{\Delta} + \mathrm{d}\Delta\lambda_{n+1}\, \nabla\mathbf{M} + \nabla\mathbf{U} = \mathbf{0} \\ &\phi + \boldsymbol{\nabla}\boldsymbol{\phi}^{\mathrm{T}}\cdot\boldsymbol{\Delta} + \boldsymbol{\nabla}\boldsymbol{\phi}_u{}^{\mathrm{T}}\cdot\mathbf{D}^{\mathrm{u}} = 0 \end{aligned} \tag{3.114}$$

is solved for $\mathrm{d}\Delta\lambda_{n+1}$, keeping in mind that the converged values of the residual $\mathbf{R}$ and the yield function ϕ are equal to zero and that the matrix $\mathbf{A}^{-1}$ has the diagonal form:

$$\mathrm{d}\Delta\lambda_{n+1} = \left.\frac{-\nabla\phi^{\mathrm{T}*}\cdot\mathbf{T}^{C-1}\cdot\mathbf{U}^{C}+\nabla\phi_u{}^{\mathrm{T}}}{\nabla\phi^{\mathrm{T}}\cdot\mathbf{A}\cdot\nabla\mathbf{M}}\right|_{n+1}\cdot\mathbf{D}^{\mathrm{u}}\,. \tag{3.115}$$

Here, $\nabla\phi^{\mathrm{T}*}$ is the upper submatrix of the matrix $\nabla\phi^{\mathrm{T}}$ which contains the vector $\mathbf{f}^{\mathbf{t}}$.
The diagonal form of the matrix $\mathbf{A}^{-1}$ allows the separation of relation $(3.114)_1$ into two independent parts if the upper and the lower submatrices of each addend are used. The identity

$$\mathbf{T}^{C}\cdot\mathrm{d}\mathbf{E}^{\mathrm{p}}+\mathrm{d}\Delta\lambda_{n+1}\,\nabla\mathbf{M}^{*}+\mathbf{U}^{C}\cdot\mathbf{D}^{\mathrm{u}}=\mathbf{0} \tag{3.116}$$

gives as a consequence the relation

$$\mathrm{d}\mathbf{E}^{\mathrm{p}}=\mathbf{L}^{C}\cdot\mathbf{D}^{\mathrm{u}}\,, \tag{3.117}$$

where

$$\mathbf{L}^{C}=\frac{-\mathbf{T}^{C-1}\cdot\nabla\mathbf{M}^{*}\left(-\nabla\phi^{\mathrm{T}*}\cdot\mathbf{T}^{C-1}\cdot\mathbf{U}^{C}+\nabla\phi_u{}^{\mathrm{T}}\right)}{\nabla\phi^{\mathrm{T}}\cdot\mathbf{A}\cdot\nabla\mathbf{M}}-\mathbf{T}^{C-1}\cdot\mathbf{U}^{C}\,. \tag{3.118}$$

$\nabla\mathbf{M}^{*}$ is the upper submatrix of the matrix $\nabla\mathbf{M}$ which contains the vector $\mathbf{g}^{\mathbf{t}}$.
The reverse transformation of the matrix $\mathbf{L}^{C}$ yields the tensor $\mathbb{L}^{C}$, i.e.

$$\mathbf{L}^{C}\Longrightarrow\mathbb{L}^{C}\quad\text{with}\quad\mathbb{L}^{C}_{ijkl}=L^{C}_{(i-1)*3+j,(k-1)*3+l} \tag{3.119}$$

and the linearization of the jump deformation tensor $\boldsymbol{\epsilon}^{\mathrm{p}}$ with respect to the update of the regular part of the displacement field $\mathrm{Grad}\,\Delta\hat{\mathbf{u}}$ can be completed

$$\mathrm{d}\epsilon^{\mathrm{p}}{}_{kp}=\mathbb{L}^{C}_{kpqr}\,\mathrm{Grad}\,\Delta\hat{u}_{qr}\,. \tag{3.120}$$

The introduction of this result in (3.131) leads to

$$\mathrm{d}\bar{F}_{ij}=\mathbb{P}_{ijqr}\,\mathrm{Grad}\,\Delta\hat{u}_{qr}\,, \tag{3.121}$$

where

$$\mathbb{P}_{ijqr}=\mathbb{A}^{-1}{}_{ijlp}\left(\mathbb{I}_{lpqr}-\bar{F}_{lk}\,\mathbb{L}^{C}_{kpqr}\right). \tag{3.122}$$

Based on (3.97) and (3.122), the regularly distributed part of the spatial velocity gradient $\bar{\mathbf{l}}$ can be evaluated:

$$\bar{\mathbf{l}}=\mathbb{L}^{\mathrm{i}}:\mathrm{Grad}\,\Delta\hat{\mathbf{u}}_{n+1}\quad\text{with}\quad\mathbb{L}^{\mathrm{i}}_{ijkl}=\mathbb{P}_{ipkl}\,\bar{F}^{-1}_{pj}\,. \tag{3.123}$$

Following the same line of thought as in Section 3.3.5, the stiffness matrix $\mathbf{K}^{IJ}$ can be evaluated from (3.96) based on (3.123). The index form of the geometric tangent operator $\mathbf{K}^{IJ}_{\text{geo}}$ is defined as

$$\left(K^{IJ}_{\text{geo}}\right)_{ab} = \mathop{\mathsf{A}}_{e=1}^{n_{\text{ele}}} \int_{\Omega^e} (\text{Grad}\, N_i)_c \; \bar{F}^{-1}_{cd} \; \tau_{de} \; \mathbb{L}^{\text{i}}_{aebf} \; (\text{Grad}\, N_j)_f \, \text{d}V \quad (3.124)$$

and the material tangent operator $\mathbf{K}^{IJ}_{\text{mat}}$ is given by

$$\left(K^{IJ}_{\text{mat}}\right)_{ab} = \mathop{\mathsf{A}}_{e=1}^{n_{\text{ele}}} \int_{\Omega^e} (\text{Grad}\, N_i)_c \; \bar{F}^{-1}_{cd} \; c_{adef} \; \mathbb{L}^{\text{i}}_{efbg} \; (\text{Grad}\, N_j)_g \, \text{d}V \,. \quad (3.125)$$

With the global linearization algorithm, the numerical implementation of the material model proposed in Sections 3.1 and 3.2 is completed for the application of constant strain type of finite elements. The more general case extended to higher order finite elements is discussed in detail in [MOSLER 2005A; MOSLER 2007].

3.3.7 Linearization $\text{d}\boldsymbol{\Sigma}/\text{d}\boldsymbol{\epsilon}^{\text{P}}$

The goal of this section is to derive the moduli $\mathbb{G}^M$ connecting the jump deformation tensor $\boldsymbol{\epsilon}^{\text{P}}$ to the MANDEL stress tensor $\boldsymbol{\Sigma}$ for a fixed conforming displacement field $\hat{\mathbf{u}}$. Starting from the identity $\boldsymbol{\Sigma} = \bar{\mathbf{C}} \cdot \boldsymbol{S}$, the linearization can be performed in three steps.

Step 1. Linearization of $\boldsymbol{\Sigma}$ with respect to the right CAUCHY-GREEN tensor $\bar{\mathbf{C}}$:

$$\text{d}\Sigma_{ko} = \underbrace{\left(\mathbb{I}^{\text{sym}}_{kjqr} \; S_{jo} + \bar{C}_{kj} \; \frac{1}{2} \; \mathbb{C}_{jkqr}\right)}_{=:\, \mathbb{A}^C_{koqr}} \text{d}\bar{C}_{qr} = \mathbb{A}^C_{koqr} \, \text{d}\bar{C}_{qr} \,, \quad (3.126)$$

where $\mathbb{I}^{\text{sym}}$ is a symmetric fourth order identity tensor and $\mathbb{C}$ is the material elastic tangent operator defined in (2.127).

Step 2. Linearization of the right CAUCHY-GREEN tensor $\bar{\mathbf{C}}$ with respect to the deformation gradient $\bar{\mathbf{F}}$:

$$\text{d}\bar{C}_{qr} = \underbrace{\left(\mathbb{I}_{jqmn} \; F_{jr} + \mathbb{I}_{jrmn} \; F_{jq}\right)}_{=:\, \mathbb{T}_{qrmn}} \text{d}\bar{F}_{mn} = \mathbb{T}_{qrmn} \, \text{d}\bar{F}_{mn} \,. \quad (3.127)$$

Step 3. Linearization of the deformation gradient $\bar{\mathbf{F}}$ as defined in (3.62) with respect to the jump deformation tensor $\boldsymbol{\epsilon}^{\text{P}}$:

$$\text{d}\bar{F}_{mn} = \underbrace{\left(-\mathbb{A}^{-1}{}_{mnip} \; \bar{F}_{il}\right)}_{=:\, \mathbb{A}^F_{mnlp}} \text{d}\epsilon^{\text{P}}{}_{lp} = \mathbb{A}^F_{mnlp} \, \text{d}\epsilon^{\text{P}}{}_{lp} \,. \quad (3.128)$$

Finally, the linearization of the MANDEL stress tensor $\boldsymbol{\Sigma}$ with respect to the jump deformation tensor $\boldsymbol{\epsilon}^{\mathrm{P}}$ has a form

$$\mathrm{d}\Sigma_{ko} = \underbrace{\mathbb{A}^{C}_{koqr}\,\mathbb{T}_{qrmn}\,\mathbb{A}^{F}_{mnlp}}_{=:\,\mathbb{G}^{M}_{kolp}}\,\mathrm{d}\epsilon^{\mathrm{P}}{}_{lp} = \mathbb{G}^{M}_{kolp}\,\mathrm{d}\epsilon^{\mathrm{P}}{}_{lp}\,. \tag{3.129}$$

3.3.8 Linearizations $\mathrm{d}\Sigma/\mathrm{d}\epsilon^{\mathrm{P}}$ and $\mathrm{d}\Sigma/\mathrm{Grad}\,\Delta\hat{u}$

The goal of this section is to derive the moduli $\mathbb{Q}$ connecting the update of the regular part of the displacement field $\mathrm{Grad}\,\Delta\hat{\mathbf{u}}$ to the MANDEL stress tensor $\boldsymbol{\Sigma}$.
Starting with the result of the previous section

$$\mathrm{d}\Sigma_{ko} = \mathbb{A}^{C}_{koqr}\,\mathbb{T}_{qrmn}\,\mathrm{d}\bar{F}_{mn}\,, \tag{3.130}$$

and linearising the deformation gradient $\bar{\mathbf{F}}$ as defined in (3.62) with respect to the jump deformation tensor $\boldsymbol{\epsilon}^{\mathrm{P}}$ and the update of the regular part of the displacement field $\mathrm{Grad}\,\Delta\hat{\mathbf{u}}$

$$\mathrm{d}\bar{F}_{mn} = \underbrace{\left(-\mathbb{A}^{-1}{}_{mnsp}\,\bar{F}_{sl}\right)}_{=:\,\mathbb{A}^{F}_{mnlp}}\,\mathrm{d}\epsilon^{\mathrm{P}}{}_{lp} + \mathbb{A}^{-1}{}_{mnsp}\,\mathrm{Grad}\,\Delta\hat{u}_{sp} \tag{3.131}$$

leads to the final form

$$\mathrm{d}\Sigma_{ko} = \mathbb{G}^{M}_{kolp}\,\mathrm{d}\epsilon^{\mathrm{P}}{}_{lp} + \mathbb{Q}_{kosp}\,\mathrm{Grad}\,\Delta\hat{u}_{sp}\,. \tag{3.132}$$

Here, the tensor operator $\mathbb{Q}$ is to be evaluated as

$$\mathbb{Q}_{kosp} = \mathbb{A}^{C}_{koqr}\,\mathbb{T}_{qrmn}\,\mathbb{A}^{-1}{}_{mnsp}\,. \tag{3.133}$$

4 Multiple surface Strong Discontinuity Approach

In this chapter, the three-dimensional finite element formulation discussed in Chapter 3 is extended to accommodate a localised material failure composed of several planar singular surfaces $\partial_s\Omega^{(\beta)}$,$\beta = 1, \ldots, n_s$ by allowing their simultaneous propagation. The procedure is named *multiple localisation surface approach* or *MLSA*. As in Chapter 3, the numerical implementation is based on the standard return-mapping algorithm of multisurface plasticity according to [SIMO 1998; SIMO & HUGHES 1998]. Since all notations, procedures and derivations presented in Chapter 3 extend straightforwardly to multisurface material failure, the developments in this chapter will be less detailed and serve mostly as a review of the same ideas transformed and expanded to accommodate the multisurface description of the problem. At the end of this chapter, the choice of principal unknowns in the return-mapping algorithm is explained on the basis of an numerical example.

4.1 Kinematics

The kinematics of MLSA is defined in line with the assumption that the basic notions and postulates of the kinematics associated with the Strong Discontinuity Approach (SDA). It is based on the propositions made in Chapter 3 remain unchanged. Similarly to the single surface approach, a displacement field of the type (3.8) is adopted. However, considering n_s active localisation surfaces within the respective finite element, (3.8) results in

$$\mathbf{u} = \hat{\mathbf{u}} + \sum_{\beta=1}^{n_s} [\![\mathbf{u}]\!]^{(\beta)} \; (\mathcal{H}_s{}^{(\beta)} - \varphi^{(\beta)}) \,. \tag{4.1}$$

As a consequence, the deformation gradient defined in (3.11) becomes

$$\mathbf{F} = 1 + \operatorname{Grad} \hat{\mathbf{u}} - \sum_{\beta=1}^{n_s} \left([\![\mathbf{u}]\!]^{(\beta)} \otimes \operatorname{Grad} \varphi^{(\beta)} \right) + \sum_{i=1}^{n_s} \left([\![\mathbf{u}]\!]^{(\beta)} \otimes \mathbf{N}^{(\beta)} \right) \; \delta_s{}^{(\beta)} \,. \tag{4.2}$$

Here, $\mathbf{N}^{(\beta)}$ represents the normal to the singular surface $\partial_s\Omega^{(\beta)}$, $[\![\mathbf{u}]\!]^{(\beta)}$ is the corresponding displacement discontinuity, $\varphi^{(\beta)}$ is the ramp function and $\delta_s{}^{(\beta)}$ is the DIRAC delta distribution associated with the localisation surface $\partial_s\Omega^{(\beta)}$.

4.2 Constitutive relations

Analogously to Section 3.2, the material response in the bulk material $\Omega^{\pm}$ is modelled as purely elastic and the material response at each of the active discontinuity surfaces $\partial_s\Omega^{(\beta)}$ is governed by means of traction-separation laws.

Following identical lines as in Section 3.2, these interface laws capturing the softening response associated with the localisation surface $\partial_s\Omega^{(\beta)}$ are based on an admissible stress

$$\mathbb{E}_{\bar{\mathbf{T}}}^{(\beta)} := \{(\bar{\mathbf{T}}^{(\beta)}, \mathbf{q}^{(\beta)}) \in \mathbb{R}^3 \times \mathbb{R}^{n_s} | \phi^{(\beta)}(\bar{\mathbf{T}}^{(\beta)}, \mathbf{q}^{(\beta)}) \leq 0\}, \tag{4.3}$$

where

$$\bar{\mathbf{T}}^{(\beta)} = \left(\bar{\mathbf{F}}^T \cdot \mathbf{P} \cdot \mathbf{N}^{(\beta)}\right)^+, \tag{4.4}$$

and on the evolution equations

$$\dot{\mathbf{J}}^{(\beta)} = \lambda^{(\beta)} \partial_{\bar{\mathbf{T}}^{(\beta)}} \phi^{(\beta)}, \quad \dot{\boldsymbol{\alpha}}^{(\beta)} = \lambda^{(\beta)} \partial_{\mathbf{q}^{(\beta)}} \phi^{(\beta)}, \tag{4.5}$$

respectively (compare to Section 3.2.2). Since the restriction $(\bar{\mathbf{T}}^{(\beta)}, \mathbf{q}^{(\beta)}) \in \mathbb{E}_{\bar{\mathbf{T}}}^{(\beta)}$ has to be fulfilled for all $\beta \in \{1, \ldots, n_s\}$, the admissible stress space $\mathbb{E}_{\bar{\mathbf{T}}}$ is defined as the intersection of all subspaces $\mathbb{E}_{\bar{\mathbf{T}}}^{(\beta)}$, i.e.

$$\mathbb{E}_{\bar{\mathbf{T}}} := \bigcap_{i=1}^{n_s} \mathbb{E}_{\bar{\mathbf{T}}}^{(\beta)}. \tag{4.6}$$

4.3 Numerical implementation

This section offers an overview of the numerical implementation of the geometrically exact kinematics of multisurface strong discontinuities presented in Section 4.1 and the constitutive model presented in Section 4.2. As in Chapter 3, the orientation and the topology of the singular surface are chosen in accordance with Section 3.3.2, i.e. parallel to the sides of the tetrahedral finite element (see Figure 3.3). The formal equivalence of the proposed material model with the model of standard finite strain plasticity stated in Chapter 3 stays unchanged for discontinuity enrichment and the return-mapping algorithm according to [SIMO 1998; SIMO & HUGHES 1998] is again the algorithm of choice. This procedure will be presented in the next sections. The trial step is defined in Section 4.3.1, followed by the definition of an inelastic loading step in 4.3.2 and the introduction of the linearization procedure in Section 4.3.4.

4.3.1 Return-mapping algorithm - elastic predictor step

The assumption that the localised material failure may follow a multiple surface path leads to the redefinition of the purely elastic deformation defined in (3.60):

$$\begin{aligned} \lambda^{(\beta)} = 0 \quad &\Longleftrightarrow \dot{\mathbf{J}}^{(\beta)} = \mathbf{0}, \quad \dot{\alpha}^{(\beta)} = \mathbf{0}, \quad \dot{\mathbf{q}}^{(\beta)} = \mathbf{0}, \quad \beta = 1, \ldots, n_s \\ &\Longrightarrow \bar{\mathbf{F}}_{n+1}^{\mathrm{tr}} = \mathbf{1} + \mathrm{Grad}\,\hat{\mathbf{u}}_{n+1} - \bar{\mathbf{F}}_{n+1}^{\mathrm{tr}} \cdot \sum_{\beta=1}^{n_s} \mathbf{J}_n^{(\beta)} \otimes \mathrm{Grad}\,\varphi^{(\beta)}. \end{aligned} \tag{4.7}$$

The trial value of the deformation gradient $\bar{F}^{\mathrm{tr}}_{n+1}$ is computed from (4.2). The jump deformation tensor ϵ^{P} is evaluated based on the fact that $\mathbf{N}^{(\beta)}$ is parallel to $\mathrm{Grad}\,\varphi^{(\beta)}$ and $\dot{\mathbf{N}}^{(\beta)} = \mathbf{0}\,, \forall \beta = 1, \ldots, n_s$

$$\epsilon^{\mathrm{P}} = \sum_{\beta=1}^{n_s} \mathbf{J}^{(\beta)} \otimes \mathrm{Grad}\,\varphi^{(\beta)}\,, \quad \dot{\epsilon}^{\mathrm{P}} = \sum_{\beta=1}^{n_{\mathrm{act}}} \lambda^{(\beta)}\, \partial_{\bar{\mathbf{T}}^{(\beta)}}\, \phi^{(\beta)} \otimes \mathrm{Grad}\,\varphi^{(\beta)}\,. \tag{4.8}$$

Here, n_{act} is the number of active singular surfaces, $n_{\mathrm{act}} \leq n_s$. Using ϵ^{P}, the existing form of the regular part of the deformation gradient $\bar{\mathbf{F}}$ can be rewritten as

$$\begin{aligned} &\bar{\mathbf{F}}^{\mathrm{tr}}_{n+1} = \mathbf{1} + \mathrm{Grad}\,\hat{\mathbf{u}}_{n+1} - \bar{\mathbf{F}}^{\mathrm{tr}}_{n+1} \cdot \epsilon^{\mathrm{P}}{}_n = \mathbb{A}^{-1} : [\mathbf{1} + \mathrm{Grad}\,\hat{\mathbf{u}}_{n+1}]\,, \\ &\mathbb{A}_{ikpq} := \mathbb{I}_{ikpq} + \left[\mathbb{I}_{ijpq}\, \epsilon^{\mathrm{P}}_{jk}\right]\big|_{t_n}\,. \end{aligned} \tag{4.9}$$

Based on the evaluated $\bar{F}^{\mathrm{tr}}_{n+1}$, the right CAUCHY-GREEN trial tensor $\bar{C}^{\mathrm{tr}}_{n+1}$ and the second PIOLA-KIRCHHOFF trial stresses S^{tr}_{n+1} can be computed and used for the calculation of the trial traction vector in each of the active directions of localisation

$$\bar{\mathbf{T}}^{(\beta)\,\mathrm{tr}}_{n+1} = \bar{\mathbf{C}}^{\mathrm{tr}}_{n+1} \cdot \mathbf{S}^{\mathrm{tr}}_{n+1} \cdot \mathbf{N}^{(\beta)}\,. \tag{4.10}$$

The trial value of the discrete loading condition (3.52) at each of the potentially active singular surfaces $\partial_{\mathrm{s}}\Omega^{(\beta)}$ reads

$$\phi^{(\beta)\,\mathrm{tr}} := \phi^{(\beta)}\,(\bar{\mathbf{T}}^{(\beta)\,\mathrm{tr}}_{n+1}, \mathbf{q}^{(\beta)\,\mathrm{tr}}_{n+1}) > 0 \quad \text{with} \quad \mathbf{q}^{(\beta)\,\mathrm{tr}}_{n+1} = \mathbf{q}^{(\beta)}_{n}\,. \tag{4.11}$$

Based on the algorithm presented in Chapter 3, a non-positive trial value of the yield function $\phi^{(\beta)\,\mathrm{tr}} \leq 0$ renders a non-active singular surface. If all four possible singular surfaces have a negative trial value of the yield function, a purely elastic loading step is signalled. For all variables whose trial value are calculated, $(\bullet)_{n+1} = (\bullet)^{\mathrm{tr}}_{n+1}$ is set and the material response is computed according to Section 3.3.5.
A positive trial value of the yield function $\phi^{(\beta)\,\mathrm{tr}} > 0$ signals a potentially *active* singular surface. The total of all potentially active singular surfaces with a positive trial value of the yield function defines a trial set of n_{act} active surfaces $\partial_{\mathrm{s}}\Omega^{(\beta)}_{\mathrm{act}}$

$$\mathbb{J}^{\mathrm{tr}}_{\mathrm{act}} := \{\beta \in \{1, \ldots, n_{\mathrm{act}}\} \mid \phi^{(\beta)\mathrm{tr}}(\bar{\mathbf{T}}^{(\beta)}, \mathbf{q}^{(\beta)}) > 0\}\,. \tag{4.12}$$

Each elastic trial step which results in $n_{\mathrm{act}} > 0$ requires an inelastic corrector step.

4.3.2 Inelastic corrector step

The inelastic corrector step in the case of multisurface material failure follows the formalism presented in Section 3.3.4. The correction of the trial step is numerically achieved by implementing the return-mapping algorithm based on the backward-EULER integration of the evolution equations (4.5). The jump deformation tensor ϵ^{p} and each of the internal displacement-like variables $\alpha^{(\beta)}$, $\beta = 1, \ldots, n_{\mathrm{act}}$ at time t_{n+1} are evaluated as

$$\epsilon^{\mathrm{p}}{}_{n+1} = \epsilon^{\mathrm{p}}{}_n + \sum_{\beta=1}^{n_{\mathrm{act}}} \Delta\lambda_{n+1}^{(\beta)}\, \partial_{\bar{\mathbf{T}}^{(\beta)}}\, \phi^{(\beta)}|_{n+1} \otimes \mathrm{Grad}\, \varphi^{(\beta)}\,, \tag{4.13}$$

$$\boldsymbol{\alpha}_{n+1}^{(\beta)} = \boldsymbol{\alpha}_n^{(\beta)} + \Delta\lambda_{n+1}^{(\beta)}\, \partial_{\mathbf{q}^{(\beta)}}\, \phi^{(\beta)}|_{n+1}\,. \tag{4.14}$$

Here, $\Delta\lambda_{n+1}^{(\beta)} := \lambda_{n+1}^{(\beta)}\,(t_{n+1} - t_n)$.
The next step of the return-mapping algorithm is the definition of the residual $\mathbf{R}$

$$\mathbf{R} := \left\{ \begin{array}{c} \mathbf{R}^{\epsilon^{\mathrm{p}}} \\ \mathbf{R}^{\alpha} \end{array} \right\}, \tag{4.15}$$

where

$$\mathbf{R}^{\epsilon^{\mathrm{p}}} = -\epsilon^{\mathrm{p}}{}_{n+1} + \epsilon^{\mathrm{p}}{}_n + \sum_{\beta=1}^{n_{\mathrm{act}}} \Delta\lambda_{n+1}^{(\beta)}\, \partial_{\bar{\mathbf{T}}^{(\beta)}}\, \phi^{(\beta)}|_{n+1} \otimes \mathrm{Grad}\, \varphi^{(\beta)} \tag{4.16}$$

and

$$\mathbf{R}^{\alpha} := \left\{ \begin{array}{l} -\boldsymbol{\alpha}_{n+1}^{(1)} + \boldsymbol{\alpha}_n^{(1)} + \Delta\lambda_{n+1}^{(1)}\, \partial_{\mathbf{q}^{(1)}}\, \phi^{(1)}|_{n+1} \\ \ldots \\ -\boldsymbol{\alpha}_{n+1}^{(n_{\mathrm{act}})} + \boldsymbol{\alpha}_n^{(n_{\mathrm{act}})} + \Delta\lambda_{n+1}^{(n_{\mathrm{act}})}\, \partial_{\mathbf{q}^{(n_{\mathrm{act}})}}\, \phi^{(n_{\mathrm{act}})}|_{n+1} \end{array} \right\}. \tag{4.17}$$

A vanishing residual $\mathbf{R}_{n+1}$ and vanishing yield functions $\phi_{n+1}^{(\beta)}$, $\beta = 1, \ldots, n_{\mathrm{act}}$ define a set of nonlinear algebraic equations to be solved

$$\mathbf{R} = 0 \quad \wedge \quad \phi_{n+1}^{(\beta)} = 0\,, \beta = 1, \ldots, n_{\mathrm{act}}\,. \tag{4.18}$$

The linearization of the residual about the current iterate using the NEWTON iterative procedure starts with the trial values of the traction vector $\bar{\mathbf{T}}_{n+1}^{(k=1)}$, the internal variable $\mathbf{q}_{n+1}^{(k=1)}$ and the yield function $\phi_{n+1}^{(k=1)}$:

$$\bar{\mathbf{T}}_{n+1}^{(\beta)(1)} = \bar{\mathbf{T}}_{n+1}^{(\beta)(1)\mathrm{tr}}\,, \quad \mathbf{q}_{n+1}^{(\beta)(1)} = \mathbf{q}_{n+1}^{(\beta)(1)\mathrm{tr}}\,, \quad \phi_{n+1}^{(\beta)(1)} = \phi_{n+1}^{(\beta)(1)\mathrm{tr}}\,. \tag{4.19}$$

If all featured yield functions have a form

$$\phi(\bar{\mathbf{T}}^{(\beta)}, q^{(\beta)}) = ||(\bar{\mathbf{T}})_m^{(\beta)}||_2 - q^{(\beta)}(\alpha^{(\beta)})\,, \tag{4.20}$$

following second derivatives vanish

$$\partial_{\bar{\mathbf{T}}^{(\beta)}\otimes\mathbf{q}^{(\beta)}}\,\phi^{(\beta)}|_{n+1} = \mathbf{0}\,,$$
$$\partial_{\mathbf{q}^{(\beta)}\otimes\bar{\mathbf{T}}^{(\beta)}}\,\phi^{(\beta)}|_{n+1} = \mathbf{0}\,,$$
$$\partial_{\mathbf{q}^{(\beta)}\otimes\mathbf{q}^{(\beta)}}\,\phi^{(\beta)}|_{n+1} = \mathbf{0}\,. \tag{4.21}$$

For an arbitrary choice of the yield function, these derivatives should be included in the linearization procedure.

The indices describing the current time iteration step $n+1$ and the current NEWTON iteration step k will be omitted in the derivation of the linearized residuals for the sake of clarity.

The linearization of the residual tensor $\mathrm{d}\mathbf{R}$ with respect to $\bar{\mathbf{T}}^{(\beta)}$, $\mathbf{q}^{(\beta)}$ and $\Delta\lambda^{(\beta)}$, $\beta = 1,\ldots,n_{\mathrm{act}}$ is evaluated for a fixed $\hat{\mathbf{u}}$ from (4.17) and (4.21)

$$\begin{aligned}
\mathrm{d}R_{ij}^{\epsilon^{\mathrm{p}}} &= -\mathrm{d}\epsilon_{ij}^{\mathrm{p}} + \sum_{\beta=1}^{n_{\mathrm{act}}} \mathrm{d}\Delta\lambda^{(\beta)}\,\partial_{\bar{\mathbf{T}}^{(\beta)}}\,\phi_i^{(\beta)}\,\mathrm{Grad}\,\varphi_j^{(\beta)} \\
&\quad + \sum_{\beta=1}^{n_{\mathrm{act}}} \Delta\lambda^{(\beta)}\,\partial_{\bar{\mathbf{T}}^{(\beta)}\otimes\bar{\mathbf{T}}^{(\beta)}}\,\phi_{ik}^{(\beta)}\,\mathrm{d}T_k^{(\beta)}\,\mathrm{Grad}\,\varphi_j^{(\beta)} \\
&= \mathbb{T}_{ijlp}^{C}\,\mathrm{d}\epsilon_{lp}^{\mathrm{p}} + \sum_{\beta=1}^{n_{\mathrm{act}}} \mathrm{d}\Delta\lambda^{(\beta)}\,G_{ij}^{t(\beta)}\,, \\
\mathrm{d}R_i^{\alpha^{(\beta)}} &= -\partial_{\mathbf{q}^{(\beta)}}\,\alpha_{ij}^{(\beta)}\,\mathrm{d}q_j^{(\beta)} + \mathrm{d}\Delta\lambda^{(\beta)}\,\partial_{\mathbf{q}^{(\beta)}}\,\phi_i^{(\beta)} \\
&= D_{ij}^{(\beta)-1}\,\mathrm{d}q_j^{(\beta)} + \mathrm{d}\Delta\lambda^{(\beta)}\,\partial_{\mathbf{q}^{(\beta)}}\,\phi_i^{(\beta)}\,,\ \beta = 1,\ldots,n_{\mathrm{act}}\,,
\end{aligned} \tag{4.22}$$

where

$$\begin{aligned}
G_{ij}^{t(\beta)} &= \partial_{\bar{\mathbf{T}}^{(\beta)}}\,\phi_i^{(\beta)}\,\mathrm{Grad}\,\varphi_j^{(\beta)}\,, \\
\mathbb{T}_{ijlp}^{C} &= -\mathbb{I}_{ijlp} + \mathbb{G}_{ijko}^{C}\,\mathbb{G}_{kolp}^{M}\,.
\end{aligned} \tag{4.23}$$

If the traction vector is transformed according to the identity $\bar{\mathbf{T}}^{(\beta)} = \bar{\mathbf{C}}\cdot\mathbf{S}\cdot\mathbf{N}^{(\beta)} = \boldsymbol{\Sigma}\cdot\mathbf{N}^{(\beta)}$ then

$$\mathbb{G}_{ijko}^{C} = \sum_{\beta=1}^{n_{\mathrm{act}}} \Delta\lambda^{(\beta)}\,\partial_{\mathbf{T}^{\bar{(\beta)}}\otimes\mathbf{T}^{\bar{(\beta)}}}\,\phi_{ik}^{(\beta)}\,N_o^{(\beta)}\,\mathrm{Grad}\,\varphi_j^{(\beta)}\,. \tag{4.24}$$

The fourth order tensor $\mathbb{G}^{M}$ in (4.23) is derived in Section 3.3.7.

The transformation rules for the change from the tensor description to the matrix description of the problem are:

$$\begin{aligned}
&\boldsymbol{\epsilon}^{\mathrm{p}} \Longrightarrow \mathbf{E}^{\mathrm{p}} && \text{with} \quad \epsilon_{ij}^{\mathrm{p}} = E_{(i-1)*3+j}^{\mathrm{p}}\,, \\
&\mathbb{T}^{C} \Longrightarrow \mathbf{T}^{C} && \text{with} \quad \mathbb{T}_{ijkl}^{C} = T_{(i-1)*3+j,(k-1)*3+l}^{C}\,, \\
&\mathbf{G}^{t(\beta)} \Longrightarrow \mathbf{g}^{t(\beta)} && \text{with} \quad G_{ij}^{t(\beta)} = g_{(i-1)*3+j}^{t(\beta)}\,,\ \beta = 1,\ldots,n_{\mathrm{act}}\,.
\end{aligned} \tag{4.25}$$

The vector representation of the residual $\mathbf{R}$ reads

$$\begin{aligned} \mathrm{d}R_i^{\epsilon^{\mathrm{p}}} &= T_{ij}^C \, \mathrm{d}E_j^{\mathrm{p}} + \sum_{\beta=1}^{n_{\mathrm{act}}} \mathrm{d}\Delta\lambda^{(\beta)} \, g_i^{t(\beta)} \,, \\ \mathrm{d}R_i^{\alpha^{(\beta)}} &= D_{ij}^{(\beta)-1} \, \mathrm{d}q_j^{(\beta)} + \mathrm{d}\Delta\lambda^{(\beta)} \, \partial_{\mathbf{q}^{(\beta)}} \phi_i^{(\beta)} \,, \beta = 1, \ldots, n_{\mathrm{act}} \,. \end{aligned} \tag{4.26}$$

The yield functions $\phi^{(\beta)} \left(\bar{\mathbf{T}}^{(\beta)}, \mathbf{q}^{(\beta)}\right)$, $\beta = 1, \ldots, n_{\mathrm{act}}$ are linearized according to

$$\begin{aligned} \mathrm{d}\phi^{(\beta)} &= \partial_{\bar{\mathbf{T}}^{(\beta)}} \phi_i^{(\beta)} \, \mathrm{d}T_i^{(\beta)} + \partial_{\mathbf{q}^{(\beta)}} \phi_i^{(\beta)} \, \mathrm{d}q_i^{(\beta)} \\ &= F_{lp}^{t(\beta)} \, \mathrm{d}\epsilon_{lp}^{\mathrm{p}} + \partial_{\mathbf{q}^{(\beta)}} \phi_i^{(\beta)} \, \mathrm{d}q_i^{(\beta)} \qquad (4.27) \\ &= f_i^{t(\beta)} \, \mathrm{d}E_i^{\mathrm{p}} + \partial_{\mathbf{q}^{(\beta)}} \phi_i^{(\beta)} \, \mathrm{d}q_i^{(\beta)} \,, \qquad (4.28) \end{aligned}$$

where

$$F_{lp}^{t(\beta)} = \partial_{\bar{\mathbf{T}}^{(\beta)}} \phi_i^{(\beta)} \, N_j^{(\beta)} \, \mathbb{G}_{ijlp}^M \,, \quad F_{ij}^{t(\beta)} = f_{(i-1)*3+j}^{t(\beta)} \,. \tag{4.29}$$

In the matrix notation, these results take the form

$$\mathbf{dR} = \mathbf{A}^{-1} \cdot \boldsymbol{\Delta} + \nabla\mathbf{M} \cdot \mathbf{d}\boldsymbol{\Delta}\boldsymbol{\lambda}_{n+1}^{(k)} \,, \quad \mathbf{d}\boldsymbol{\phi} = \nabla\boldsymbol{\phi}^{\mathrm{T}} \cdot \boldsymbol{\Delta} \,, \tag{4.30}$$

with the notations

$$\mathbf{A}^{-1} := \left[\begin{array}{ccc} \mathbf{T}^C & & \mathbf{0} \\ & \mathbf{D}^{(1)-1} & \\ \mathbf{0} & & \cdots \\ & & \mathbf{D}^{(n_{\mathrm{act}})-1} \end{array} \right] \Bigg|_{n+1}^{(k)} \,, \tag{4.31}$$

$$\boldsymbol{\Delta} := \left[\begin{array}{c} \mathrm{d}\mathbf{E}^{\mathrm{p}} \\ \mathrm{d}\mathbf{q}^{(1)} \\ \cdots \\ \mathrm{d}\mathbf{q}^{(n_{\mathrm{act}})} \end{array} \right] \Bigg|_{n+1}^{(k)} \,, \; \mathbf{d}\boldsymbol{\Delta}\boldsymbol{\lambda}_{n+1}^{(k)} := \left[\begin{array}{c} \mathrm{d}\Delta\lambda^{(1)} \\ \cdots \\ \mathrm{d}\Delta\lambda^{(n_{\mathrm{act}})} \end{array} \right] \Bigg|_{n+1}^{(k)} \,, \tag{4.32}$$

$$\nabla\mathbf{M} := \left[\begin{array}{ccc} \mathbf{g}^{t(1)} & \cdots & \mathbf{g}^{t(n_{\mathrm{act}})} \\ \partial_{\mathbf{q}^{(1)}} \phi^{(1)} & & \\ & \cdots & \\ & & \partial_{\mathbf{q}^{(n_{\mathrm{act}})}} \phi^{(n_{\mathrm{act}})} \end{array} \right] \Bigg|_{n+1}^{(k)} \tag{4.33}$$

and

$$\nabla\boldsymbol{\phi}^{\mathrm{T}} := \left[\begin{array}{ccc} \mathbf{f}^{t(1)} ; & \partial_{\mathbf{q}^{(1)}} \phi^{(1)} & \\ & \cdots & \\ \mathbf{f}^{t(n_{\mathrm{act}})} ; & & \partial_{\mathbf{q}^{(1)}} \phi^{(n_{\mathrm{act}})} \end{array} \right] \Bigg|_{n+1}^{(k)} \,. \tag{4.34}$$

The update of the LAGRANGE multiplier $\mathbf{d}\Delta\boldsymbol{\lambda}_{n+1}^{(k)}$ is computed from the linearized form of the set of equations (4.18)

$$\mathbf{R} + \mathbf{A}^{-1} \cdot \boldsymbol{\Delta} + \nabla\mathbf{M} \cdot \mathbf{d}\Delta\boldsymbol{\lambda}_{n+1}^{(k)} = \mathbf{0}, \quad \boldsymbol{\phi} + \nabla\boldsymbol{\phi}^{\mathrm{T}} \cdot \boldsymbol{\Delta} = \mathbf{0} \tag{4.35}$$

as

$$\mathbf{d}\Delta\boldsymbol{\lambda}_{n+1}^{(k)} = \left. \frac{\boldsymbol{\phi} - \nabla\boldsymbol{\phi}^{\mathrm{T}} \cdot \mathbf{A} \cdot \mathbf{R}}{\nabla\boldsymbol{\phi}^{\mathrm{T}} \cdot \mathbf{A} \cdot \nabla\mathbf{M}} \right|_{n+1}^{(k)} \Rightarrow \Delta\boldsymbol{\lambda}_{n+1}^{(k+1)} = \Delta\boldsymbol{\lambda}_{n+1}^{(k)} + \mathbf{d}\Delta\boldsymbol{\lambda}_{n+1}^{(k)}. \tag{4.36}$$

The update of the state variables $\boldsymbol{\Delta}_a$ is calculated from $(4.35)_1$

$$\boldsymbol{\Delta}_a = -\mathbf{D}^J \cdot \mathbf{A} \cdot \left(\mathbf{R} + \nabla\mathbf{M} \cdot \mathbf{d}\Delta\boldsymbol{\lambda}_{n+1}^{(k)} \right) \Big|_{n+1}^{(k)}, \tag{4.37}$$

where

$$\mathbf{D}^J := \left[\begin{array}{cc} \mathbf{I} & 0 \\ 0 & -\mathbf{D} \end{array} \right] \Big|_{n+1}^{(k)}, \quad \boldsymbol{\Delta}_a := \left[\begin{array}{c} \mathrm{d}\mathbf{E}^{\mathrm{p}} \\ \mathrm{d}\boldsymbol{\alpha} \end{array} \right] \Big|_{n+1}^{(k)}, \tag{4.38}$$

and consequently

$$\left[\begin{array}{c} \mathbf{E}^{\mathrm{p}} \\ \boldsymbol{\alpha}^{(1)} \\ \cdots \\ \boldsymbol{\alpha}^{(n_{\mathrm{act}})} \end{array} \right] \Big|_{n+1}^{(k+1)} = \left[\begin{array}{c} \mathbf{E}^{\mathrm{p}} \\ \boldsymbol{\alpha}^{(1)} \\ \cdots \\ \boldsymbol{\alpha}^{(n_{\mathrm{act}})} \end{array} \right] \Big|_{n+1}^{(k)} + \left[\begin{array}{c} \mathrm{d}\mathbf{E}^{\mathrm{p}} \\ \mathrm{d}\boldsymbol{\alpha}^{(1)} \\ \cdots \\ \mathrm{d}\boldsymbol{\alpha}^{(n_{\mathrm{act}})} \end{array} \right] \Big|_{n+1}^{(k)}. \tag{4.39}$$

4.3.3 Determination of active singular surfaces

The set of potentially active singular surfaces entering the inelastic corrector step $\mathbb{J}_{\mathrm{act}}^{\mathrm{tr}}$ is not necessarily constant if the trial value of $n_{\mathrm{act}} > 1$. The condition $\phi^{(\beta)\mathrm{tr}}(\bar{\mathbf{T}}^{(\beta)}, \mathbf{q}^{(\beta)}) > 0$ does not necessarily lead to $\Delta\lambda_{n+1}^{(\beta)} > 0$ and $\phi_{n+1}^{(\beta)} = 0$ in the converged state of the inelastic corrector step $n+1$ for each of the singular surfaces signalling activity in the trial state. According to [SIMO & HUGHES 1998], if the trial value $\bar{\mathbf{T}}_{n+1}^{\mathrm{tr}}$ characterising the corner point between two spaces of admissible stresses $\mathbb{E}_{\bar{\mathbf{T}}}^{(1)}$ and $\mathbb{E}_{\bar{\mathbf{T}}}^{(2)}$ falls in the corner region of the stress space spanned by the gradients of the respective yield functions (in the case of associative flow rules), the converged values of $\Delta\lambda_{n+1}^{(1,2)} > 0$ and the actual stress state $\bar{\mathbf{T}}_{n+1}$ is at the intersection of two yield surfaces. If its position is outside this corner region and in one of the characteristic half stress spaces spanned by the gradients of the yield functions $\phi_{n+1}^{(1,2)}$, this half space defines the inactive surface signalled by $\Delta\lambda_{n+1}^{(\beta)} < 0$. This fact leads to the conclusion that the actual set of active discontinuities $\mathbb{J}_{\mathrm{act}} \subseteq \mathbb{J}_{\mathrm{act}}^{\mathrm{tr}}$, which needs to be modified in the inelastic corrector step.

The trial set of active singular surfaces $\mathbb{J}_{\text{act}}^{\text{tr}}$ is altered at each step of the iterative solution presented in this chapter. If the specific working set of singular surfaces entering the inelastic corrector step is $\mathbb{J}_{\text{act},0}^{(n+1)} = \mathbb{J}_{\text{act}}^{\text{tr}}$, its update can be evaluated following one of the two alternative procedures:

Procedure 1 *The working set is updated at the end of the iterative procedure.* The working set of active singular surfaces $\mathbb{J}_{\text{act},0}^{(n+1)} = \mathbb{J}_{\text{act}}^{\text{tr}}$ remains unchanged during the iterative process until it converges to the consistent solution. After the characteristic residual of the NEWTON procedure is driven to zero, the converged values of $\Delta\lambda_{n+1}^{(\beta)}$ are checked $\forall\beta \in \mathbb{J}_{\text{act},0}^{(n+1)}$. If all $\Delta\lambda_{n+1}^{(\beta)} > 0$ the working set $\mathbb{J}_{\text{act},0}^{(n+1)}$ becomes the actual set $\mathbb{J}_{\text{act}}^{(n+1)}$, the final converged state is defined and the corrector step is finished. If $\Delta\lambda_{n+1}^{(\beta)} < 0$ the β-singular surface is removed from $\mathbb{J}_{\text{act},0}^{(n+1)}$ leading to a new working set of active singular surfaces $\mathbb{J}_{\text{act},1}^{(n+1)}$. The complete corrector step is repeated with $\mathbb{J}_{\text{act},1}^{(n+1)}$. The working set $\mathbb{J}_{\text{act},i}^{(n+1)}$ must be modified until all $\Delta\lambda_{n+1}^{(\beta)} > 0$.

Procedure 2 *The working set is updated during the iterative procedure.* The non-negativity of the consistency parameter $\Delta\lambda_{n+1}^{(\beta)(k+1)}$ is checked at the end of each iterative step (k). If any $\Delta\lambda_{n+1}^{(\beta)(k+1)} < 0$ the β-singular surface is removed from $\mathbb{J}_{\text{act}}^{(n+1)(k)}$ and the iteration is restarted from $k = 0$ with the updated working set.

The correction of the trial set of active singular surfaces $\mathbb{J}_{\text{act}}^{\text{tr}}$ in the algorithm presented in this chapter follows *Procedure 1*. In that manner, the actual set of active singular surfaces $\mathbb{J}_{\text{act}}^{\text{tr}}$ for each inelastic global iteration step is evaluated based on the converged state of the local corrective procedure.
The whole procedure for the determination of active singular surfaces is summarised in Figure 4.1.

4.3.4 Linearization

In order to evaluate the regularly distributed part of the spatial velocity gradient $\bar{\mathbf{l}}$ in the rate form of the principal of virtual work (3.96), the conforming part of the deformation gradient $\bar{\mathbf{F}}$ is linearized with respect to a set of independent variables $(\bar{\mathbf{T}}^{(\beta)}, \mathbf{q}^{(\beta)}, \Delta\hat{\mathbf{u}})$, $\beta = 1, \ldots, n_{\text{act}}$. The return-mapping algorithm is performed using the converged state of the inelastic corrector step.
The linearization of the residual $\mathbf{R}$ given in (4.15) leads to

1. *Evaluate the residuals (4.15) and the yield function*

$$\mathbf{R} := \left\{ \begin{array}{c} \mathbf{R}^{\epsilon^{\mathrm{p}}} \\ \mathbf{R}^{\alpha} \end{array} \right\}\Big|_{n+1}^{(k)}, \quad \phi_{n+1}^{(\beta)(k)} = \phi_{n+1}^{(\beta)\mathrm{tr}}, \forall \beta \in \mathbb{J}_{\mathrm{act},i}^{(n+1)} .$$

2. *Check convergence*

   IF $\phi_{n+1}^{(\beta)(k)} \leq TOL_1, \forall \beta \in \mathbb{J}_{\mathrm{act},i}^{(n+1)}$ and $||\mathbf{R}||_{n+1}^{(k)} \leq TOL_2$ THEN: *EXIT*

3. *Calculate elastic moduli (2.127) and consistent tangent moduli (4.31)*

4. *Obtain the increment to the consistency parameters* $\mathrm{d}\boldsymbol{\Delta\lambda}_{n+1}^{(k)}$ *(4.36)*

5. *Obtain the incremental state variables* $\boldsymbol{\Delta}_a$ *(4.38)*

6. *Update the state variables (4.39) and the consistency parameters (4.36)*

   Set $k \leftarrow k+1$ and Goto 1.

7. *Check the converged values of consistency parameters* $\Delta\lambda_{n+1}^{(\beta)(k+1)} \forall \beta \in \mathbb{J}_{\mathrm{act},i}^{(n+1)}$

   IF $\Delta\lambda_{n+1}^{(\beta)(k+1)} > TOL_3, \forall \beta \in \mathbb{J}_{\mathrm{act},i}^{(n+1)}$ THEN:

   EXIT

   ELSE Update $\mathbb{J}_{\mathrm{act},i+1}^{(n+1)} := \{\beta \in \mathbb{J}_{\mathrm{act},i}^{(n+1)} \mid \Delta\lambda_{n+1}^{(\beta)(k+1)} > 0\}$

   Set $k = 1$ and Goto 1.

   ENDIF

Figure 4.1: Multisurface return-mapping algorithm - plastic corrector iteration

$$\begin{aligned} \mathrm{d}R_{ij}^{\epsilon^{\mathrm{p}}} &= -\mathrm{d}\epsilon_{ij}^{\mathrm{p}} + \sum_{\beta=1}^{n_{\mathrm{act}}} \mathrm{d}\Delta\lambda^{(\beta)}\, \partial_{\bar{\mathbf{T}}^{(\beta)}} \phi_i^{(\beta)}\, \mathrm{Grad}\, \varphi_j^{(\beta)} \\ &\quad + \sum_{\beta=1}^{n_{\mathrm{act}}} \Delta\lambda^{(\beta)}\, \partial_{\bar{\mathbf{T}}^{(\beta)} \otimes \bar{\mathbf{T}}^{(\beta)}} \phi_{ik}^{(\beta)}\, \mathrm{d}T_k^{(\beta)}\, \mathrm{Grad}\, \varphi_j^{(\beta)} \end{aligned} \tag{4.40}$$

$$\mathrm{d}R_{ij}^{\epsilon^{\mathrm{p}}} = \mathbb{T}^C_{ijlp}\,\mathrm{d}\epsilon^{\mathrm{p}}_{lp} + \mathbb{U}^C_{ijsp}\mathrm{Grad}\,\Delta\hat{u}_{sp} + \sum_{\beta=1}^{n_{\mathrm{act}}} \mathrm{d}\Delta\lambda^{(\beta)}\, G_{ij}^{t(\beta)}\,, \tag{4.41}$$

$$\begin{aligned}\mathrm{d}R_i^{\alpha^{(\beta)}} &= -\partial_{\mathbf{q}^{(\beta)}}\,\alpha_{ij}^{(\beta)}\,\mathrm{d}q_j^{(\beta)} + \mathrm{d}\Delta\lambda^{(\beta)}\,\partial_{\mathbf{q}^{(\beta)}}\,\phi_i^{(\beta)} \\ &= D_{ij}^{(\beta)-1}\,\mathrm{d}q_j^{(\beta)} + \mathrm{d}\Delta\lambda^{(\beta)}\,\partial_{\mathbf{q}^{(\beta)}}\,\phi_i^{(\beta)}\,,\ \beta = 1,\ldots,n_{\mathrm{act}}\,,\end{aligned} \tag{4.42}$$

where $\mathbf{G}^{\mathbf{t}}$, $\mathbb{T}^C$ and $\mathbb{U}^C$ are the tensor operators defined in (4.23) and (3.106). The *vector* form of $\mathbf{dR}$ can be derived as

$$\begin{aligned}\mathrm{d}R_i^{\epsilon^{\mathrm{p}}} &= T_{ij}^C\,\mathrm{d}E_j^{\mathrm{p}} + U_{ij}^C\,D_j^{\mathrm{u}} + \sum_{\beta=1}^{n_{\mathrm{act}}} \mathrm{d}\Delta\lambda^{(\beta)}\,g_i^{t(\beta)}\,, \\ \mathrm{d}R_i^{\alpha^{(\beta)}} &= D_{ij}^{(\beta)-1}\,\mathrm{d}q_j^{(\beta)} + \mathrm{d}\Delta\lambda^{(\beta)}\,\partial_{\mathbf{q}^{(\beta)}}\,\phi_i^{(\beta)}\,,\ \beta = 1,\ldots,n_{\mathrm{act}}\,,\end{aligned} \tag{4.43}$$

where the transformation rules for $\mathbf{T}^C$, $\mathbf{g}^t$ and $\mathbf{E}^{\mathrm{p}}$ can be found in (3.74) and for $\mathbf{D}^{\mathrm{u}}$ and $\mathbf{U}^C$ in (3.108).
The linearization of the yield function $\phi\,(\bar{\mathbf{T}}, \mathbf{q}, \Delta\hat{\mathbf{u}})$ leads to

$$\begin{aligned}\mathrm{d}\phi^{(\beta)} &= \partial_{\bar{\mathbf{T}}^{(\beta)}}\,\phi_i^{(\beta)}\,\mathrm{d}T_i^{(\beta)} + \partial_{\mathbf{q}^{(\beta)}}\,\phi_i^{(\beta)}\,\mathrm{d}q^{(\beta)}{}_i \\ &= F_{lp}^{t(\beta)}\,\mathrm{d}\epsilon^{\mathrm{p}}_{lp} + F_{lp}^{u(\beta)}\,\mathrm{Grad}\,\Delta\hat{u}_{lp} + \partial_{\mathbf{q}^{(\beta)}}\,\phi_i^{(\beta)}\,\mathrm{d}q_i^{(\beta)} \qquad (4.44) \\ &= f_i^{t(\beta)}\,\mathrm{d}E_i^{\mathrm{p}} + f_i^{u(\beta)}\,D_i^{\mathrm{u}} + \partial_{\mathbf{q}^{(\beta)}}\,\phi_i^{(\beta)}\,\mathrm{d}q_i^{(\beta)}\,, \qquad (4.45)\end{aligned}$$

where $\mathbf{F}^t$ and $\mathbf{f}^t$ are defined in (4.29) and

$$F_{lp}^{u(\beta)} = \partial_{\bar{\mathbf{T}}^{(\beta)}}\,\phi_i^{(\beta)}\,N_j^{(\beta)}\,\mathbb{Q}_{ijlp}\,,\quad F_{ij}^{u(\beta)} = f_{(i-1)*3+j}^{u(\beta)}\,. \tag{4.46}$$

The linearizations of $\mathbf{R}$ and $\boldsymbol{\phi}$ take the form

$$\begin{aligned}\mathbf{dR} &= \mathbf{A}^{-1}\cdot\boldsymbol{\Delta} + \nabla\mathbf{M}\cdot\mathbf{d}\boldsymbol{\Delta\lambda}_{n+1} + \nabla\mathbf{U}\,, \\ \mathbf{d}\boldsymbol{\phi} &= \boldsymbol{\nabla\phi}^{\mathrm{T}}\cdot\boldsymbol{\Delta} + \boldsymbol{\nabla\phi}_u{}^{\mathrm{T}}\cdot\mathbf{D}^{\mathrm{u}}\,.\end{aligned} \tag{4.47}$$

The definitions of $\mathbf{A}^{-1}$, $\nabla\mathbf{M}$, $\boldsymbol{\Delta}$ and $\boldsymbol{\nabla\phi}^{\mathrm{T}}$ can be found in (4.31)-(4.34), $\nabla\mathbf{U}$ is given in (3.113) and

$$\boldsymbol{\nabla\phi}_u{}^{\mathrm{T}} := \begin{bmatrix} \mathbf{f}^{u(1)} \\ \cdots \\ \mathbf{f}^{u(n_{\mathrm{act}})} \end{bmatrix}\,. \tag{4.48}$$

The solution of the set of equations

$$\begin{aligned}&\mathbf{R} + \mathbf{A}^{-1}\cdot\boldsymbol{\Delta} + \nabla\mathbf{M}\cdot\mathbf{d}\boldsymbol{\Delta\lambda}_{n+1} + \nabla\mathbf{U} = \mathbf{0} \\ &\boldsymbol{\phi} + \boldsymbol{\nabla\phi}^{\mathrm{T}}\cdot\boldsymbol{\Delta} + \boldsymbol{\nabla\phi}_u{}^{\mathrm{T}}\cdot\mathbf{D}^{\mathrm{u}} = \mathbf{0}\end{aligned} \tag{4.49}$$

is the update of the consistency parameter $\mathbf{d}\boldsymbol{\Delta\lambda}_{n+1}$

$$\mathbf{d}\boldsymbol{\Delta\lambda}_{n+1} = \left.\frac{-\boldsymbol{\nabla\phi}^{\mathrm{T}*}\cdot\mathbf{T}^{C-1}\cdot\mathbf{U}^C + \boldsymbol{\nabla\phi}_u{}^{\mathrm{T}}}{\boldsymbol{\nabla\phi}^{\mathrm{T}}\cdot\mathbf{A}\cdot\nabla\mathbf{M}}\right|_{n+1}\cdot\mathbf{D}^{\mathrm{u}}\,. \tag{4.50}$$

Here, $\nabla\boldsymbol{\phi}^{\mathrm{T}^*}$ is the upper submatrix of the matrix $\nabla\boldsymbol{\phi}^{\mathrm{T}}$ which contains the vectors $\mathbf{f}^{t(\beta)}$, $\beta = 1, \ldots, n_{\mathrm{act}}$.
The separation of the relation $(4.49)_1$ into two independent relations relating the upper submatrices of each addend is based on the diagonal form of the matrix $\mathbf{A}^{-1}$ and leads to

$$\mathbf{T}^C \cdot \mathrm{d}\mathbf{E}^{\mathrm{p}} + \nabla\mathbf{M}^* \cdot \mathrm{d}\boldsymbol{\Delta\lambda}_{n+1} + \mathbf{U}^C \cdot \mathbf{D}^{\mathrm{u}} = \mathbf{0}\,. \tag{4.51}$$

The rest of the linearization procedure is given in the sequence (3.117)-(3.123) and the final forms of the geometric stiffness matrix $\mathbf{K}^{IJ}_{\mathrm{geo}}$ and stiffness matrix $\mathbf{K}^{IJ}_{\mathrm{mat}}$ are given in (3.124) and (3.125). That way, all computations necessary for the the solution of the $(n+1)$-st loading step $\hat{\mathbf{u}}_{n+1}$ are completed and the standard finite element procedure can be applied.

4.4 Explicit multiple surface SDA

The numerical procedure for the evaluation of the material response in the case of localised multisurface failure, presented in previous sections of this chapter, can be reformulated if the implicit relation (4.7) describing the regular part of the deformation gradient $\bar{\mathbf{F}}$ is transformed into an explicit relation of the type

$$\bar{\mathbf{F}}_{n+1} = \underbrace{\mathbf{1} + \mathrm{Grad}\,\hat{\mathbf{u}}_{n+1}}_{\hat{\mathbf{F}}_{n+1}} - \hat{\mathbf{F}}_{n+1} \cdot \sum_{\beta=1}^{n_s} \mathbf{J}_n^{(\beta)} \otimes \mathrm{Grad}\,\varphi^{(\beta)}\,. \tag{4.52}$$

This kind of transformation is possible only if an equivalence between the formulations (4.7) and (4.52) can be established. In the case when the single surface localisation ($n_s = 1$) has a form of a slip plane (e.g. (3.41)) with the orientation proposed in Section 3.3.2, the definition (4.7) degenerates to the definition (4.52) based on the orthogonality of vectors $\mathbf{J}$ and $\mathrm{Grad}\,\varphi$. If the regular part of the deformation gradient resulting from the implicit formulation (4.7) is named $\bar{\mathbf{F}}^i$ and the one resulting from the explicit formulation (4.52) is $\bar{\mathbf{F}}^e$, this equivalence can be proven by

$$\begin{aligned}
\bar{F}^i_{ij} &= \hat{F}_{ij} - \bar{F}^i_{ik}\, J_k\, \mathrm{Grad}\,\varphi_j \\
&= \hat{F}_{ij} - \left(\hat{F}_{ik} - \bar{F}^i_{il}\, J_l\, \mathrm{Grad}\,\varphi_k\right) J_k\, \mathrm{Grad}\,\varphi_j \\
&= \hat{F}_{ij} - \hat{F}_{ik}\, J_k\, \mathrm{Grad}\,\varphi_j - \bar{F}_{il}\, J_l \underbrace{\mathrm{Grad}\,\varphi_k\, J_k}_{0}\, \mathrm{Grad}\,\varphi_j \\
&= \hat{F}_{ij} - \hat{F}_{ik}\, J_k\, \mathrm{Grad}\,\varphi_j \\
&= \bar{F}^e_{ij}\,.
\end{aligned} \tag{4.53}$$

Here, the indices n and $n+1$ describing the iteration step have been omitted for the sake of clarity. In reference to the multisurface localisation, the

formulation (4.52) represents the idea that the total inelastic contribution to the regular part of the deformation gradient can be evaluated as a sum of contributions of individual localisation processes $\beta = 1 \dots n_s$. The similarity between two formulations in the case of multisurface material failure will be shown through the results of a numerical simulation in Chapter 5.
If definition (4.52) is utilised in the numerical procedure presented in previous sections of this chapter, the procedure must be reformulated accordingly.
Starting with the elastic predictor step of the return-mapping algorithm presented in Section 4.3.1, relation (4.9) is altered in the following manner

$$\begin{aligned} \bar{\mathbf{F}}^{\mathrm{tr}}_{n+1} &= \hat{\mathbf{F}}^{\mathrm{tr}}_{n+1} - \hat{\mathbf{F}}^{\mathrm{tr}}_{n+1} \cdot \boldsymbol{\epsilon}^{\mathrm{p}}{}_n = \mathbb{A}^e : \hat{\mathbf{F}}^{\mathrm{tr}}_{n+1} \,, \\ \mathbb{A}^e_{ijlp} &:= \mathbb{I}_{ijlp} - \left[\mathbb{I}_{iklp}\, \epsilon^{\mathrm{p}}_{kj}\right]\Big|_{t_n} \,. \end{aligned} \tag{4.54}$$

This change in the predictor step leads to some necessary alterations in the local linearization procedure presented in Section 3.3.7. The linearization of the deformation gradient $\bar{\mathbf{F}}$ as defined in (4.52) with respect to the jump deformation tensor $\boldsymbol{\epsilon}^{\mathrm{p}}$ can be defined as

$$\mathrm{d}\bar{F}_{mp} = -\hat{F}_{ml}\, \mathrm{d}\epsilon^{\mathrm{p}}{}_{lp} \,, \tag{4.55}$$

and the linearization of the MANDEL stress tensor $\boldsymbol{\Sigma}$ with respect to the jump deformation tensor $\boldsymbol{\epsilon}^{\mathrm{p}}$ has the form

$$\mathrm{d}\Sigma_{ko} = \underbrace{-\mathbb{A}^C_{koqr}\, \mathbb{T}_{qrmp}\, \hat{F}_{ml}}_{=:\, \mathbb{G}^M_{kolp}}\, \mathrm{d}\epsilon^{\mathrm{p}}{}_{lp} = \mathbb{G}^M_{kolp}\, \mathrm{d}\epsilon^{\mathrm{p}}{}_{lp} \,. \tag{4.56}$$

Consequently, the global linearization procedure presented in Section 3.3.8 must be reformulated to accommodate the regular part of the deformation gradient $\bar{\mathbf{F}}$ in the form (4.52). Starting with the new form of the linearized $\bar{\mathbf{F}}$ with respect to the jump deformation tensor $\boldsymbol{\epsilon}^{\mathrm{p}}$ and the update of the regular part of the displacement field $\operatorname{Grad} \Delta\hat{\mathbf{u}}$

$$\mathrm{d}\bar{F}_{mn} = -\hat{F}_{ml}\, \mathrm{d}\epsilon^{\mathrm{p}}{}_{ln} + \mathbb{A}^e_{mnsp} \operatorname{Grad} \Delta\hat{u}_{sp} \tag{4.57}$$

leads to the final form

$$\mathrm{d}\Sigma_{ko} = \mathbb{G}^M_{konl}\, \mathrm{d}\epsilon^{\mathrm{p}}{}_{ln} + \mathbb{Q}_{kosp} \operatorname{Grad} \Delta\hat{u}_{sp} \,. \tag{4.58}$$

Here, the linearization operator $\mathbb{G}^M$ is defined in (4.56) and the operator $\mathbb{Q}$ is to be evaluated as

$$\mathbb{Q}_{kosp} = \mathbb{A}^C_{koqr}\, \mathbb{T}_{qrmn}\, \mathbb{A}^e_{mnsp} \,. \tag{4.59}$$

If the elastic predictor step calculated according to this transformation is correct, the elastic unloading procedure given in Section 3.3.5 can be performed if the fourth order tensor $\mathbb{L}^e$ connecting the regularly distributed part of the

spatial velocity gradient $\bar{\mathrm{I}}$ to the update of the regular part of the displacement field Grad $\Delta\hat{\mathbf{u}}$ is evaluated according to

$$\mathbb{L}^{\mathrm{e}}_{ijlp} = \mathbb{A}^{e}_{iklp}\, \bar{F}^{-1}_{pj} \,. \tag{4.60}$$

Aside from the change of the linearization tensor operator $\mathbb{G}^{M}$ given in (4.56), the original corrective procedure in the case of an inelastic loading step showed in Section 4.3.2 stays uninfluenced by this alteration.
The linearization algorithm given in Section 4.3.4 remains unchanged except for the fourth order tensor $\mathbb{P}$ defined in (3.122). The definition of this tensor is now

$$\mathbb{P}_{ijlp} = \mathbb{A}^{e}_{ijlp} - \hat{F}_{ik}\, \mathbb{L}^{C}_{kjlp} \,. \tag{4.61}$$

In the case of the explicit formulation, the inversion of the fourth order tensor $\mathbb{A}$ appearing in (4.9) can thus be avoided. This simple strategy significantly improves the numerical performance of both the local and the global NEWTON procedure in the case when this tensor operator and consequently the tangent of the iterative procedure are ill-conditioned.

4.4.1 Inelastic corrector step

The determination of the active set of singular surfaces $\mathbb{J}_{\mathrm{act}}$ in the case of multisurface material failure, presented in 4.3.3, is numerically achieved by implementing the return-mapping algorithm based on the backward-EULER integration of the evolution equations (4.5). The actual choice of active singular surfaces during or at the end of the iterative process relies on the assumption that the vanishing residual and the corresponding state variables of the iterative procedure always correspond to the actual state. However, the NEWTON iterative procedure guarantees an asymptotic quadratic convergence only for sufficiently smooth functions. This section offers a comparative analysis between the converged solution of the local NEWTON iterative procedure and a solution obtained from a specific variational formulation (such as [ORTIZ & STEINER 1999]), in the case when the function to be linearized satisfies this condition only to a certain extent. This analysis is useful for the estimation of the possible numerical problems related to this basic property of the iterative procedure in question. Once the possible numerical instabilities are recognised, an effective solution is offered.
According to prerequisite of the explicit MLSA, following assumptions are made for numerical examples presented below:

- purely elastic material response in the bulk material (see Section 3.2.1)
- multisurface localisation by means of VON MISES-type of yield surface given in (3.41)

- orientation of the localisation surface proposed in Section 3.3.2
- softening response characterised by the internal variable $q^{(\beta)}$ with an exponential evolution of the type

$$q^{(\beta)}(\alpha^{(\beta)}) = f_{\mathrm{tu}} \cdot \exp\left(-\frac{\alpha^{(\beta)}}{H}\right), \tag{4.62}$$

  with the material strength f_{tu} and the softening parameter H

The fact that the VON MISES-type yield functions are utilised for the description of the singularities in an uniaxial tension test, the material displacement jump $\mathbf{J}^{(\beta)}$, $\beta = 1 \ldots n_s$ is assumed to have a constant direction perpendicular to the normal $\mathbf{N}^{(\beta)}$

$$\mathbf{J}^{(\beta)} = \Delta\lambda^{(\beta)}\, \mathbf{M}^{(\beta)} \quad \text{with} \quad \mathbf{M}^{(\beta)} \cdot \mathbf{N}^{(\beta)} = 0\,. \tag{4.63}$$

According to the constitutive model presented in Section 3.2.2, the HELMHOLTZ free energy is additively decomposed into a part characterising the hyperelastic material response in $\Omega^{\pm}$ and an additional term which describes the localised deformation at the singular surface $\partial_{\mathrm{s}}\Omega$ in the form given in (3.29). The integration of (3.29) leads to

$$\begin{aligned} \mathcal{I}_h &= \int_{\Omega} \Psi(\bar{\mathbf{C}}, \mathbf{J}^{1\ldots n_{act}}, \boldsymbol{\alpha}^{1\ldots n_{act}})\, \mathrm{d}V \\ &= \int_{\Omega} \Psi_{\mathrm{reg}}(\bar{\mathbf{C}})\, \mathrm{d}V \\ &\quad + \sum_{\beta=1}^{n_{\mathrm{act}}} \int_{\partial_{\mathrm{s}}\Omega^{(\beta)}} \Psi_{\mathrm{sing}}^{(\beta)}(\mathbf{J}^{(\beta)}, \boldsymbol{\alpha}^{(\beta)})\, \mathrm{d}A\,. \end{aligned} \tag{4.64}$$

In this manner, the HELMHOLTZ free energy of the whole system is decomposed into a part corresponding to the bulk material and a part corresponding to the singular surface $\partial_{\mathrm{s}}\Omega$. Since the evolution equations (4.5) which describe the characteristic material response obey the normality rule, the constitutive update can be obtained from a variational principle. If the variational constitutive update presented in [ORTIZ & STEINER 1999] is applied to the case of VON MISES plasticity, the minimisation of the potential $\mathcal{I}_h$ with respect to the state variables $(\mathbf{J}, \alpha)$ delivers the reduced potential which only depends on the rate of the deformation. For constant direction of the displacement jump $\mathbf{J}$, the reduced potential is a function of $\Delta\lambda$. Since the yield function ϕ is a positively homogeneous function of degree one, the minimisation of the potential $\mathcal{I}_h$ is equivalent to the given yield condition:

$$\arg \inf_{\Delta\lambda} \mathcal{I}_h(\bar{\mathbf{C}}, \mathbf{J}, \alpha) \Longleftrightarrow \Delta\lambda \geq 0 : \phi\,(\bar{\mathbf{T}}, q) = 0\,. \tag{4.65}$$

In other words, the minimum of the above defined potential corresponds to the solution of the resulting set of algebraic differential equations (4.18) in the NEWTON iteration scheme. Based on this statement, the converged solution of the NEWTON-type iterative procedure presented in Section 4.3.2 can be compared to the solutions of the minimisation problem obtained via state of the art optimisation algorithms. However, since this work does not exploit this kind of variational constitutive formulation to any major extent, and the scientific field covering the standard dissipative media is significant, the presentation of the principles and methods of variational constitutive modelling is omitted. The reader is referred to [MOSLER 2007] for a comprehensive survey of variational updates.
The bulk part of the HELMHOLTZ free energy $\Psi_{\text{reg}}(\bar{\mathbf{C}})$ is evaluated using the stored-energy functional defined in (2.125). The singular part is evaluated from

$$q^{(\beta)}(\alpha^{(\beta)}) = \frac{\partial \Psi^{(\beta)}_{\text{sing}}(\boldsymbol{\alpha}^{(\beta)})}{\partial \alpha^{(\beta)}} \,. \tag{4.66}$$

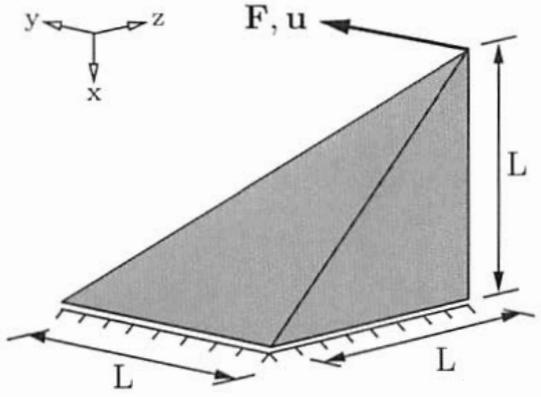

L	=	0.5	[m]
E	=	$1.0 \cdot 10^7$	[kN/m^2]
ν	=	0.2	
f_{tu}	=	500	[kN/m^2]
H	=	0.0008	[m]

Figure 4.2: Numerical model of one-element shear test: setup

In order to perform a comparative analysis between the results of a numerical simulation by MLSA and the results of the minimisation procedure, a single element model is designed and the results of the local iteration are compared to the results of the minimisation of the potential defined in (4.64). The numerical model is presented in Figure 4.2. A single element with a characteristic dimension L is pulled incrementally in shear in y-direction up to 0.01 m. The material parameters are chosen such to ensure a target-function $\mathcal{I}_h$ with multiple local extrema.
After the beginning of the localisation process, one specific iteration step is singled out for the comparative analysis and the results of a single inelastic corrector step are evaluated based on the minimisation of the potential $\mathcal{I}_h$.

According to the calculated trial state, the trial set of active singular surfaces $\mathbb{J}_{\text{act}}^{\text{tr}}$ includes two potentially active singular surfaces, i.e. one with the normal in x-direction ($\beta = 1$) and the other with the normal in y-direction ($\beta = 4$). The prescribed displacement field, the material parameters and the trial state are the input for the evaluation of the integral $\mathcal{I}_h$ and for the optimisation algorithm. The 3D-plot of the resulting integral $\mathcal{I}_h$ as a function of LAGRANGE multipliers $\Delta\lambda^{(1)}$ and $\Delta\lambda^{(4)}$ is given in Figure 4.3.

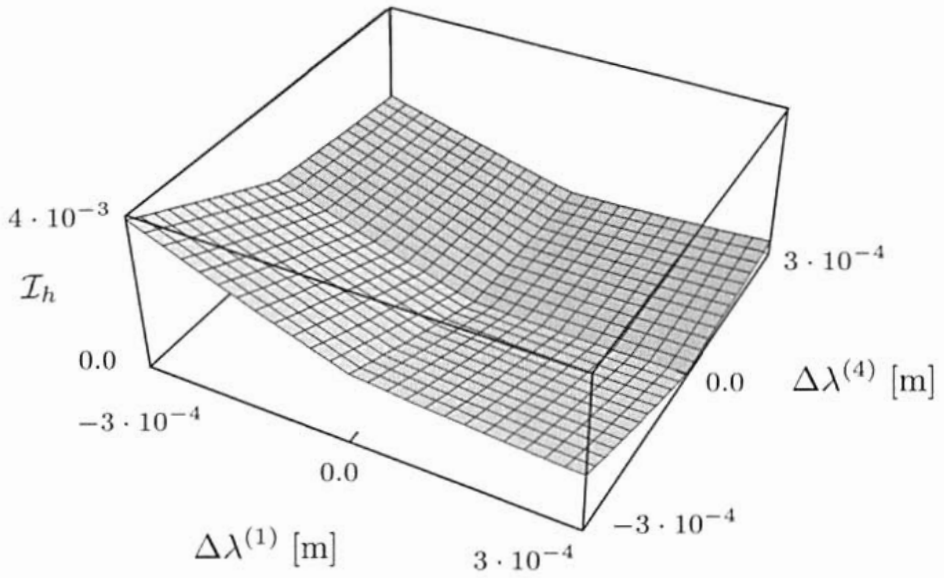

Figure 4.3: 3D plot of the potential $\mathcal{I}_h$ as a function of $\Delta\lambda^{(1)}$ and $\Delta\lambda^{(4)}$

The same function is given as a 2D contour plot in Figure 4.4. NEWTON iterative procedure renders a converged set of two actually active singular surfaces. The resulting values of LAGRANGE multipliers $(\Delta\lambda^{(1)}, \Delta\lambda^{(4)}) = (1.0386994 \cdot 10^{-5}, 1.0386994 \cdot 10^{-5})$ are depicted in Figure 4.4 by point 1. The set of LAGRANGE multipliers $(\Delta\lambda^{(1)}, \Delta\lambda^{(4)} = 2.15982 \cdot 10^{-5}, 0)$ which minimises the potential $\mathcal{I}_h$ is depicted as point 2 in the same figure. The discrepancy of the results can be explained after a closer look at the function $\mathcal{I}_h$. If the parameter $\Delta\lambda^{(4)}$ is taken to be a linear function of the parameter $\Delta\lambda^{(1)}$ for the sake of graphical description, the result for the potential $\mathcal{I}_h(\Delta\lambda^{(1)})$ is given in the diagram a) in Figure 4.5. The diagram shows a function with two extrema, a local maximum in point 1 and a global minimum in point 2. This leads to the conclusion that the converged state of the local iteration in the corrector step in the MLSA numerical analysis corresponds to the local extremum of the potential $\mathcal{I}_h$, whereas the optimisation algorithm succeeds in finding a globally minimising set $(\Delta\lambda^{(1)}, \Delta\lambda^{(4)})$ and excludes the singular surface (4) from the trial set of active singular surfaces $\mathbb{J}_{\text{act}}^{\text{tr}}$, leading to the set $\mathbb{J}_{\text{act}}$ with a single surface singularity in direction (1). If this updated set of active surfaces is given as the trial state to the optimisation algorithm and

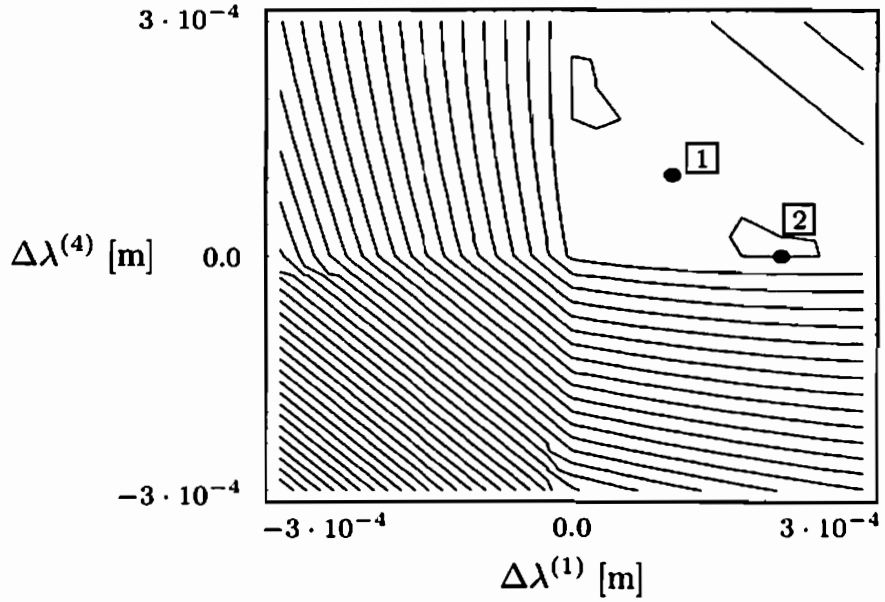

Figure 4.4: 2D contour plot of the potential $\mathcal{I}_h$ as a function of $\Delta\lambda^{(1)}$ and $\Delta\lambda^{(4)}$

the corrector step of MLSA, the integral $\mathcal{I}_h(\Delta\lambda^{(1)})$ becomes a function of one variable with a single global minimum at $\Delta\lambda^{(1)} = 2.15982 \cdot 10^{-5}$, recognised by both the MLSA and the optimisation algorithm.
Similar comparative analysis is then performed on an element belonging to a spatial discretization in an actual numerical simulation, in order to analyse the influence of the material parameter H characterising the softening response on the smoothness of the function $\mathcal{I}_h$. An uniaxial compression test on a simple cuboid structure is simulated using two different softening parameters. The geometry of the finite element discretization with 42 elements, as well as the material parameters are given in Figure 4.6. The element chosen for the comparative analysis is the darkened element in Figure 4.6.
The displacement field corresponding to the downward displacement of the top of $1.8 \cdot 10^{-2}$ m, the material parameters and the trial state with a single potentially active singular surface are the input for the evaluation of the integral $\mathcal{I}_h$ and for the optimisation algorithm. The resulting function $\mathcal{I}_h(\Delta\lambda^{(1)})$, the output of the MLSA corrector step (point 1) and the optimisation procedure (point 2) are depicted in the diagram *a*) in Figure 4.7 for the softening parameter $H_1 = 0.001$ m and in the diagram *b*) for the softening parameter $H_2 = 0.05$ m.
The analysis of the diagram *b*) shows that both numerical procedures deliver the same output $(\Delta\lambda^{(1)}, \mathcal{I}_h(\Delta\lambda^{(1)})) = (2.1697 \cdot 10^{-6}, 0.0525)$ and lead to a unique correction of the trial step. Diagram *a*) displays once more a difference in the output values of two algorithms. The coordinates of point 1 are

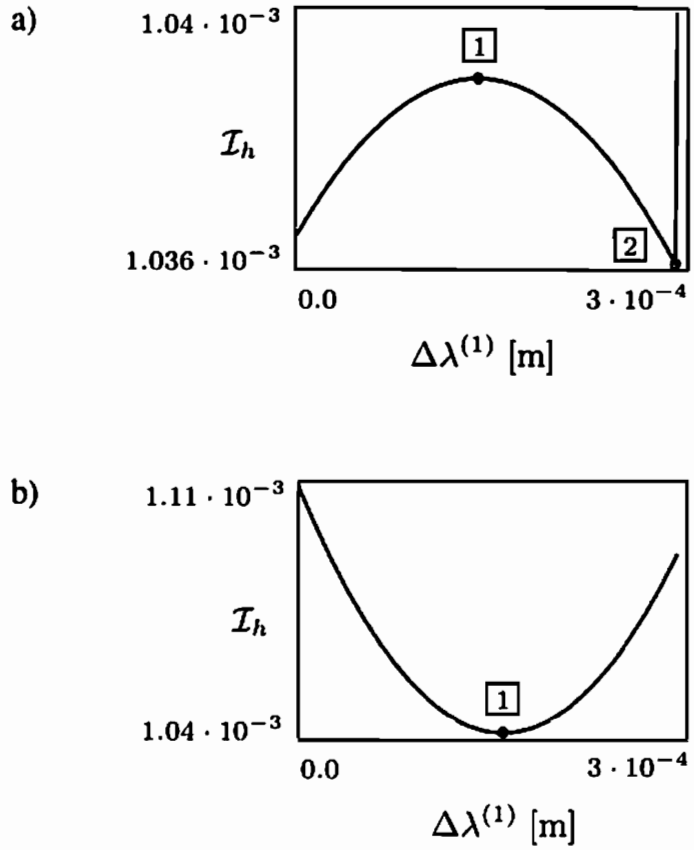

Figure 4.5: Potential $\mathcal{I}_h$ as a function of $\Delta\lambda^{(1)}$; one element shear test: a) return-mapping algorithm and b) minimisation procedure

$(\Delta\lambda^{(1)}, \mathcal{I}_h(\Delta\lambda^{(1)})) = (-2.693 \cdot 10^{-6}, 0.05278)$. Its position defines a local extremum of the function $\mathcal{I}_h$. $(\Delta\lambda^{(1)}, \mathcal{I}_h(\Delta\lambda^{(1)})) = (1.2865946 \cdot 10^{-3}, 0.0484)$ are the coordinates of point 2. Its position defines the global minimum of the function $\mathcal{I}_h$. Based on the algorithm for the update of the trial set of active surfaces $\mathbb{J}_{\text{act}}^{\text{tr}}$ presented in Section 4.3.3, the negative converged value of the consistency parameter signals the reduction of n_{act} by one and the update of the $\mathbb{J}_{\text{act}}^{\text{tr}}$. However, in this particular case, the reduction of n_{act} by one leads to $n_{\text{act}} = 0$. This is a non-physical solution, since the offset of an inelastic corrector step by the predictor step guaranties that a minimum of one singular surface actually evolves. This leads to the conclusion that the local corrector step of the MLSA results in a non-physical solution if it converges to the local instead of the global extremum of the characteristic potential function $\mathcal{I}_h$.
The difference in the smoothness of the target function stemming from the variance of the softening parameter H leads to a reasoned judgement that the definition of this specific material parameter can strongly influence the performance of the numerical procedure through the convergence rate of the applied iterative procedure. Since the material parameter H is a constant which, ac-

cording to the fracture energy concept (see [MOSLER, J. & MESCHKE G. 2004; MOSLER 2002] for details) depends on the total dissipated energy, fracture energy, characteristic length and material strength, it is to be evaluated and kept constant throughout the simulation. In order to prevent the kind of numerical instability presented above, an alternative form of the inelastic corrector step can be used.

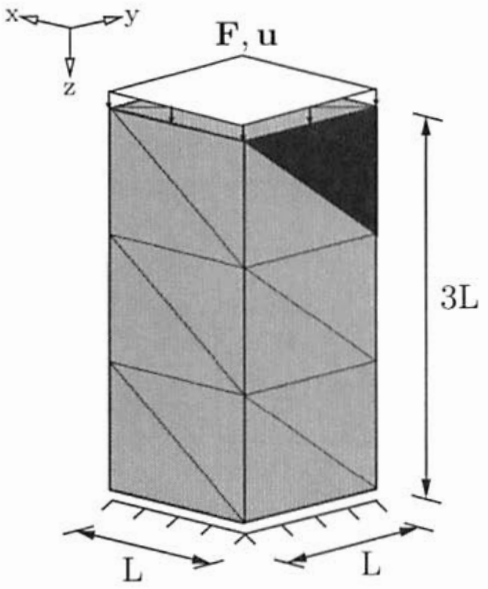

L	=	3.0	[m]
E	=	$2.0 \cdot 10^4$	[kN/m^2]
ν	=	0.45	
f_{tu}	=	20	[kN/m^2]
H_1	=	0.001	[m]
H_2	=	0.05	[m]

Figure 4.6: Numerical model of uniaxial compression test: setup

The correction of the trial step is numerically achieved by implementing the return-mapping algorithm based on the backward-EULER integration of the evolution equations, presented in Section 4.3.2. To rule out an eventual existence of negative converged consistency parameter in the case of single surface failure, the consistency parameters $\Delta\lambda^{(\beta)}_{n+1} := \lambda^{(\beta)}_{n+1}\,(t_{n+1} - t_n)$ are defined as a square

$$\Delta\lambda^{(\beta)}_{n+1} = \left(a^{(\beta)}_{n+1}\right)^2 . \tag{4.67}$$

The jump deformation tensor $\boldsymbol{\epsilon}^{\mathrm{p}}$ and each of the internal displacement-like variables $\alpha^{(\beta)}$, $\beta = 1, \ldots, n_s$ at time t_{n+1} are in this case evaluated as

$$\boldsymbol{\epsilon}^{\mathrm{p}}{}_{n+1} = \boldsymbol{\epsilon}^{\mathrm{p}}{}_{n} + \sum_{\beta=1}^{n_s} \left(a^{(\beta)}_{n+1}\right)^2 \partial_{\bar{\mathbf{T}}^{(\beta)}} \phi^{(\beta)}|_{n+1} \otimes \mathrm{Grad}\, \varphi^{(\beta)} , \tag{4.68}$$

$$\boldsymbol{\alpha}^{(\beta)}_{n+1} = \boldsymbol{\alpha}^{(\beta)}_{n} + \left(a^{(\beta)}_{n+1}\right)^2 \partial_{\mathbf{q}^{(\beta)}} \phi^{(\beta)}|_{n+1} . \tag{4.69}$$

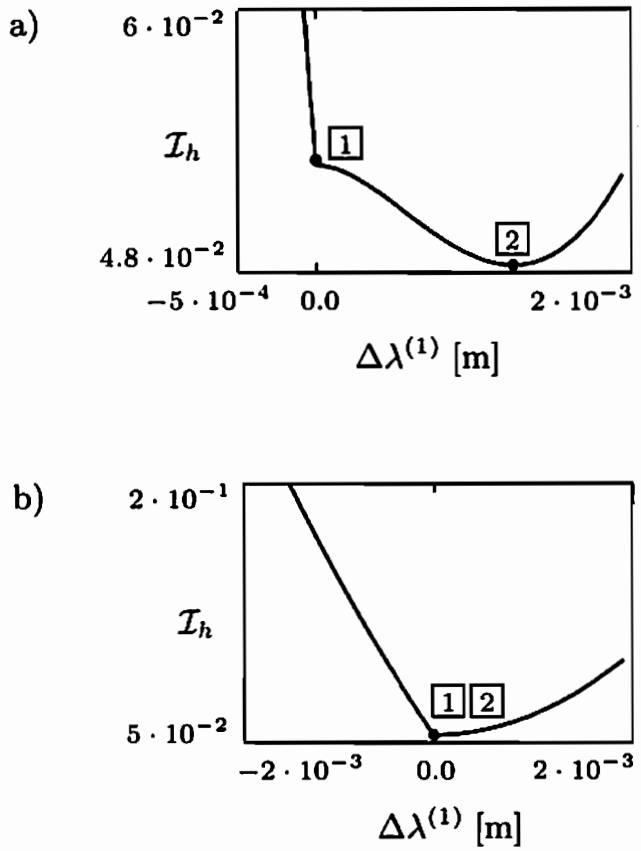

Figure 4.7: Potential $\mathcal{I}_h$ as a function of $\Delta\lambda^{(1)}$; uniaxial compression test: a) $H_1 = 0.001\,\mathrm{m}$ and b) $H_2 = 0.05\,\mathrm{m}$

The resulting linearization of the residual $\mathbf{dR}$ in the matrix notation is given by

$$\mathbf{dR} = \mathbf{A}^{-1} \cdot \boldsymbol{\Delta} + 2\nabla\mathbf{M} \cdot \mathbf{A}^{q} \cdot \mathbf{da}_{n+1}^{(k)}, \quad \mathbf{d}\phi = \nabla\phi^{\mathrm{T}} \cdot \boldsymbol{\Delta} \tag{4.70}$$

with the notations given in (4.31), (4.32), (4.33) and

$$\mathbf{A}^{q} := \left[\begin{array}{ccc} a^{(1)} & & \\ & \cdots & \\ & & a^{(n_{\mathrm{act}})} \end{array} \right] \Bigg|_{n+1}^{(k)} . \tag{4.71}$$

The update of the LAGRANGE multiplier is defined as

$$\mathbf{da}_{n+1}^{(k)} := \left[\begin{array}{c} \mathrm{d}a^{(1)} \\ \cdots \\ \mathrm{d}a^{(n_{\mathrm{act}})} \end{array} \right] \Bigg|_{n+1}^{(k)} , \tag{4.72}$$

and it is computed from the linearized form of the set of equations (4.70)

$$\mathbf{R} + \mathbf{A}^{-1} \cdot \boldsymbol{\Delta} + 2\nabla\mathbf{M} \cdot \mathbf{A}^{q} \cdot \mathbf{da}_{n+1}^{(k)} = \mathbf{0}, \quad \phi + \nabla\phi^{\mathrm{T}} \cdot \boldsymbol{\Delta} = 0 \tag{4.73}$$

as

$$\mathbf{da}_{n+1}^{(k)} = \left. \frac{\phi - \nabla\phi^{\mathrm{T}} \cdot \mathbf{A} \cdot \mathbf{R}}{2\nabla\phi^{\mathrm{T}} \cdot \mathbf{A} \cdot \nabla\mathbf{M} \cdot \mathbf{A}^{q}} \right|_{n+1}^{(k)} . \tag{4.74}$$

The update of the state variables $\boldsymbol{\Delta}_a$ is calculated from $(4.73)_1$

$$\boldsymbol{\Delta}_a = -\mathbf{D}^J \cdot \mathbf{A} \cdot (\mathbf{R} + 2\nabla\mathbf{M} \cdot \mathbf{A}^q \cdot \mathbf{da}) \Big|_{n+1}^{(k)} . \tag{4.75}$$

Tensors $\mathbf{D}^J$ and $\boldsymbol{\Delta}_a$ are given in (4.38), and (4.39) gives the final form of the update of the state variables.

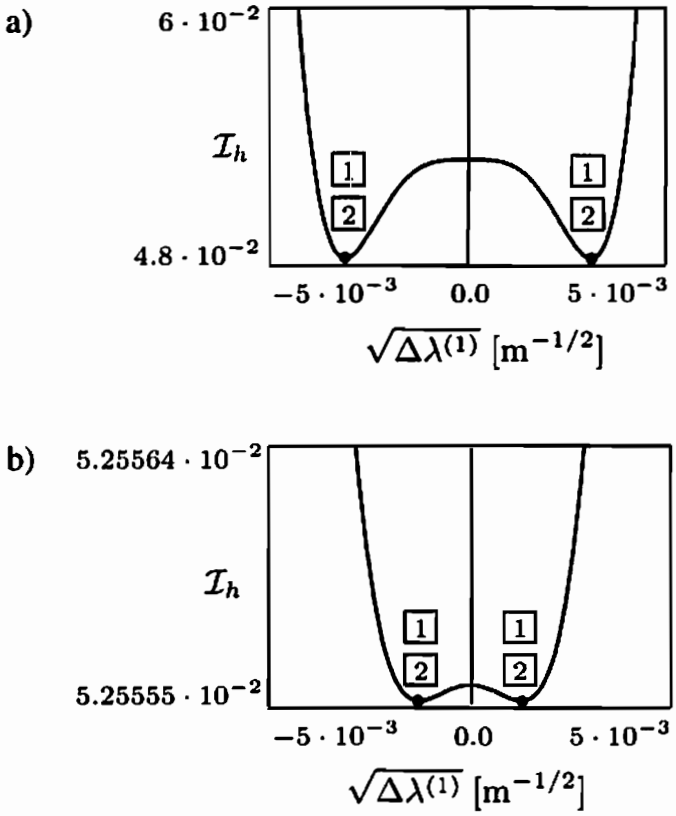

Figure 4.8: Potential $\mathcal{I}_h$ as a function of $\sqrt{\Delta\lambda^{(1)}}$; uniaxial compression test: a) $H_1 = 0.001$ m and b) $H_2 = 0.05$ m

Implementation of this alternative version of the inelastic corrector step prevents the appearance of negative values of the consistency parameters $\lambda^{(\beta)}$, $\beta = 1, \ldots, n_{\mathrm{act}}$. This fact influences the process of determination of the active singular surfaces given in Section 4.3.3 in such way that the inactive surface is now signalled by $\Delta\lambda_{n+1}^{(\beta)} = \left(a_{n+1}^{(\beta)}\right)^2 = 0$. These surfaces are recognised and singled out after the iterative procedure has converged to zero, and the trial

set of active surfaces is updated if necessary.
The example presented in Figures 4.6 and 4.7 can be used to show how this kind of intervention reflects on the numerical instabilities mentioned before. The same numerical simulation is performed once more with the quadratic formulation of the consistency parameters. The result is given in Figure 4.8 for both values of softening parameters. Both diagrams show that the quadratic formulation of the parameters $\Delta\lambda^{(\beta)}$ neutralises the original discrepancy between two numerical procedures. For the softening parameter $H_1 = 0.001\,\mathrm{m}$ both algorithms deliver the same output $(a^{(1)}, \mathcal{I}_h(a^{(1)})) = (0.035869, 0.0484)$ and lead to a unique correction of the trial step. The same conclusion can be made for the softening parameter $H_2 = 0.05\,\mathrm{m}$, where the minimising couple of variables has the values $(a^{(1)}, \mathcal{I}_h(a^{(1)})) = (0.0015178, 0.0525)$. Both sets of results define the global minimum of the function $\mathcal{I}_h$.
If the diagrams *a*) or *b*) in Figures 4.7 and 4.8 are compared to each other, the influence of the quadratic definition of $\Delta\lambda^{(\beta)}$ on the shape of the target function $\mathcal{I}_h$ in the region of interest can easily be recognised. By using the root of $\Delta\lambda^{(\beta)}$, the function $\mathcal{I}_h$ becomes a symmetric function with respect to the $\mathcal{I}_h$-axis. The difference in the smoothness of the function $\mathcal{I}_h$ after the variation of the softening parameter H remains.
If the interventions presented in the last two sections of this chapter, namely the explicit formulation and the quadratic procedure for the inelastic corrector step, are incorporated in the original algorithm of MLSA, possible numerical instabilities can be identified and regulated inside the framework of MLSA, without any major changes in the algorithm.

4.5 Principal unknowns driving the localisation process

The choice of independent variables for the linearization procedure in the present work is the set $(\bar{\mathbf{T}}, \mathbf{q}, \Delta\lambda)$. For this set of variables, the continuity condition $(3.55)_2$ is solved (for fixed $\hat{\mathbf{u}}$) when inelastic loading is signalled by the elastic predictor step. The appropriate algorithm is given in Section 3.3.4 for the single surface SDA and in Section 4.3.2 for MLSA. In both cases, the solution is driven by the set of unknowns $(\boldsymbol{\epsilon}^{\mathrm{P}}, \mathbf{q}, \Delta\lambda)$ (see relations (3.80) and (4.32)). However, other choices of principal unknowns for the return-mapping algorithm are also possible. [MOSLER 2006] chooses the set $(\bar{\mathbf{T}}, \mathbf{q}, \Delta\lambda)$. Another possible choice is the set $(\boldsymbol{\Sigma}, \mathbf{q}, \Delta\lambda)$, where $\boldsymbol{\Sigma}$ denotes the MANDEL stress tensor. In order to advocate the choice made in this work, the differences between two local inelastic corrector steps in MLSA based on sets of unknowns $(\boldsymbol{\epsilon}^{\mathrm{P}}, \mathbf{q}, \Delta\lambda)$ and $(\boldsymbol{\Sigma}, \mathbf{q}, \Delta\lambda)$ will be briefly presented. The resulting alteration of the global localisation procedure is then relatively straightforward and will not be presented here.
The alternative choice $(\boldsymbol{\Sigma}, \mathbf{q}, \Delta\lambda)$ of the driving set of unknowns in the return-

mapping algorithm influences the linearization of the residual $\mathbf{R}$ given in (4.22)

$$\begin{aligned} \mathrm{d}R_{ij}^{\epsilon^{\mathrm{p}}} &= -\mathrm{d}\epsilon_{ij}^{\mathrm{p}} + \sum_{\beta=1}^{n_{\mathrm{act}}} \mathrm{d}\Delta\lambda^{(\beta)}\, \partial_{\bar{\mathbf{T}}^{(\beta)}}\, \phi_i^{(\beta)}\, \mathrm{Grad}\, \varphi_j^{(\beta)} \\ &\quad + \sum_{\beta=1}^{n_{\mathrm{act}}} \Delta\lambda^{(\beta)}\, \partial_{\bar{\mathbf{T}}^{(\beta)} \otimes \bar{\mathbf{T}}^{(\beta)}}\, \phi_{ik}^{(\beta)}\, \mathrm{d}T_k^{(\beta)}\, \mathrm{Grad}\, \varphi_j^{(\beta)} \\ &= \mathbb{T}_{ijlp}^{\Sigma}\, \mathrm{d}\Sigma_{lp}^{\mathrm{p}} + \sum_{\beta=1}^{n_{\mathrm{act}}} \mathrm{d}\Delta\lambda^{(\beta)}\, G_{ij}^{t(\beta)} \,. \end{aligned} \tag{4.76}$$

Tensor $\mathbf{G}^{t(\beta)}$ is given in (4.23) and

$$\mathbb{T}_{ijlp}^{\Sigma} = \mathbb{G}_{ijlp}^{C} + \mathbb{G}_{ijlp}^{M} \,. \tag{4.77}$$

Fourth order $\mathbb{G}^C$ can be found in (4.24) and the fourth order tensor $\mathbb{G}^M$ is derived in Section 3.3.7. The linearization (4.28) of the yield functions $\phi^{(\beta)}\,(\bar{\mathbf{T}}^{(\beta)}, \mathbf{q}^{(\beta)})\,, \beta = 1, \ldots, n_{\mathrm{act}}$ now has the form

$$\begin{aligned} \mathrm{d}\phi^{(\beta)} &= \partial_{\bar{\mathbf{T}}^{(\beta)}}\, \phi_i^{(\beta)}\, \mathrm{d}T_i^{(\beta)} + \partial_{\mathbf{q}^{(\beta)}}\, \phi_i^{(\beta)}\, \mathrm{d}q_i^{(\beta)} \\ &= F_{lp}^{\Sigma(\beta)}\, \mathrm{d}\Sigma_{lp}^{\mathrm{p}} + \partial_{\mathbf{q}^{(\beta)}}\, \phi_i^{(\beta)}\, \mathrm{d}q_i^{(\beta)} \,, \end{aligned} \tag{4.78}$$

where

$$F_{lp}^{\Sigma(\beta)} = \partial_{\bar{\mathbf{T}}^{(\beta)}}\, \phi_l^{(\beta)}\, N_p^{(\beta)} \,, \quad F_{ij}^{\Sigma(\beta)} = f_{(i-1)*3+j}^{\Sigma(\beta)} \,. \tag{4.79}$$

In the resulting set of equations (4.30), the operator $\mathbf{A}^{-1}$, the vector of state variables $\boldsymbol{\Delta}$ and $\boldsymbol{\nabla}\boldsymbol{\phi}^{\mathrm{T}}$ have the form:

$$\mathbf{A}^{-1} := \left[\begin{array}{ccc} \mathbf{T}^{\Sigma} & & \mathbf{0} \\ & \mathbf{D}^{(1)-1} & \\ \mathbf{0} & & \cdots \\ & & \mathbf{D}^{(n_{\mathrm{act}})-1} \end{array} \right] \Bigg|_{n+1}^{(k)} \,, \quad \boldsymbol{\Delta} := \left[\begin{array}{c} \mathrm{d}\Sigma^{v} \\ \mathrm{d}\mathbf{q}^{(1)} \\ \cdots \\ \mathrm{d}\mathbf{q}^{(n_{\mathrm{act}})} \end{array} \right] \Bigg|_{n+1}^{(k)} \,, \tag{4.80}$$

$$\boldsymbol{\nabla}\boldsymbol{\phi}^{\mathrm{T}} := \left[\begin{array}{ccc} \mathbf{f}^{\Sigma(1)}\,; & \partial_{\mathbf{q}^{(1)}}\, \phi^{(1)} & \\ & \cdots & \\ \mathbf{f}^{\Sigma(n_{\mathrm{act}})}\,; & & \partial_{\mathbf{q}^{(1)}}\, \phi^{(n_{\mathrm{act}})} \end{array} \right] \Bigg|_{n+1}^{(k)} \,. \tag{4.81}$$

Here, tensor to vector transformation $\Sigma_{ij} = \Sigma_{(i-1)*3+j}^{v}$ is utilised for the MANDEL stress tensor $\boldsymbol{\Sigma}$. The update of the LAGRANGE multiplier $\mathbf{d}\boldsymbol{\Delta}\boldsymbol{\lambda}_{n+1}^{(k)}$ is computed from (4.36) and the update of the state variables $\boldsymbol{\Delta}_{\alpha}$ is calculated from

(4.38). Together with already defined and unchanged procedures for the elastic unloading and the predictor step, this alterations of the original inelastic corrector step and corresponding changes in the global linearization procedure lead to the solution of $(n+1)$-st loading step $\hat{\mathbf{u}}_{n+1}$ and the standard finite element procedure can be applied.
This form of MLSA is then tested in numerical simulations of the behaviour of a soft rock already damaged by some unknown loading history in a triaxial compression test. Different unstructured spatial discretization with constant-strain tetrahedral elements are utilised in the simulation of the experimental setup (see Section 5.1). An evaluation of the numerical results shows that an abrupt stop in the iterative procedure occurs due to the loss of convergence. A thorough investigation of possible causes for this kind of behaviour of the numerical scheme, lead to the following conclusion. In the specific case of multisurface preexisting micro-cracks, the loss of convergence in the local iteration of the numerical procedure based on the unknowns $(\boldsymbol{\Sigma}, \mathbf{q}, \Delta\lambda)$ can be attributed to the singularity of the tangent operator $\mathbf{A}$ in some elements of the mesh. By studying the structure of this tangent, the singularity can be directed to the moduli $\mathbb{G}^M$ (Section 3.3.7) connecting the jump deformation tensor $\boldsymbol{\epsilon}^{\mathrm{P}}$ to the MANDEL stress tensor $\boldsymbol{\Sigma}$ for a fixed conforming displacement field $\hat{\mathbf{u}}$. One possible solution in pursuit of regularity is to use the symmetry of the MANDEL stress tensor $\boldsymbol{\Sigma}$ and the right CAUCHY-GREEN tensor $\bar{\mathbf{C}}$ and reduce the order of the tangent operator $\mathbf{A}$. However, due to non-symmetry of the jump deformation tensor $\boldsymbol{\epsilon}^{\mathrm{P}}$ and the fact that the inverse of the linearization (3.127) of the right CAUCHY-GREEN tensor $\bar{\mathbf{C}}$ with respect to the deformation gradient $\bar{\mathbf{F}}$

$$\mathrm{d}\bar{F}_{qr} = \mathbb{T}^{-1}_{qrmn}\, \mathrm{d}\bar{C}_{mn} \tag{4.82}$$

cannot be calculated directly (only through pseudoinverse), this solution strategy is not suitable for this specific problem. In order to avoid loss of information due to the symmetry of the MANDEL stress tensor, the set of principal unknowns is defined as $(\boldsymbol{\epsilon}^{\mathrm{P}}, \mathbf{q}, \Delta\lambda)$.

5 Numerical examples

In this chapter, a finite element formulation presented in Chapters 3 and 4 is tested on different three-dimensional simulations of the often used benchmark problems in the numerical analysis of the localised material failure at finite strains, namely the uniaxial tension or compression test (see [ARMERO & GARIKIPATI 1996; GARIKIPATI 1996; LARSSON, STEINMANN & RUNESSON 1998; BORJA 2002; MOSLER 2006; FEIST & HOFSTETTER 2007]), and the L-shaped panel (see [LACKNER 1999; HUEMER 1998; MENRATH 1999; MOSLER, J. & MESCHKE G. 2004; JÄGER, STEINMANN & KUHL 2008]). Despite the fact that numerous contributions to SDA have been presented over the years, three-dimensional implementations and their applications are relatively rare [MOSLER 2002; CHAVEZ 2003; FEIST & HOFSTETTER 2007; SANCHO, PLANAS, FATHY, GALVEZ & CENDOŃ 2007].
The uniaxial tension test presented in Section 5.2 is used as a test example for the comparison of the implicit and the explicit Multiple Localisation Surface Approach methods defined in Chapter 4, as well as for the thorough investigation of the basic numerical properties of the MLSA, such as the convergence behaviour and the spatial discretization sensitivity. The numerical analysis of the failure of a L-shaped panel in Section 5.3 includes the comparative analysis of implicit to explicit MLSA formulation, as well as the results of three different simulations in terms of load-displacement diagrams, softening response and overall deformation of the numerical models.
The numerical example presented in Section 5.1 is the evaluation of the ultimate loading based on the standard triaxial compression test of a soft rock sample, which is a benchmark for the numerical analysis of the material behaviour in geomaterials (see e.g. [BORJA, REGUEIRO & LAI 2000] for the results of a two-dimensional simulation based on the SDA kinematics in the infinitesimal regime).

5.1 Triaxial compression test of a soft rock sample

In order to present the applicability and the performance of the numerical method presented in Chapter 4, namely the multiple surface SDA, the numerical algorithm is now used to simulate the behaviour of a soft rock already damaged by some unknown loading history in a triaxial compression test. The initial damage in the material is understood in the sense of pre-existing micro-cracks. In order to simulate the initial state of the material, the compressive strength f_{tu} is element-wise stochastically distributed. The micro-cracks forming in the material can assume one of the four possible direction defined in Section 3.3.2. In this manner, an arbitrary pre-loading history of the examined material, which leads to a certain level of damage, can be accounted for. The intention of the numerical analysis presented in this section is to prove that, despite the connection of the localisation process to the geometry of the finite

element spatial discretization, the resulting macroscopic material response can be uniquely evaluated.
The dimensions and the material parameters of the numerical model are given in Figure 5.1.

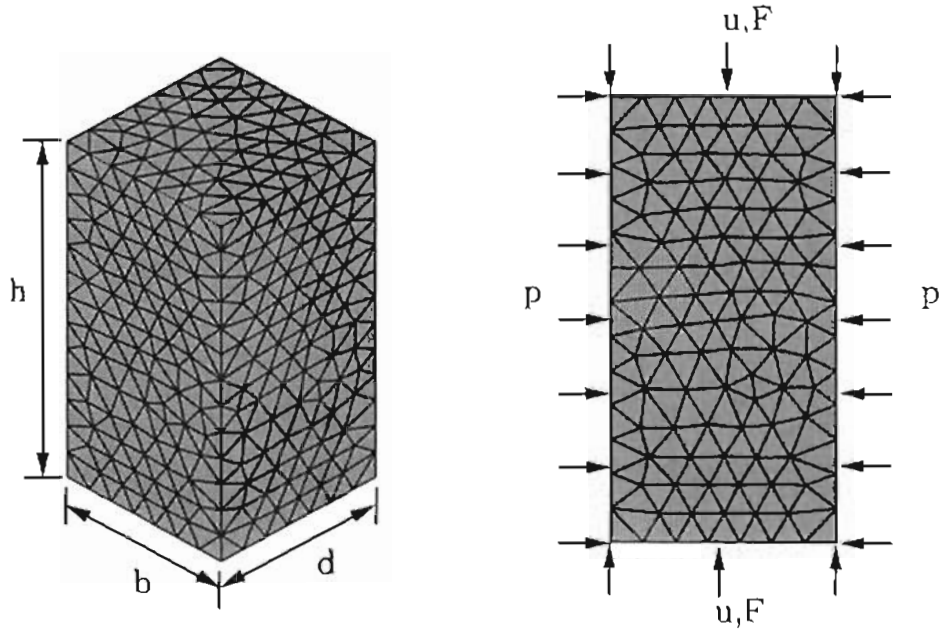

b	=	4	[cm]
d	=	4	[cm]
h	=	8	[cm]
p	=	1	[kN/cm^2]
E	=	1500	[kN/cm^2]
ν	=	0.31	
f_{tu}	=	4.0 – 6.0	[kN/cm^2]
H	=	0.3	[cm]

Figure 5.1: Numerical model of a triaxial compression test: setup

In accordance with Section 3.2.1, a hyperelastic neo-HOOKE-type model is adopted for the material in $\Omega^{\pm}$. The inelastic material behaviour at each of the localization surfaces $\partial_s\Omega^{(\beta)}$ is modelled using a VON MISES type yield function

$$\phi(\bar{\mathbf{T}}^{(\beta)}, q^{(\beta)}) = \|(\bar{\mathbf{T}})_m^{(\beta)}\|_2 - q^{(\beta)}(\alpha^{(\beta)}) \tag{5.1}$$

with

$$(\bar{\mathbf{T}})_m^{(\beta)} := \bar{\mathbf{T}}^{(\beta)} - (\bar{\mathbf{T}}^{(\beta)} \cdot \mathbf{N})^{(\beta)}\, \mathbf{N}^{(\beta)}\,. \tag{5.2}$$

The softening response, characterised by the internal variable $q^{(\beta)}$ has the

exponential evolution of the type

$$q^{(\beta)}(\alpha^{(\beta)}) = f_{\mathrm{tu}} \cdot \exp\left(-\frac{\alpha^{(\beta)}}{H}\right) \tag{5.3}$$

with the compressive material strength f_{tu} and the softening parameter H. The condition for the propagation of the discontinuity $\partial_{\mathrm{s}}\Omega^{(\beta)}$ is in accordance with Section 3.3.3 the positive value of the corresponding yield function, i.e. $\phi^{(\beta)}(\bar{\mathbf{T}}^{(\beta)}, q^{(\beta)}) > 0 \ \wedge \ \phi^{(\beta)} = \max_{\beta^*} \phi^{(\beta^*)}$. This singularity condition yields the possibility of a multiple surface singularity inside each finite element although the single surface approach is utilised in each iteration step, both globally and locally.

In order to show the independence of the final result of the numerical simulation on the spatial discretization, two different unstructured discretizations, *mesh I* with 3588 and *mesh II* with 5884 constant-strain tetrahedral elements are considered for the determination of the maximum allowed load. Both models are displaced downward at the top boundary, at prescribed increments and up to the ultimate load. It should be pointed out that the element-wise stochastic distribution of the compressive strength renders two quantitatively different samples of the material with arbitrary distributions of pre-existing cracks.

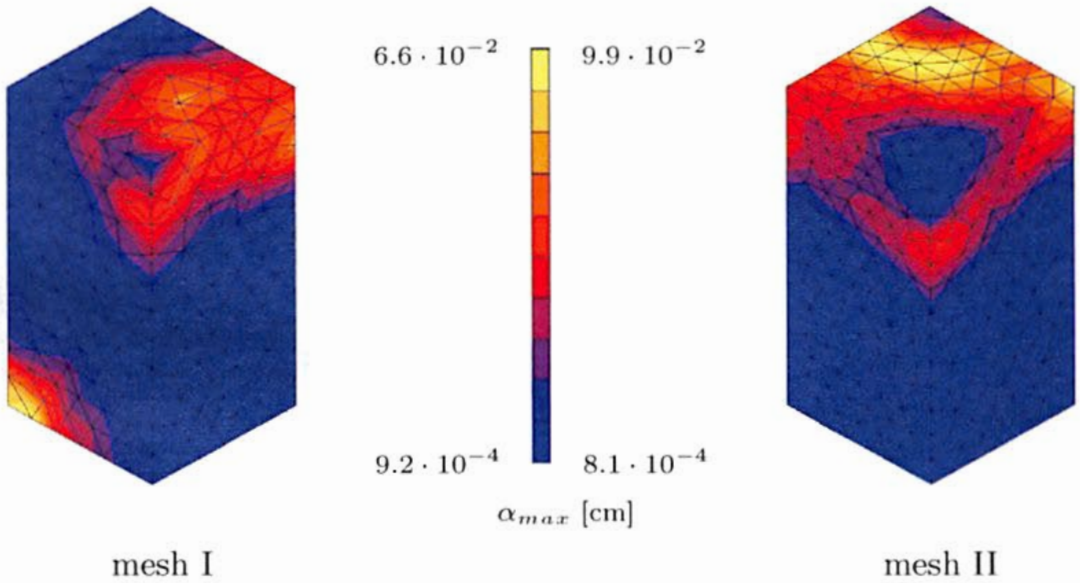

Figure 5.2: Distribution of the internal variable α_{max} for both meshes

The distribution of the internal variable α_{max}, which represents the maximum of the relative displacements in each of the four possible localisation directions, is given in Figure 5.2 for both meshes. The difference in the final distribution of singularities which can be observed in Figure 5.2 highlights the fact that

the initial states of two numerically modelled samples are not identical, based on the supposed pre-loading history of the localised material failure.

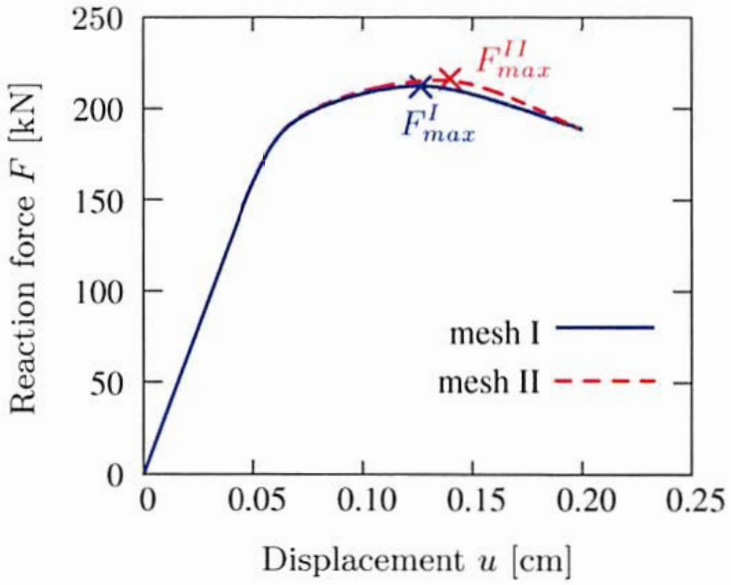

Figure 5.3: Load-displacement diagram for both meshes

The resulting load-displacement diagrams, showing the reaction force at the top F with respect to the vertical displacement at the top u, are displayed in Figure 5.3. The estimated ultimate load for mesh I is reached for the vertical displacement of the top $u = 0.12565\,\text{cm}$ and has the intensity $F^{I}_{max} = 211.77\,\text{kN}$. For the spatial discretization with the finite element mesh II, the ultimate load is evaluated at $F^{II}_{max} = 214.94\,\text{kN}$ for the vertical displacement of the top of $u = 0.1339\,\text{cm}$.
The difference between two spatial discretizations in the obtained average material response to the compressive load is then calculated to be 1.5%. Hence, the resulting ultimate compressive loading can be considered as uniquely determined and the overall mechanical response resulting from the numerical simulation based on the multiple surface SDA as independent of the considered discretization of the micro-scale.

5.2 Uniaxial tension test of a notched bar

This section includes a numerical analysis of the formation and the propagation of shear bands in a bar. The geometry and the material parameters are illustrated in Figure 5.4. The bar is clamped on its bottom boundary and subjected to a vertical displacement on its top boundary, at prescribed increments.
Based on the choice presented in Section 3.2.1, a hyperelastic neo-HOOKE-type model is adopted for the material in $\Omega^{\pm}$. In order to analyse slip band

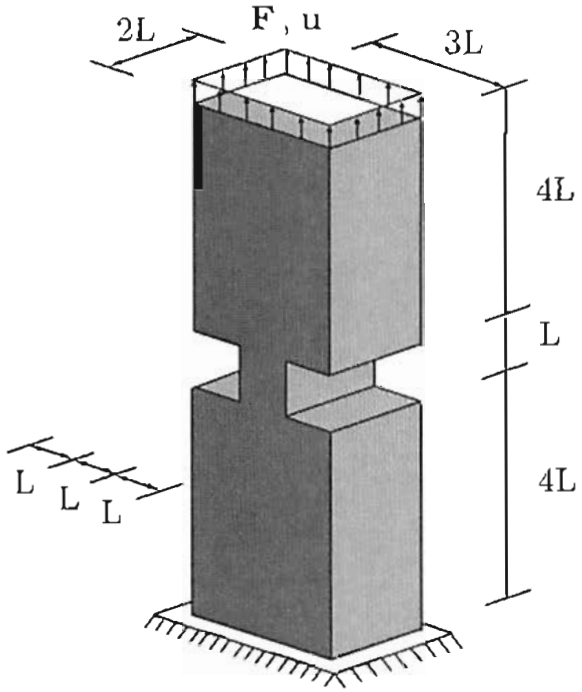

L	=	1	[m]
E	=	$1.0 \cdot 10^7$	[kN/m^2]
ν	=	0.2	
f_{tu}	=	1000	[kN/m^2]
H	=	0.001	[m]

Figure 5.4: Numerical model of an uniaxial tension test: setup

formation in the material, the numerical model presented in Chapter 4 is utilised. The inelastic material behaviour at each of the localisation surfaces $\partial_s\Omega^{(\beta)}$ is modelled using a VON MISES type yield function

$$\phi(\bar{\mathbf{T}}^{(\beta)}, q^{(\beta)}) = ||(\bar{\mathbf{T}})_m^{(\beta)}||_2 - q^{(\beta)}(\alpha^{(\beta)}) \tag{5.4}$$

with

$$(\bar{\mathbf{T}})_m^{(\beta)} := \bar{\mathbf{T}}^{(\beta)} - (\bar{\mathbf{T}}^{(\beta)} \cdot \mathbf{N})^{(\beta)}\, \mathbf{N}^{(\beta)}\,. \tag{5.5}$$

The softening response is characterised by the internal variable $q^{(\beta)}$ with an exponential evolution of the type

$$q^{(\beta)}(\alpha^{(\beta)}) = f_{tu} \cdot \exp\left(-\frac{\alpha^{(\beta)}}{H}\right) \tag{5.6}$$

with the material strength in tension f_{tu} and the softening parameter H. The condition for the propagation of the discontinuity $\partial_s\Omega^{(\beta)}$ is, in accordance with Section 3.3.3, the positive value of the corresponding yield function, i.e. $\phi^{(\beta)}(\bar{\mathbf{T}}^{(\beta)}, q^{(\beta)}) > 0$. This form of the singularity condition leads to a possible multiple surface singularity inside each finite element, treated both globally and locally by the MLSA as defined in Chapter 4.
The assessment of the mesh dependence of the final result of the numerical simulation is based on three different spatial discretizations, *mesh I* with 2400,

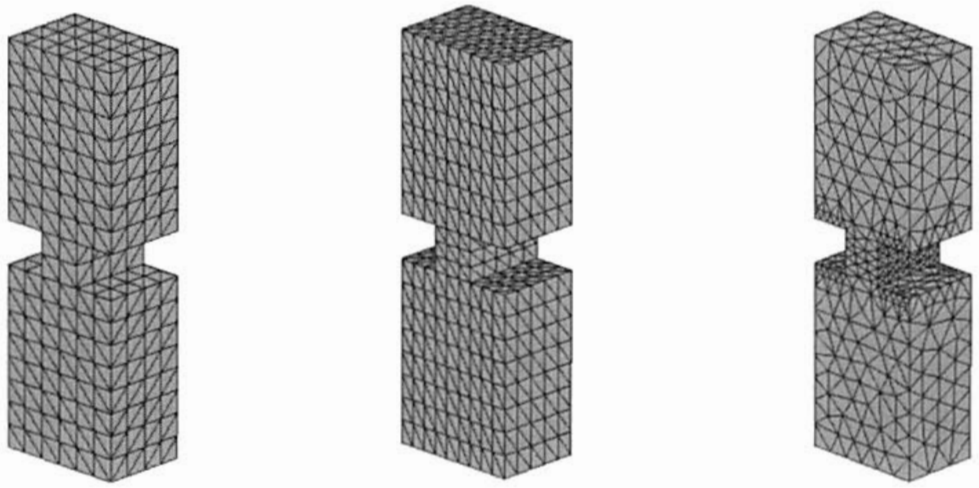

mesh I *mesh II* *mesh III*

Figure 5.5: Numerical study of the tension test: finite element discretizations

mesh II with 4590 and unstructured *mesh III* with 4541 constant-strain tetrahedral elements. Model *I* is also used to show that the difference between two formulations presented in Chapter 4, namely the implicit and the explicit formulation of the MLSA, is nearly vanishing. All finite element discretizations are illustrated in Figure 5.5.

A comparative analysis is performed in relation to the assumption utilised in Section 4.4 in order to set a starting point for the explicit formulation of MLSA. Namely, it is assumed that the implicit formulation of the regular part of the deformation gradient (4.2) and the explicit formulation (4.52) lead to nearly the same result in the case of a slip-plane type of localisation even for the multisurface localisation failure. In order to show this similarity, both the implicit and the explicit numerical model are alternatively used in the simulation of an uniaxial tension test on the spatial discretization *mesh I*.

The actual multisurface material failure occurring in the model is illustrated by the converged value of the vector of internal variables $\alpha^{(\beta)}$, representing the relative displacements in each of the four possible localisation directions and corresponding to the upward displacement of the top of $2.0 \cdot 10^{-3}$ m, for an arbitrarily chosen element (25)

$$\left[\begin{array}{c} \alpha^{(1)} \\ \alpha^{(2)} \\ \alpha^{(3)} \\ \alpha^{(4)} \end{array} \right] \Bigg|_{25}^{(2.0 \cdot 10^{-3})} = \left[\begin{array}{c} 8.10415321 \cdot 10^{-4} \\ 1.77766857 \cdot 10^{-3} \\ 1.3925358 \cdot 10^{-3} \\ 0.0 \end{array} \right] . \tag{5.7}$$

Additionally, in order to prove the necessary asymptotic quadratic convergence of the local NEWTON iteration procedure in the case of multisurface singularities, the evolution of the EUCLIDEAN norm R_i^l of the residual vector $\mathbf{R}_\mathbf{i}^\mathbf{l}$, obtained by combining both parts of (4.18) is listed in Table 5.1 for the same global iteration step ($2.0 \cdot 10^{-3}$ m) and the same element (25).

Iteration i	Residual R_i
1	24.2425661
2	$5.48514838 \cdot 10^{-4}$
3	$1.31274192 \cdot 10^{-9}$

Table 5.1: Convergence profile of the local NEWTON-type iteration for the element 25; displacement increment of magnitude $\triangle u = 0.00005$ cm; EUCLIDEAN norm of the residual R_i^l; convergence tolerance $1 \cdot 10^{-8}$

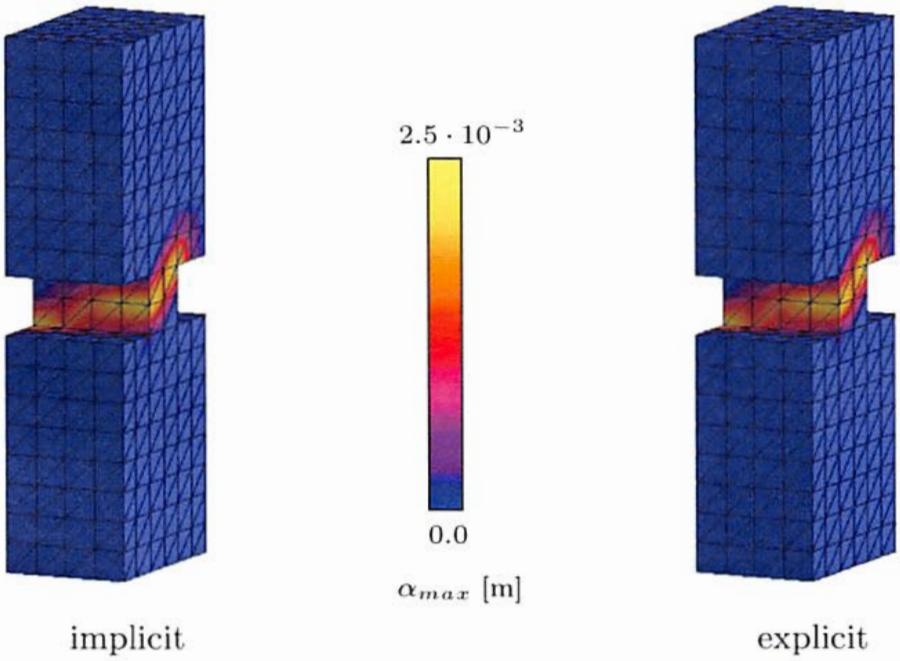

Figure 5.6: Distribution of the internal variable α_{max} for the *mesh I* using the implicit and the explicit formulation of MLSA

The distribution of the internal variable α_{max}, which represents the maximum of the relative displacements in each of the four possible localisation directions, is given in Figure 5.6 for both the implicit and the explicit numerical

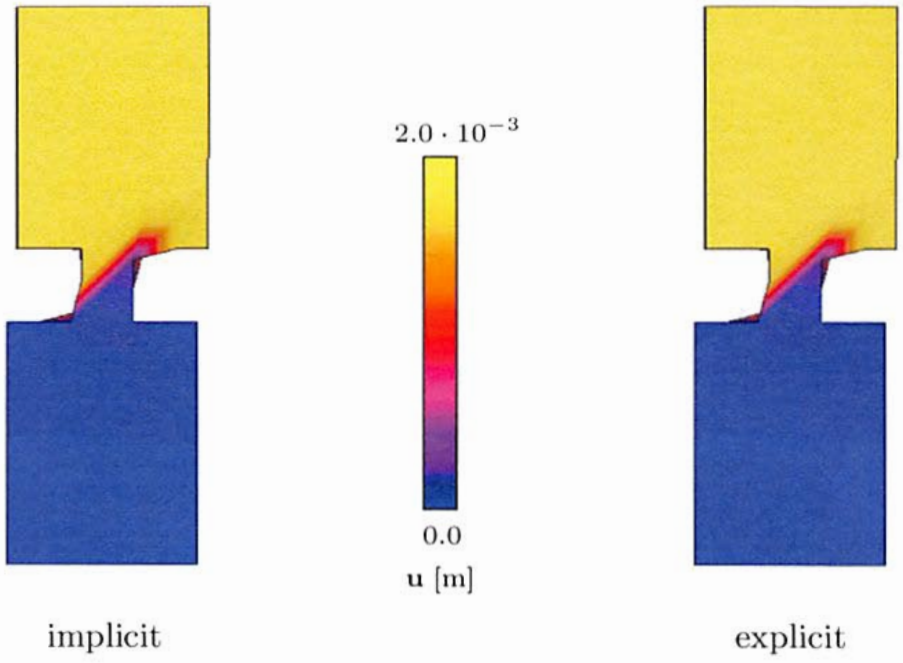

Figure 5.7: Deformed shape (magnification factor 100) and the scalar plot of the total displacement for the *mesh I* using the implicit and the explicit formulation of MLSA

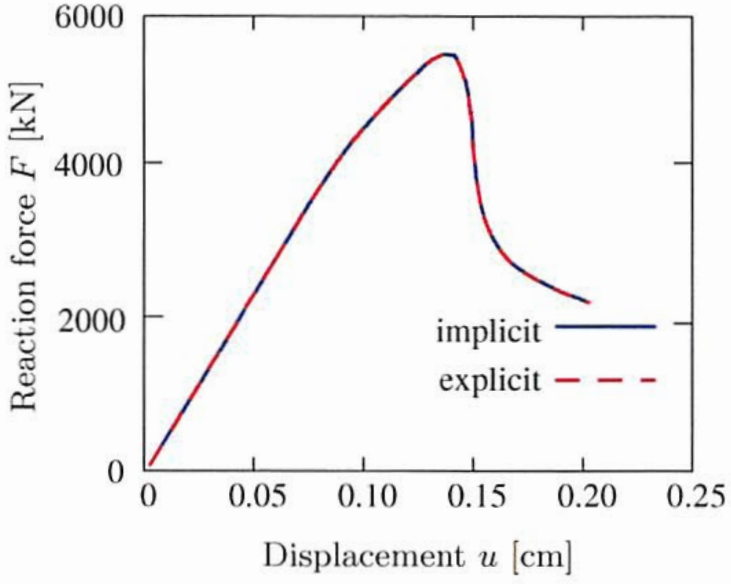

Figure 5.8: Load-displacement diagram for the *mesh I* using the implicit and the explicit formulation of MLSA

procedure at the upward displacement of the top of $2.0 \cdot 10^{-3}$ m. The resulting load-displacement diagrams, showing the reaction force at the top F with respect to the vertical displacement at the top u, are displayed in Figure 5.8. The deformed shape of the geometry (magnification factor 100) and the scalar plot of the total displacement of the finite element discretization are given in Figure 5.7. Comparison of the results illustrated in those three figures shows that both procedures deliver an identical softening response and it leads to the conclusion that the implicit and the explicit definition of the MLSA can be assumed equivalent in the case of a slip-plane type of multisurface localised failure.
The evaluation of the mesh dependency of the MLSA method is performed via explicit MLSA. It is based on two basic criteria. The first criterion is the number of elements in the finite element discretization of the given geometry for two similarly structured meshes (*mesh I* and *mesh II*). If the resulting distributions of the internal variable α_{max} given in Figure 5.9 are compared, a qualitative agreement between two discretizations may be stated. In order to make this statement stronger, the resulting deformed shapes and the total displacement illustrated in Figure 5.10 are compared to each other. Both spatial discretizations lead to the expected mode-II failure, resulting in formation of shear bands with normal vectors oriented at approximately 45° to the direction of maximum principal stress, analogous to the analytical solution.
The second criterion is the level of structuralization of the mesh (*mesh II* and *mesh III*). The resulting distributions of the internal variable α_{max} for the structured *mesh II* and for the unstructured *mesh III* are given in Figure 5.11 and the deformed shape and the total displacement plot in Figure 5.12. Based on these two figures, it could be concluded that both discretizations predict a mode-II failure with shear bands oriented approximately at 45° to the direction of maximum principal stress. The resulting shear band in the unstructured mesh is slightly less articulated than the perfectly formed shear band in the structured mesh. However, two meshes can be assumed equivalent in regard to the qualitative evaluation of the material softening by multisurface localised failure.

Additional information about the independence of the results of the numerical simulation by means of MLSA from the finite element discretization can be obtained from the resulting load-displacement diagrams for meshes *I*, *II* and *III*, showing the reaction force at the top F with respect to the vertical displacement at the top u, which are given in Figure 5.13. The estimated ultimate load for the mesh I is reached for the vertical displacement of the top $u = 0.14075\,\text{cm}$ and has the intensity $F^{I}_{max} = 5640.03\,\text{kN}$. For the spatial discretization with the finite element mesh II, the ultimate load is evaluated at $F^{II}_{max} = 5444.43\,\text{kN}$ for the vertical displacement of the top of $u = 0.1375\,\text{cm}$, and for the spatial discretization with the finite element mesh III, the ultimate load is evaluated at $F^{III}_{max} = 5309.0\,\text{kN}$ for the vertical displacement of

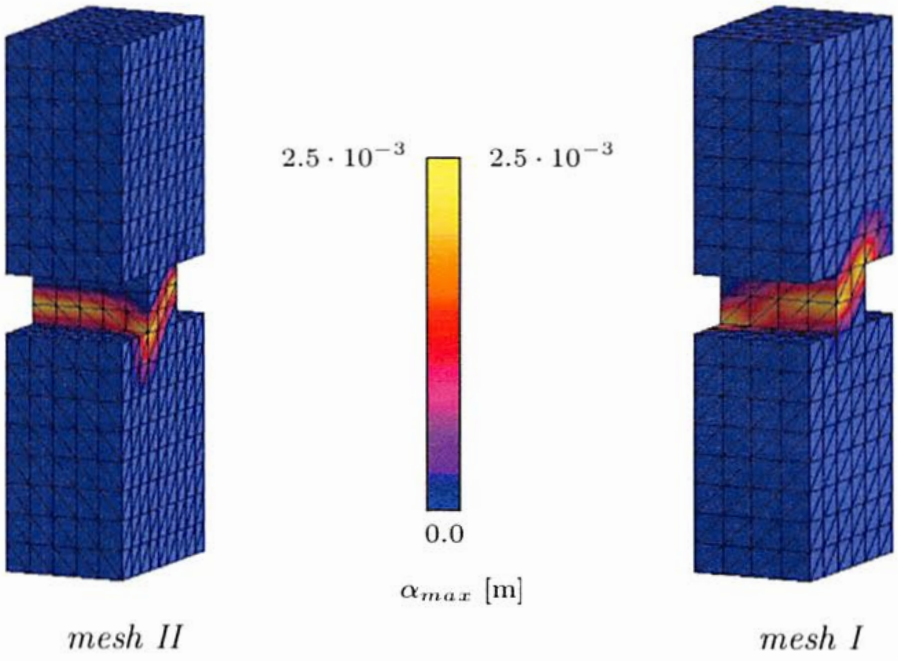

Figure 5.9: Distribution of the internal variable α_{max} for meshes *I* and *II*

the top of $u = 0.13655\,\text{cm}$. The difference in the obtained ultimate compressive load between spatial discretizations is then calculated to be 2.46% for two qualitatively different meshes (*mesh II* and *mesh III*) and 3.6% between two quantitatively different meshes (*mesh I* and *mesh II*). Consequently, the resulting ultimate loading can be considered as uniquely determined and the results of the numerical simulation based on the MLSA can be assumed independent from the finite element discretization.
The convergence profiles for the global iteration based on the NEWTON-type numerical procedure are given in Table 5.2 for the load step corresponding to the upward displacement of the top $u = 0.1786\,\text{cm}$. First few steps show the known property of the NEWTON iterative scheme, namely its conditional quadratic convergence. However, based on the complete evolution of the given maximum norms, an asymptotic quadratic convergence can be assigned to the linearization procedure presented in Section 4.4.

5.3 L-shaped panel

This section includes a numerical analysis of an L-shaped panel by means of MLSA (see Chapter 4). The geometry and the material parameters are illustrated in Figure 5.14. The panel is subjected to a vertical displacement on its right-hand face, at prescribed increments.

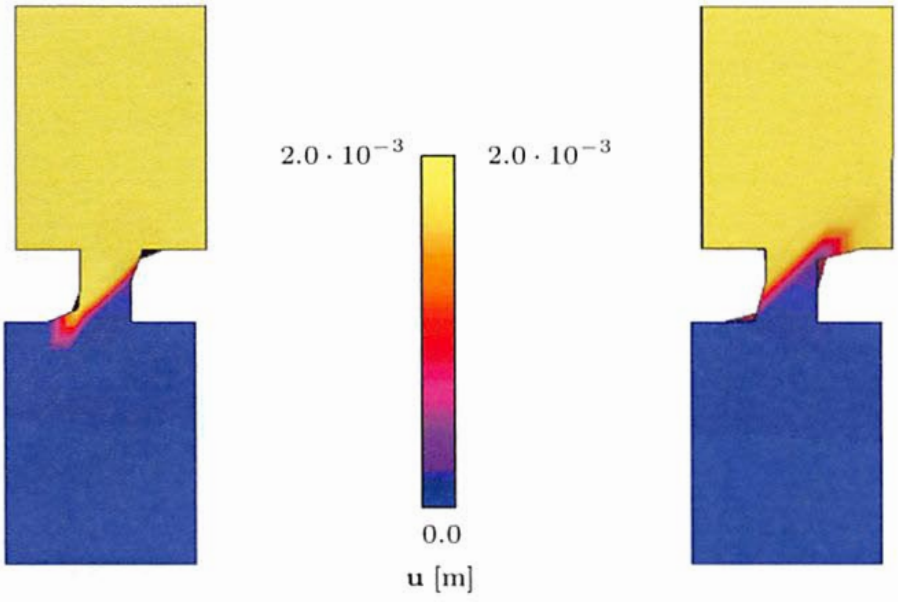

Figure 5.10: Deformed shape (magnification factor 100) and the scalar plot of the total displacement for meshes *I* and *II*

Iteration i	Relative error of the residuals $\mathbf{R}_i$		
	mesh I	mesh II	mesh III
1	2.77763	1.48142	$2.13091 \cdot 10^{-1}$
2	$1.39047 \cdot 10^{-1}$	$1.15165 \cdot 10^{-1}$	$3.56515 \cdot 10^{-2}$
3	$3.26807 \cdot 10^{-1}$	$2.49267 \cdot 10^{-1}$	$4.90471 \cdot 10^{-2}$
...	...	...	...
6	$1.42375 \cdot 10^{-1}$	$6.20148 \cdot 10^{-2}$	$9.10678 \cdot 10^{-2}$
7	$5.75583 \cdot 10^{-3}$	$1.01518 \cdot 10^{-4}$	$4.64601 \cdot 10^{-4}$
8	$1.45152 \cdot 10^{-7}$	$7.79825 \cdot 10^{-8}$	$2.06204 \cdot 10^{-7}$

Table 5.2: Convergence profile of the global NEWTON-type iteration; displacement increment of magnitude $\triangle u = 0.00005$ cm; relative error of the residuals in the maximum norm; convergence tolerance $3 \cdot 10^{-7}$

In compliance with Section 3.2.1, a hyperelastic neo-HOOKE-type model is adopted for the bulk material in $\Omega^{\pm}$. The inelastic material model exploited for the description of the crack opening at each of the localisation surfaces

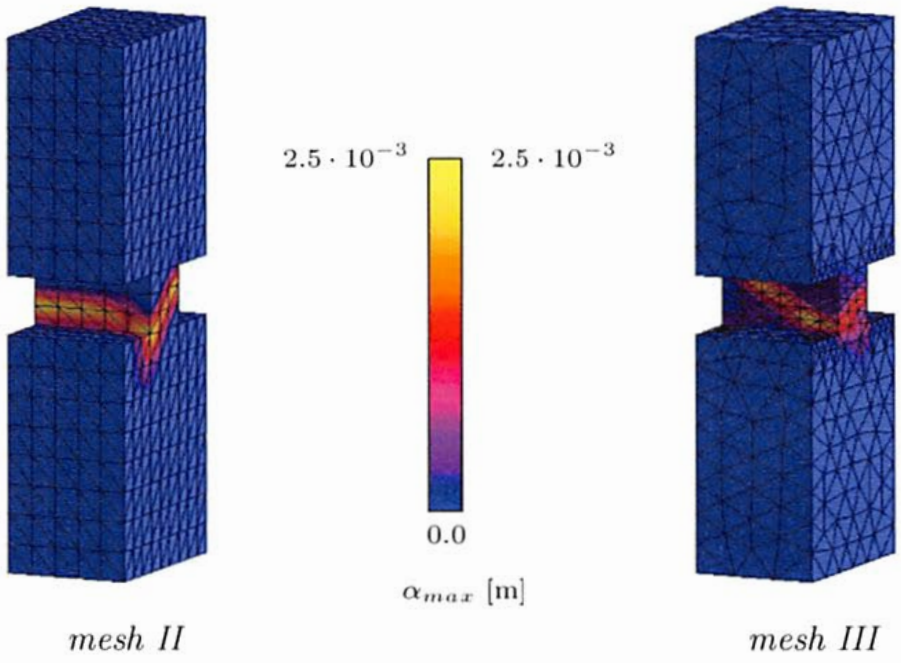

Figure 5.11: Distribution of the internal variable α_{max} for meshes *II* and *III*

$\partial_s\Omega^{(\beta)}$ is of VON MISES type with the yield function according to (5.4). The post peak response associated with the localisation surface $\partial_s\Omega^{(\beta)}$ is controlled by the exponential softening law (5.6).

A comparative analysis with intention to prove the similarity between the implicit and the explicit formulation of the MLSA is performed on *mesh I* with 1452 constant-strain tetrahedral elements (see Figure 5.15). The results in terms of the distribution of the internal variable α_{max} representing the maximum of the relative displacements out of all four possible localisation directions, load-displacement diagram, the deformed shape and the scalar plot of the total displacement are depicted in Figure 5.17. The distribution of α_{max} and the scalar plot of the total displacement $\mathbf{u}$ are given for the prescribed displacement of $2.745 \cdot 10^{-3}$ m. Load-displacement diagrams show the reaction force at the right side face of the model F with respect to the vertical displacement of this face u. The deformed shape of the geometry has a magnification factor 100. Based on the presented results, it can be concluded that both procedures deliver an identical softening response. Therefore, the implicit and the explicit definition of the MLSA can be assumed equivalent in the case of a multisurface localised failure in the form of sliding modes. Taking into account the conclusions made in this and previous section, numerically more efficient explicit formulation of MLSA can be is chosen as a preferable numerical tool

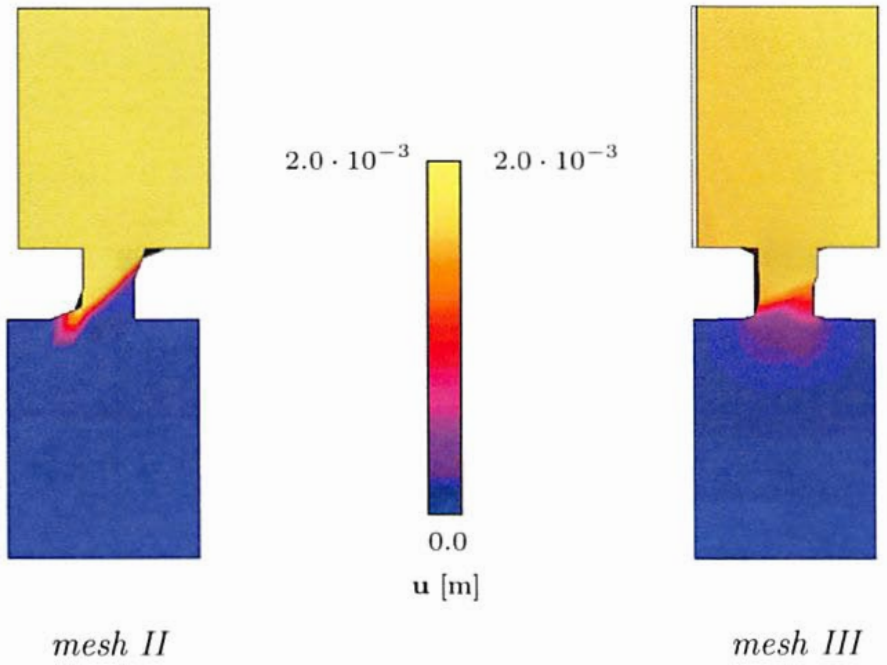

Figure 5.12: Deformed shape (magnification factor 100) and the scalar plot of the total displacement for meshes *II* and *III*

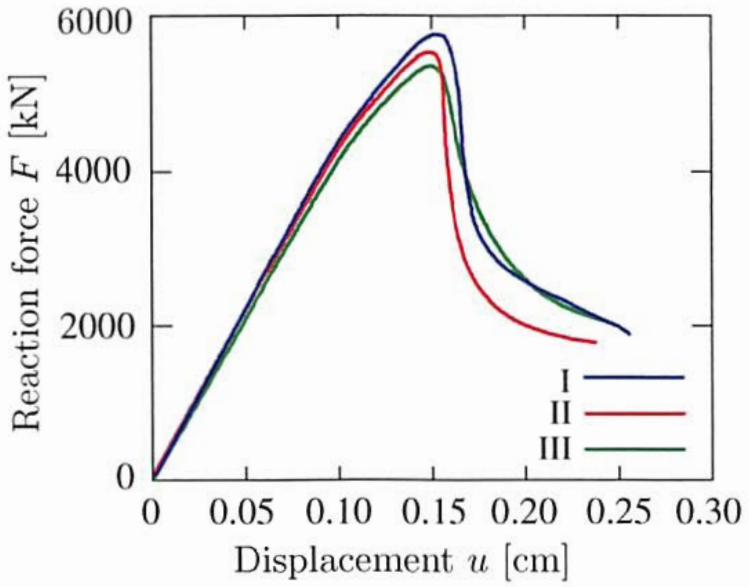

Figure 5.13: Load-displacement diagram for meshes *I*, *II* and *III*

in the implementation of MLSA in the case of slip-planes-type multisurface localised failure.

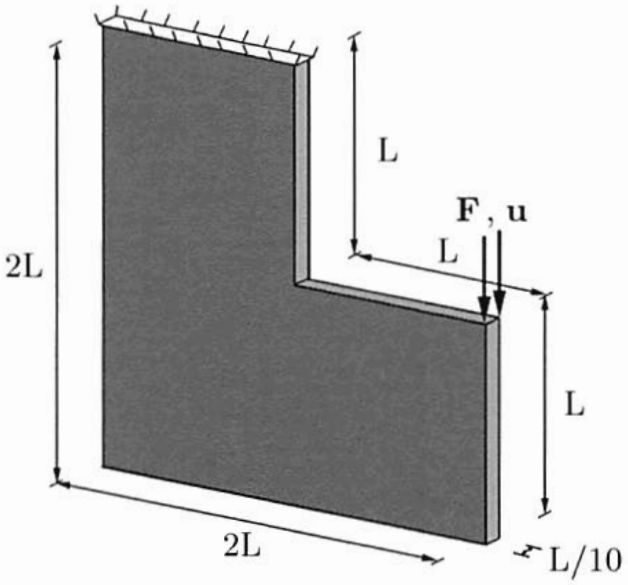

L	=	0.5	[m]
E	=	$1.0 \cdot 10^7$	[kN/m^2]
ν	=	0.2	
f_{tu}	=	1000	[kN/m^2]
H	=	0.0002	[m]

Figure 5.14: Numerical model of L-shaped panel: setup

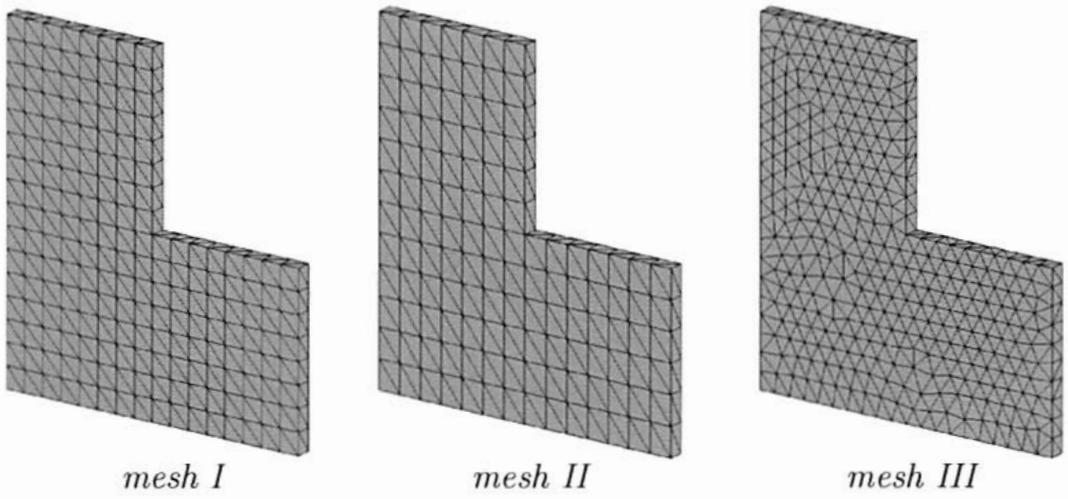

Figure 5.15: Numerical study of L-shaped slab: finite element discretizations

The influence of the spatial discretization on the performance of the MLSA is evaluated based on the results for the above mentioned mesh *I* and additional two meshes - mesh *II* with 756 constant-strain tetrahedral elements and mesh *III* with 2114 constant-strain tetrahedral elements (see Figure 5.15). The distribution of the internal variable α_{max} for all three meshes is illustrated in Figure 5.18 for the prescribed displacement of $u = 0.2745$ cm. This distribution simulates the shear band formed in the slab under the given load. According to the experimental results for concrete presented in [Winkler, Hofstetter & Lehar 2004] for a similar setup, the characteristic crack topology

should have a slightly curved shape in the corner region of the panel followed by a horizontal propagation. This form of the crack propagation can be observed in all meshes and a qualitative agreement between three discretizations may be stated. As an additional information, the resulting deformed shapes magnified by 100 and the total displacement, showing noticeably good agreement, are illustrated in Figure 5.19. Load-displacement diagrams are depicted in Figure 5.16. The estimated ultimate load for the mesh I is reached for the vertical displacement of the right face $u = 0.1165\,\text{cm}$ and has the intensity $F^{I}_{max} = 8.65813\,\text{kN}$. For the spatial discretization with the finite element mesh II, the ultimate load is evaluated at $F^{II}_{max} = 9.16672\,\text{kN}$ for the vertical displacement of the right face of $u = 0.118550\,\text{cm}$. Corresponding results for the mesh III are $F^{II}_{max} = 9.03823\,\text{kN}$ for $u = 0.14425\,\text{cm}$. These results yield a difference of $4.5 - 5.5\%$ in the evaluated ultimate loading between the given spatial discretizations. Adding the similarity of the post-peak response in the presented simulations to the similarity of the determined ultimate load leads to the conclusion that the results of the numerical simulation based on the MLSA can be assumed independent from the finite element discretization.

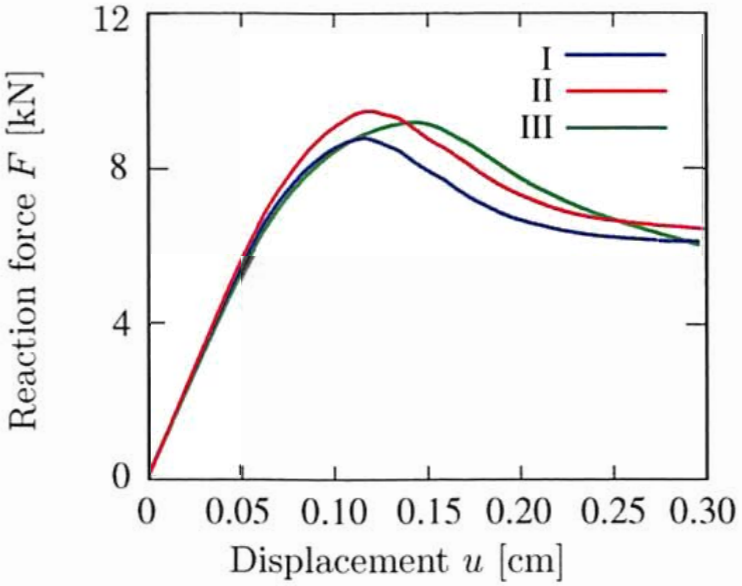

Figure 5.16: Load-displacement diagram for meshes *I*, *II* and *III*

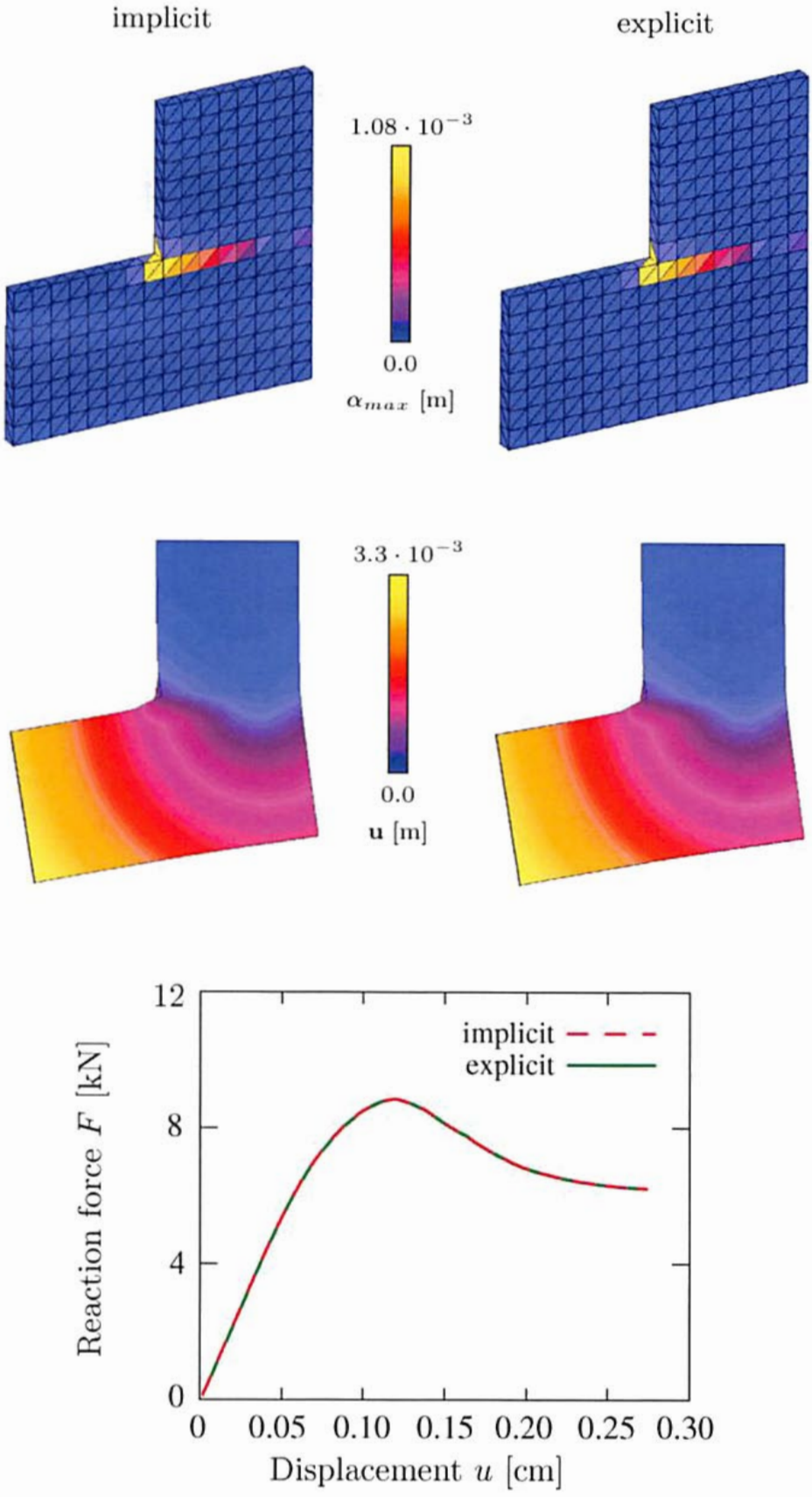

Figure 5.17: Comparative analysis: implicit and explicit MLSA (*mesh I*)

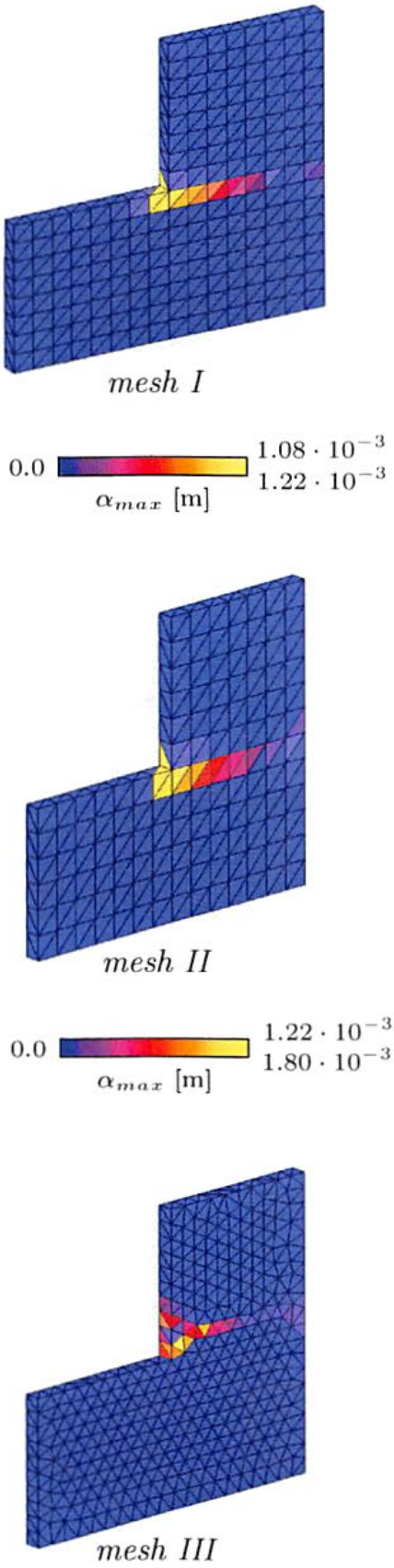

Figure 5.18: Distribution of the internal variable α_{max} for meshes *mesh I*, *II* and *III*

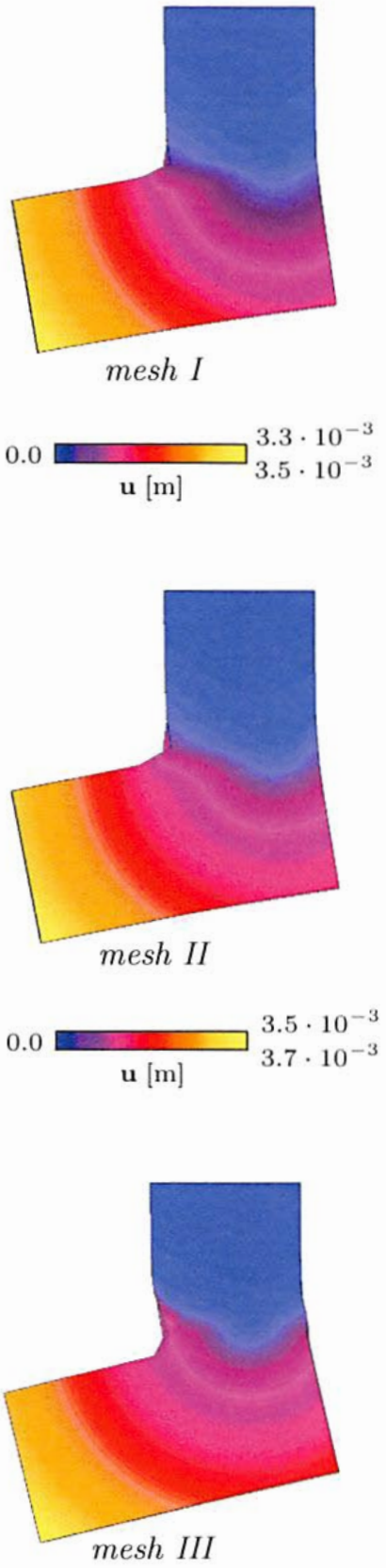

Figure 5.19: Deformed shape (magnification factor 100) and the scalar plot of the total displacement for meshes *mesh I*, *II* and *III*

6 Summary and outlook

6.1 Summary

The Multiple Localisation Surface Approach (MLSA), a geometrically nonlinear finite element approximation for highly localised deformation in structures undergoing material failure in the form of strain softening, is presented in this thesis. The basis for its numerical implementation in this class of problems is defined through the elaboration of the Strong Discontinuity Approach (SDA). In contrast to classical continuum mechanics, the deformation gradient is additively decomposed into a conforming part corresponding to a smooth deformation mapping and an enhanced part reflecting the final failure kinematics. The advocated implementation of the Enhanced Assumed Strain (EAS) concept leads to the elimination of the additional degrees of freedom (displacement jump) on the material point level. More precisely, the traction continuity condition at the singular surface is re-written in the form that carries a formal equivalence to the yielding condition known from standard plasticity. Hence, the resulting set of constitutive equations can be solved using well-known algorithms of computational plasticity, such as the return-mapping algorithm. No assumptions regarding the type of finite elements or the interface law connecting the displacement discontinuity with the conjugate traction vector have to be made. The implementation presented in this dissertation concerns constant-strain tetrahedral elements. However, the approximation of the displacement field can also be of higher order.
The main property of the presented numerical application is the simultaneous propagation of multiple intersecting discontinuities within each finite element. The choice of the topology and the orientation of singular surfaces inside each finite element is based on the fact that the developed numerical scheme should also be suitable for the description of the mechanical behaviour of materials with an arbitrary distribution of pre-existing micro-defects. Since the element-wise stochastically distributed pre-existing internal surfaces are, in general, non-conforming, the numerical procedure can experience locking and non-physical results. Therefore, the topology and the orientation of the discontinuities in a three-dimensional setting are defined based on the following criteria:

- Multiple planar localisation surfaces inside each finite element are allowed.

- Localisation surfaces are always oriented parallel to one of the finite element sides.

The chosen topology of the intersecting discontinuities yields a symmetric tangent operator in the finite element application. It leads to an enriched space of admissible internal surfaces spanned by the proposed numerical model. In

this manner, the presented algorithm can also be applied to the description of the mechanical behaviour of materials with pre-existing micro-defects under loading.
Based on two alternating definitions of the conforming part of the deformation gradient, an implicit and an explicit formulation of the Multiple Localisation Surface Approach are developed. The implicit formulation allows the incorporation of any plasticity based cohesive law and can be applied to a broad range of damage theories as well. The explicit formulation corresponds to the special case of plastic deformations occurring in slip bands and can be employed for numerical simulations of localised failure in a wide range of materials, such as ductile metals and geomaterials. Both the explicit and the implicit formulation of MLSA can be implemented using an alternative quadratic procedure for the inelastic corrector step, where the nonnegativity of the LAGRANGE multiplier is enforced. If this procedure is incorporated in the original algorithm of MLSA, possible numerical instabilities can be identified and regulated inside the framework of MLSA, without any major changes in the algorithm. The comparative analysis between the constitutive update according to the local return-mapping algorithm and the constitutive update based on the variational formulation is used for the verification of the stabilisation techniques.
The basic properties of the proposed numerical solution, namely its applicability and numerical performance, are investigated through several fully three-dimensional numerical examples. In the first example, the numerical algorithm is used for the simulation of the behaviour of an already damaged soft rock in a triaxial compression test. The initial damage in the material is represented by pre-existing micro-cracks. The analysis is used for the determination of the ultimate load. The second numerical example is an analysis of the formation and the propagation of shear bands in a bar under uniaxial tension. In the third numerical example, a three-dimensional analysis of the crack propagation in the L-shaped panel under loading is investigated. The results of the numerical examples give rise to the conclusion that the difference between the implicit and the explicit formulation nearly vanishes in the presence of a multisurface localisation in the form of shear bands. Based on the resulting distributions of the internal variable describing the softening response in the material, as well as the load-displacement diagrams, the proposed numerical procedure can be assumed independent of the spatial discretization. Consequently, the suggested numerical framework can be applied in numerical simulations of a wide range of problems involving localised material failure in the geometrically nonlinear regime.

6.2 Outlook

In this dissertation, a finite element based procedure for the numerical simulation of the multiple surface material failure at finite strains is presented. The

numerical algorithm is based on the application of the Strong Discontinuity Approach. Possible directions for future work may include:

- extension to higher order elements
- variational formulation

The numerical implementation presented in this work is associated with constant strain finite elements. An extension to higher order elements may lead to the generalisation of the procedure and improve its applicability. In the case of single surface SDA, such an extension can be found in [MOSLER 2005A] for the linearized kinematics and in [MOSLER 2007] for the geometrically nonlinear problems.
In order to overcome the limiting properties of the return-mapping algorithm, a variational constitutive update can be applied for the update of the softening response. A brief prospect of the possible structure of this alternative form of MLSA is already presented in Section 4.4.1. However, the respective modifications need to be theoretically systematised and tested on different numerical examples.

References

ARMERO, F. (1999). Large-scale modeling of localized dissipative mechanisms in a local continuum: applications to the numerical simulation of strain localization in rate-dependent inelastic solids. *Mechanics of Cohesive-Frictional Materials 4*, 101–131.

ARMERO, F. AND K. GARIKIPATI (1995). Recent advances in the analysis and numerical simulation of strain localization in inelastic solids. In D.R.J. Owen, E Oñate, and E. Hinton (Eds.), *Proc., 4th Int. Conf. Computational Plasticity*, Volume 1, 547–561.

ARMERO, F. AND K. GARIKIPATI (1996). An analysis of strong discontinuities in multiplicative finite strain plasticity and their relation with the numerical simulation of strain localization in solids. *International Journal for Solids and Structures 33*, 2863–2885.

ASARO, R.J. (1983). Micromechanics of crystals and polycrystals. *Advances in Applied Mechanics 23*, 1–115.

BAŞAR, Y AND D. WEICHERT (2000). *Nonlinear continuum mechanics of solids.* Springer.

BARENBLATT, G.I. (1962). The mathematical theory of equilibrium cracks in brittle fracture. *Adv. Appl. Mech. 7*, 55–129.

BATHE, K.J. (1995). *Finite element procedures.* Springer.

BAŽANT, Z.P. AND G. PIJAUDIER-CABOT (1988). Nonlocal damage, localization, instability and convergence. *Journal of Applied Mechanics 55*, 287–293.

BELYTSCHKO, T.AND LIU, W.K. AND B. MORAN (2000). *Nonlinear finite Elements for Continua and Structures.* Wiley, NY.

BOLTZMANN, L. (1874). Zur Theorie der elastischen Nachwirkung. *Sitzgsber. Akad. Wiss. Wien 70*, 275–306.

BORJA, R.I. (2000). A finite element model for strain localization analysis of strongly discontinuous fields based on standard galerkin approximation. *Computer Methods in Applied Mechanics and Engineering 190*, 1529–1549.

BORJA, R.I. (2002). Finite element simulation of strain localization with large deformation: capturing strong discontinuity using a Petrov-Galerkin multiscale formulation. *Computer Methods in Applied Mechanics and Engineering 191*, 2949–2978.

BORJA, R.I. AND A.R. REGUEIRO (2001). Strain localization in frictional materials exhibiting displacement jumps. *Computer Methods in Applied Mechanics and Engineering 190*, 2555–2580.

BORJA, R.I., A.R. REGUEIRO AND T.Y. LAI (2000). Fe modelling of strain localization in soft rock. *Journal of Geotechnical and Geoenvironmental Engineering 126*, 335–343.

BRUHNS, O.T. (2003). *Advanced Mechanics of Solids.* Springer.

CALLARI, C. AND F. ARMERO (2004). Analysis and numerical simulation of strong discontinuities in finite strain poroplasticity. *Computer Methods in Applied Mechanics and Engineering 193*, 2941–2986.

CHAVEZ, EWV. (2003). *A three dimensional setting for strong discontinuities modelling in failure mechanics.* Ph. D. thesis, UPC Barcelona.

CIARLET, P. (1988). *Mathematical elasticity. Volume I: Three-dimensional elasticity.* North-Holland Publishing Company, Amsterdam.

DE BORST, R. (1986). *Non-linear analysis of frictional materials.* Ph. D. thesis, Technical University Delft.

DE BORST, R. (2001). Some recent issues in computational mechanics. *International Journal for Numerical Methods in Engineering 52*, 63–95.

DOLBOW, J., N. MOËS AND T. BELYTSCHKO (2002). An extended finite element method for modeling crack growth with frictional contact. *Computer Methods in Applied Mechanics and Engineering submitted.*

DUGDALE, D.S. (1960). Yielding of steel sheets containing slits. *Journal of the Mechanics and Physics of Solids 8*, 100–108.

DUMSTORFF, P., J. MOSLER AND G. MESCHKE (2003, COMPLAS 2003: 07.-10.04.2003 in Barcelona). Advanced discretisation methods for cracked structures: The strong discontinuity approach vs. the extended finite element method. In E. Onate D.R.J. Owen and B. Suaŕez (Eds.), *Computational Plasticity VII*, p. 89. CIMNE. CD-ROM.

DVORKIN, E.N., A. M. CUITIÑO AND G. GIOIA (1990). Finite elements with displacement interpolated embedded localization lines insensitive to mesh size and distortions. *International Journal for Numerical Methods in Engineering 30*, 541–564.

FEIST, C. AND G. HOFSTETTER (2007). Three-dimensional fracture simulations based on the sda. *International Journal for Numerical and Analytical Methods in geomechanics 31*, 189–212.

GARIKIPATI, K. (1996). *On strong discontinuities in inelastic solids and their numerical simulation.* Ph. D. thesis, Stanford University.

GARIKIPATI, K. AND T.J.R. HUGHES (1998). A study of strain localization in a multiple scale framework - the one-dimensional problem. *Computer Methods in Applied Mechanics and Engineering 159*(3-4), 193–222.

GASSER, T. AND G. HOLZAPFEL (2003). Geometrically non-linear and consistently linearized embedded strong discontinuity models for 3d problems with an application to the dissection analysis of soft biological tissues. *Computer Methods in Applied Mechanics and Engineering 192*, 5059–5098.

GREEN, A.E. AND P.M. NAGHDI (1965). A general theory of an elastic-plastic continuum. *Arch. Rat. Mech. Anal.* (18), 251–281.

HAIRER, E. AND G. WANNER (2000). *Solving ordinary differential equations II, Stiff and differential-algebraic problems.* Springer Series in Computational Mathematics. Springer, Berlin, Heidelberg, New York.

HILL, R. (1950). *The mathematical theory of plasticity.* Oxford University Press, Oxford, U.K.

HILL, R. (1958). A general theory of uniqueness and stability in elastic-plastic solids. *Journal of the Mechanics and Physics of Solids 6*, 236–249.

HILL, R. (1965). Generalized constitutive relations for incremental deformation of metal crystals by multislip. *Journal of the Mechanics and Physics of Solids 14*, 95–102.

HILL, R. (1968). On constitutive inequalities for simple materials. *Journal of Mechanics and Physics of Solids* (16), 229–242; 315–322.

HILL, R. AND J.R. RICE (1973). Elastic potentials and the structure of inelastic constitutive laws. *SIAM Journal on Applied Mathematics 25*(3), 448–461.

HUEMER, T. (1998). *Automatische Vernetzung und adaptive nichtlineare statische Berechnung von Flächentragwerken mittels vierknotiger finiter Elemente.* Ph. D. thesis, Institut für Festigkeitslehre, Technische Universität Wien.

HUGHES, T.J.R. (2000). *The Finite Element Method - Linear Static and Dynamic Finite Element Analysis.* Dover Publications, Inc.

JIRÁSEK, M. (1999). Conditions of uniqueness for finite elements with embedded cracks. Technischer Bericht, LSC Internal Report 99/04, Technical University, Prag, Czech.

JIRÁSEK, M. (2000). Comparative study on finite elements with embedded cracks. *Computer Methods in Applied Mechanics and Engineering 188*, 307–330.

JIRÁSEK, M. AND T.B. BELYTSCHKO (2002). Computational resolution of strong discontinuities. In *Proceedings of the Fifth World Congress on Computational Mechanics (WCCM V).*

JIRÁSEK, M. AND T. ZIMMERMANN (2001). Embedded crack model: Part I: Basic formulation, Part II: Combination with smeared cracks. *International Journal for Numerical Methods in Engineering 50*, 1269–1305.

JÄGER, P., P. STEINMANN AND E. KUHL (2008). Modelling three-dimensional crack propagation - a comparison of crack path tracking strategies. *International Journal for Numerical Methods in Engineering 75*, 577 – 599.

KLISINSKI, M., K. RUNESSON AND S.. STURE (1991). Finite element with inner softening band. *Journal of Engineering Mechanics (ASCE) 117*(3), 575–587.

KUHL, D. AND MESCHKE G. (2002). Finite element methods in linear structural mechanics - lecture notes. Ruhr-Universität Bochum.

LACKNER, R. (1999). *Adaptive finite element analysis of reinforced concrete plates and shells.* Ph. D. thesis, Institut für Festigkeitslehre, Technische Universität Wien.

LARRSON, R. AND K. RUNESSON (1996). Element-embedded localization band based on regularized displacement discontinuity. *Journal of Engineering*

Mechanics (ASCE) 122, 402–411.

LARSSON, L., K. RUNESSON AND M. ÅKESSON (1995). Embedded localization band based on regularized strong discontinuity. In D.R.J. Owen, E Oñate, and E. Hinton (Eds.), *Proc., 4th Int. Conf. Computational Plasticity*, Volume 1, 599–610.

LARSSON, R., P. STEINMANN AND K. RUNESSON (1998). Finite element embedded localization band for finite strain plasticity based on a regularized strong discontinuity. *Mechanics of Cohesive-Frictional Materials 4*, 171–194.

LEE, E.H. (1969). Elastic-plastic deformation at finite strains. *Journal of Applied Mechanics* (36), 1–6.

LUBLINER, J. (1997). *Plasticity theory.* Maxwell Macmillan International Edition.

MANDEL, J. (1972). Plasticité classique et viscoplasticité. In *Cours and Lectures au CISM*, Volume No.97. ICSM: Springer-Verlag, New York.

MARSDEN, J.E. AND T.J.R. HUGHES (1994). *Mathematical foundation of elasticity.* Dover, New York.

MENRATH, H. (1999). *Numerische Simulation des nichtlinearen Tragverhaltens von Stahlverbundtr"agern.* Ph. D. thesis, Bericht des Instituts für Baustatik Nr. 29, Universität Stuttgart.

MIEHE, C. AND J. SCHRÖDER (1994). Post-critical discontinuous analysis of small-strain softening elastoplastic solids. *Archive of Applied Mechanics 64*, 267–285.

MOËS, N., J. DOLBOW AND T. BELYTSCHKO (1999). A finite element method for crack growth without remeshing. *International Journal for Numerical Methods in Engineering 46*, 131–150.

MOSLER, J. (2002). *Finite Elemente mit sprungstetigen Abbildungen des Verschiebungsfeldes für numerische Analysen lokalisierter Versagenszustände in Tragwerken.* Ph. D. thesis, Ruhr Universität Bochum.

MOSLER, J. (2004a). A novel algorithmic framework for the numerical implementation of locally embedded strong discontinuities. *Computer Methods in Applied Mechanics and Engineering.* submitted.

MOSLER, J. (2004b). On advanced solution strategies to overcome locking effects in strong discontinuity approaches. *International Journal for Numerical Methods in Engineering.* submitted.

MOSLER, J. (2004c). On the modeling of highly localized deformations induced by material failure: The strong discontinuity approach. *Archives of Computational Methods in Engineering 11*(4), 389–446.

MOSLER, J. (2005a). A novel algorithmic framework for the numerical implementation of locally embedded strong discontinuities. *Computer Methods in Applied Mechanics and Engineering 194*(45-47), 4731–4757.

MOSLER, J. (2005b). Numerical analyses of discontinuous material bifurcation: Strong and weak discontinuities. *Computer Methods in Applied Mechanics*

and Engineering 194(9-11), 979–1000.

MOSLER, J. (2005c). On the efficient implementation of an elastoplastic damage model for large-scale analyses of material failure: A multiscale approach. *Computers & Structures 83*(4-5), 369–382.

MOSLER, J. (2006). Modeling strong discontinuities at finite strains - a novel numerical implementation. *Computer Methods in Applied Mechanics and Engineering 195*(33-36), 4396–4419.

MOSLER, J. (2007). On the numerical modeling of localized material failure at finite strains by means of variational mesh adaption and cohesive elements. In *Mitteilungen aus dem Institut für Mechanik*. Ruhr-Universität Bochum. Habilitation.

MOSLER, J. AND O.T. BRUHNS (2004). A 3D anisotropic elastoplastic-damage model using discontinuous displacement fields. *International Journal for Numerical Methods in Engineering 60*, 923–948.

MOSLER, J. AND G. MESCHKE (2000). 3D FE analysis of cracks by means of the strong discontinuity approach. In E. Oñate, G. Bugeda, and B. Suárez (Eds.), *European Congress on Computational Methods in Applied Sciences and Engineering*.

MOSLER, J. AND G. MESCHKE (2001). FE-modeling of displacement discontinuities in inelastic continua. *Zeitschrift für Angewandte Mathematik und Mechanik 81*(Suppl. 4), 875–876.

MOSLER, J. AND G. MESCHKE (2002). A comparison of embedded discontinuity approaches with fracture energy based smeared crack models. In *Fifth World Congress on Computational Mechanics*.

MOSLER, J. AND G. MESCHKE (2003a). 3D modeling of strong discontinuities in elastoplastic solids: Fixed and rotating localization formulations. *International Journal for Numerical Methods in Engineering 57*, 1553–1576.

MOSLER, J. AND G. MESCHKE (2003b). Embedded cracks vs. smeared crack models: A comparison of elementwise discontinuous crack path approaches with emphasis on mesh bias. *Computer Methods in Applied Mechanics and Engineering*. accepted.

MOSLER, J. AND L. STANKOVIĆ (2005a). An efficient finite element formulation based on the strong discontinuity approach for modelling material failure at finite strains. In D.R.J. Owen, E. Oñate, and B. Suárez (Eds.), *VIII International Conference on Computational Plasticity*, 861–864.

MOSLER, J. AND L. STANKOVIĆ (2005b). Locally embedded strong discontinuities at finite strains - numerical implementation. In *PAMM*, Volume 5, 347–348.

MOSLER, J. AND MESCHKE G. (2004). Embedded crack vs. smeared crack models: A comparison of elementwise discontinuous approaches with emphasis on mesh bias. *Computer Methods in Applied mechanics and Engineering 193*(30-32), 3351–3375.

NEEDLEMAN, A. (1990). An analysis of decohesion along an imperfect interface. *International Journal of Fracture 42*, 21–40.

OGDEN, R.W. (1997). *Non-linear Elastic Deformations.* Dover Publications, Inc., NY.

OLIVER, J. (1995a). Continuum modelling of strong discontinuities in solid mechanics. In D.R.J. Owen, E Oñate, and E. Hinton (Eds.), *Proc., 4th Int. Conf. Computational Plasticity*, Volume 1, 455–479.

OLIVER, J. (1995b, 12). Continuum modelling of strong discontinuities in solid mechanics using damage models. *Computational Mechanics 17*(1-2), 49–61.

OLIVER, J. (1996). Modelling strong discontinuities in solid mechanics via strain softening constitutive equations part 1: Fundamentals. part 2: Numerical simulations. *International Journal for Numerical Methods in Engineering 39*, 3575–3623.

OLIVER, J. (1998). The strong discontinuity approach: An overview. *Computational Mechanics*, 1–19.

OLIVER, J. (2000). On the discrete constitutive models induced by strong discontinuity kinematics and continuum equations. *International Journal for Solids and Structures 37*, 7207–7229.

OLIVER, J., A.E. HUESPE, M.D.G. PULIDO AND E. SAMANIEGO (2003). On the strong discontinuity approach in finite deformation settings. *International Journal for Numerical Methods in Engineering 56*, 1051–1082.

OLIVER, J., A.E. HUESPE, E. SAMANIEGO AND E.W.V. CHAVES (2002). On Strategies for Tracking Strong Discontinuities in Computational Failure Mechanics. In *Fifth World Congress on Computational Mechanics.*

OLIVER, J. AND J.C. SIMO (1994). Modelling strong discontinuities in solid mechanics by means of strain softening constitutive equations. In H. Mang, N. Bićanić, and R. de Borst (Eds.), *Computational Modelling of concrete structures*, 363–372. Pineridge press.

OLIVER, J., HUESPE, A.E. AND SANCHEZ, P.J. (2006). A comparative study on finite elements for capturing strong discontinuities: E-fem vs. x-fem. *Computer Methods in Applied mechanics and Engineering 195.* 4732-4752.

ORTIZ, M. (2002). Computational solid mechanics - course notes. California Institute of technology.

ORTIZ, M. (2003). Continuum mechanics - course notes. California Institute of technology.

ORTIZ, M., Y. LEROY AND A. NEEDLEMAN (1987). A finite-element method for localized failure analysis. *Computer Methods in Applied Mechanics and Engineering 61*, 189–214.

ORTIZ, M. AND A. PANDOLFI (1999). Finite-deformation irreversible cohesive elements for three-dimensional crack-propagation analysis. *International Journal for Numerical Methods in Engineering 44*, 1267–1282.

ORTIZ, M. AND L. STEINER (1999). The variational formulation of viscoplastic constitutive updates. *Computer Methods in Applied Mechanics and Engineering 171*, 419–444.

PIETRUSZCZAK, S. AND Z. MROŹ (1981). Finite element analysis of deformation of strain-softening materials. *International Journal for Numerical Methods in Engineering 17*, 327–334.

PIJAUDIER-CABOT, G. AND Z.P. BAŽANT (1987). Nonlocal damage theory. *Journal of Engineering Mechanics (ASCE) 113*, 1512–1533.

SANCHO, J.M., J. PLANAS, AM. FATHY, JC. GALVEZ AND DA. CENDOŃ (2007). Three-dimensional simulation of concrete fracture using embedded crack element without enforcing crack path continuity. *International Journal for Numerical and Analytical Methods in geomechanics 31*, 173–187.

SIMO, J.C. (1992). Algorithms for static and dynamic multiplicative plasticity that preserve the classical return mapping schemes of the infinitesimal theory. *Computational Mechanics 99*, 61–112.

SIMO, J.C. (1998). Numerical analysis of classical plasticity. In P.G. Ciarlet and J.J. Lions (Eds.), *Handbook for numerical analysis*, Volume IV. Elsevier, Amsterdam.

SIMO, J.C., F. ARMERO AND R.L. TAYLOR (1993). Improved versions of assumed enhanced strain tri-linear elements for 3d deformation problems. *Computer Methods in Applied Mechanics and Engineering 110*, 359–386.

SIMO, J.C. AND T.J.R. HUGHES (1998). *Computational inelasticity*. Springer, New York.

SIMO, J.C. AND J. OLIVER (1994). A new approach to the analysis and simulation of strain softening in solids. In Z.P. Bažant, Z. Bittnar, M. Jirásek, and J. Mazars (Eds.), *Fracture and Damage in Quasibrittle Structures*, 25–39. E. &F.N. Spon, London.

SIMO, J.C., J. OLIVER AND F. ARMERO (1993). An analysis of strong discontinuities induced by strain softening in rate-independent inelastic solids. *Computational Mechanics 12*, 277–296.

SIMO, J.C. AND S. RIFAI (1990). A class mixed assumed strain methods and the method of incompatible modes. *International Journal for Numerical Methods in Engineering 29*, 1595–1638.

SIMO, J. AND ARMERO, F. (1992). Geometrically non-linear enhanced strain mixed methods and the method of incompatible modes. *International Journal for numerical Methods in Engineering 33*, 1413–1449.

SIMO, J.C. AND RIFAI, M.S. (1990). A class of mixed assumed strain methods and the method of incompatible modes. *International Journal for Numerical Methods in Engineering 29*, 1595–1638.

SNYMAN, M. F., W. W. BIRD AND J. B. MARTIN (1991). A simple formulation of a dilatant joint element governed by Coulomb friction. *Engineering Computations 8*, 215–229.

STAKGOLD, I. (1967). *Boundary value problems of mathematical physics*, Volume I. Macmillien Series in Advanced Mathematics and theoretical physics.

STAKGOLD, I. (1998). *Green's functions and boundary value problems.* Wiley.

STANKOVIĆ, L. AND J. MOSLER (2006a). Numerical prediction of macroscopic material failure. In *PAMM*, Volume 6, 197–198.

STANKOVIĆ, L. AND J. MOSLER (2006b). Prediction of macroscopic material failure based on microscopic cohesive laws. In C.A. Mota Soares, J.A.C. Martins, H.C. Rodrigues, and J.A.C. Ambrósio (Eds.), *III European Conference on Computational Mechanics, Solids, Structures and Coupled Problems in Engineering.*

STANKOVIĆ, L. AND J. MOSLER (2007). Numerical analysis of shear bands in solids by means of computational homogenization. In *PAMM*, Volume 7, in press.

STEINMANN, P. AND P. BETSCH (2000). A localization capturing FE-interface based on regularized strong discontinuities at large inelastic strains. *International Journal for Solids and Structures 37*, 4061–4082.

SUKUMAR, N., N. MOËS, B. MORAN AND T. BELYTSCHKO (2000). Extended finite element method for three-dimensional crack modelling. *International Journal for Numerical Methods in Engineering 48*, 1549–1570.

TAYLOR, G.I. (1938). Plastic strain in metals. *Journal of Institute of Metals 62*, 307–324.

TAYLOR, R.L., J.C. SIMO, O.C. ZIENKIEWICZ AND A.C.H. CHAN (1986). The patch test-A condition for assessing FEM convergence. *International Journal for Numerical Methods in Engineering 22*, 39–62.

TRUESDELL, C. AND W. NOLL (1965). The nonlinear field theories. In S. Flügge (Ed.), *Handbuch der Physik*, Volume 3. Springer-Verlag, Berlin.

TRUESDELL, C. AND R. TOUPIN (1960). The classical field theories. In S. Flügge (Ed.), *Handbuch der Physik*, Volume 3. Springer-Verlag, Berlin.

VERFÜRTH, R. (2000). Einführung in die numerische Mathematik - Vorlesungsskriptum sommersemester 2000. Ruhr-Universität Bochum.

WANG, C.C. AND C. TRUESDELL (1973). *Introduction to Rational Elasticity.* Noordhoff International Publishing, Leyden.

WELLS, G.N. (2001). *Discontinuous modelling of strain localisation and failure.* Ph. D. thesis, TU Delft.

WELLS, G.N. AND L.J. SLUYS (2001a). A new method for modelling cohesive cracks using finite elements. *International Journal for Numerical Methods in Engineering 50*, 2667–2682.

WELLS, G.N. AND L.J. SLUYS (2001b). Three-dimensional embedded discontinuity model for brittle fracture. *International Journal for Solids and Structures 38*, 897–913.

WINKLER, B., G. HOFSTETTER AND H. LEHAR (2004). Application of a constitutive model for concrete to the analysis of a precast segmental tunnel lining. *International Journal for Numerical and Analytical Methods in ge-*

omechanics 28, 797–819.

XIAO, H., O.T. BRUHNS AND A. MEYERS (2000a). The choice of objective rates in finite elastoplasticity: general results on the uniqueness of the logarithmic rate. *Proceedings of the Royal Society London A* (456), 1865–1882.

XIAO, H., O.T. BRUHNS AND A. MEYERS (2000b). A consistent finite elastoplasticity theory combining additive and multiplicative decomposition of the stretching and the deformation gradient. *International Journal of Plasticity* (16), 143–177.

XIAO, H., O.T. BRUHNS AND A. MEYERS (2006). Elastoplasticity beyond small deformations. *Acta Mechanica* (182), 31–111.

Mitteilungen aus dem Institut für Mechanik

Nr. 1 Theodor Lehmann:
Große elasto-plastische Formänderungen (Dezember 1976)

Nr. 2 Bogdan Raniecki/Klaus Thermann:
Infinitesimal Thermoplasticity and Kinematics of Finite Elastic-Plastic Deformations. Basic Concepts (Juni 1978)

Nr. 3 Wolfgang Krings:
Beitrag zur Finiten Element Methode bei linearem, viskoelastischem Stoffverhalten (Januar 1976)

Nr. 4 Burkhard Lücke:
Theoretische und experimentelle Untersuchung der zyklischen elastoplastischen Blechbiegung bei endlichen Verzerrungen (Januar 1976)

Nr. 5 Knut Schwarze:
Einfluß von Querschnittsverformungen bei dünnwandigen Stäben mit stetig gekrümmter Profilmittellinie (Februar 1976)

Nr. 6 Hubert Sommer:
Ein Beitrag zur Theorie des ebenen elastischen Verzerrungszustandes bei endlichen Formänderungen (Januar 1977)

Nr. 7 H. Stumpf/F. J. Biehl:
Die Methode der orthogonalen Projektionen und ihre Anwendung zur Berechnung orthotroper Platten (März 1977)

Nr. 8 Albert Meyers:
Ein Beitrag zum optimalen Entwurf von schnellaufenden Zentrifugenschalen (April 1977)

Nr. 9 Berend Fischer:
Zur zyklischen, elastoplastischen Beanspruchung eines dickwandigen Zylinders bei endlichen Verzerrungen (April 1977)

Nr. 10 Wojciech Pietraszkiewicz:
Introduction to the Non-Linear Theory of Shells (Mai 1977)

Nr. 11 Wilfried Ullenboom:
Optimierung von Stäben unter nichtperiodischer dynamischer Belastung (Juni 1977)

Nr. 12 Jürgen Güldenpfennig:
Anwendung eines Modells der Vielkristallplastizität auf ein Problem gekoppelter elastoplastischer Wellen (Juli 1977)

Nr. 13 Pawel Rafalski:
Minimum Principles in Plasticity (März 1978)

Nr. 14 Peter Hilgers:
Der Einsatz eines Mikrorechners zur hybriden Optimierung und Schwingungsanalyse (Juli 1978)

Nr. 15 Hans-Albert Lauert:
Optimierung von Stäben unter dynamischer periodischer Beanspruchung bei Beachtung von Spannungsrestriktionen (August 1979)

Nr. 16 Martin Fritz:
Berechnung der Auflagerkräfte und der Muskelkräfte des Menschen bei ebenen Bewegungen aufgrund von kinematographischen Aufnahmen (Juli 1979)

Nr. 17 H. Stumpf/F. J. Biehl:
Approximations and Error Estimates in Eigenvalue Problems of Elastic Systems with Application to Eigenvibrations of Orthotropic Plates (Dezember 1979)

Nr. 18 Uwe Kohlberg:
Variational Principles and their Numerical Application to Geometrically Nonlinear v. Karman Plates (Juli 1979)

Nr. 19 Heinz Antes:
Über Fehler und Möglichkeiten ihrer Abschätzung bei numerischen Berechnungen von Schalentragwerken (Januar 1980)

Nr. 20 Czeslaw Wozniak:
Large Deformations of Elastic and Non-Elastic Plates, Shells and Rods (März 1980)

Nr. 21 Maria K. Duszek:
Problems of Geometrically Non-Linear Theory of Plasticity (Juni 1980)

Nr. 22 Burkhard von Bredow:
Optimierung von Stäben unter stochastischer Erregung (Dezember 1980)

Nr. 23 Jürgen Preuss:
Optimaler Entwurf von Tragwerken mit Hilfe der Mehrzielmethode (Februar 1981)

Nr. 24 Ekkehard Großmann:
Kovarianzanalyse mechanischer Zufallsschwingungen bei Darstellung der mehrfachkorrelierten Erregungen durch stochastische Differentialgleichungen (Februar 1981)

Nr. 25 Dieter Weichert:
Variational Formulation and Solution of Boundary-Value Problems in the Theory of Plasticity and Application to Plate Problems (März 1981)

Nr. 26 Wojciech Pietraszkiewicz:
On Consistent Approximations in the Geometrically Non-Linear Theory of Shells (Juni 1981)

Nr. 27 Georg Zander:
Zur Bestimmung von Verzweigungslasten dünnwandiger Kreiszylinder unter kombinierter Längs- und Torsionslast (September 1981)

Nr. 28 Pawel Rafalski:
An Alternative Approach to the Elastic-Viscoplastic Initial-Boundary Value Problem (September 1981)

Nr. 29 Heinrich Oeynhausen:
Verzweigungslasten elastoplastisch deformierter, dickwandiger Kreiszylinder unter Innendruck und Axialkraft (November 1981)

Nr. 30 F.-J. Biehl:
Zweiseitige Eingrenzung von Feldgrößen beim einseitigen Kontaktproblem (Dezember 1981)

Nr. 31 Maria K. Duszek:
Foundations of the Non-Linear Plastic Shell Theory (Juni 1982)

Nr. 32 Reinhard Piltner:
Spezielle finite Elemente mit Löchern, Ecken und Rissen unter Verwendung von analytischen Teillösungen (Juli 1982)

Nr. 33 Petrisor Mazilu:
Variationsprinzipe der Thermoplastizität
I. Wärmeausbreitung und Plastizität (Dezember 1982)

Nr. 34 Helmut Stumpf:
Unified Operator Description, Nonlinear Buckling and Post-Buckling Analysis of Thin Elastic Shells (Dezember 1982)

Nr. 35 Bernd Kaempf:
Ein Exremal-Variationsprinzip für die instationäre Wärmeleitung mit einer Anwendung auf thermoelastische Probleme unter Verwendung der finiten Elemente (März 1983)

Nr. 36 Alfred Kraft:
Zum methodischen Entwurf mechanischer Systeme im Hinblick auf optimales Schwingungsverhalten (Juli 1983)

Nr. 37 Petrisor Mazilu:
Variationsprinzipe der Thermoplastizität
II. Gekoppelte thermomechanische Prozesse (August 1983)

Nr. 38 Klaus-Detlef Mickley:
Punktweise Eingrenzung von Feldgrößen in der Elastomechanik und ihre numerische Realisierung mit Fundamental-Splinefuntionen (November 1983)

Nr. 39 Lutz-Peter Nolte:
Beitrag zur Herleitung und vergleichende Untersuchung geometrisch nichtlinearer Schalentheorien unter Berücksichtigung großer Rotationen (Dezember 1983)

Nr. 40 Ulrich Blix:
Zur Berechnung der Einschnürung von Zugstäben unter Berücksichtigung thermischer Einflüsse mit Hilfe der Finite-Element-Methode (Dezember 1983)

Nr. 41 Peter Becker:
Zur Berechnung von Schallfeldern mit Elementmethoden (Februar 1984)

Nr. 42 Dietmar Bouchard:
Entwicklung und Anwendung eines an die Diskrete-Fourier-Transformation angepaßten direkten Algorithmus zur Bestimmung der modalen Parameter linearer Schwingungssysteme (Februar 1984)

Nr. 43 Uwe Zdebel:
Theoretische und experimentelle Untersuchungen zu einem thermoplastischen Stoffgesetz (Dezember 1984)

Nr. 44 Jan Kubik:
Thermodiffusion Flows in a Solid with a Dominant Constituent (April 1985)

Nr. 45 Horst J. Klepp:
Über die Gleichgewichtslagen und Gleichgewichtsbereiche nichtlinearer autonomer Systeme (Juni 1985)

Nr. 46 J. Makowsky/L.-P. Nolte/H. Stumpf:
Finite In-Plane Deformations of Flexible Rods - Insight into Nonlinear Shell Problems (Juli 1985)

Nr. 47 Franz Karl Labisch:
Grundlagen einer Analyse mehrdeutiger Lösungen nichtlinearer Randwertprobleme der Elastostatik mit Hilfe von Variationsverfahren (August 1985)

Nr. 48 J. Chroscielewski/L.-P. Nolte:
Strategien zur Lösung nichtlinearer Probleme der Strukturmechanik und ihre modulare Aufbereitung im Konzept MESY (Oktober 1985)

Nr. 49 Karl-Heinz Bürger:
Gewichtsoptimierung rotationssymmetrischer Platten unter instationärer Erregung (Dezember 1985)

Nr. 50 Ulrich Schmid:
Zur Berechnung des plastischen Setzens von Schraubenfedern (Februar 1987)

Nr. 51 Jörg Frischbier:
Theorie der Stoßbelastung orthotroper Platten und ihr experimentelle Überprüfung am Beispiel einer unidirektional verstärkten CFK-Verbundplatte (März 1987)

Nr. 52 W. Tampczynski:
Strain history effect in cyclic plasticity (Juli 1987)

Nr. 53 Dieter Weichert:
Zum Problem geometrischer Nichtlinearitäten in der Plastizitätstheorie (Dezember 1987)

Nr. 54 Heinz Antes/Thomas Meise/Thomas Wiebe:
Wellenausbreitung in akustischen Medien
Randelement-Prozeduren im 2-D Frequenzraum und im 3-D Zeitbereich (Januar 1988)

Nr. 55 Wojciech Pietraszkiewicz:
Geometrically non-linear theories of thin elastic shells (März 1988)

Nr. 56 Jerzy Makowski/Helmut Stumpf:
Finite strain theory of rods (April 1988)

Nr. 57 Andreas Pape:
Zur Beschreibung des transienten und stationären Verfestigungsverhaltens von Stahl mit Hilfe eines nichtlinearen Grenzflächenmodells (Mai 1988)

Nr. 58 Johannes Groß-Weege:
Zum Einspielverhalten von Flächentragwerken (Juni 1988)

Nr. 59 Peihua Liu:
Optimierung von Kreisplatten unter dynamischer nicht rotationssymmetrischer Last (Juli 1988)

Nr. 60 Reinhard Schmidt:
Die Anwendung von Zustandsbeobachtern zur Schwingungsüberwachung und Schadensfrüherkennung auf mechanische Konstruktionen (August 1988)

Nr. 61 Martin Pitzer:
Vergleich einiger FE-Formulierungen auf der Basis eines inelastischen Stoffgesetzes (Juli 1988)

Nr. 62 Jerzy Makowski/Helmut Stumpf:
Geometric structure of fully nonlinear and linearized Cosserat type shell theory (Dezember 1988)

Nr. 63 O. T. Bruhns:
Große plastische Formänderungen – Bad Honnef 1988 (Januar 1989)

Nr. 64 Khanh Chau Le/Helmut Stumpf/Dieter Weichert:
Variational principles of fracture mechanics (Juli 1989)

Nr. 65 Guido Obermüller:
Ein Beitrag zur Strukturoptimierung unter stochastischen Lasten (Juni 1989)

Nr. 66 Herbert Diehl:
Ein Materialmodell zur Berechnung von Hochgeschwindigkeitsdeformationen metallischer Werkstoffe unter besonderer Berücksichtigung der Schädigung durch Scherbänder (Juni 1989)

Nr. 67 Michael Geis:
Zur Berechnung ebener, elastodynamischer Rißprobleme mit der Randelementmethode (November 1989)

Nr. 68 Günter Renker:
Zur Identifikation nichtlinearer strukturmechanischer Systeme (November 1989)

Nr. 69 Berthold Schieck:
Große elastische Dehnungen in Schalen aus hyperelastischen inkompressiblen Materialien (November 1989)

Nr. 70 Frank Szepan:
Ein elastisch-viskoplastisches Stoffgesetz zur Beschreibung großer Formänderungen unter Berücksichtigung der thermomechanischen Kopplung (Dezember 1989)

Nr. 71 Christian Scholz:
Ein Beitrag zur Gestaltsoptimierung druckbelasteter Rotationsschalen (Dezember 1989)

Nr. 72 J. Badur/H. Stumpf:
On the influence of E. and F. Cosserat on modern continuum mechanics and field theory (Dezember 1989)

Nr. 73 Werner Fornefeld:
Zur Parameteridentifikation und Berechnung von Hochgeschwindigkeitsdeformationen metallischer Werkstoffe anhand eines Kontinuums-Damage-Modells (Januar 1990)

Nr. 74 J. Saczuk/H. Stumpf:
On statical shakedown theorems for non-linear problems (April 1990)

Nr. 75 Andreas Feldmüller:
Ein thermoplastisches Stoffgesetz isotrop geschädigter Kontinua (April 1991)

Nr. 76 Ulfert Rott:
Ein neues Konzept zur Berechnung viskoplastischer Strukturen (April 1991)

Nr. 77 Thomas Heinrich Pingel:
Beitrag zur Herleitung und numerischen Realisierung eines mathematischen Modells der menschlichen Wirbelsäule (Juli 1991)

Nr. 78 O. T. Bruhns:
Große plastische Formänderungen – Bad Honnef 1991 (Dezember 1991)

Nr. 79 J. Makowski/J. Chroscielewski/H. Stumpf:
Computational Analysis of Shells Undergoing Large Elastic Deformation Part I: Theoretical Foundations

Nr. 80 J. Chroscielewski/J. Makowski/H. Stumpf:
Computational Analysis of Shells Undergoing Large Elastic Deformation Part II: Finite Element Implementation

Nr. 81 R. H. Frania/H. Waller:
Entwicklung und Anwendung spezieller finiter Elemente für Kerbspannungsprobleme im Maschinenbau (Mai 1992)

Nr. 82 B. Bischoff-Beiermann:
Zur selbstkonsistenten Berechnung von Eigenspannungen in polykristallinem Eis unter Berücksichtigung der Monokristallanisotropie (Juli 1992)

Nr. 83 J. Pohé:
Ein Beitrag zur Stoffgesetzentwicklung für polykristallines Eis (Februar 1993)

Nr. 84 U. Kikillus:
Ein Beitrag zum zyklischen Kiechverhalten von Ck 15 (Mai 1993)

Nr. 85 T. Guo:
Untersuchung des singulären Rißspitzenfeldes bei stationärem Rißwachstum in verfestigendem Material (Juni 1993)

Nr. 86 Achim Menne:
Identifikation der dynamischen Eigenschaften von hydrodynamischen Wandlern (Januar 1994)

Nr. 87 Uwe Folchert:
Identifikation der dynamischen Eigenschaften hydrodynamischer Kupplungen (Januar 1994)

Nr. 88 Jörg Körber:
Ein verallgemeinertes Finite-Element-Verfahren mit asymptotischer Stabilisierung angewendet auf viskoplastische Materialmodelle (April 1994)

Nr. 89 Peer Schieße:
Ein Beitag zur Berechnung des Deformationsverhaltens anisotrop geschädigter Kontinua unter Berücksichtigung der thermoplastischen Kopplung (April 1994)

Nr. 90 Egbert Schopphoff:
Dreidimensionale mechanische Analyse der menschlichen Wirbelsäule (Juli 1994)

Nr. 91 Christoph Beerens:
Zur Modellierung nichtlinearer Dämpfungsphänomene in der Strukturmechanik (Juli 1994)

Nr. 92 K. C. Le/H. Stumpf:
Finte elastoplasticity with microstructure (November 1994)

Nr. 93 O. T. Bruhns:
Große plastische Formänderungen – Bad Honnef 1994 (Dezember 1994)

Nr. 94 Armin Lenzen:
Untersuchung von dynamischen Systemen mit der Singulärwertzerlegung – Erfassung von Strukturveränderungen (Dezember 1994)

Nr. 95 J. Makowski/H. Stumpf:
Mechanics of Irregular Shell Structures (Dezember 1994)

Nr. 96 J. Chroscielewski/J. Makowski/H. Stumpf:
Finte Elements for Irregular Nonlinear Shells (Dezember 1994)

Nr. 97 W. Krings/A. Lenzen/u. a.:
Festschrift zum 60. Geburtstag von Heinz Waller (Februar 1995)

Nr. 98 Ralf Podleschny:
Untersuchung zum Instabilitätsverhalten scherbeanspruchter Risse (April 1995)

Nr. 99 Bernd Westerhoff:
Eine Untersuchung zum geschwindigkeitsabhängigen Verhalten von Stahl (Juli 1995)

Nr. 100 Marc Mittelbach:
Simulation des Deformations- und Schädigungsverhaltens beim Stoßversuch mit einem Kontinuums-Damage-Modell (Dezember 1995)

Nr. 101 Ulrich Hoppe:
Über grundlegende Konzepte der nichtlinearen Kontinuumsmechanik und Schalentheorie (Mai 1996)

Nr. 102 Marcus Otto:
Erweiterung des Kaustikenverfahrens zur Analyse räumlicher Spannungskonzentrationen (Juni 1996)

Nr. 103 Horst Lanzerath:
Zur Modalanalyse unter Verwendung der Randelementemethode (Juli 1996)

Nr. 104 Andreas Wichtmann:
Entwicklung eines thermodynamisch konsistenten Stoffgesetzes zur Beschreibung der Reckalterung (August 1996)

Nr. 105 Bjarne Fosså:
Ein Beitrag zur Fließflächenmessung bei vorgedehnten Stählen (Oktober 1996)

Nr. 106 Khanh Cha Le:
Kontinuumsmechanisches Modellieren von Medien mit veränderlicher Mikrostruktur (Dezember 1996)

Nr. 107 Holger Behrens:
Nichtlineare Modellierung und Identifikation hydrodynamischer Kupplungen mit allgemeinen diskreten Modellansätzen (Januar 1997)

Nr. 108 Johannes Moosheimer:
Gesteuerte Schwingungsdämpfung mit Elektrorheologischen Fluiden (Juli 1997)

Nr. 109 Dirk Klaus Anding:
Zur simultanen Bestimmung materialabhängiger Koeffizienten inelastischer Stoffgesetze (Oktober 1997)

Nr. 110 Stephan Weng:
Ein Evolutionsmodell zur mechanischen Analyse biologischer Strukturen (Dezember 1997)

Nr. 111 Michael Strassberger:
Aktive Schallreduktion durch digitale Zustandsregelung der Strukturschwingungen mit Hilfe piezo-keramischer Aktoren (Dezember 1997)

Nr. 112 Hans-Jörg Becker:
Simultation des Deformationsverhaltens polykristallinen Eises auf der Basis eines monokristallinen Stoffgesetzes (Dezember 1997)

Nr. 113 Thomas Nerzak:
Modellierung und Simulation der Ausbreitung adiabatischer Scherbänder in metallischen Werkstoffen bei Hochgeschwindigkeitsdeformationen (Dezember 1997)

Nr. 114 O. T. Bruhns:
Große plastische Formänderungen (März 1998)

Nr. 115 Jan Steinhausen:
Die Beschreibung der Dynamik von Antriebssträngen durch Black-Box-Modelle hydrodynamischer Kupplungen (August 1998)

Nr. 116 Thomas Pandorf:
Experimentelle und numerische Untersuchungen zur Kerbspitzenbeanspruchung bei schlagbelasteten Biegeproben (August 1998)

Nr. 117 Claus Oberste-Brandenburg:
Ein Materialmodell zur Beschreibung der Austenit-Martensit Phasentransformation unter Berücksichtigung der transformationsinduzierten Plastizität (Juni 1999)

Nr. 118 Michael Märtens:
Regelung mechanischer Strukturen mit Hilfe piezokeramischer Stapelaktoren (Dezember 1999)

Nr. 119 Dirk Kamarys:
Detektion von Strukturveränderungen durch neue Identifikationsverfahren in der experimentellen Modalanalyse (Dezember 1999)

Nr. 120 Wolfgang Hiese:
Gültigkeitskriterien zur Bestimmung von Scherbruchzähigkeiten (Januar 2000)

Nr. 121 Peter Jaschke:
Mathematische Modellierung des Betriebsverhaltens hydrodynamischer Kupplungen mit hybriden Modellansätzen (Februar 2000)

Nr. 122 Stefan Müller:
Zum Einsatz von semi-aktiven Aktoren zur optimalen Schwingungsreduktion in Tragwerken (Februar 2000)

Nr. 123 Dirk Eichel:
Zur Kondensation strukturdynamischer Aufgaben mit Hilfe von Polynommatrizen (Juni 2000)

Nr. 124 Andreas Bürgel:
Bruchmechanische Kennwerte beim Wechsel im Versagensverhalten dynamisch scherbeanspruchter Risse (August 2000)

Nr. 125 Daniela Lürding:
Modellierung großer Deformationen in orthotropen, hyperelastischen Schalenstrukturen (März 2001)

Nr. 126 Thorsten Quent:
Ein mikromechanisch begründetes Modell zur Beschreibung des duktilen Verhaltens metallischer Werkstoffe bei endlichen Deformationen unter Berücksichtigung von Porenschädigung (Mai 2001)

Nr. 127 Ndzi C. Bongmba:
Ein finites anisotropes Materialmodell auf der Basis der Hencky-Dehnung und der logarithmischen Rate zur Beschreibung duktiler Schädigung (Mai 2001)

Nr. 128 Henning Schütte:
Ein finites Modell für spröde Schädigung basierend auf der Ausbreitung von Mikrorissen (August 2001)

Nr. 129 Henner Vogelsang:
Parameteridentifikation für ein selbstkonsistentes Stoffmodell unter Berücksichtigung von Phasentransformationen (Dezember 2001)

Nr. 130 Jörn Mosler:
Finite Elemente mit sprungstetigen Abbildungen des Verschiebungsfeldes für numerische Analysen lokalisierter Versagenszustände (Dezember 2002)

Nr. 131 Karin Preusch:
Hierarchische Schalenmodelle für nichtlineare Kontinua mit der p-Version der Finite-Element Methode (Mai 2003)

Nr. 132 Christoph Müller:
Thermodynamic modeling of polycrystalline shape memory alloys at finite strains (August 2003)

Nr. 133 Martin Heiderich:
Ein Beitrag zur zerstörungsfreien Schädigungsanalyse (Juni 2004)

Nr. 134 Raoul Costamagna:
Globale Materialbeziehungen für das geklüftete Gebirge (Juli 2004)

Nr. 135 Markus Böl:
Numerische Simulation von Polymernetzwerken mit Hilfe der Finite-Elemente-Methode (Januar 2005)

Nr. 136 Gregor Kotucha:
Regularisierung von Problemen der Topologieoptimierung unter Einbeziehung von Dichtegradienten (August 2005)

Nr. 137 Michael Steiner:
Deformations- und Versagensverhalten innendruckbeanspruchter Stahlrohre durch Stoßbelastung (Februar 2006)

Nr. 138 Dirk Bergmannshoff:
Das Instabilitätsverhalten zug-/scherbeanspruchter Risse bei Variation des Belastungspfades (Dezember 2006)

Nr. 139 Olaf Schilling:
Über eine implizite Partikelmethode zur Simulation von Umformprozessen (Januar 2007)

Nr. 140 Jörn Mosler:
On the numerical modeling of localized material failure at finite strains by means of variational mesh adaption and cohesive elements (Mai 2007)

Nr. 141 Rainer Fechte-Heinen:
Mikromechanische Modellierung von Formgedächtnismaterialien (Juni 2007)

Nr. 142 Christian Grabe:
Experimental testing and parameter identification on the multidimensional material behavior of shape memory alloys (Juni 2007)

Nr. 143 Markus Peters:
Modellierung von Rissausbreitung unter Verwendung der p-Version der XFEM mit einer adaptiven Integrationsmethode (Juli 2007)

Nr. 144 Claus Oberste-Brandenburg:
Thermomechanical modeling of shape memory alloys at different length scales (Juli 2007)

Nr. 145 Stefan Reichling:
Das inverse Problem der quantitativen Ultraschallelastografie unter Berücksichtigung großer Deformationen (Juli 2007)

Nr. 146 Kianoush Molla-Abbasi:
A Consistent Anisotropic Brittle Damage Model Based on the Concept of Growing Elliptical Cracks (Januar 2008)

Nr. 147 Sandra Ilic:
Application of the multiscale FEM to the modeling of composite materials (August 2008)

Nr. 148 Patrick Luig:
A consistent Eulerian rate model for shape memory alloys (Oktober 2008)

Nr. 149 Lidija Stanković:
Describing multiple surface localised failure by means of strong discontinuities at finite strains (Februar 2009)

Mitteilungen aus dem Institut für Mechanik
RUHR-UNIVERSITÄT BOCHUM
Nr. 149

978-3-935892-27-8